



University
of Glasgow

Kettles, Fraser J. (2016) *Synthesis, structure and magnetic properties of heterometallic complexes towards single-molecule magnets using flexible aminopolyol ligands*. PhD thesis.

<https://theses.gla.ac.uk/7488/>

Copyright and moral rights for this work are retained by the author

A copy can be downloaded for personal non-commercial research or study, without prior permission or charge

This work cannot be reproduced or quoted extensively from without first obtaining permission in writing from the author

The content must not be changed in any way or sold commercially in any format or medium without the formal permission of the author

When referring to this work, full bibliographic details including the author, title, awarding institution and date of the thesis must be given

Enlighten: Theses

<https://theses.gla.ac.uk/>
research-enlighten@glasgow.ac.uk

Synthesis, structure and magnetic properties
of heterometallic complexes towards single-
molecule magnets using flexible aminopolyol
ligands

Fraser J. Kettles

MChem

Submitted in fulfilment of the requirements for the
Degree of Doctor of Philosophy

School of Chemistry
College of Science and Engineering
University of Glasgow

2016

Abstract

The work presented herein describes the synthesis, structure and magnetic characterisation of new $3d$, $3d-4f$ and $4f$ complexes synthesised using flexible aminopolyol ligands. The flexibility of these ligands provides rich topological chemistry and in total, forty-five new complexes have been synthesised. The overall aim was to find new single molecule magnets (SMMs) as such molecules have a potential application as ultra-high density data storage media.

Using a combination of a rational and serendipitous approach, the ligand N,N,N',N' -tetrakis(2-hydroxyethyl)ethylenediamine (H_4edte) was used to synthesise two new families of $3d-4f$ complexes: $\{Ln^{III}Cu^{II}_3(H_2edte)_3\}$ and $\{Ln^{III}_4Zn^{II}_2\}$. One new SMM; $\{Tb^{III}Cu^{II}_3(H_2edte)_3\}$ (**6**) was found - confirmed by both magnetic susceptibility and magnetisation hysteresis measurements. $\{Dy^{III}Cu^{II}_3(H_2edte)_3\}$ (**7**) behaved as a field induced SMM; exhibiting fast ground state quantum tunnelling of its magnetisation in zero-field. Inelastic neutron scattering spectroscopy for **6** and **7** found that magnetic relaxation proceeds through the first excited magnetic state which corresponds to a Cu^{II} spin flip – highlighting the role that $3d-4f$ exchange plays in the relaxation dynamics. Magnetic susceptibility measurements were also carried out for the Gd^{III} and Dy^{III} analogues of the $\{Ln^{III}_4Zn^{II}_2\}$ series and are presented.

A new family of single-ion $\{Ln^{III}\}$ complexes was synthesised using H_4edte , magnetic susceptibility measurements were carried out for the Tb^{III} and Dy^{III} analogues and are discussed.

A wide range of new $3d$ complexes were synthesised using H_4edte , these include a number of $\{3d\}$ monomers, a rare mixed valent $\{Mn^{II}Mn^{III}\}$ dimer, a $\{Cu_8\}$ complex, a heterometallic $\{Cu_6Ni_2\}$ complex, and a large $\{Mn^{III}_{10}Cu^{II}_5\}$ complex whose magnetic properties are discussed.

The ligand N,N,N',N' -tetrakis(2-hydroxyethyl)-1,3-diaminopropane (H_4pdte), closely related to H_4edte , was synthesised and used to form a $\{Ln^{III}Cu^{II}_3(H_2pdte)_3\}$ series analogous to the $\{LnCu_3(H_2edte)_3\}$ series. Magnetic susceptibility measurements were carried out and magneto-structural differences between the two series are discussed.

Acknowledgements.....	1
Author's declaration.....	3
Abbreviations.....	4
Compound List.....	6
1. Introduction.....	8
1.1 Magnetisation and Susceptibility.....	8
1.2 Ferromagnetism and Antiferromagnetism.....	10
1.3 Modelling Exchange Interactions.....	13
1.4 Single-Molecule Magnets.....	14
1.5 Slow Magnetic Relaxation.....	17
1.6 Quantifying the Performance of SMMs.....	19
1.7 Moving on From {Mn ₁₂ } Toward Higher Energy Barriers.....	23
1.8 Lanthanide ions – 4 <i>f</i> Orbitals.....	24
1.9 Designing Ln ^{III} Crystal Fields.....	28
1.10 Magnetic Relaxation in Ln ^{III} SMMs.....	30
1.11 3 <i>d</i> -4 <i>f</i> SMMs.....	31
1.12 Synthetic Methods – Aminopolyol Ligands.....	32
1.13 References.....	34
2. Synthesis, Structure and Magnetic Properties of {LnCu ₃ (H ₂ edte) ₃ } Series.....	37
2.1 Introduction.....	37
2.2 Experimental.....	42
2.2.1 Synthesis of [Cu ₂ (H ₃ edte) ₂][NO ₃] ₂ (1).....	42
2.2.2 Synthesis of [PrCu ₃ (H ₂ edte) ₃ (NO ₃)] [NO ₃] ₂ ·0.5MeOH (2).....	42
2.2.3 Synthesis of [NdCu ₃ (H ₂ edte) ₃ (NO ₃)] [NO ₃] ₂ ·0.5MeOH (3).....	43
2.2.4 Synthesis of [EuCu ₃ (H ₂ edte) ₃ (NO ₃)] [NO ₃] ₂ ·0.5MeOH (4).....	43
2.2.5 Synthesis of [GdCu ₃ (H ₂ edte) ₃ (NO ₃)] [NO ₃] ₂ ·0.5MeOH (5).....	44
2.2.6 Synthesis of [TbCu ₃ (H ₂ edte) ₃ (NO ₃)] [NO ₃] ₂ ·0.5MeOH (6).....	44
2.2.7 Synthesis of [DyCu ₃ (H ₂ edte) ₃ (NO ₃)] [NO ₃] ₂ ·0.5MeOH (7).....	45
2.2.8 Synthesis of [ErCu ₃ (H ₂ edte) ₃ (NO ₃)] [NO ₃] ₂ ·0.5MeOH (8).....	46

2.2.9 Synthesis of $[\text{YbCu}_3(\text{H}_2\text{edte})_3(\text{NO}_3)][\text{NO}_3]_2 \cdot 0.5\text{MeOH}$ (9).....	46
2.3 Results and Discussion.....	47
2.3.1 Synthesis.....	47
2.3.2 Discussion of the Crystal Structure of $[\text{Cu}_2(\text{H}_3\text{edte})_2][\text{NO}_3]_2$ (1).....	48
2.3.3 Discussion of the $\{\text{LnCu}_3(\text{H}_2\text{edte})_3\}$ Series' Structure.....	50
2.3.3.1 Torsion Angles.....	54
2.3.3.2 SHAPE Analysis.....	55
2.4 Magnetism.....	57
2.4.1 Static Magnetic Properties of $\{\text{PrCu}_3(\text{H}_2\text{edte})_3\}$ (2).....	57
2.4.2 Dynamic Magnetic Properties of 2	58
2.4.3 Static Magnetic Properties of $\{\text{NdCu}_3(\text{H}_2\text{edte})_3\}$ (3).....	59
2.4.4 Dynamic Magnetic Properties of 3	60
2.4.5 Magnetic Susceptibility Measurements for $\{\text{GdCu}_3(\text{H}_2\text{edte})_3\}$ (5).....	61
2.4.6 Magnetisation vs. Field Measurements for 5	62
2.4.7 Magnetic Susceptibility Measurements for $\{\text{TbCu}_3\}$ (6) and $\{\text{DyCu}_3\}$ (7).....	63
2.4.8 Magnetisation vs. Field Measurements for 6 and 7	64
2.4.9 Dynamic Magnetic Properties of $\{\text{TbCu}_3\}$ (6).....	66
2.4.9.1 Ac Susceptibility.....	66
2.4.9.2 Magnetisation vs. Swept dc Field Scans.....	68
2.4.10 Dynamic Magnetic Properties of $\{\text{DyCu}_3\}$ (7).....	69
2.4.10.1 Ac Susceptibility.....	69
2.4.10.2 Magnetisation vs. Swept dc Field Scans.....	71
2.5 Inelastic Neutron Scattering.....	72
2.5.1 INS of $\{\text{TbCu}_3\}$ (6).....	72
2.5.2 INS of $\{\text{DyCu}_3\}$ (7).....	74
2.6 Conclusions and Future Work.....	76
2.7 References.....	78

3.	Synthesis, Structure and Magnetic Properties of $\{\text{LnCu}_3(\text{H}_2\text{pdte})_3\}$ Series.....	81
3.1	Introduction.....	81
3.2	Experimental.....	85
3.2.1	Synthesis of <i>N,N,N',N'</i> -tetrakis-(2-hydroxyethyl)-1,3-diaminopropane (10).....	85
3.2.2	Synthesis of $[\text{YCu}_3(\text{H}_2\text{pdte})_3(\text{NO}_3)][\text{NO}_3]\cdot 0.5\text{MeOH}$ (11).....	85
3.2.3	Synthesis of $[\text{PrCu}_3(\text{H}_2\text{pdte})_3(\text{NO}_3)][\text{NO}_3]\cdot 0.5\text{MeOH}$ (12).....	86
3.2.4	Synthesis of $[\text{NdCu}_3(\text{H}_2\text{pdte})_3(\text{NO}_3)][\text{NO}_3]\cdot 0.5\text{MeOH}$ (13).....	86
3.2.5	Synthesis of $[\text{EuCu}_3(\text{H}_2\text{pdte})_3(\text{NO}_3)][\text{NO}_3]\cdot 0.5\text{MeOH}$ (14).....	87
3.2.6	Synthesis of $[\text{GdCu}_3(\text{H}_2\text{pdte})_3(\text{NO}_3)][\text{NO}_3]\cdot 0.5\text{MeOH}$ (15).....	87
3.2.7	Synthesis of $[\text{TbCu}_3(\text{H}_2\text{pdte})_3(\text{NO}_3)][\text{NO}_3]\cdot 0.5\text{MeOH}$ (16).....	88
3.2.8	Synthesis of $[\text{DyCu}_3(\text{H}_2\text{pdte})_3(\text{NO}_3)][\text{NO}_3]\cdot 0.5\text{MeOH}$ (17).....	88
3.2.9	Synthesis of $[\text{HoCu}_3(\text{H}_2\text{pdte})_3(\text{NO}_3)][\text{NO}_3]\cdot 0.5\text{MeOH}$ (18).....	89
3.2.10	Synthesis of $[\text{ErCu}_3(\text{H}_2\text{pdte})_3(\text{NO}_3)][\text{NO}_3]\cdot 0.5\text{MeOH}$ (19).....	89
3.2.11	Synthesis of $[\text{YbCu}_3(\text{H}_2\text{pdte})_3(\text{NO}_3)][\text{NO}_3]\cdot 0.5\text{MeOH}$ (20).....	90
3.3	Results and Discussion.....	90
3.3.1	Synthesis.....	90
3.3.2	Discussion of the $\{\text{LnCu}_3(\text{H}_2\text{pdte})_3\}$ Series' Structure.....	92
3.3.2.1	Torsion Angles.....	96
3.3.2.2	SHAPE analysis.....	97
3.4	Magnetism.....	100
3.4.1	Static Magnetic Properties of $\{\text{GdCu}_3(\text{H}_2\text{pdte})_3\}$ (15).....	100
3.4.2	Static Magnetic Properties of $\{\text{TbCu}_3(\text{H}_2\text{pdte})_3\}$ (16).....	104
3.4.3	Dynamic Magnetic Properties of 16	107
3.4.4	Static Magnetic Properties of $\{\text{DyCu}_3(\text{H}_2\text{pdte})_3\}$ (17).....	109
3.4.5	Dynamic Magnetic Properties of 17	111
3.5	Conclusions and Future Work.....	112
3.6	References.....	114

4.	Synthesis, Structure and Magnetic Properties of a $\{Ln_4Zn_2\}$ Series with the Ligand H_4edte	116
4.1	Introduction.....	116
4.2	Experimental.....	118
4.2.1	Synthesis of $[Eu^{III}_4Zn^{II}_2(OH)_2(H_2edte)_4(NO_3)_2Cl_2(MeOH)_2][NO_3]_2$ (21).....	118
4.2.2	Synthesis of $[Gd^{III}_4Zn^{II}_2(OH)_2(H_2edte)_4(NO_3)_2Cl_2(MeOH)_2][NO_3]_2$ (22).....	119
4.2.3	Synthesis of $[Tb^{III}_4Zn^{II}_2(OH)_2(H_2edte)_4(NO_3)_2Cl_2(MeOH)_2][NO_3]_2$ (23).....	119
4.2.4	Synthesis of $[Dy^{III}_4Zn^{II}_2(OH)_2(H_2edte)_4(NO_3)_2Cl_2(MeOH)_2][NO_3]_2$ (24).....	120
4.2.5	Synthesis of $[Ho^{III}_4Zn^{II}_2(OH)_2(H_2edte)_4(NO_3)_2Cl_2(MeOH)_2][NO_3]_2$ (25).....	120
4.2.6	Synthesis of $[Er^{III}_4Zn^{II}_2(OH)_2(H_2edte)_4(NO_3)_2Cl_2(MeOH)_2][NO_3]_2$ (26).....	121
4.2.7	Synthesis of $[Yb^{III}_4Zn^{II}_2(OH)_2(H_2edte)_4(NO_3)_2Cl_2(MeOH)_2][NO_3]_2$ (27).....	122
4.3	Results and Discussion.....	122
4.3.1	Synthesis.....	122
4.3.2	Discussion of the $\{Ln_4Zn_2\}$ Series' Structure.....	124
4.3.3	Powder Diffraction Data.....	130
4.4	Magnetism.....	133
4.4.1	Static Magnetic Properties of $\{Gd_4Zn_2\}$ (22).....	133
4.4.2	Static Magnetic Properties of $\{Dy_4Zn_2\}$ (24).....	138
4.4.3	Dynamic Magnetic Properties of 24	139
4.5	Conclusions and Future Work.....	143
4.6	References.....	145
5.	Monometallic Complexes of $4f$ ions with H_4edte	148
5.1	Introduction.....	148
5.2	Experimental.....	152

5.2.1 Synthesis of $[\text{Y}(\text{H}_4\text{edte})(\text{NO}_3)_2][\text{NO}_3]$ (28).....	152
5.2.2 Synthesis of $[\text{La}(\text{H}_4\text{edte})(\text{NO}_3)_2][\text{NO}_3]$ (29).....	152
5.2.3 Synthesis of $[\text{Pr}(\text{H}_4\text{edte})(\text{NO}_3)_2][\text{NO}_3]$ (30).....	153
5.2.4 Synthesis of $[\text{Nd}(\text{H}_4\text{edte})(\text{NO}_3)_2][\text{NO}_3]$ (31).....	153
5.2.5 Synthesis of $[\text{Gd}(\text{H}_4\text{edte})(\text{NO}_3)_2][\text{NO}_3]$ (32).....	154
5.2.6 Synthesis of $[\text{Tb}(\text{H}_4\text{edte})(\text{NO}_3)_2][\text{NO}_3]$ (33).....	154
5.2.7 Synthesis of $[\text{Dy}(\text{H}_4\text{edte})(\text{NO}_3)_2][\text{NO}_3]$ (34).....	155
5.2.8 Synthesis of $[\text{Ho}(\text{H}_4\text{edte})(\text{NO}_3)_2][\text{NO}_3]$ (35).....	155
5.2.9 Synthesis of $[\text{Er}(\text{H}_4\text{edte})(\text{NO}_3)_2][\text{NO}_3]$ (36).....	156
5.3 Results and Discussion.....	157
5.3.1 Synthesis.....	157
5.3.2 Discussion of the $\{\text{Ln}(\text{H}_4\text{edte})\}$ Series' Structure.....	158
5.4 Magnetism.....	167
5.4.1 Static Magnetic Properties of $\{\text{Tb}(\text{H}_4\text{edte})\}$ (33).....	167
5.4.2 Dynamic Magnetic Properties of 33	168
5.4.3 Static Magnetic Properties of $\{\text{Dy}(\text{H}_4\text{edte})\}$ (34).....	169
5.4.4 Dynamic Magnetic Properties of 34	170
5.5 Conclusions and Future Work.....	171
5.6 References.....	172
6. <i>3d</i> Metal Complexes with H_4edte	174
6.1 Introduction.....	174
6.2 Experimental.....	177
6.2.1 Synthesis of $[\text{Mn}(\text{H}_4\text{edte})(\text{NO}_3)][\text{NO}_3]$ (37).....	177
6.2.2 Synthesis of $[\text{Co}(\text{H}_4\text{edte})(\text{NO}_3)][\text{NO}_3]_2$ (38).....	177
6.2.3 Synthesis of $[\text{Co}(\text{H}_4\text{edte})\text{Cl}][\text{Cl}]$ (39).....	178

6.2.4 Synthesis of [Ni(H ₄ edte)(EtOH)][NO ₃] ₂ (40).....	178
6.2.6 Synthesis of [Ni(H ₄ pdte)][NO ₃] ₂ (41).....	179
6.2.5 Synthesis of [Zn(H ₃ edte)][NO ₃] (42).....	179
6.2.7 Synthesis of [Mn ^{II} Mn ^{III} (Hedte)(H ₃ edte)][ClO ₄] (43).....	180
6.2.8 Synthesis of [Cu ₈ (OAc) ₂ (OMe) ₂ (OH) ₂ (H ₃ edte) ₂ (H ₂ edte) ₂ (OBz) ₂][NO ₃] ₂ [PF ₆] ₂ ·MeOH - ·H ₂ O (44).....	180
6.2.9 Synthesis of [Cu ₆ Ni ₂ (H ₂ edte) ₄ (NO ₃) ₂ (H ₂ O) ₂ (MeOH) ₂ (OH) ₂][NO ₃] ₄ ·2MeOH (45).....	181
6.2.10 Synthesis of [Mn ₁₀ Cu ₅ O ₈ (OBz) ₈ (Hedte) ₄ (H ₂ O) ₄][NO ₃] ₄ ·8MeOH (46).....	181
6.3 Results and Discussion.....	182
6.3.1 Synthesis.....	182
6.3.1.1 Synthesis of 3 <i>d</i> Monomers.....	182
6.3.1.2 Synthesis of Polynuclear Complexes.....	183
6.3.2 Discussion of the Crystal Structure of [Mn(H ₄ edte)(NO ₃)] [NO ₃] (37).....	185
6.3.3 Discussion of the Crystal Structure of [Co(H ₄ edte)(NO ₃)] [NO ₃] ₂ (38).....	187
6.3.4 Discussion of the Crystal Structure of [Co(H ₄ edte)Cl] [Cl] (39).....	189
6.3.5 Discussion of the Crystal Structure of [Ni(H ₄ edte)(EtOH)] [NO ₃] ₂ (40).....	191
6.3.6 Discussion of the Crystal Structure of [Zn(H ₃ edte)] [NO ₃] (41).....	193
6.3.7 Discussion of the Crystal Structure of [Ni(H ₄ pdte)] [NO ₃] ₂ (42).....	195

6.3.8 Discussion of the Crystal Structure of [Mn ^{II} Mn ^{III} (Hedte)(H ₃ edte)][ClO ₄] (43).....	197
6.3.9 Discussion of the Crystal Structure of [Cu ₈ (OAc) ₂ (OMe) ₂ (OH) ₂ (H ₃ edte) ₂ (H ₂ edte) ₂ (OBz) ₂][NO ₃] ₂ [PF ₆] ₂ ·MeOH - ·H ₂ O (44).....	200
6.3.10 Discussion of the Crystal Structure of [Cu ₆ Ni ₂ (H ₂ edte) ₄ (NO ₃) ₂ (H ₂ O) ₂ (MeOH) ₂ (OH) ₂][NO ₃] ₄ ·2MeOH (45).....	204
6.3.11 Discussion of the Crystal Structure of [Mn ₁₀ Cu ₅ O ₈ (OBz) ₈ (Hedte) ₄ (H ₂ O) ₄][NO ₃] ₄ ·8MeOH (46).....	209
6.4 Magnetism.....	218
6.4.1 Static Magnetic Properties of {Mn ₁₀ Cu ₅ } (47).....	218
6.4.2 Dynamic Magnetic Properties of 48	219
6.5 Conclusions and Future Work.....	220
6.6 References.....	221
7. Conclusions.....	224
7.1 {LnCu ₃ (H ₂ edte) ₃ } Series.....	224
7.2 {LnCu ₃ (H ₂ pdte) ₃ } Series.....	225
7.3 {Ln ₄ Zn ₂ } Series.....	225
7.4 {Ln} Series.....	226
7.5 3d Complexes.....	226
7.6 Final remarks.....	227
Appendix.....	228
References.....	229

Acknowledgments

First and foremost, I would like to thank my supervisor Dr Mark Murrie. Thank you for giving me the opportunity to work on such an interesting project and for the four years of excellent guidance and faithful support. Your patience and generosity were invaluable to me and I appreciate immensely the time you took on my behalf. Thank you also to my second supervisor Dr Daniel Price, your insightful explanations and general enthusiasm were inspiring.

Thank you to my fellow work colleagues throughout the years. Thank you to Dr Andrew Farrell for his guidance during my early forays into the world of crystallography. Also for giving me the opportunity to see what it feels like to be a grown man who'd never had a hangover. I'm sorry about your first hangover. Thank you to Dr Fraser Douglas for trying to warn me just how terrible the writing up process can be, the term entering the wormhole was certainly apt. Also, thank you Fraser for completely ruining my bathroom on more than one occasion. Thank you to Dr Vicki Milway for your guidance throughout our time working together. Our discussions about beavers and social faux pas, and of course chemistry will never be forgotten. Thank you to Dr Laura Sharp for showing me how to make ice cream with a football. Thank you to Dr Katie Marriot for educating me on the world of actual beer and that the Queen does indeed cry when someone doesn't make the tea right. Thank you to Maria-Jose Heras for always questioning my motives, in the nicest way. Thank you to Dr Gavin Craig for being there every time somebody needed a swift put down. Every time Alexey Ganin referred to his clubbing shoes and every time somebody on the internet did something wrong. Also, thank you for your efforts maintaining the SQUID and helping me collect data.

To my other compatriots in the department; thank you Francois Yazigi, your calm laid back demeanour helped me through many a stressful situation. Hopefully one day you won't be so stressed yourself. The relentless smoke breaks helped calm my nerves, they also helped me take an extra 3 months probably to finish, however, I'm truly happy I got to spend more time with you. I would also like to thank you for letting me stay in your flat when I had no flat of my own, you really were a good friend. Thank you to Dr Ommid Anamimoghadam for showing me just what Glasgow has to offer on a night out. Thank you to Isabel Abanades for all the Serrano ham, teaching me Spanish and generally being an exceptional friend. Also, thank you for your help, along with Ross Marshall, for your guidance with powder X-ray.

Thank you to Dr Stephen Sproules, your kindness and generosity in giving me a home in the final months of writing up were a massive help. Thank you to Jim Gallagher for helping keep the SQUID here in Glasgow alive. Thank you to Dr Steven Magennis for your moral and academic support. Thank you to Dr Claire Wilson for the many hours you put in teaching me the ways of crystallography, I learned a lot and you were a great and very patient teacher.

Thank you to Dr Lynne Thomas for the help with the crystallography presented in Chapter 2. Thank you as well to Dr Stephan Ochsenein for collecting and modelling the INS data and modelling the magnetic susceptibility data in Chapter 2. Thank you to Dr Floriana Tuna, for collecting magnetic data presented in Chapters 2, 3 and 4.

Thank you to my friends outside of work, especially Laurence Green, living with you for a year and causing trouble for another here in Glasgow truly was some of the best times of my life. Thank you for showing me how to be at peace when everything around me was in total anarchy. Thank you also to David Lockhart. Although you were only in Glasgow a short time, you did try your best to make me late for work every Wednesday. The other friends who visited, Nick Clark, Eddie Harper, Jamie and Alice Crawford, Jonni Wan, Calum Lorimer, Kieren McCruden, Joe Gammie and John Fitzharris, thank you for your friendship and moral support too. Thank you to Kirsty Moreland, you were a great friend and flat mate. Thank you for the support you gave me this year.

Finally, thank you to my family. Thank you to my Dad Bryan Kettles for providing me moral and financial support when I needed it most. Thank you to my brother Donald, for dealing with a somewhat unpredictable brother over the years but always being there to talk to. Thank you for always making me laugh. Thank you to my mum Patricia Kettles. In so many ways I dedicate this to you. You always brought me up to believe in myself and to dig deep when things weren't going my way. You inspire me every day.

Author's Declaration

The work contained in this thesis, submitted for the degree of doctor of philosophy, is my own original work, except where due reference is made to others. No material within has been previously submitted for a degree at this or any other university.

Abbreviations

ac	Alternating current
acac	Acetylacetonate
BVS	Bond valence sum
ChSM	Continuous SHAPE measurement
CSD	Cambridge structural database
Dc	Direct current
DCM	Dichloromethane
DEA	Diethanolamine
DFT	Density functional theory
DMF	Dimethylformamide
Dppz	Dipyridylphenazine
Dpq	Dipyridylquinoxaline
ES-MS	Electrospray mass spectrometry
Et ₂ O	Diethylether
EtOH	Ethanol
F _{calc}	Calculated structure-factor amplitude
F _{obs}	Observed structure factor amplitude
FT-IR	Fourier transform infra-red
<i>g</i>	Landé g-factor
H ₄ edte	<i>N,N,N',N'</i> -tetrakis(2-hydroxyethyl)ethylenediamine
H ₄ pdte	<i>N,N,N',N'</i> -tetrakis(2-hydroxyethyl)propylenediamine
Hfac	Hexafluoroacetylacetone
INS	Inelastic neutron scattering
K	Kelvin
k _B	Boltzmann constant ($1.38 \times 10^{-23} \text{ JK}^{-1}$)
MeCN	Acetonitrile
MeOH	Methanol

Nadca	Sodium dicyanamide
NEt ₃	Triethylamine
NMR	Nuclear magnetic resonance
OAc	Acetate
OBz	Benzoate
Oe	Oersted
Pc	Pthalocyanine
POM	Polyoxometalate
PXRD	Powder X-ray diffraction
Py	Pyridine
QTM	Quantum tunnelling of the magnetisation
SIM	Single ion magnet
SMM	Single-molecule magnet
SQUID	Superconducting quantum interference device
T	Temperature
T_B	Blocking temperature
THF	Tetrahydrofuran
TLC	Thin layer chromatography
U_{eff}	Effective energy barrier to magnetic reorientation
ZFS	Zero-field splitting
θ	Torsion angle (°)
μ_B	Bohr magneton ($9.274 \times 10^{-24} \text{ JT}^{-1}$)
Φ	Skew angle

Compound List

1. $[\text{Cu}_2(\text{H}_3\text{edte})_2][\text{NO}_3]_2$
2. $[\text{PrCu}_3(\text{H}_2\text{edte})_3(\text{NO}_3)][\text{NO}_3]_2 \cdot 0.5\text{MeOH}$
3. $[\text{NdCu}_3(\text{H}_2\text{edte})_3(\text{NO}_3)][\text{NO}_3]_2 \cdot 0.5\text{MeOH}$
4. $[\text{EuCu}_3(\text{H}_2\text{edte})_3(\text{NO}_3)][\text{NO}_3]_2 \cdot 0.5\text{MeOH}$
5. $[\text{GdCu}_3(\text{H}_2\text{edte})_3(\text{NO}_3)][\text{NO}_3]_2 \cdot 0.5\text{MeOH}$
6. $[\text{TbCu}_3(\text{H}_2\text{edte})_3(\text{NO}_3)][\text{NO}_3]_2 \cdot 0.5\text{MeOH}$
7. $[\text{DyCu}_3(\text{H}_2\text{edte})_3(\text{NO}_3)][\text{NO}_3]_2 \cdot 0.5\text{MeOH}$
8. $[\text{ErCu}_3(\text{H}_2\text{edte})_3(\text{NO}_3)][\text{NO}_3]_2 \cdot 0.5\text{MeOH}$
9. $[\text{YbCu}_3(\text{H}_2\text{edte})_3(\text{NO}_3)][\text{NO}_3]_2 \cdot 0.5\text{MeOH}$
10. *N,N,N',N'*-tetrakis-(2-hydroxyethyl)-1,3-diaminopropane (H_4pdte)
11. $[\text{YCu}_3(\text{H}_2\text{pdte})_3(\text{NO}_3)][\text{NO}_3]_2 \cdot 0.5\text{MeOH}$
12. $[\text{PrCu}_3(\text{H}_2\text{pdte})_3(\text{NO}_3)][\text{NO}_3]_2 \cdot 0.5\text{MeOH}$
13. $[\text{NdCu}_3(\text{H}_2\text{pdte})_3(\text{NO}_3)][\text{NO}_3]_2 \cdot 0.5\text{MeOH}$
14. $[\text{EuCu}_3(\text{H}_2\text{pdte})_3(\text{NO}_3)][\text{NO}_3]_2 \cdot 0.5\text{MeOH}$
15. $[\text{GdCu}_3(\text{H}_2\text{pdte})_3(\text{NO}_3)][\text{NO}_3]_2 \cdot 0.5\text{MeOH}$
16. $[\text{TbCu}_3(\text{H}_2\text{pdte})_3(\text{NO}_3)][\text{NO}_3]_2 \cdot 0.5\text{MeOH}$
17. $[\text{DyCu}_3(\text{H}_2\text{pdte})_3(\text{NO}_3)][\text{NO}_3]_2 \cdot 0.5\text{MeOH}$
18. $[\text{HoCu}_3(\text{H}_2\text{pdte})_3(\text{NO}_3)][\text{NO}_3]_2 \cdot 0.5\text{MeOH}$
19. $[\text{ErCu}_3(\text{H}_2\text{pdte})_3(\text{NO}_3)][\text{NO}_3]_2 \cdot 0.5\text{MeOH}$
20. $[\text{YbCu}_3(\text{H}_2\text{pdte})_3(\text{NO}_3)][\text{NO}_3]_2 \cdot 0.5\text{MeOH}$
21. $[\text{Eu}^{\text{III}}_4\text{Zn}^{\text{II}}_2(\text{H}_2\text{edte})_4(\text{NO}_3)_2\text{Cl}_2(\text{MeOH})_2(\text{OH})_2][\text{NO}_3]_2$
22. $[\text{Gd}^{\text{III}}_4\text{Zn}^{\text{II}}_2(\text{H}_2\text{edte})_4(\text{NO}_3)_2\text{Cl}_2(\text{MeOH})_2(\text{OH})_2][\text{NO}_3]_2$
23. $[\text{Tb}^{\text{III}}_4\text{Zn}^{\text{II}}_2(\text{H}_2\text{edte})_4(\text{NO}_3)_2\text{Cl}_2(\text{MeOH})_2(\text{OH})_2][\text{NO}_3]_2$
24. $[\text{Dy}^{\text{III}}_4\text{Zn}^{\text{II}}_2(\text{H}_2\text{edte})_4(\text{NO}_3)_2\text{Cl}_2(\text{MeOH})_2(\text{OH})_2][\text{NO}_3]_2$
25. $[\text{Ho}^{\text{III}}_4\text{Zn}^{\text{II}}_2(\text{H}_2\text{edte})_4(\text{NO}_3)_2\text{Cl}_2(\text{MeOH})_2(\text{OH})_2][\text{NO}_3]_2$
26. $[\text{Er}^{\text{III}}_4\text{Zn}^{\text{II}}_2(\text{H}_2\text{edte})_4(\text{NO}_3)_2\text{Cl}_2(\text{MeOH})_2(\text{OH})_2][\text{NO}_3]_2$
27. $[\text{Yb}^{\text{III}}_4\text{Zn}^{\text{II}}_2(\text{H}_2\text{edte})_4(\text{NO}_3)_2\text{Cl}_2(\text{MeOH})_2(\text{OH})_2][\text{NO}_3]_2$
28. $[\text{Y}(\text{H}_4\text{edte})(\text{NO}_3)_2][\text{NO}_3]$
29. $[\text{La}(\text{H}_4\text{edte})(\text{NO}_3)_2][\text{NO}_3]$
30. $[\text{Pr}(\text{H}_4\text{edte})(\text{NO}_3)_2][\text{NO}_3]$
31. $[\text{Nd}(\text{H}_4\text{edte})(\text{NO}_3)_2][\text{NO}_3]$
32. $[\text{Gd}(\text{H}_4\text{edte})(\text{NO}_3)_2][\text{NO}_3]$
33. $[\text{Tb}(\text{H}_4\text{edte})(\text{NO}_3)_2][\text{NO}_3]$
34. $[\text{Dy}(\text{H}_4\text{edte})(\text{NO}_3)_2][\text{NO}_3]$

35. $[\text{Ho}(\text{H}_4\text{edte})(\text{NO}_3)_2][\text{NO}_3]$
36. $[\text{Er}(\text{H}_4\text{edte})(\text{NO}_3)_2][\text{NO}_3]$
37. $[\text{Mn}(\text{H}_4\text{edte})(\text{NO}_3)][\text{NO}_3]$
38. $[\text{Co}(\text{H}_4\text{edte})(\text{H}_2\text{O})][\text{NO}_3]_2$
39. $[\text{Co}(\text{H}_4\text{edte})\text{Cl}][\text{Cl}]$
40. $[\text{Ni}(\text{H}_4\text{edte})(\text{EtOH})][\text{NO}_3]_2$
41. $[\text{Ni}(\text{H}_4\text{pdte})][\text{NO}_3]_2$
42. $[\text{Zn}(\text{H}_3\text{edte})][\text{NO}_3]$
43. $[\text{Mn}^{\text{II}}\text{Mn}^{\text{III}}(\text{Hedte})(\text{H}_3\text{edte})][\text{ClO}_4]$
44. $[\text{Cu}_8(\text{OAc})_2(\text{MeOH})_2(\text{OH})_2(\text{H}_2\text{edte})_4(\text{OBz})_2][\text{NO}_3]_2[\text{PF}_6]_2 \cdot \text{MeOH} \cdot \text{H}_2\text{O}$
45. $[\text{Cu}_6\text{Ni}_2(\text{H}_2\text{edte})_4(\text{NO}_3)_2(\text{H}_2\text{O})_2(\text{MeOH})_2(\text{OH})_2][\text{NO}_3]_4 \cdot 2\text{MeOH}$
46. $[\text{Mn}_{10}\text{Cu}_5\text{O}_8(\text{OBz})_8(\text{Hedte})_4(\text{H}_2\text{O})_4][\text{NO}_3]_4 \cdot 8\text{MeOH}$

1. Introduction

1.1 Magnetisation and Susceptibility

An electron has an associated magnetic moment which is the combination of its spin moment and its orbital angular momentum. The spin of an electron is $s = \frac{1}{2}$ and is composed of two m_s microstates $m_s = \pm \frac{1}{2}$ which correspond to the orientation of the spin relative to a magnetic field. In the absence of a field, the two m_s states are degenerate, however when a field is applied the degeneracy is removed; the m_s state orientated parallel to the field is lowered in energy whilst the antiparallel's energy is increased (Figure 1.1).¹

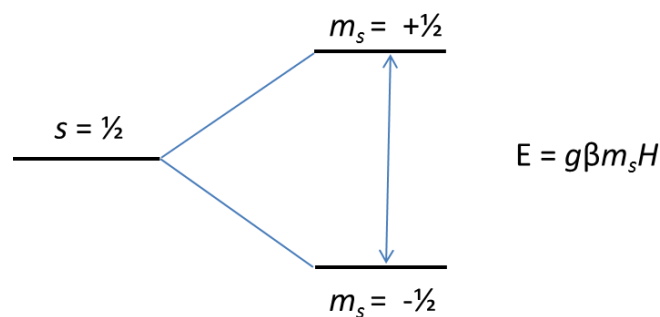


Figure 1.1: Zeeman splitting of an electron's m_s microstates in a magnetic field H , the $-\frac{1}{2}$ m_s state aligns parallel with H so is lowered in energy.

This splitting in energy is known as Zeeman splitting, with the energy of each state given by Equation 1.1, where g is the Landé g -value, β is the Bohr Magneton and H is the magnetic field strength. In accordance with Maxwell-Boltzmann statistics, a sample population of unpaired electrons will favourably populate the lowest energy m_s state in a magnetic field. As the field is increased, or thermal energy decreased, the population of the ground state increases. Therefore, in a large enough field eventually only the ground state will be populated, at which point the saturation magnetisation has been reached (Equation 1.2).²

$$E = m_s g \beta H$$

$$M_{sat} = gS$$

Equations 1.1 and 1.2

Magnetic susceptibility is a measure of how readily a material can be magnetised. In a homogenous magnetic field H , a sample will acquire a magnetisation M , the ratio of which gives the volume susceptibility χ_v (Equation 1.3).

$$\chi_v = \frac{dM}{dH}$$

Equation 1.3

In weak fields, χ is independent of temperature, giving Equation 1.4.

$$\chi_v = \frac{M}{H}$$

Equation 1.4

More commonly a material's susceptibility is reported as its molar magnetic susceptibility (χ), which is a combination of the material's paramagnetic and diamagnetic susceptibilities (Equation 1.5).³

$$\chi = \chi_{para} + \chi_{dia}$$

Equation 1.5

Paramagnetic susceptibility is generated by unpaired electrons within a material and is usually much greater than the diamagnetic susceptibility. Diamagnetic susceptibility arises from the interaction of paired electrons with a magnetic field. When placed in a magnetic field, a small magnetic moment opposite in sign to the applied field is induced hence diamagnetic materials (those with no unpaired electrons) are repelled from a magnetic field. Even for paramagnetic metal ions, there is still a diamagnetic contribution due to filled orbital subshells which needs to be accounted for. Estimation of the diamagnetic contribution is often done using Pascal's constants, or by using the approximation given by Equation 1.6, where Mw is the molecular weight of the material.⁴

$$\chi_{dia} = \frac{1}{2} Mw \times 10^{-6} \text{ cm}^3 \text{ mol}^{-1}$$

Equation 1.6

The Curie law relates the magnetic susceptibility of a material with temperature and is given in Equation 1.7, where N is Avagadro's number, k_B is the Boltzmann constant, T is temperature and S the ground state spin.

$$\chi = \frac{Ng^2\beta^2}{3k_B T} S(S+1)$$

Equation 1.7

A useful approximation of the Curie law is given in Equation 1.8; conveniently, the value of the constants $N\beta^2/3k_B$ is $\frac{1}{8}$ (in cgs units).

$$\chi T = \frac{g^2}{8} S(S+1)$$

Equation 1.8

A paramagnetic material consists of magnetic ions which do not interact with each other. When a field is applied, the magnetic moments of the ions align with the field, and an increase in susceptibility is observed. As the temperature is increased, the spins tend to randomise and a decrease in susceptibility is observed. For a pure paramagnet, obeying Curie behaviour, χT is temperature independent. When the magnetic ions begin to interact with each other, χT is no longer independent of temperature; hence graphs of χT vs. T provide information on the nature of magnetic ordering within a material.

1.2 Ferromagnetism and Antiferromagnetism

Spontaneous ordering of adjacent magnetic moments profoundly affects a material's magnetic properties. There are two main types of ordering; ferromagnetic and antiferromagnetic. Ferromagnetism occurs when magnetic moments on neighbouring ions spontaneously align parallel to each other and antiferromagnetism when they align antiparallel (Figure 1.2).

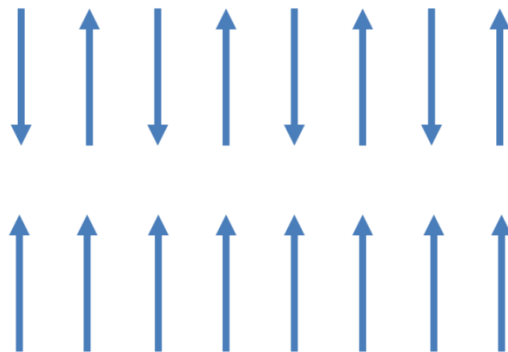


Figure 1.2: Schematic representation of antiferromagnetic (top) and ferromagnetic (bottom) alignment of magnetic moments.

For a pure paramagnet, that is where no exchange interactions are present, a graph of $1/\chi$ vs. T will be a straight line passing through the origin (Figure 1.3). However, when either ferromagnetic or antiferromagnetic ordering is present, the intercept of the straight line deviates from the origin.

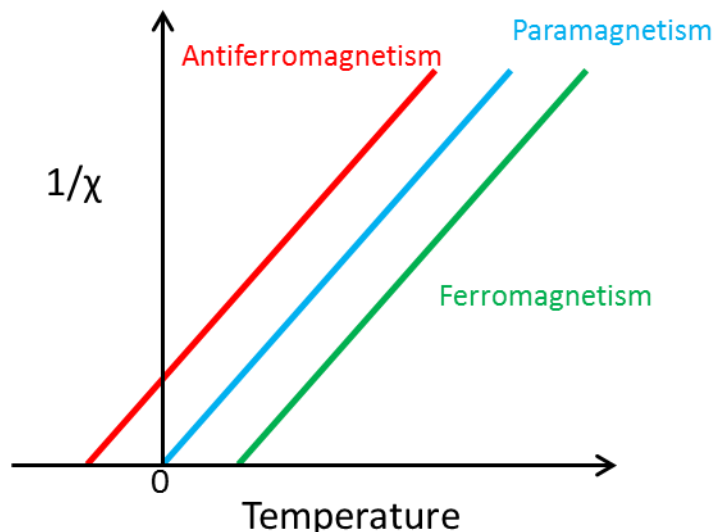


Figure 1.3: Graph of $1/\chi$ vs. T for a pure paramagnet (blue), an antiferromagnet (red) and ferromagnet (green).

This is accounted for by the Weiss-constant (θ) in the Curie-Weiss law (Equation 1.9) which represents an estimate of the strength of the magnetic exchange interaction between ions. A negative θ corresponds to antiferromagnetic coupling and a positive ferromagnetic coupling, the larger the magnitude, the stronger the coupling.

$$\chi = \frac{C}{T - \theta}$$

Equation 1.9

Exchange interactions between neighbouring magnetic centres lead to magnetic ordering. There are two main types of exchange interaction; direct exchange and superexchange. Direct exchange occurs between centres whose magnetic orbitals are close enough in space to overlap directly. An example of this is the Mo^{III} dimer; $[\text{X}_3\text{Mo}(\mu\text{-X})_3\text{MoX}_3]^{3-}$, where X = halide, where the antiferromagnetic coupling between Mo^{III} ions was largely attributed to direct overlap of d -orbitals facilitated by their close proximity (Figure 1.4).⁵

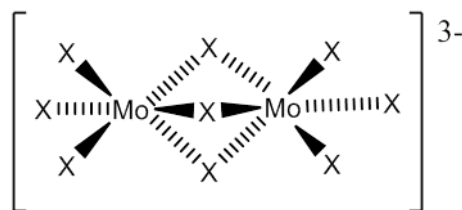


Figure 1.4: Molecular structure of $[X_3Mo(\mu-X)_3MoX_3]^{3-}$ (where $X = \text{halide}$) which exhibits direct exchange between unpaired electrons on the Mo^{III} ions.

The defining aspect of superexchange is an intermediary diamagnetic atom/ion bridging between the magnetic centres. Goodenough-Kanamori rules⁶ provide a basis to describe the superexchange mechanism, relating the M-L-M (M = metal with unpaired electrons, L = bridge) bond angle to the observed ordering (Figures 1.5 and 1.6). Common bridging species are oxygen or chloride, whose frontier orbitals are p -orbitals.

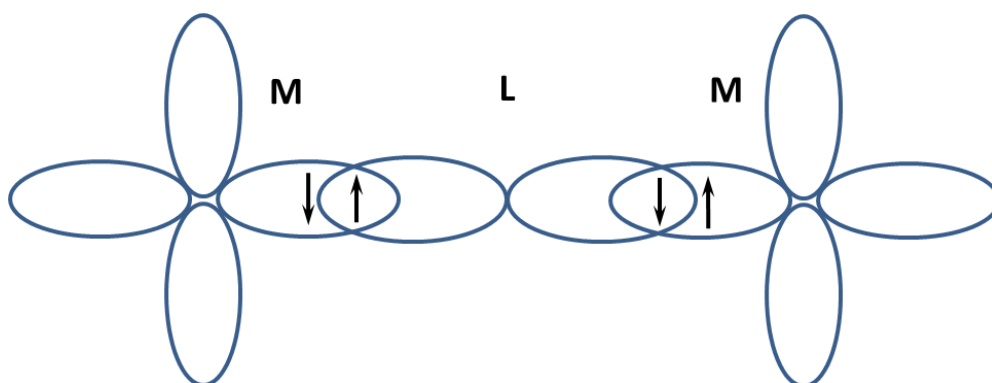


Figure 1.5: Superexchange when M-L-M is 180° , resulting in antiferromagnetic ordering of magnetic centres.

When M-L-M is 180° (Figure 1.5), the unpaired electron on the first metal ion pairs with the electron of opposite spin in the bridging ligand's p -orbital. The other electron in the same p -orbital, with opposite spin, then pairs with the unpaired electron in the second metal ion – leading to antiferromagnetic ordering. When the M-L-M angle is 90° , the exchange becomes ferromagnetic between metal ions (Figure 1.6). This is driven by electrons in orthogonal p -orbitals on the bridging atom aligning ferromagnetically with each other - in accordance with Hund's first rule⁸ – thus, the two metal ion's electrons will also be aligned ferromagnetically.

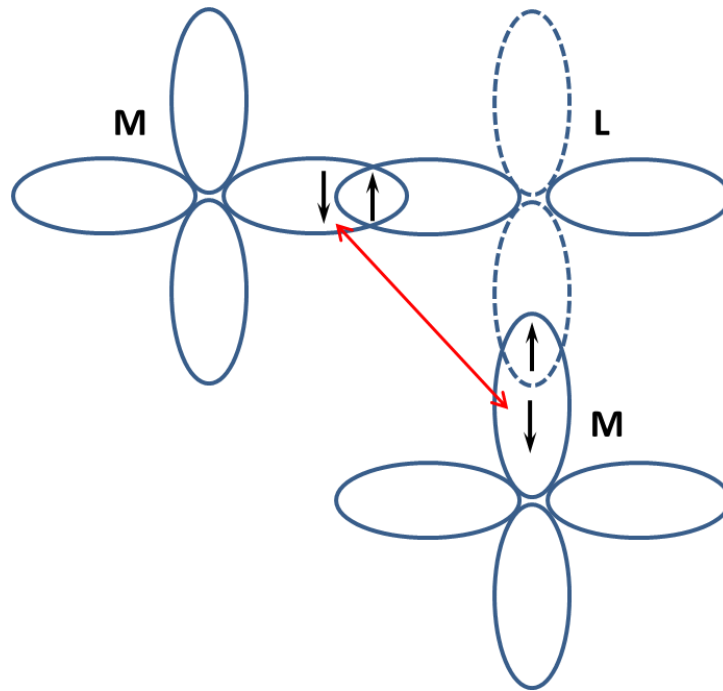


Figure 1.6: Superexchange when $M-L-M$ is 90° , resulting in ferromagnetic ordering of magnetic centres.

The superexchange mechanism works well for $3d$ metal ions, however is not as readily applicable to $4f$ ions due to their buried nature and resulting poorer overlap with bridging ligand orbitals.⁹

1.3 Modelling Exchange Interactions

If we consider a simple example of two interacting metal centres each with $s = \frac{1}{2}$, the two spins can either align ferromagnetically or antiferromagnetically (Figure 1.7).

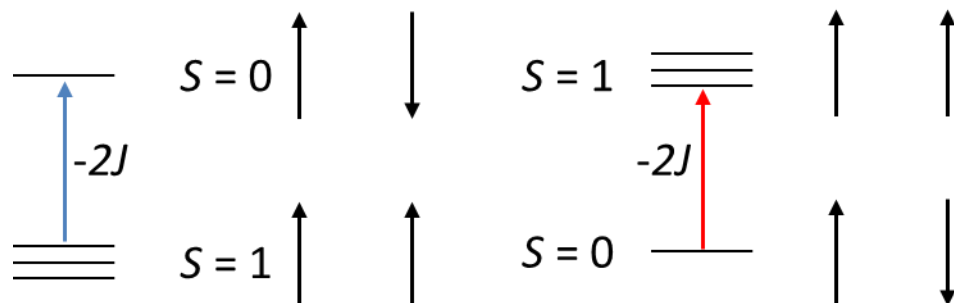


Figure 1.7: System of two $s = \frac{1}{2}$ ions interacting ferromagnetically (left) and antiferromagnetically (right). The excited states are separated from the ground states relative to the strength of the exchange interaction, represented by $-2J$.

If the two spins couple antiferromagnetically, the total spin of the system is $S = 0$, which is lower in energy compared to the $S = 1$ state (left, Figure 1.7). Conversely, if the exchange is ferromagnetic the $S = 1$ state will be lower in energy compared to the $S = 0$ state (right Figure 1.7). The strength of the exchange interaction is represented by $-2J$, where J is referred to as the isotropic exchange constant. The stronger the exchange (larger $|J|$), the larger the energy separation between the two S states. For interacting spins, the simplest spin Hamiltonian (Equation 1.10) can be used to define the energy of the system.¹⁰

$$\hat{H} = -2J\vec{s}_1 \cdot \vec{s}_2$$

Equation 1.10

It should be noted that there are other forms of the spin Hamiltonian where the sign of J and/or the factor of 2 vary. Here, the $-2J$ version is used; a negative value of J corresponds to antiferromagnetic exchange, and positive to ferromagnetic exchange. Care therefore needs to be taken when comparing J parameters from different sources. The Hamiltonian can be extended to account for other factors that might be contributing to the system's energy; such as Zeeman splitting, spin-orbit coupling, the crystal field and the nuclear hyperfine interaction. Hamiltonians can also be written for systems with larger numbers of spin centres with multiple exchange pathways $J_1, J_2...$ etc. Magnetisation and susceptibility data as a function of temperature can be modelled using a Hamiltonian to assess the nature and strength of the magnetic exchange, the magnitude of g and the ground state spin of the system.

1.4 Single-Molecule Magnets

A single-molecule magnet (SMM) is defined as a coordination complex which retains its magnetisation after it has been removed from an applied magnetic field due to an intrinsic energy barrier to magnetic relaxation.¹¹ The first SMM was $[\text{Mn}_8^{\text{III}}\text{Mn}_4^{\text{IV}}\text{O}_{12}(\text{OAc})_{16}(\text{H}_2\text{O})_4] \cdot 4\text{H}_2\text{O} \cdot 2\text{HOAc}$ (abbreviated to $\{\text{Mn}_{12}\}$ hereafter) and has become the most studied SMM to date. It was first synthesised by Lis in 1980¹² but it was not until 1993 that its magnetic properties were studied.¹² $\{\text{Mn}_{12}\}$ provides an excellent starting point to introduce and discuss the properties of SMMs in general. Although based on $3d$ metals only, many of the concepts are analogous to those for $3d-4f$ and $4f$ SMMs (see later). The $\{\text{Mn}_{12}\}$ molecule (Figure 1.8) consists of a central $\{\text{Mn}^{\text{IV}}_4\text{O}_4\}$ core bridged to an outer $\{\text{Mn}^{\text{III}}_8\}$ ring through O^{2-} and OAc^- groups. The inner Mn^{IV} ions couple

antiferromagnetically to the outer Mn^{III} ions, giving the molecule a spin ground state of $S = 10$.

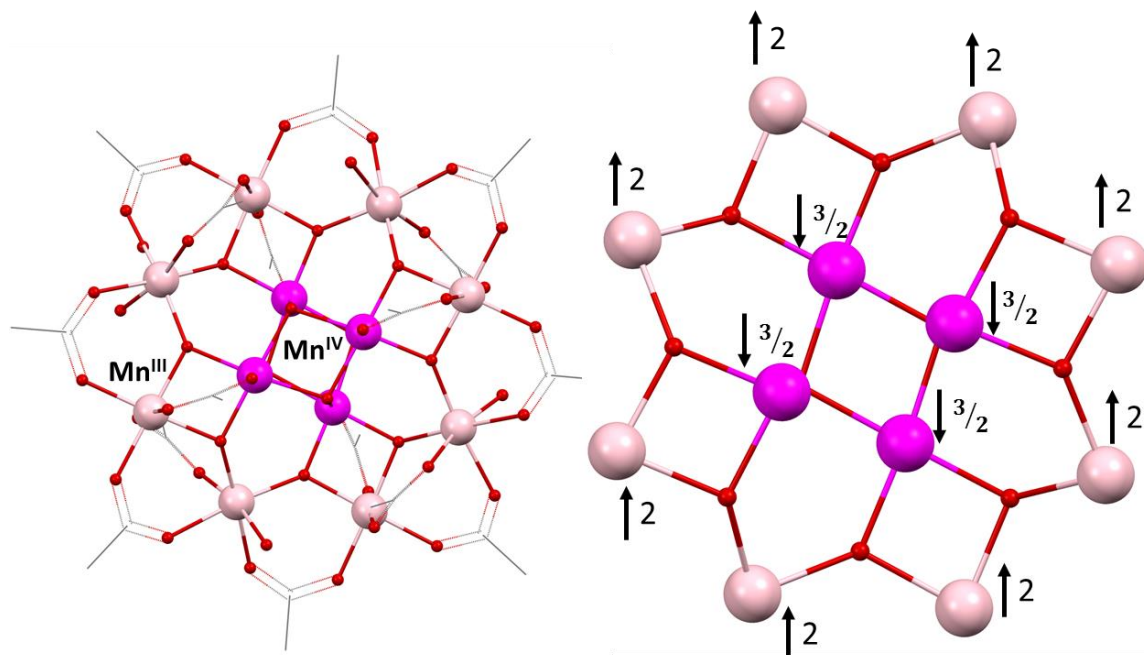


Figure 1.8: (Left) *Molecular structure of $\{Mn_{12}\}$ adapted from reference 14.* (Right) *Arrangement of spins in $\{Mn_{12}\}$. Atom colours: pink, Mn^{III} ; purple, Mn^{IV} ; red, O; grey, C. H-atoms and solvent molecules omitted for clarity.*

The $S = 10$ state is split further, without the application of a magnetic field, into $M_s = 0, \pm 1, \pm 2, \pm 3, \pm 4, \dots, \pm 10$ states which occupy a double well energy potential (Figure 1.9).

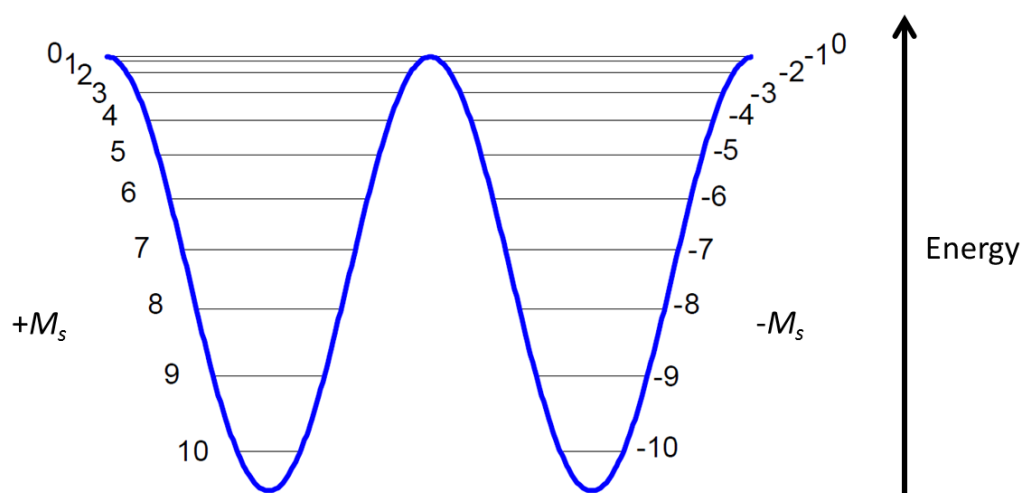


Figure 1.9: *Double well potential of M_s states of $\{Mn_{12}\}$ in zero applied field. In the absence of an applied field, M_s states of the same size are degenerate, i.e. the $M_s = -10$ state is degenerate with its $+10$ counterpart. Figure adapted from reference 22.*

The splitting of the M_s states without an applied magnetic field is a phenomenon referred to as zero-field splitting (ZFS) and is a consequence of spin-orbit coupling associated with the Mn ions. ZFS gives the molecule a magnetic anisotropy and is quantified using the axial ZFS parameter D . The magnitude of D dictates the energy separation of the M_s states, and the sign dictates the ordering of the states. $\{\text{Mn}_{12}\}$ has a negative D value which orders the M_s states from highest to lowest (Figure 1.9) and is an essential prerequisite for SMM behaviour.¹⁵ Having a negative D ensures that the ground M_s state is degenerate - the origin of magnetic bistability. The M_s quantum number describes the projection of the molecule's spin moment onto its z -axis, with the highest number M_s state having the greatest projection on z (Figure 1.10). This results in what is known as an easy-axis of magnetisation, also referred to as Ising-type anisotropy whereby the magnetic moment preferentially orients along the z -axis. In effect, the complex can be magnetised in either an 'up' or 'down' fashion along the easy axis. On the other hand, when D is positive, the non-degenerate $M_s = 0$ state is the ground state. This results in easy plane magnetic anisotropy (and a hard axis) whereby the magnetic moment energetically favours free rotation in the xy plane therefore cannot be magnetised in the 'up' or 'down' sense.⁹

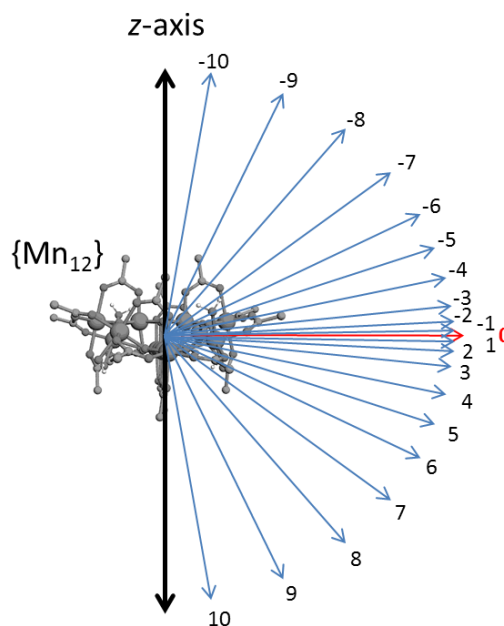


Figure 1.10: Schematic representation of projection of the magnetic moments of the M_s states onto the z -axis of $\{\text{Mn}_{12}\}$. The $M_s \pm 10$ states have the largest projection on z , leading to uniaxial anisotropy. Adapted from reference 22.

In a sample population of $\{\text{Mn}_{12}\}$ molecules, the M_s states are populated depending on the amount of thermal energy available. If there is only enough thermal energy for the $M_s \pm 10$ states to be populated, the sample will be in equilibrium with 50% of the molecules in the

+10 state and 50% in the -10 state (left, Figure 1.11, where X represents an individual $\{Mn_{12}\}$ molecule).

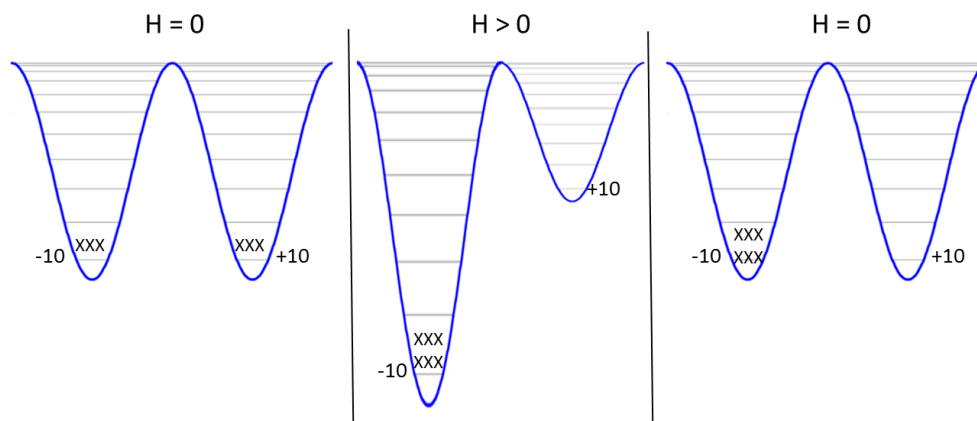


Figure 1.11: (left) Energy splitting (not to scale) of $\{Mn_{12}\}$ M_s states in zero field with equal population of ± 10 states. (centre) After a field is applied, the state with lowest energy in the field ($M_s = -10$) becomes populated. (right) After the field is removed, the molecules remain magnetised in the $M_s = -10$ state.

When the sample population is placed in a magnetic field, still at low temperature, one side of the double well is energetically stabilised. The ordering of the states (from lowest to highest) becomes $M_s = -10, -9, -8, \dots, 0, \dots, +8, +9, +10$, therefore if the field is strong enough, 100% of the sample population will be magnetised in the $M_s = -10$ state (centre, Figure 1.11). When the field is removed, the molecules retain their magnetisation due to an energy barrier to magnetic relaxation – the definition of an SMM. A net magnetisation for the sample is retained for as long as the molecules remain magnetised on one side of the well, return to 50-50 occupation signifies a return to zero net sample magnetisation.

1.5 Slow Magnetic Relaxation

There are three main ways in which a population of SMMs can lose their overall magnetisation: absorption of thermal energy, quantum tunnelling of the magnetisation (QTM) and a combination of both.^{15,16} These relaxation mechanisms are also present in $4f$ SMMs (Section 1.10). Revisiting the double potential well, the depth of the well governs the amount of thermal energy required to achieve ‘over the barrier’ magnetic relaxation. Absorption of thermal energy in the form of phonons promotes molecules into excited spin states. Once they absorb enough energy, equivalent to U , they reach the top of the barrier, at which point they can then relax (through phonon emission) down into the other side –

re-establishing magnetic equilibrium. The depth of the well is proportional to the molecule's spin ground state and the magnitude of D and can be calculated using Equation 1.11 for molecules with integer spin ground states and Equation 1.12 for non-integer spin ground states.

$$U = S^2|D|$$

$$U = \left(S^2 - \frac{1}{4}\right)|D|$$

Equation 1.11 and 1.12

Therefore to increase the energy barrier, complexes with a large spin ground state and large magnetic anisotropy are desired. As mentioned in Section 1.4, the sign of D dictates the energetic ordering of the M_s states. For magnetic bistability D needs to be negative; if D is positive, the singlet $M_s = 0$ state lies lowest in energy.

The second relaxation mechanism, QTM, is a non-thermally activated process; instead of molecules climbing over the barrier they can spontaneously tunnel to the other side (Figure 1.12).

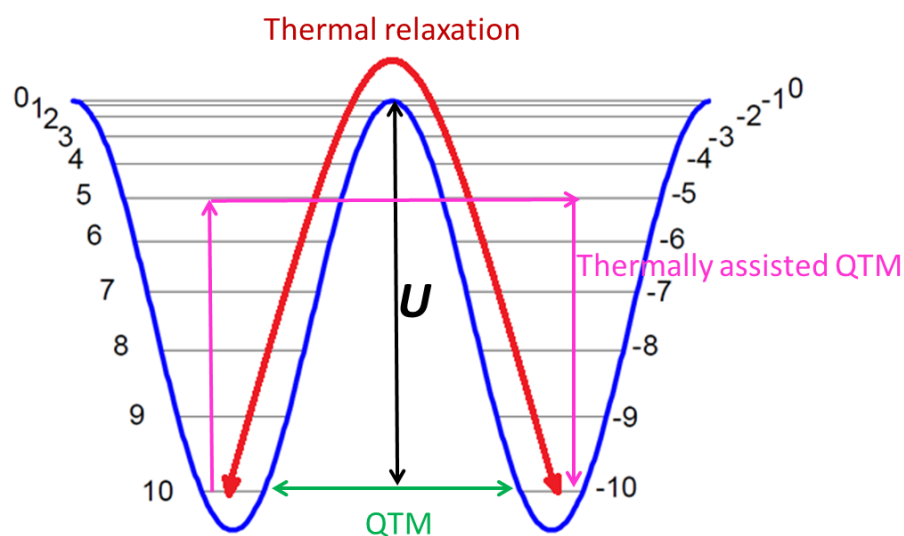


Figure 1.12: Relaxation paths in 3d SMMs. Thermal ‘over the barrier’ relaxation (red arrow), QTM ‘through the barrier’ (green arrow) and thermally assisted QTM (purple arrows).

In order for QTM to occur, there needs to be a quantum mechanical admixing of wavefunctions of the M_s states on either side of the barrier. Admixing can be caused by applying a magnetic field in the xy plane, known as a transverse field, which induces

admixing of M_s states differing by ± 1 . Admixing can also be induced by transverse magnetic anisotropy which is a property of the molecule itself. The ZFS Hamiltonian contains the transverse anisotropy term (Equation 1.13).

$$\hat{H}_{ZFS} = D \underbrace{\left[\hat{S}_Z^2 - \frac{1}{3} S(S+1) \right]}_{\text{Axial term}} + E \underbrace{(\hat{S}_X^2 - \hat{S}_Y^2)}_{\text{Transverse term}}$$

Equation 1.13

In Equation 1.13, E is the transverse (or rhombic) ZFS parameter. A non-zero E term results in admixing of M_s states differing by ± 2 and facilitates QTM.¹⁶ Importantly, the E term vanishes for complexes with axial symmetry, hence they show greatly suppressed QTM. The E term also vanishes for complexes with at least C_3 symmetry as demonstrated by a $\{\text{Mn}_6\text{Cr}\}$ complex reported by Glaser *et al.*¹⁷ The six Mn^{III} ions are bridged to a central Cr^{III} ion through CN^- ligands with the C_3 symmetry axis passing through the central Cr^{III} ion.

The third relaxation mechanism is known as thermally assisted QTM, whereby molecules in thermally excited M_s states tunnel through to the opposite side of the well. In fact, tunnelling between $\pm M_s$ states nearer the top of the barrier has a higher probability.¹⁸ When thermally assisted tunnelling is accounted for, the effective energy barrier, U_{eff} , is less than the thermally activated barrier (U). The effective barrier is often reported as an indication of the performance of a SMM.

1.6 Quantifying the Performance of SMMs

In order for a complex to be fully considered as a SMM, it needs to have an energy barrier to magnetisation reversal, as well as show magnetic bistability once an applied field is removed – magnetic hysteresis.

To search for slow magnetic relaxation, alternating current (ac) susceptibility measurements can be carried out.¹⁹ This involves applying a small magnetic field which oscillates at different frequencies (ν) to a sample at low temperatures (usually 10 - 1.8 K). When the induced magnetisation of the sample is able to keep up with the oscillating field, an in-phase susceptibility (χ') is measured. Once ν becomes large enough, the sample's

magnetisation can no longer keep up with the field due to the energy barrier, leading to the emergence of out-of-phase susceptibility (χ'') signals. The overall susceptibility of a compound is a combination of the in-phase and out-of-phase susceptibilities, shown in Equations 1.14 – 1.16 where φ is the phase shift. Therefore, the emergence of χ'' signals is accompanied by a concomitant decrease in the respective χ' signals (Figure 1.13).

$$\chi' = \chi \cos\varphi$$

$$\chi'' = \chi \sin\varphi$$

$$\chi = \sqrt{\chi''^2 + \chi'^2}$$

Equations 1.14 – 1.16

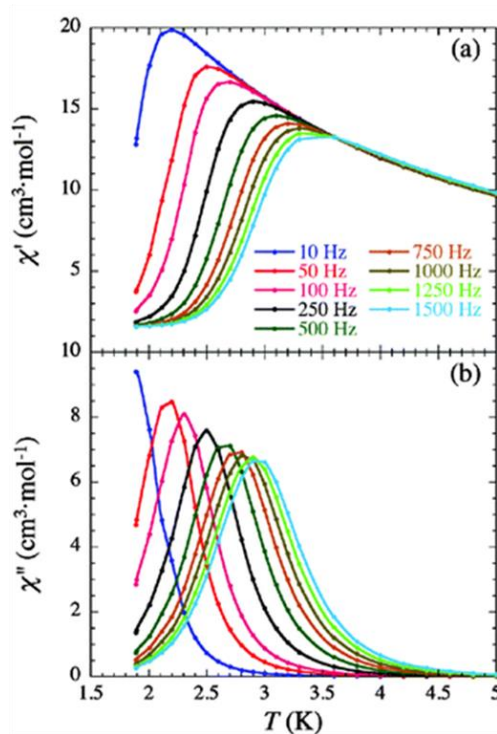


Figure 1.13: *Temperature dependent ac susceptibility data for a $\{Mn_4\}$ SMM,²⁰ illustrating temperature dependent decrease in χ' and concomitant increase in χ'' . Out-of-phase signals begin to appear at higher temperatures and higher frequencies.*

The maxima of the out-of-phase signals are frequency and temperature dependent for SMMs and can be used to calculate U_{eff} . The magnetic relaxation behaviour of SMMs follows an Arrhenius law for a thermally activated process - where U_{eff} is the activation energy (Equation 1.17).

$$\tau = \tau_0 \exp\left(\frac{U_{eff}}{k_B T}\right)$$

$$\tau = \frac{1}{2\pi\nu}$$

Equation 1.17

Where T is the temperature at which the maximum in χ'' is observed at a particular frequency, ν (in Hz), k_B is the Boltzmann constant, τ the relaxation time (in s) and τ_0 a constant (sometimes referred to as the attempt frequency). In the thermal relaxation regime, a plot of $\ln \tau$ vs. $1/T$ gives a straight line with gradient equal to U_{eff}/k_B and intercept equal to τ_0 . At low enough temperatures, only QTM is possible and a deviation from Arrhenius behaviour is observed (Figure 1.14).

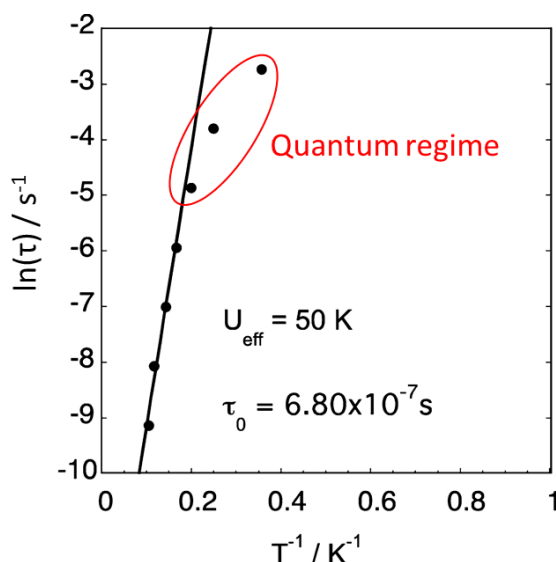


Figure 1.14: Arrhenius plot for a Dy^{III} mononuclear SMM.²¹ Magnetic relaxation in Ln^{III} SMMs is analogous to 3d SMMs and can be modelled in the same way (Section 1.10). The straight line corresponds to thermal regime relaxation where thermal and thermally assisted tunnelling mechanisms are present. The deviation (red circle) indicates where relaxation enters the quantum regime. Eventually the data points become horizontal as the temperature decreases – indicating temperature independent relaxation.

Ac measurements can be performed with an additional dc field applied to the sample to suppress QTM; the dc field off sets degenerate M_s states on either side of the potential well, theoretically blocking QTM (Figure 1.15).

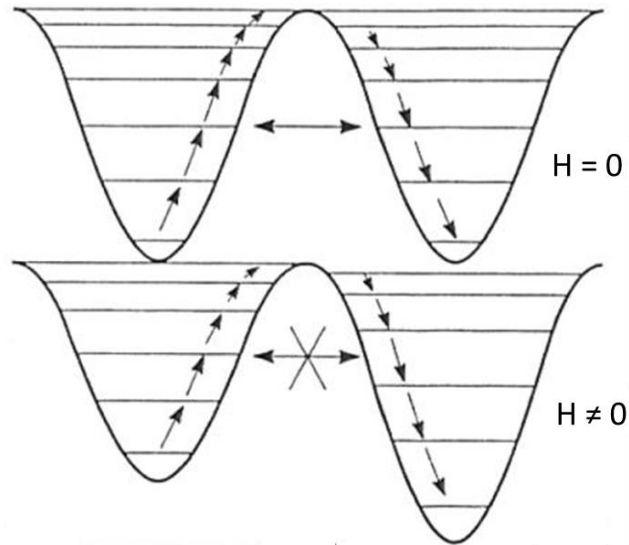


Figure 1.15: Schematic representation of the offsetting of degenerate M_s states when a small dc field (H) is applied – inhibiting QTM. Adapted from reference 13.

Another method used to quantify the performance of SMMs is a magnetisation vs. swept field measurement. This involves magnetising a sample at very low temperatures in one direction, then sweeping the field back through zero to magnetise the sample in the opposite direction. For an SMM, there will be a remnant magnetisation at zero applied field due to the energy barrier to magnetic relaxation – resulting in open hysteresis loops. The temperature at which hysteresis loops begin to open up is referred to as the blocking temperature (T_B) and is also used to quantify SMM performance. Hysteresis loops (and T_B) are temperature and sweep rate dependent; wider loops being observed at higher sweep rates and lower temperatures.¹⁹ Importantly therefore, care needs to be taken when comparing values of T_B in the literature. Hysteresis measurements show whether or not a compound displays fast ground state QTM and hence cannot retain its magnetic bistability in zero field. This is the reason for which hysteresis measurements are required as well as ac measurements; a complex can have non-zero χ'' signals but have no magnetic memory in the absence of an applied field. A signature of SMMs, differentiating them from bulk magnetic materials are steps in their hysteresis loops (Figure 1.16). As the field is applied and one side of the potential well is lowered in energy, different M_s states on either side of the well come in and out of resonance resulting in sudden drops in the magnetisation as QTM occurs between the resonant levels.

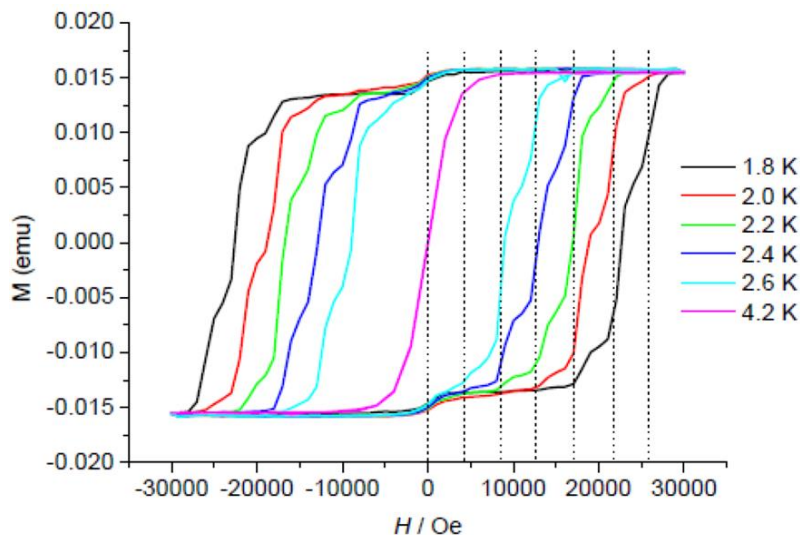


Figure 1.16: Hysteresis loops for $\{Mn_{12}\}$, taken from reference 22. The steps are due to loss of magnetisation due to QTM as M_s states across the barrier come into resonance.

1.7 Moving on from $\{Mn_{12}\}$ Toward Higher Energy Barriers

Since the discovery of $\{Mn_{12}\}$ and its derivatives, many research groups focussed on synthesising new $3d$ complexes with larger energy barriers by searching for complexes with larger spin ground states than $S = 10$. Using Equation 1.11 ($U = S^2/D$), a rationale of aiming for larger spin ground states was adopted because conceptually it was simpler than increasing D and the energy barrier was proportional to the square of S . This approach led to the synthesis of some high nuclearity Mn complexes, the largest example being a $\{Mn_{84}\}$ complex; $[Mn^{III}_{84}O_{72}(OAc)_{78}(OMe)_{24}(MeOH)_{12}(H_2O)_{42}(OH)_6] \cdot xH_2O \cdot yCHCl_3$.²³ Unfortunately though, due to dominant intramolecular antiferromagnetic exchange the complex had a disappointingly small spin ground state of $S = 6$ and a U_{eff} of 18 K, far behind the best for the $\{Mn_{12}\}$ series of 74.4 K.²⁴ Another interesting example was an $\{Mn_{19}\}$ complex which had an extremely large spin ground state of $83/2$.²⁵ Again though, SMM performance was still surpassed by the $\{Mn_{12}\}$ series due to $\{Mn_{19}\}$ exhibiting weak magnetic anisotropy. These examples highlight the difficulty in achieving both a large spin ground state and strong magnetic anisotropy.²⁶ An alternative approach is to use lanthanide ions such as Tb^{III} and Dy^{III} , both of which have a large spin and can exhibit strong uniaxial magnetic anisotropy.²⁷

1.8 Lanthanide Ions - 4f Orbitals

The lanthanides are a series of 14 elements (Figure 1.17) from cerium to lutetium characterised by a sequential filling of the seven 4f-orbitals (Figure 1.18). All lanthanides, given the general symbol Ln, can form a +3 oxidation state which is by far the most common. Despite having no 4f electrons, lanthanum and yttrium are also generally included under the term lanthanide due to their similar ionic radii and chemistry.

39 Y														
57 La	58 Ce	59 Pr	60 Nd	61 Pm	62 Sm	63 Eu	64 Gd	65 Tb	66 Dy	67 Ho	68 Er	69 Tm	70 Yb	71 Lu

Figure 1.17: *The lanthanide elements with their atomic numbers from cerium to lutetium including yttrium and lanthanum*

The 4f orbitals are poorly shielded from the nucleus, causing them to be radially buried beneath filled orbital subshells. Their buried nature has significant implications for their chemistry and magnetic properties. Firstly, lanthanides are hard acceptors and prefer hard donor ligands such as fluorine and oxygen; secondly, they exhibit weak magnetic exchange via the superexchange mechanism due to poor orbital overlap with bridging ligands. Thirdly, Ln^{III} ions are only weakly influenced by crystal field effects compared to 3d ions, therefore their magnetic properties are much more strongly influenced by spin-orbit coupling. The 4f-orbitals can be considered as degenerate for the free ions, this means that through spin conserved electron transitions, a large unquenched orbital angular momentum is generated – resulting in significant magnetic anisotropy for Ln^{III} ions.²⁸

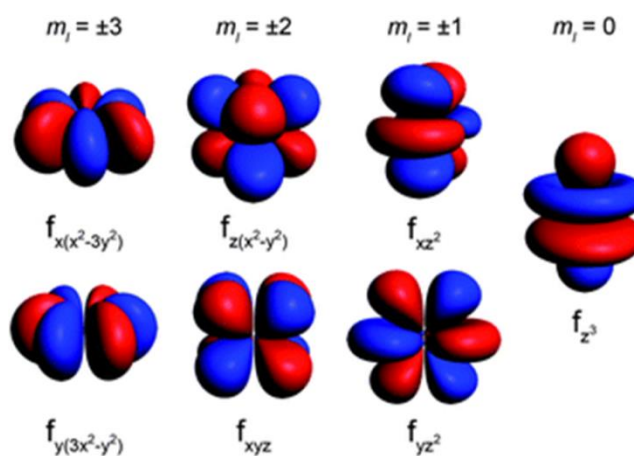


Figure 1.18: *Radial distribution of the seven 4f orbitals depending on m_l .*²⁸

Due to the pronounced spin-orbit coupling for Ln^{III} ions, treatment as spin only ions is no longer adequate. The orbital moment, L , couples with the spin moment, S , to generate J ; the total angular momentum. J can take values given by Equation 1.18.

$$J = L+S, L+S-1 \dots L-S$$

Equation 1.18

The value L is the summation of all the individual m_l values for a particular ion, an example for Tb^{III} is given in Figure 1.19:

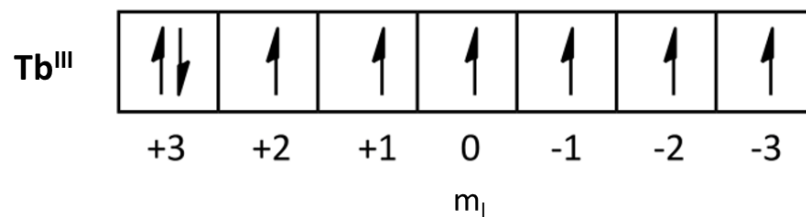


Figure 1.19: Electron configuration of Tb^{III} according to Hund's rules.

Tb^{III} has $L = (3+3+2+1+0-1-2-3) = 3$ and $S = 3$, because it has more than a half-filled $4f$ subshell, according to Hund's rules, L and S are additive in this case, whereas for less than half filled, they are subtractive:

1. The term with maximum spin multiplicity lies lowest in energy
2. The term with maximum L lies lowest in energy
3. For less than half-filled subshells, the level with the lowest value of J lies lowest in energy ($J = L - S$), while the highest J lies lowest when a subshell is more than half full ($J = L + S$).

*Hund's rules for the ground state of a free ion.*²⁹

Therefore for a free Tb^{III} ion, the total angular momentum state with lowest energy is $J = 6$. The quantum numbers L , S and J can be combined into a single term symbol: $(^{2S+1})L_J$, where L is a letter dictated by L 's value (Table 1.1). Therefore Tb^{III} is given the term symbol 7F_6 .

L	0	1	2	3	4	5	6
Term symbol	S	P	D	F	G	H	I

Table 1.1: Values of total orbital momentum with corresponding term symbol.

For all the lanthanides except Gd^{III} , J is the best quantum number to describe their magnetic properties. Because Gd^{III} has a f^7 electron count, it has no net orbital angular momentum due to each orbital being singly occupied, in this case $L = 0$ and Gd^{III} can be described as a spin only ion. For the remaining ions, the equations used to calculate susceptibility become:

$$\chi T = \frac{g_J^2}{8} J(J + 1)$$

$$g_J = 1 + \frac{J(J + 1) + S(S + 1) - L(L + 1)}{2J(J + 1)}$$

$$M_{\text{sat}} = g_J J$$

Equations 1.19 – 1.21

To understand the magnetic properties of lanthanide based SMMs it is necessary to firstly consider the energy separation of the electronic states of the Ln^{III} ions; the energy diagram for Dy^{III} ($4f^9$) is given in Figure 1.20. Firstly, the different states are generated by filling the $4f$ orbitals in different ways, the lowest energy terms dictated by Hund's rules. Before spin-orbit coupling of L and S is considered, the states are split by electronic repulsion alone; the ground state deduced by Hund's first and second rules with excited states having decreasing values of L . Each of these states is then split by spin-orbit coupling into different J states; for Dy^{III} , the ${}^6\text{H}_{15/2}$ lies lowest in energy. Finally, the spin orbit coupled states are split by the crystal field into $(2J+1) m_J$ states, also known as Stark sublevels.

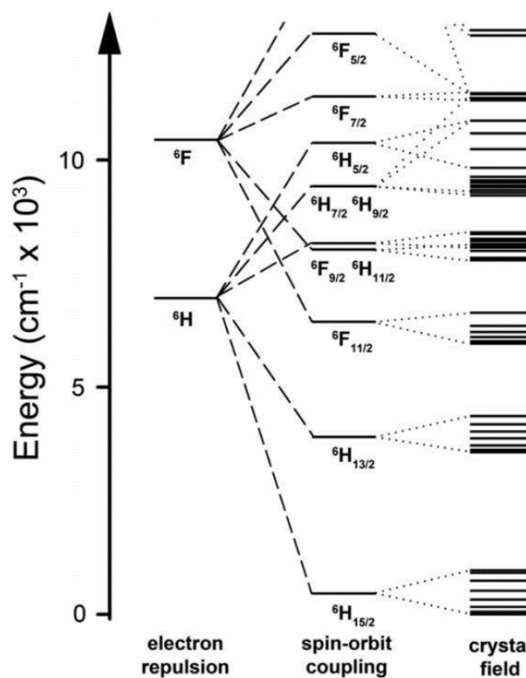


Figure 1.20: Energy diagram of Dy^{III} . The spin orbit coupled states are split into Stark sublevels by the crystal field.²⁸

The Stark sublevels are ordered in energy depending on the crystal field's geometry and electrostatic point charge's strength. The largest m_J state is not necessarily the lowest in energy, as illustrated by the energy distribution of the m_J states in the first Ln^{III} SMMs (Figure 1.21).³⁰ The SMMs in question are the axially symmetric $[\text{Ln}^{\text{III}}\text{Pc}_2]^- \text{TBA}^+$ series where TBA is tetrabutylammonium and H_2Pc is phthalocyanine.

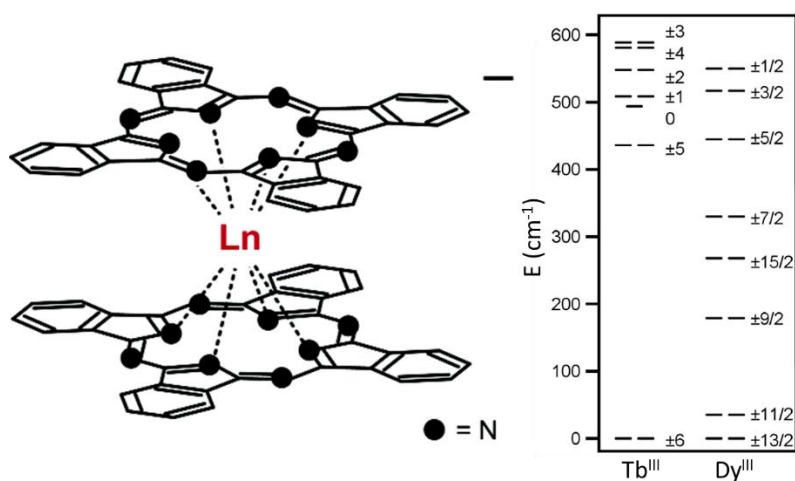


Figure 1.21: (Left) Schematic representation of $[\text{Ln}^{\text{III}}\text{Pc}_2]^-$ series. (Right) splitting of m_J sublevels of the Tb^{III} and Dy^{III} analogues. The Tb^{III} analogue has a much larger energy gap between the ground and first excited states. Taken from reference 30.

As can be seen in Figure 1.21, for Dy^{III} the highest $m_J = \pm 15/2$ state does not lie lowest in energy whereas for Tb^{III} the highest $m_J = \pm 6$ state is lowest in energy. Due to the axial nature of the crystal field, the m_J levels are organised in degenerate $\pm m_J$ pairs. Importantly, for Ln^{III} ions with an odd number of $4f$ electrons - referred to as Kramer's ions - the crystal field always produces degenerate pairs $\pm m_J$ levels, however for Ln^{III} ions with an even number (non-Kramer's ions), the crystal field needs to be axially symmetric for the pairs to be degenerate.³¹ Degenerate pairs of $\pm m_J$ states are crucially important for SMM behaviour in Ln^{III} complexes; degeneracy leads to a bistable magnetic ground state analogous to $\pm M_s$ state bistability in $3d$ complexes. Another important point to note in Figure 1.21 is the large energy separation between the ground $m_J = \pm 6$ and first excited $m_J = \pm 5$ states for $\{\text{TbPc}_2\}$. This large gap is also crucial for slow magnetic relaxation in Ln^{III} species – see later.

1.9 Designing Ln^{III} Crystal Fields

For an Ln^{III} complex to display SMM behaviour the crystal field needs to stabilise high value m_J states relative to the lower value ones in order to induce Ising-type magnetic anisotropy. Also, the crystal field needs to be axially symmetric to ensure a degenerate $\pm m_J$ ground state for non-Kramer's systems. A model proposed by Rinehart and Long³² predicts which types of crystal fields will achieve this for particular Ln^{III} ions. The model firstly classifies each Ln^{III} ion by its f -electron density distribution associated with its ground spin-orbit coupled state (Figure 1.22). The f -electron cloud's shape arises from the strong angular dependence of the f -orbitals: those with largest m_l are oblate and lie in the x - y plane (Figure 1.18), while the smaller m_l states lie in the z -direction (prolate). In accordance with Hund's rules, the largest m_l states are populated first, causing an oblate (pancake-like) charge distribution. As the subsequent lower m_l orbitals are populated, this adds in a prolate (cigar-like) shape contribution. The overall shape is the sum of the shapes of all the occupied m_l orbitals. The three density shape classifications are oblate (Ce^{III} , Pr^{III} , Nd^{III} , Tb^{III} , Dy^{III} and Ho^{III}), prolate (Pm^{III} , Sm^{III} , Er^{III} , Tm^{III} and Yb^{III}) and spherical (Gd^{III} and Lu^{III}).

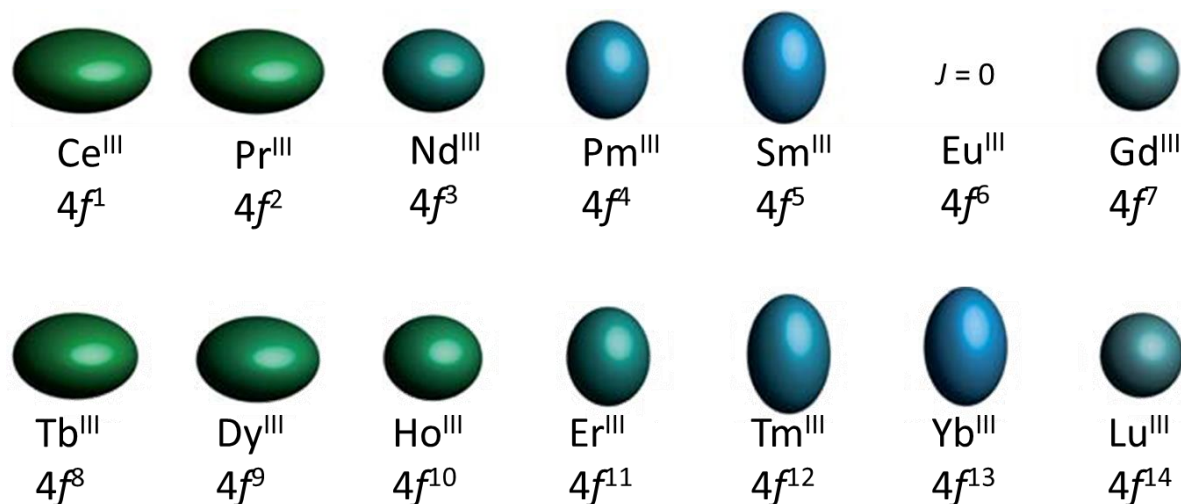


Figure 1.22: Electron density distribution for the ground spin-orbit coupled states of the Ln^{III} ions. Ions with oblate density are green and prolate are blue. The spherical ions are Gd^{III} and Lu^{III} . Eu^{III} has zero total angular momentum due to the cancelation of its spin moment with its orbital moment: $L = S$, $J = L - S$ for $4f^{<7}$. Adapted from reference 32.

To achieve Ising-type anisotropy, they proposed that oblate ions require axially symmetric crystal fields, and prolate ions require equatorially oriented crystal fields (Figure 1.24). Rotating an oblate electron density (and its associated magnetic moment) through an axially symmetric crystal field is less energetically favourable compared to rotating it through an equatorial crystal field; the reverse is true for prolate ions (Figure 1.23). Oblate ions in equatorial crystal fields, or prolate ions in axial crystal fields will exhibit easy plane magnetic anisotropy.

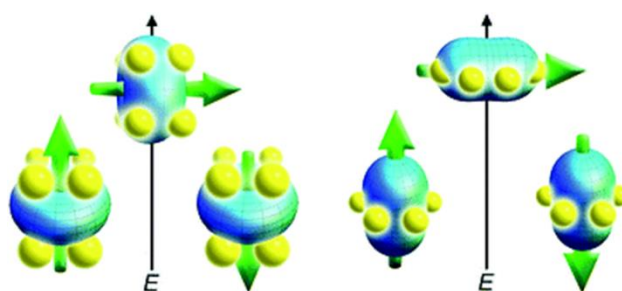


Figure 1.23: (Right) Oblate ion in axially symmetric crystal field. (Left) Prolate ion in equatorially symmetric crystal field. Rotating the magnetic moment through the crystal field increases the energy of the systems – resulting in Ising-type magnetic anisotropy.

The model is backed up by the $\{\text{Ln}^{\text{III}}\text{Pc}_2\}$ ($\text{Ln}^{\text{III}} = \text{Tb}^{\text{III}}$ and Dy^{III}) SMMs, both having oblate ions and axial crystal fields. Another example is the $\text{Er}^{\text{III}}[\text{N}(\text{SiMe}_3)_2]_3$ SMM reported by Tang *et al.*,³³ where the prolate Er^{III} ion is in an equatorial crystal field with local C_3 symmetry (Figure 1.24). $\text{Er}^{\text{III}}[\text{N}(\text{SiMe}_3)_2]_3$ exhibits easy axis magnetic anisotropy,

whilst the Dy^{III} analogue does not, due to stabilisation of the lower m_J sublevels – as predicted by the model.

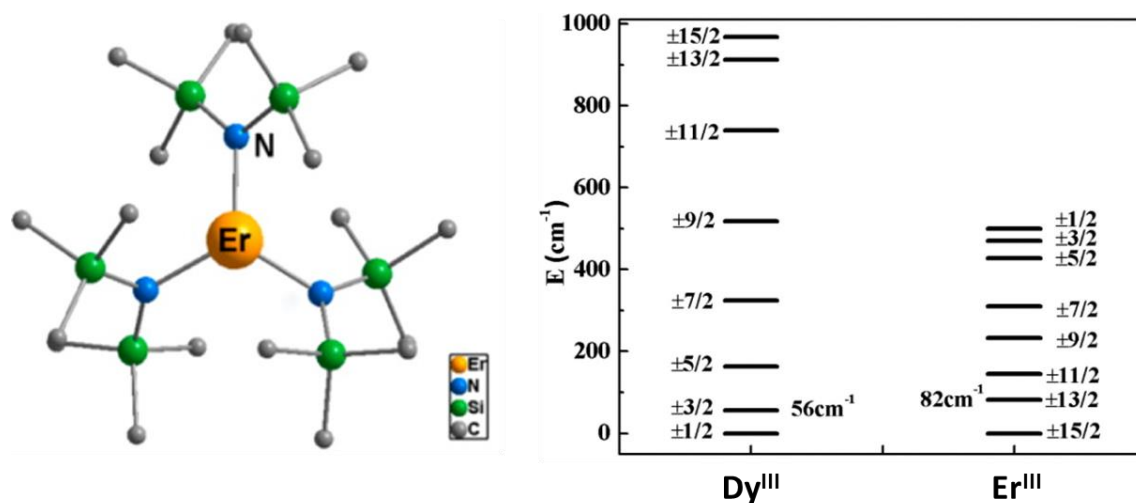


Figure 1.24: (Left) Molecular structure of $\text{Ln}^{\text{III}}[\text{N}(\text{SiMe}_3)_2]_3$ where $\text{Ln}^{\text{III}} = \text{Er}^{\text{III}}$. (Right) Energy splitting of m_J sublevels for Dy^{III} and Er^{III} analogues. Adapted from reference 33.

1.10 Magnetic Relaxation in Ln^{III} SMMs

In Ln^{III} SMMs, relaxation predominantly occurs through a thermally assisted tunnelling process involving the first excited m_J state; QTM through excited states is greatly enhanced compared to through the ground m_J state.²⁸ Hence in order to have a high U_{eff} , the crystal field needs to induce a large energy separation between the ground and first excited states, as observed for $\{\text{TbPc}_2\}$ (Figure 1.21). QTM in general is much more prevalent for Ln^{III} SMMs than 3d SMMs, mainly due to the extreme sensitivity of Ln^{III} ions to small distortions from ideal axiality of the crystal field.³¹ For oblate ions, perfect axial symmetry theoretically blocks QTM from occurring, therefore Ln^{III} ions with high local symmetry point groups; $C_{\infty v}$, $D_{\infty h}$, S_8 , D_{4d} , D_{5h} and D_{6d} will be expected to show heavily suppressed QTM. In addition to crystal field distortions, hyperfine and quadrupole interactions between the 4f electrons and the nucleus as well as intermolecular dipolar interactions enhance QTM.^{34,35} Magnetic dilution can be used to suppress QTM due to dipolar interactions.³⁶ This involves synthesising a diamagnetic analogue of the SMM using Y^{III}, La^{III} or Lu^{III}, then growing a crystal composed of (for example) 90% diamagnetic analogue and 10% paramagnetic analogue. A dc field can also be used to suppress QTM in Ln^{III} SMMs,³⁶ however, the mechanism is not well understood.³⁷

1.11 3d-4f SMMs

One attractive approach toward new SMMs is to incorporate highly anisotropic Ln^{III} ions into 3d based exchange coupled systems.³⁸⁻⁴¹ The first advantage of this approach is that ions such as Tb^{III} and Dy^{III} can generate much stronger single ion anisotropy compared to 3d ions. Secondly, certain 3d-4f pairings are known to favour ferromagnetic exchange, for example Tb^{III} or Dy^{III} with Cu^{II},³⁷ and thirdly, 3d-4f exchange ($\approx 10^3$ s of cm⁻¹) is stronger than 4f-4f exchange ($\approx 10^1$ cm⁻¹)⁴² which can lead to larger magnetic moments and larger energy barriers compared to purely 4f polynuclear complexes. The first 3d-4f SMM to compete with {Mn₁₂} was a {Mn₂₁Dy} complex; [Mn^{IV}₃Mn^{III}₁₈Dy^{III}O₂₀(OH)₂(O₂C^tBu)₂₀(O₂CH)₄(NO₃)(H₂O)₇·5MeNO₂·H₂O, with a U_{eff} of 74 K.⁴³ However, this complex was still surpassed by the {Mn₆} complex reported by Brechin *et al.*⁴⁴ with $U_{eff} = 86$ K. A break-through was achieved with the synthesis of a {Mn₆Tb₂} complex; [Mn^{III}₆O₃(saO)₆(OCH₃)₆Tb^{III}₂(MeOH)₄(H₂O)₂] where saOH₂ is salicylaldehyde.⁴⁵ This complex surpassed both {Mn₁₂} and {Mn₆} with a U_{eff} of 103 K. Recently, Powell *et al.*, inspired by a {Zn₂Dy} SMM⁴⁶ ($U_{eff} = 439$ K) replaced the diamagnetic Zn^{II} ions with paramagnetic Fe^{II} ions and found their new {Fe₂Dy} complex had a record U_{eff} of 459 K.⁴⁷ The structures of the {Zn₂Dy} and {Fe₂Dy} complexes were very similar, both with their central Dy^{III} ions in highly axial crystal fields with local D_{5h} symmetry – generating strong Ising-type anisotropy and significantly suppressing QTM. The main difference was the added spin and anisotropy of the Fe^{II} ions which was cooperatively aligned with the Dy^{III} ion's anisotropy axis. {Fe₂Dy}, full formula; [Fe^{II}₂Dy(L)₂(H₂O)]ClO₄·2H₂O, where L = 2,2',2''-(((nitritoltris(ethane-2,1-diyl))tris(azanediyl))tris(methylene))tris(4-chlorophenol), exhibited ferromagnetic Fe^{II}-Dy^{III} exchange. Coupling between 3d and 4f ions leads to the mixing of m_s and m_J states to form new M_{tot} states which better describe the complex's magnetic energy level structure.⁴⁸ The ground $m_J = \pm 15/2$ sublevel of Dy^{III} couples with the two $m_s = 2$ states of the Fe^{II} ions to give a ground state $M_{tot} = \pm 23/2$. Importantly, because M_{tot} is a non-integer, the complex behaves as a Kramer's ion with a guaranteed degenerate ground state and a suppression of QTM due to the absence of time reversal symmetry.⁴⁹ {Fe₂Dy} is a remarkable example of the 3d-4f approach, it exhibits the highest U_{eff} of any 3d-4f SMM as well as 3d SMM; the highest belonging to [Fe^I(C(SiMe₃)₃)₂] (325 K).⁵⁰ It still however is outperformed by the [TbPcPc'] monometallic 4f SMM reported by Torres *et al.* with $U_{eff} = 938$ K.⁵¹ Having a single ion eliminates the complications of aligning anisotropy axes within a polynuclear cluster, however, using the 3d-4f approach there is potential to synthesise complexes with larger magnetic moments than those accessible by 4f SIMs which could potentially lead to

even higher U_{eff} values. The challenge remains to find complexes with perfect alignment of single ion anisotropies.

1.12 Synthetic methods – Aminopolyol Ligands

In general SMMs are synthesised using either rational design or serendipitous self-assembly.⁵² Rational design uses deliberate engineering of ligands to synthesise a preconceived complex. Ideally, ligands are designed to control important factors such as bridging angles between metal ions, crystal field geometries and what types of ions (e.g. $3d$ or $4f$) will favourably occupy certain binding pockets when a few are available.⁵³⁻⁵⁷ Manipulation of a pre-synthesised complex by substitution of bridging ligands and/or ligand modification to help improve desirable structural properties is also a form of rational design.^{54,55} Another manifestation of rational design is to use a so-called building block approach;⁵⁸ this involves employing a ligand capable of chelating a metal ion, which upon removal of protons - by addition of base - can form bridges to other metal ions.

Serendipitous self-assembly is more focussed on designing reaction conditions that will favourably lead to new complexes. The approach is a necessary part toward finding new, perhaps unimagined structural topologies. Once new structures are found, a more rational treatment can be applied to subtly manipulate the structure to help improve desired properties as mentioned previously.

The choice of aminopolyol ligands – those with flexible carbon based arms combining N and O donor atoms - can fit both strategies.³⁹ A huge amount of research has been dedicated to using aminopolyol ligands to form, $3d$, $3d-4f$ and $4f$ complexes. Some of the most lucrative ligands being triethanolamine (H_3tea) and substituted diethanolamines ($RdeaH_2$ where $R = H$ or C_nH_{2n-1}). The defining characteristics of these types of ligand are their ability to both chelate metal centres and/or bridge to others through removal of their hydroxyl protons – allowing for a rational synthetic approach. They have a rich structural chemistry, owed to their flexibility, which allows them to adopt a vast number of coordination modes and an ability to accommodate a wide variety of ionic radii – suiting a serendipitous approach. The ligand which this thesis is primarily based on, N,N,N',N' -tetrakis-(2-hydroxyethyl)-ethylenediamine (H_4edte) is particularly interesting taking into account the possible coordination modes, ability to chelate and its deprotonatable sites. The nature of H_4edte 's structure lends itself to both a building block approach and serendipitous approach, both of which were thoroughly investigated for this work.

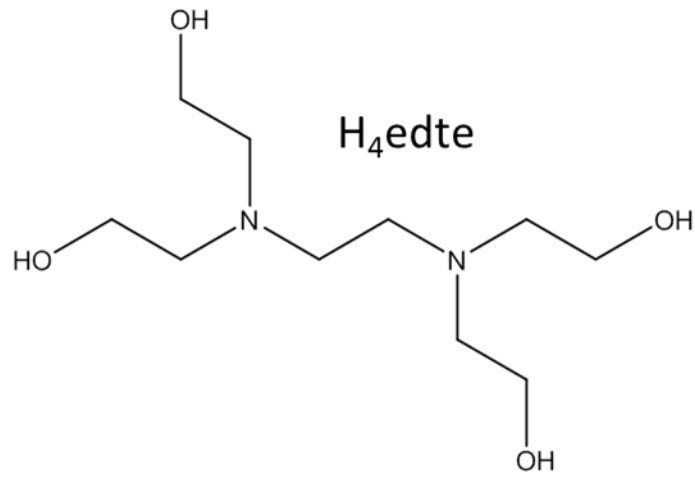


Figure 1.25: *The aminopolyol ligand H_4edte .*

1.13 References

- (1) Magnetism and Transition Metal complexes, F. E. Mabbs, D. J. Machin, Dover, New York (2008).
- (2) Magnetism in Condensed Matter, S. Blundell, OUP (2001).
- (3) Magnetochemistry, A. F. Orchard, OUP, (2003).
- (4) Molecular Magnetism, O. Kahn, VCH Publishers Inc., USA (1993).
- (5) G. A. Medley, R. Stranger, *Inorg. Chem.* 33 (1994) 3976–3985.
- (6) J. B. Goodenough, *J. Phys. Chem. Solids*, 6 (1958) 287-297.
- (7) J. Kanamori, *J. Phys. Chem. Solids*, 10 (1959) 87-98.
- (8) Inorganic Chemistry, C. E. Housecroft, A. G. Sharpe, 2nd edition, Pearson Education Ltd. (2005).
- (9) L. Sorace, C. Benelli, D. Gatteschi, *Chem. Soc. Rev.* 40 (2011) 3092-3104.
- (10) D. Gatteschi, R. Sessoli and J. Villain, *Molecular Nanomagnets*, Oxford University Press, (2006).
- (11) R. Sessoli, D. Gatteschi, A. Caneschi, M. A. Novak, *Nature*, 365 (1993) 141-143.
- (12) T. Lis, *Acta Crystallographica Section B* 36 (1980) 2042-2046.
- (13) R. Sessoli, H. L. Tsai, A. R. Schake, S. Wang, J. B. Vincent, K. Folting, D. Gatteschi, G. Christou, D. N. Hendrickson, *J. Am. Chem. Soc.* 115 (1993) 1804.
- (14) R. Bagai, G. Christou, *Chem. Soc. Rev.* 38 (2009) 1011-1026.
- (15) *Introduction to Molecular Magnetism*, C. Benelli, D. Gatteschi, Wiley-VCH (2015).
- (16) D. Gatteschi, R. Sessoli, *Angew. Chem. Int. Ed.* 42 (2003) 268-297.
- (17) T. Glaser, M. Heidemeier, T. Weyhermüller, R.-D. Hoffman, H. Rupp, P. Müller, *Angew. Chem. Int. Ed.* 45 (2006) 6033-6037.
- (18) D. Gatteschi, R. Sessoli, *Angew. Chem. Int. Ed.* 42 (2003) 268-297.
- (19) *Molecular Materials*, D. W. Bruce, D. O'Hare, R. I. Walton, John Wiley and Sons (2010).
- (20) A. M. Ako, V. Mereacre, I. J. Hewitt, R. Clérac, L. Lecren, C. E. Anson, A. K. Powell, *J. Mater Chem.* 16 (2006) 2579-2586.
- (21) V. E. Campbell, R. Guillot, E. Riviere, P. – T. Brun, W. Wernsdorfer, T. Mallah, *Inorg. Chem.* 52 (2013) 5194-5200.
- (22) J. van Slageren, *Introduction to molecular magnetism*, University of Stuttgart.
- (23) A. J. Tasiopoulos, A. Vinslava, W. Wernsdorfer, K. A. Abboud, G. Christou, *Angew. Chem. Int. Ed.* 43 (2004) 2117-2121.

- (24) N. E. Chakov, S.-C. Lee, A. G. Harter, P. L. Kuhns, A. P. Reves, S. O. Hill, N. S. Dalal, W. Wernsdorfer, K. A. Abboud, G. Christou, *J. Am. Chem. Soc.* 128 (2006) 6975-6989.
- (25) S. Nayak, M. Evangelisti, A. K. Powell, J. Reedijk, *Chem. Eur. J.* 16 (2010) 12865-12872.
- (26) F. Neese, D. A. Pantazis, *Faraday Discuss.* 148 (2011) 229-238.
- (27) D.N. Woodruff, R.E.P. Winpenny, R. Layfield, *Chem. Rev.* 113 (2013) 5110–5148.
- (28) J. Tang, P. Zhang, *Lanthanide Single-Molecule Magnets*, Springer (2015).
- (29) *Inorganic Chemistry*, C. E. Housecroft, A. G. Sharpe, 2nd edition, Pearson Education Ltd. (2005).
- (30) N. Ishikawa, M. Sugita, T. Ishikawa, S. Koshihara and Y. Kaizu, *J. Phys. Chem. B*, 108 (2004) 11265-11271.
- (31) L. Ungur, L. F. Chibotaru, *Phys. Chem. Chem. Phys.* 13 (2011) 20086-20090.
- (32) J.D. Rinehart, J.R. Long, *Chem. Sci.* 2 (2011) 2078–2085.
- (33) P. Zhang, L. Zhang, C. Wang, S. Xue, S.-Y. Lin, J. Tang, *J. Am. Chem. Soc.* 136 (2014) 4484-4487.
- (34) N. Ishikawa, M. Sugita, W. Wernsdorfer, *Angew. Chem. Int. Ed.* 44(2005) 2931-2935.
- (35) N. Ishikawa, M. Sugita, W. Wernsdorfer, *J. Am. Chem. Soc.* 127 (2005) 3650-3651.
- (36) S.-D. Jiang, B.-W. Wang, G. Su, Z.-M. Wang, S. Gao, *Angew. Chem. Int. Ed.* 49 (2010) 7448-7451.
- (37) C. Benelli, D. Gatteschi, *Chem. Rev.* 102 (2002) 2369 – 2387.
- (38) L. R. Piquer, E. C. Sañudo, *Dalton Trans.* 44 (2015) 8771–8780.
- (39) H. L. C. Feltham, S. Brooker, *Coord. Chem. Rev.* 276 (2014) 1–33.
- (40) J. W. Sharples, D. Collison, *Coord. Chem. Rev.* 260 (2014) 1-20.
- (41) R. Sessoli, A. Powell, *Coord. Chem. Rev.* 253 (2009) 2328-2341.
- (42) J. P. Costes, J. M. C. Juan, F. Dahan, F. Nicodeme, *Dalton Trans.* (2003) 1272-1275.
- (43) C. Papatriantafyllopoulou, W. Wernsdorfer, K. A. Abboud, G. Christou, *Inorg. Chem.* 50 (2011) 421-423.
- (44) C. J. Milios, A. Vinslava, W. Wernsdorfer, S. Moggach, S. Parsons, S. P. Perlepes, G. Christou, E. K. Brechin, *J. Am. Chem. Soc.* 129 (2007) 2754-2755.
- (45) M. Holynska, D. Premuzic, I. R. Jeon, W. Wernsdorfer, R. Clerac and S. Dehnen, *Chem. Eur. J.* 17 (2011) 9605-9610.
- (46) J.-L. Liu, Y.-C. Chen, Y.-Z. Zheng, W.-Q. Lin, L. Ungur, W. Wernsdorfer, L. F. Chibotaru, M.-L. Tong, *Chem. Sci.* 4 (2013) 3310 – 3316.

- (47) J.-L. Liu, J. Y. Wu, Y.-C. Chen, V. Mereacre, A. K. Powell, L. Chibotaru, X.-M. Chen, M.-L. Tong, *Angew. Chem. Int. Ed.* 53 (2014) 12966-12970.
- (48) F. J. Kettles, V. A. Milway, F. Tuna, R. Valiente, L. H. Thomas, W. Wernsdorfer, S. T. Ochsenbein, M. Murrie, *Inorg. Chem.* 53 (2014) 8970-8978.
- (49) S.D. Jiang, B.W. Wang, S. Gao, *Molecular Nanomagnets and Related Phenomena*, Chapter 2, pp 111-141.
- (50) J. M. Zadrozny, D. Xiao, M. Atanasov, G. J. Long, F. Grandjean, F. Neese, J. R. Long, *Nat. Chem.* 5 (2013) 577 – 581.
- (51) C. R. Ganivet, B. Ballesteros, G. de La Torre, J. M. Clemente-Juan, E. Coronado, T. Torres, *Chem. Eur. J.* 19 (2013) 1457 – 1465.
- (52) R.E.P. Winpenny, *J. Chem. Soc. Dalton*, (2002) 1–10.
- (53) H. L. C. Feltham, Y. Lan, F. Klöwer, L. Ungur, L. F. Chibotaru, A. K. Powell, S. Brooker, *Chem. Eur. J.* 17 (2011) 4362-4365.
- (54) H. L. C. Feltham, F. Klöwer, S. A. Cameron, Y. Lan, M. Tropicano, S. Faulkner, A. K. Powell, S. Brooker, *Dalton Trans.* 40 (2011) 11425-11432.
- (55) H. L. C. Feltham, R. Clerac, A. K. Powell, S. Brooker, *Inorg. Chem.* 50 (2011) 4232-4234.
- (56) H. L. C. Feltham, R. Clerac, L. Ungur, V. Vieru, L. F. Chibotaru, A. K. Powell, S. Brooker, *Inorg. Chem.* 51 (2012) 10603-10612.
- (57) H. L. C. Feltham, R. Clerac, L. Ungur, L. F. Chibotaru, A. K. Powell, S. Brooker, *Inorg. Chem.* 52 (2013) 3236-3240.
- (58) K. S. Pedersen, J. Bendix, R. Clérac, *Chem. Commun.* 50 (2014) 4396-4415.

2. Synthesis, Structure and Magnetic Properties of a $\{\text{LnCu}_3(\text{H}_2\text{edte})_3\}$ Series

2.1 Introduction

Synthesis of $3d$ - $4f$ mixed metal complexes is an attractive approach toward the discovery of new single molecule magnets (SMMs).¹⁻³⁸ Certain lanthanide ions, namely Tb^{III} and Dy^{III} , have large spins and, crucially, large easy axis single ion anisotropies. These ions also show a propensity for ferromagnetic exchange with $3d$ metal ions^{1,5-16,19-38} and so clusters with large ground spin states and strong axial anisotropy can be synthesised.

The use of flexible aminopolyol ligands which can chelate metal ions and also bridge to others upon deprotonation have provided many examples of new SMMs.⁴ Excluding the work presented in this chapter, the ligand N,N,N',N' -tetrakis(2-hydroxyethyl)ethylenediamine (H_4edte) has provided two examples of $3d$ - $4f$ SMMs.^{5,6} The first example was a $\{\text{Mn}^{\text{II}}_2\text{Mn}^{\text{III}}_2\text{Tb}^{\text{III}}_2\}$ complex, full formula $[\text{Mn}^{\text{II}}_2\text{Mn}^{\text{III}}_2\text{Tb}_2\text{O}_2(\text{O}_2\text{C}^t\text{Bu})_6(\text{H}_2\text{edte})_2(\text{NO}_3)_2]$, synthesised by Christou *et al.*⁵ The Gd^{III} , Dy^{III} , Ho^{III} and Y^{III} analogues were also synthesised, but only the Tb^{III} analogue (Figure 2.1) showed SMM properties.

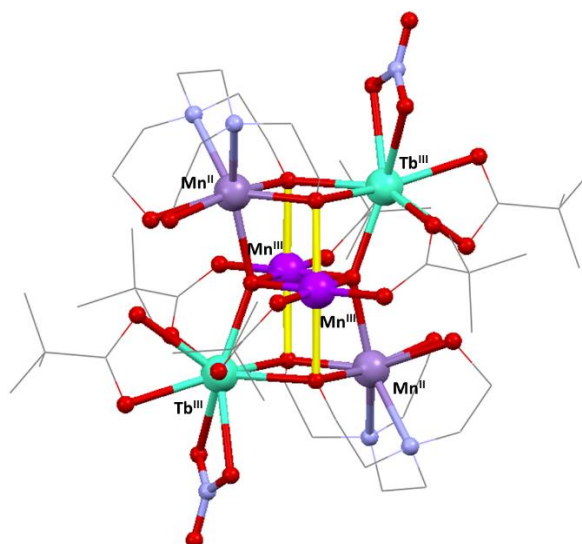


Figure 2.1: Structure of $[\text{Mn}^{\text{II}}_2\text{Mn}^{\text{III}}_2\text{Tb}_2\text{O}_2(\text{O}_2\text{C}^t\text{Bu})_6(\text{H}_2\text{edte})_2(\text{NO}_3)_2]$, CSD ref. code; IBOVIG. H-atoms and lattice solvent molecules are not shown. The Mn^{III} Jahn-Teller axes are highlighted in yellow. Atom colours: Tb^{III} , turquoise; Mn^{II} , faded purple; Mn^{III} , deep purple; O, red; N, blue; C, grey.

The complexes contained two $\text{H}_2\text{edte}^{2-}$ ligands chelating the two Mn^{II} ions in the structure through all of their donor atoms. The ligand provides alkoxo bridges between the Mn^{II} ions and adjacent Ln^{III} and Mn^{III} ions. The structure was remarkable when reported as it was the first example of a $3d\text{-}4f$ double face fused cubane (see Figure 2.1).

In order to investigate the magnetic exchange between manganese ions, and the effects these were having on the overall magnetic properties, the paramagnetic Ln^{III} ions were substituted with diamagnetic Y^{III} ions. Magnetic characterisation of the Y^{III} complex showed strong antiferromagnetic coupling between the Mn^{III} ions and weaker ferromagnetic coupling between Mn^{II} and Mn^{III} . The Gd^{III} analogue, synthesised to help simplify magnetic characterisation due to its spin only nature, was found to have a ground state spin value of $S = 12$ resulting from ferromagnetic exchange between the two Gd^{III} ions ($S = 7/2$) and the two Mn^{II} ions ($s = 5/2$). The calculated value for D was close to zero which was expected for the magnetically isotropic Gd^{III} ion but disappointing considering the parallel alignment of the Jahn-Teller axes of the Mn^{III} ions. The Tb^{III} analogue was found to have frequency dependent out-of-phase (χ'') ac susceptibility signals above 1.8 K without an additional applied direct current (dc) field. An Arrhenius plot of the ac data (see Section 1.6) gave an estimated energy barrier to magnetic reorientation (U_{eff}) value of 20 K. Finally, stepped hysteresis loops were observed below 0.9 K (0.035 Ts^{-1}) for the Tb^{III} complex in magnetisation *vs.* dc field scans whose coercivity increased with increasing scan rate, as expected for a SMM.

The second example of a $3d\text{-}4f$ complex with H_4edte was a $\{\text{Fe}^{\text{III}}_4\text{Dy}^{\text{III}}_2\}$ complex, full formula: $[\text{Fe}^{\text{III}}_4\text{Dy}^{\text{III}}_2(\mu_4\text{-O}_2)(\text{NO}_3)_2(\text{O}_2\text{C}^t\text{Bu})_6(\text{Hedte})_2] \cdot 4\text{CH}_3\text{CN} \cdot \text{C}_6\text{H}_5\text{OH}$, reported by Powell *et al.*⁶ (Figure 2.2). The complex contains two Hedte^{3-} ligands, each acting as a pentadentate chelate to two separate Fe^{III} ions. The ligands also bridge through their alkoxide arms to neighbouring Fe^{III} and Dy^{III} ions.

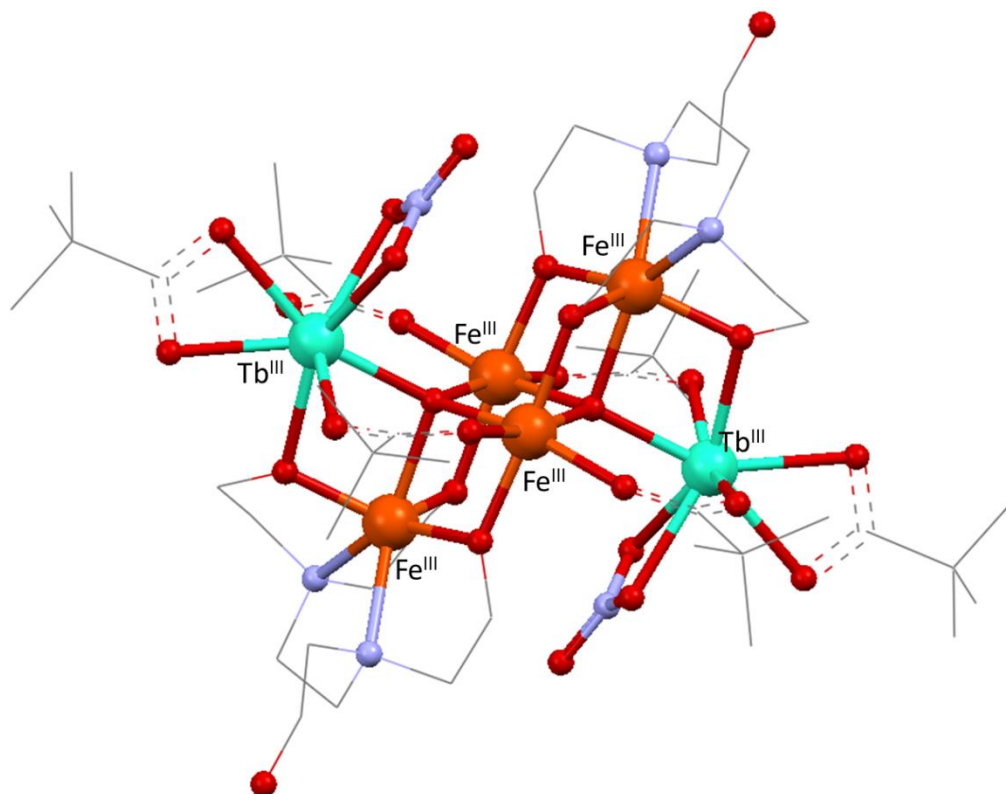


Figure 2.2: Structure of Powell's $\{\text{Fe}^{\text{III}}_4\text{Dy}^{\text{III}}_2\}$ complex, CSD ref. code GUMJAA. H-atoms and lattice solvent molecules not shown. Atom colours: Tb^{III} , turquoise; Fe^{III} , orange; O, red; N, blue; C, grey.

The complex was found to have a U_{eff} of 30.8 K in the presence of a dc applied field of 1200 Oe. The Gd^{III} and Y^{III} analogues were also synthesised in order to investigate the $\text{Fe}^{\text{III}}\text{-Fe}^{\text{III}}$ and $\text{Fe}^{\text{III}}\text{-Gd}^{\text{III}}$ magnetic exchange interactions. Using the Gd^{III} analogue, they found weak antiferromagnetic coupling ($J = -0.12 \text{ cm}^{-1}$) between the outer Fe^{III} ions and Gd^{III} ions and weak ferromagnetic coupling ($J = 0.24 \text{ cm}^{-1}$) between the inner Fe^{III} ions and Gd^{III} ions.

The use of $\text{Mn}^{\text{III}}/\text{Mn}^{\text{II}}$ ions, or Fe^{III} ions are a good choice to combine with Ln^{III} ions as they have the largest spin values of the 3d metals. However, the more modest Cu^{II} ion with $s = 1/2$, has also been proven to be a good choice.¹⁹⁻³⁸ In fact, Cu^{II} has been found to have a significant propensity for ferromagnetic exchange interactions with Ln^{III} ions⁴⁹ such as Gd^{III} , Tb^{III} and Dy^{III} . This attribute, along with copper's inherent chemical versatility have led to a number of examples of $\{\text{LnCu}\}$ SMMs.⁵⁻³⁸ $\{\text{LnCu}\}$ complexes have also led to some very interesting insights into the magnetic interactions between 3d and 4f ions.¹⁷ Interestingly, the first reported 3d-4f SMM was a $\{\text{Cu}_2\text{Tb}_2\}$ complex reported by Mzroniski *et al.*¹ (Figure 2.3).

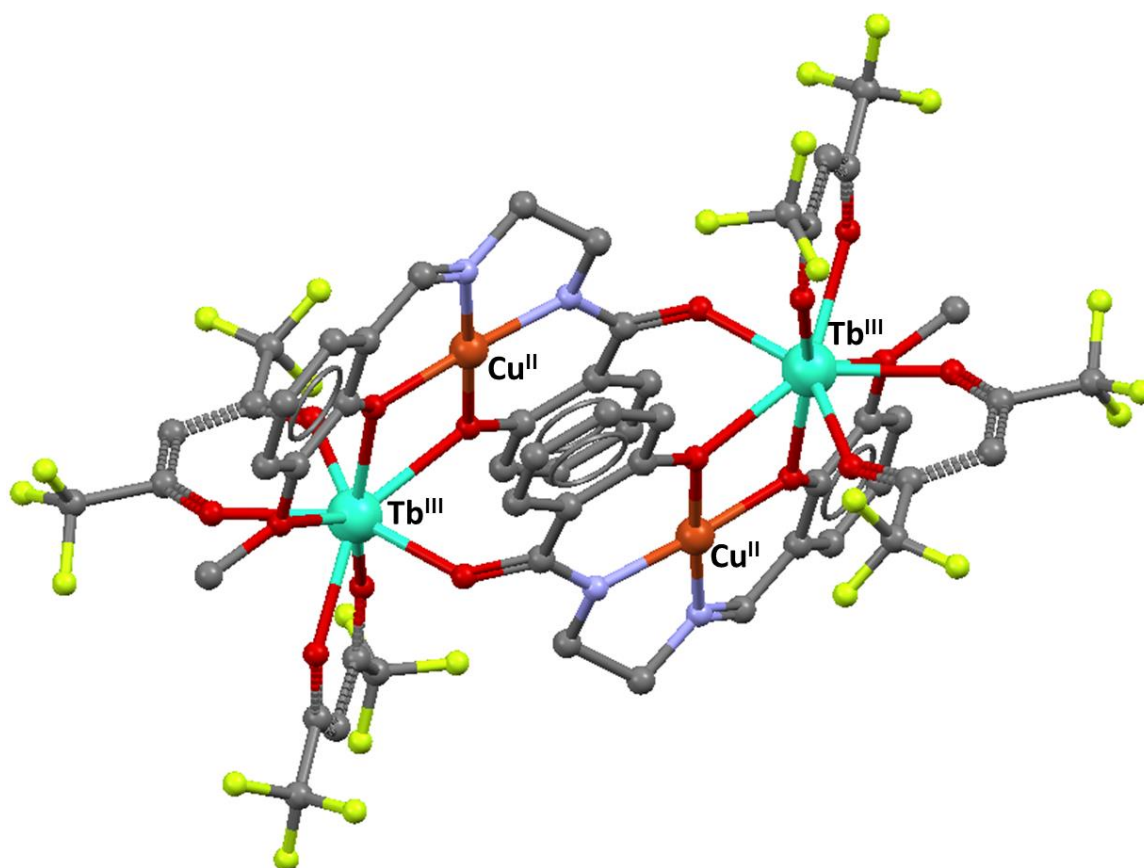


Figure 2.3: Structure of $[\text{Cu}_2\text{Tb}_2\text{L}(\text{hfac})_2]_2$, CSD ref. code; MUTKER. Atom colours: Tb^{III} , turquoise; Cu^{II} , orange; O, red; N, blue; C, grey; F, yellow.

The cyclic tetranuclear complex; $[\text{Cu}_2\text{Tb}_2\text{L}(\text{hfac})_2]_2$, where $\text{H}_3\text{L} = 1$ -(2-hydroxybenzamido)-2-(2-(2-hydroxy-3-methoxy-benzylideneamino)-ethane and $\text{Hhfac} =$ hexafluoroacetylacetonate, showed frequency dependent χ'' peaks without an additional applied dc field. Arrhenius analysis of the χ'' data gave a U_{eff} estimation of 21 K. In order to study whether the slow magnetic relaxation was solely due to the single-ion effects of the Tb^{III} ions, the Cu^{II} ions were substituted with Ni^{II} . In a square planar crystal field, Ni^{II} is diamagnetic, therefore any observed magnetic behaviour would be purely due to the Tb^{III} ions. Interestingly, the Ni^{II} analogue showed no χ'' signals, indicating that the combination of Cu^{II} and Tb^{III} ions were causing the slow relaxation. The $\{\text{Dy}_2\text{Cu}_2\}$ analogue was also synthesised but only the onset of slow relaxation was observed down to 2 K, again with zero applied dc field.

Since the first $\{\text{LnCu}\}$ SMM described above, there has been a flurry of research dedicated to trying to find new $\{\text{LnCu}\}$ SMMs with higher anisotropy barriers.¹⁹⁻³⁸ The majority of the research has been focused on macrocyclic²⁶ or Schiff base²⁰⁻²² compounds, reminiscent of the complexes studied during early investigations into magnetic exchange in binuclear

$\{\text{GdCu}\}$ complexes.³⁹⁻⁴¹ There have also been examples of $\{\text{LnCu}\}$ complexes using amino acids as ligands which show the onset of slow magnetic relaxation down to 1.8 K.¹⁸

Of the eight new $3d-4f$ compounds presented in this chapter, two exhibit SMM behaviour, evidenced by out of phase ac susceptibility signals and single crystal magnetic hysteresis measurements. Inelastic neutron scattering (INS) experiments were also carried out to help model the exchange interactions between the Ln^{III} and Cu^{II} ions.

2.2 Experimental

2.2.1 Synthesis of [Cu₂(H₃edte)₂][NO₃]₂ (1)

To a stirred solution of H₄edte (12.68 g, 53.68 mmol) in 100 ml MeCN was added slowly a solution of Cu(NO₃)₂·3H₂O (6.65 g, 27.52 mmol) in 100 ml MeCN. The reaction was stirred vigorously for 24 hours resulting in a green precipitate which was filtered, washed with MeCN (3 x 15 ml) and oven dried @ 60° C for two days. Yield = 95% (9.5 g) based on Cu^{II}. Blue-green plate-like crystals suitable for X-ray diffraction were grown by dissolving 0.05 g precipitate in 5 ml MeOH and vapour diffusing with Et₂O. Crystals analyse as **1**, (Cu₂C₂₀H₄₆N₆O₁₄), analysis (%) calc (found) C, 33.28 (33.24); H 6.42 (6.47); N 11.64 (11.52). Selected IR data (cm⁻¹): 3471 (w), 3215 (br), 2955.05 (w), 2914.54 (w), 2887.53 (w), 2856.67 (w), 1477.52 (w), 1452.45 (w), 1373.36 (m), 1348.29 (m), 1313.57 (m), 1265.35 (m), 1230.63 (m), 1165.04 (w), 1111.03 (w), 1099.46 (m), 1078.24 (s), 1066.67 (s), 1041.60 (m), 1028.09 (m), 1016.52 (m), 1004.95 (m), 991.44 (m), 972.16 (w), 922 (m), 914.29 (m), 902.72 (m), 883.43 (m), 868 (m), 827.49 (m), 758.05 (m), 723.33 (m), 713.69 (m), 640.13 (m). IR and CHN data for the crystals match those of the precipitate.

2.2.2 Synthesis of [PrCu₃(H₂edte)₃(NO₃)] [NO₃]₂·0.5MeOH (2)

To a stirred solution of [Cu₂(H₃edte)₂][NO₃]₂ (0.4g, 0.55 mmol) and NEt₃ (0.21 ml, 1.5 mmol) in MeOH (20 ml), Pr(NO₃)₃·6H₂O (0.108 g, 0.25 mmol) was added. The reaction was stirred at room temperature overnight to yield a blue precipitate which was collected by filtration, washed with EtOH and then air dried. Yield = 83% (0.25 g) based on Pr^{III}. Thin blue plate-like needles of **2**, suitable for X-ray diffraction, were grown by dissolving ≈ 0.02 g precipitate in 5 ml MeOH and vapour diffusing with THF. Crystals analyse as **2**, (PrCu₃C_{30.5}H₆₈N₉O_{21.5}), analysis (%) calc. (found): C 29.54 (29.27), H 5.45 (5.46), N 10.34 (10.05). Selected IR peaks (cm⁻¹): 3200 (br), 2926.11 (w), 2879.82 (w), 2841.24 (w), 2681.14 (w), 2634.85 (w), 1465.95 (m), 1437.02 (m), 1371.43 (m), 1348.35 (m), 1292.35 (s), 1263.42 (m), 1170.83 (w), 1151.54 (w), 1139.97 (w), 1076.32 (s), 1057.03 (s), 1043.52 (s), 1016.52 (s), 968.30 (m), 918.15 (m), 904.64 (m), 891.14 (m), 875.71 (m), 827.49 (m), 819.77 (w), 786.98 (w), 759.98 (w), 731.05 (m), 692.47 (w), 669.32 (w), 655.85 (w), 613.38 (m). IR and CHN data for the crystals match those of the precipitate.

2.2.3 Synthesis of [NdCu₃(H₂edte)₃(NO₃)] [NO₃]₂·0.5MeOH (3)

To a stirred solution of [Cu₂(H₃edte)₂][NO₃]₂ (0.4 g 0.55 mmol) and NEt₃ (0.21 ml, 1.5 mmol) in MeOH (20 ml), Nd(NO₃)₃·6H₂O (0.109 g, 0.25 mmol) was added. The reaction was stirred at room temperature overnight to yield a blue precipitate which was collected by filtration, washed with EtOH and then air dried. Yield = 82% (0.25 g) based on Nd^{III}. Thin blue plate-like needles of **3**, suitable for X-ray diffraction, were grown by dissolving ≈ 0.02 g precipitate in 5 ml MeOH and vapour diffusing with THF. Crystals analyse as **3**, (NdCu₃C_{30.5}H₆₈N₉O_{21.5}), analysis (%) calc. (found): C 29.4 (29.36), H 5.44 (5.45), N 10.30 (10.04). Selected IR peaks (cm⁻¹): 3200 (br), 2926.11 (w), 2891.39 (w), 2841.24 (w), 2750.58 (w), 2740.94 (w), 2681.14 (w), 2654.14 (w), 2632.92 (w), 1465.95 (m), 1437.02 (m), 1367.58 (m), 1292.35 (s), 1263.42 (m), 1170.83 (w), 1149.61 (w), 1139.97 (w), 1076.32 (s), 1057.03 (s), 1047.38 (s), 1016.52 (s), 970.23 (m), 918.15 (m), 906.57 (m), 891.14 (m), 877.64 (m), 848.71 (w), 827.49 (m), 819.77 (m), 788.91 (w), 759.98 (w), 731.05 (m), 682.82 (w), 611.45 (m). IR and CHN data for the crystals match those of the precipitate.

Larger, better formed crystals of **3** can be obtained by a second method: to a stirred solution of [Cu₂(H₃edte)₂][NO₃]₂ (0.4g, 0.55 mmol) and NEt₃ (0.42 ml, 1.5 mmol) in MeOH (20 ml), NdCl₃·6H₂O (0.0.088 g, 0.25 mmol) was added. The reaction was heated at 90°C for 6 hours, cooled to room temperature and filtered. Crystals of **3** form by slow evaporation of the mother liquor over a week. IR and CHN data match those of the crystals obtained from the first method.

2.2.4 Synthesis of [EuCu₃(H₂edte)₃(NO₃)] [NO₃]₂·0.5MeOH (4)

To a stirred solution of [Cu₂(H₃edte)₂][NO₃]₂ (0.4 g 0.55 mmol) and NEt₃ (0.21 ml, 1.5 mmol) in MeOH (20 ml), EuCl₃·6H₂O (0.092 g, 0.25 mmol) was added. The reaction was stirred at room temperature overnight then filtered and placed in a sealed vial. Blue plate-like needles of **4** suitable for X-ray diffraction were grown by vapour diffusion of Et₂O into small portions of the mother liquor. Crystals analyse as **4**, (EuCu₃C_{30.5}H₆₈N₉O_{21.5}), analysis (%) calc. (found): C 29.26 (29.12), H 5.40 (5.41), N 10.24 (9.88). Selected IR peaks (cm⁻¹): 3200 (br), 2926.11 (w), 2842.53 (w), 2740.38 (w), 2681.14 (w), 2644.23 (w), 1465.95 (m), 1437.02 (m), 1370.60 (m), 1292.35 (s), 1263.42 (m), 1170.83 (w), 1150.65 (w), 1139.95 (w), 1076.32 (s), 1057.03 (s), 1045.49 (s), 1016.52 (s), 970.24 (m), 918.15

(m), 903.87 (m), 891.14 (m), 875.22 (m), 827.49 (m), 819.78 (m), 784.55 (w), 759.98 (w), 731.05 (m), 688.00 (w), 613.02 (m).

2.2.5 Synthesis of [GdCu₃(H₂edte)₃(NO₃)] [NO₃]₂·0.5MeOH (5)

To a stirred solution of [Cu₂(H₃edte)₂][NO₃]₂ (0.4 g 0.55 mmol) and NEt₃ (0.21 ml, 1.5 mmol) in MeOH (20 ml), Gd(NO₃)₃·6H₂O (0.112 g, 0.25 mmol) was added. The reaction was stirred at room temperature overnight to yield a blue precipitate which was collected by filtration, washed with EtOH and then air dried. Yield = 89% (0.28 g) based on Gd^{III}. Thin blue plate-like crystals of **5**, suitable for X-ray diffraction, were grown by dissolving ≈ 0.02 g precipitate in 5 ml MeOH and vapour diffusing with THF. Crystals analyse as **5**, (GdCu₃C_{30.5}H₆₈N₉O_{21.5}), analysis (%) calc. (found): C 29.24 (29.0) H 5.47 (5.41) N 10.06 (9.91). Selected IR peaks (cm⁻¹): 3200 (br), 2893.32 (w), 2866.32 (w), 2833.52 (w), 2683.07 (w), 1465.55 (m), 1440.87 (m), 1383.01 (m), 1338.64 (m), 1303.92 (s), 1263.42 (m), 1170.83 (w), 1151.54 (w), 1139.97 (w), 1078.24 (s), 1057.03 (s), 1016.52 (s), 987.59 (m), 970.23 (m), 916.22 (m), 904.64 (m), 891.14 (m), 875.71 (m), 848.71 (w), 827.49 (w), 819.77 (w), 788.91 (w), 761.91 (w), 736.83 (m), 719.47(w), 690.54 (w), 667.39 (w), 613.38 (m). IR and CHN data for the crystals match those of the precipitate.

Larger, better formed crystals of **5** can be obtained by a second method: To a stirred solution of [Cu₂(H₃edte)₂][NO₃]₂ (0.4 g, 0.55 mmol) and NEt₃ (0.42 ml, 1.5 mmol) in MeOH (20 ml), GdCl₃·6H₂O (0.094 g, 0.25 mmol) was added. The reaction was heated at 90°C for 6 hours, cooled to room temperature and filtered. Crystals of **5** form by slow evaporation of the mother liquor over a week. IR and CHN data match those of the crystals obtained from the first method.

2.2.6 Synthesis of [TbCu₃(H₂edte)₃(NO₃)] [NO₃]₂·0.5MeOH (6)

To a stirred solution of [Cu₂(H₃edte)₂][NO₃]₂ (0.4 g 0.55 mmol) and NEt₃ (0.21 ml, 1.5 mmol) in MeOH (20 ml), Tb(NO₃)₃·5H₂O (0.108 g, 0.25 mmol) was added. The reaction was stirred at room temperature overnight to yield a blue precipitate which was collected by filtration, washed with EtOH and then air dried. Yield 88% (0.27 g) based on Tb^{III}. Thin blue plate-like needles of **6**, suitable for X-ray diffraction, were grown by dissolving ≈ 0.02 g precipitate in 5 ml MeOH and vapour diffusing with THF. Crystals analyse as **6**,

(TbCu₃C_{30.5}H₆₈N₉O_{21.5}), analysis (%) calc. (found): C 29.20 (29.04), H 5.46 (5.37), N 10.05 (9.94). Selected IR peaks (cm⁻¹): 3200 (br), 2928.04 (w), 2895.25 (w), 2864.39 (w), 2833.52 (w), 1465.95 (m), 1440.87 (m), 1383.01 (m), 1348.29 (m), 1338.64 (m), 1303.92 (s), 1263.42 (m), 1170.83 (w), 1151.54 (w), 1139.97 (w), 1078.24 (s), 1057.03 (s), 1016.52 (s), 987.59 (m), 970.23 (m), 916.22 (m), 904.64 (m), 891.14 (m), 875.71 (m), 844.85 (w), 827.49 (m), 819.77 (w), 788.91 (w), 758.05 (w), 736.83 (m), 725.26 (w), 677.04 (w), 657.75 (w), 613.38 (m). IR and CHN data for the crystals match those of the precipitate.

Larger, better formed crystals of **6** can be obtained by a second method: To a stirred solution of [Cu₂(H₃edte)₂][NO₃]₂ (0.27 g, 0.37 mmol) and NEt₃ (0.1 ml, 0.75 mmol) in MeOH (20 ml), TbCl₃·6H₂O (0.0093 g, 0.25 mmol) was added. The reaction was heated at 90°C for 6 hours, cooled to room temperature and filtered. Crystals of **6** form by slow evaporation of the mother liquor over a week. IR and CHN data match those of the crystals obtained from the first method.

2.2.7 Synthesis of [DyCu₃(H₂edte)₃(NO₃)][NO₃]₂·0.5MeOH (7)

To a stirred solution of [Cu₂(H₃edte)₂][NO₃]₂ (0.4 g 0.55 mmol) and NEt₃ (0.21 ml, 1.5 mmol) in MeOH (20 ml), Dy(NO₃)₃·5H₂O (0.109 g, 0.25 mmol) was added. The reaction was stirred at room temperature overnight to yield a blue precipitate which was collected by filtration, washed with EtOH and then air dried. Yield = 76% (0.24 g) based on Dy^{III}. Thin blue plate-like crystals of **7**, suitable for X-ray diffraction, were grown by dissolving ≈ 0.02 g precipitate in 5 ml MeOH and vapour diffusing with THF. Crystals analyse as **7**, (DyCu₃C_{30.5}H₆₈N₉O_{21.5}), analysis (%) calc. (found): C 29.01 (28.66), H 5.36 (5.49), N 10.15 (9.80). Selected IR peaks (cm⁻¹): 3200 (br), 2974.33 (w), 2947.33 (w), 2897.18 (w), 2843.17 (w), 1610.61 (w), 1460.16 (m), 1435.09 (m), 1413.87 (m), 1383.01 (m), 1354.07 (m), 1313.57 (s), 1259.56 (m), 1234.48 (m), 1170.83 (w), 1149.61 (w), 1107.18 (w), 1078.24 (s), 1057.03 (s), 1033.88 (s), 1014.59 (s), 985.66 (m), 922.00 (m), 908.50 (m), 893.07 (m), 883.43 (m), 869.92 (m), 844.85 (w), 825.56 (m), 817.85 (w), 756.12 (w), 725.26 (m), 646.17 (w), 605.67 (m). IR and CHN data for the crystals match those of the precipitate.

Larger, better formed crystals can be obtained by a second method: To a stirred solution of [Cu₂(H₃edte)₂][NO₃]₂ (0.27 g, 0.37 mmol) and NEt₃ (0.1 ml, 0.75 mmol) in MeOH (20 ml), DyCl₃·6H₂O (0.0096 g, 0.25 mmol) was added. The reaction was heated at 90°C for 6

hours, cooled to room temperature and filtered. Crystals of **7** form by slow evaporation of the mother liquor over a week. IR and CHN data match those of the crystals obtained from the first method.

2.2.8 Synthesis of [ErCu₃(H₂edte)₃(NO₃)][NO₃]₂·MeOH (8)

To a stirred solution of [Cu₂(H₃edte)₂][NO₃]₂ (0.4 g 0.55 mmol) and NEt₃ (0.21 ml, 1.5 mmol) in MeOH (20 ml), Dy(NO₃)₃·5H₂O (0.109 g, 0.25 mmol) was added. The reaction was stirred at room temperature overnight to yield a blue precipitate which was collected by filtration, washed with EtOH and then air dried. Yield = 83% (0.24 g) based on Er^{III}. Thin blue plate-like crystals of **8**, suitable for X-ray diffraction, were grown by dissolving ≈ 0.02 g precipitate in 5 ml MeOH and vapour diffusing with THF. Crystals analyse as **8**, (ErCu₃C_{30.5}H₆₈N₉O_{21.5}), analysis (%) calc. (found): C 28.85 (28.48), H 5.49 (5.42), N 10.09 (9.72). Selected IR peaks (cm⁻¹): 3200 (br), 2912.61 (w), 2902.96 (w), 2852.81 (w), 2843.17 (w), 1464.02 (m), 1438.94 (m), 1413.87 (m), 1375.29 (m), 1354.07 (m), 1315.50 (s), 1259.56 (m), 1234.48 (w), 1170.83 (w), 1151.54 (w), 1139.97 (w), 1080.17 (s), 1057.03 (s), 1035.81 (m), 1016.52 (s), 985.66 (w), 933.58 (m), 922.00 (m), 908.50 (m), 893.07 (w), 883.43 (w), 869.92 (w), 825.56 (m), 817.85 (w), 758.05 (w), 725.26 (m), 675.11 (w), 607.60 (m). IR and CHN data for the crystals match those of the precipitate.

2.2.9 Synthesis of [YbCu₃(H₂edte)₃(NO₃)][NO₃]₂·0.5MeOH (9)

To a stirred solution of [Cu₂(H₃edte)₂][NO₃]₂ (0.4 g 0.55 mmol) and NEt₃ (0.21 ml, 1.5 mmol) in MeOH (20 ml), Yb(NO₃)₃·5H₂O (0.109 g, 0.25 mmol) was added. The reaction was stirred at room temperature overnight to yield a blue precipitate which was collected by filtration, washed with EtOH and then air dried. Yield = 88% (0.27 g) based on Yb^{III}. Thin blue plate-like crystals of **9**, suitable for X-ray diffraction, were grown by dissolving ≈ 0.02 g precipitate in 5 ml MeOH and vapour diffusing with THF. Crystals analyse as **9** (YbCu₃C_{30.5}H₆₈N₉O_{21.5}), analysis (%) calc. (found): C 28.98 (28.80), H 5.49 (5.31), N 9.81 (9.70). Selected IR peaks (cm⁻¹): 3200 (br), 2949.26 (w), 2912.61 (w), 2901.04 (w), 2852.81 (w), 2843.17 (w), 1610.61 (w), 1462.09 (m), 1437.02 (m), 1413.87 (m), 1384.84 (m), 1367.58 (m), 1354.07 (m), 1311.64 (s), 1257.63 (m), 1232.55 (m), 1170.83 (w), 1149.61 (w), 1105.25 (w), 1080.17 (s), 1060.88 (s), 1033.88 (s), 1014.59 (s), 985.66 (m),

922.00 (m), 908.50 (m), 893.07 (m), 883.43 (m), 869.92 (w), 844.85 (w), 825.56 (w), 817.85 (m), 756.12 (w), 682.82 (w), 655.82 (m), 605.67 (m). IR and CHN data for the crystals match those of the precipitate.

Larger, better formed crystals of **9** can be obtained by a second method: to a stirred solution of [Cu₂(H₃edte)₂][NO₃]₂ (0.27 g, 0.37 mmol) and NEt₃ (0.42 ml, 3 mmol) in MeOH (20 ml), YbCl₃·6H₂O (0.0097 g, 0.25 mmol) was added. The reaction was heated at 90°C for 6 hours, cooled to room temperature and filtered. Crystals of **9** form by slow evaporation of the mother liquor over a week. IR and CHN data match those of the crystals obtained from the first method.

2.3 Results and Discussion

2.3.1 Synthesis

The series of complexes [LnCu₃(H₂edte)₃(NO₃)][NO₃]₂·0.5MeOH where Ln = Pr^{III} (**2**), Nd^{III} (**3**), Eu^{III} (**4**), Gd^{III} (**5**), Tb^{III} (**6**), Dy^{III} (**7**), Er^{III} (**8**), Yb^{III} (**9**), can be synthesised by reacting a preformed copper complex; [Cu₂(H₃edte)₂][NO₃]₂ (**1**) with triethylamine and the respective lanthanide nitrate salt in the mmol ratio 0.55 : 1.5 : 0.25. These ratios were found to produce an optimised yield of microcrystalline precipitate which could be recrystallised by dissolving ≈ 0.02 g in 5 ml MeOH and vapour diffusing with Et₂O. For the analogues Nd^{III}, Gd^{III}, Tb^{III}, Dy^{III} and Yb^{III}, the crystals obtained by recrystallising the precipitate were very fine needles. It was found that by using slightly different ratios (see Section 2.2) and replacing the lanthanide nitrate salt with the chloride salt, larger crystals could be obtained by slow evaporation of the mother liquor. When the lanthanide chloride salts were used, no precipitate formed in the reactions, presumably due to the lack of available nitrate counter ions. Attempts to synthesise the Y^{III}, La^{III} and Ho^{III} were unsuccessful, the remaining lanthanide ions were not attempted. Complex **1** can be synthesised in high yield (95% based on Cu^{II}) by reacting two equivalents of H₄edte with one equivalent of Cu(NO₃)₂·3H₂O in MeCN. The dimer precipitates out as a green microcrystalline powder which can be easily recrystallised by dissolving ≈ 50 mg in 5 ml MeOH and vapour diffusing with Et₂O. The complexes in the {LnCu₃} series can be synthesised without using the preformed copper dimer as starting material; instead just using Cu(NO₃)₂·3H₂O and H₄edte in a one pot reaction with NEt₃ and the respective lanthanide salt. However, in all cases, the yields were poorer.

2.3.2 Discussion of the Crystal Structure of $[\text{Cu}_2(\text{H}_3\text{edte})_2][\text{NO}_3]_2$ (**1**)

The dimeric copper complex **1**, used as starting material in the preparation of the $\{\text{LnCu}_3(\text{H}_2\text{edte})_3\}$ series, crystallises in the monoclinic space group $P2_1/c$. The asymmetric unit consists of one Cu^{II} ion chelated by an $\text{H}_3\text{edte}^{1-}$ ligand and a lattice nitrate anion (Figure 2.4). The ligand binds to Cu^{II} through both N donors and three oxygen donors, one of which has been deprotonated, the final arm is unbound but has retained its hydroxyl proton. The unit cell consists of two molecules of **1** and four lattice nitrate anions.

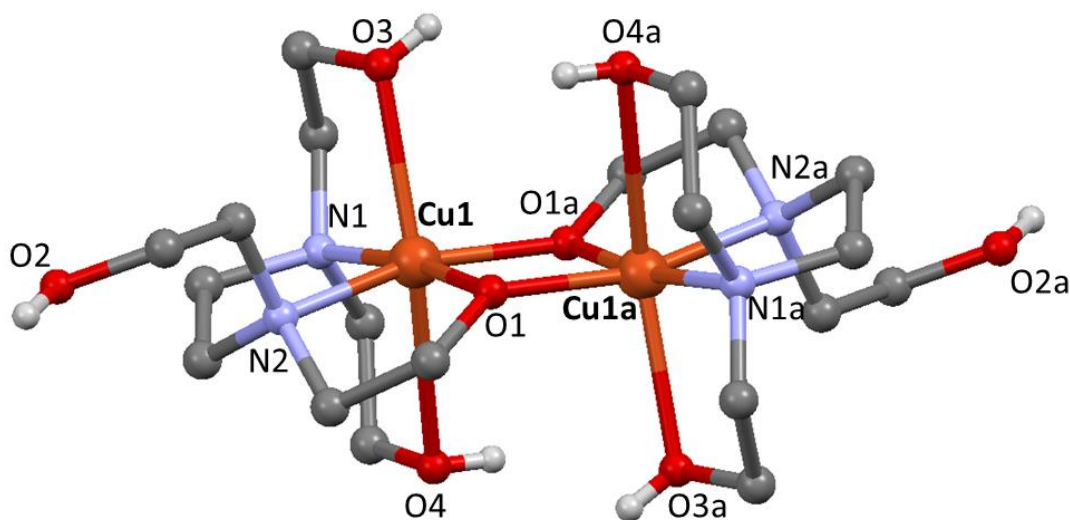


Figure 2.4: Crystal structure of **1** with C-H protons and nitrate counterions omitted. Atom colours: C, grey; N, blue; O, red; H, white; Cu^{II} orange.

The complex consists of two $\{\text{Cu}(\text{H}_3\text{edte})\}$ units with an inversion centre between them. The deprotonated O1 atom of the ligand acts as an alkoxo bridge between the Cu^{II} ions with Cu1-O1-Cu1a angle = $99.42(4)^\circ$. Each Cu^{II} ion is in a distorted octahedral geometry with atoms O3 and O4 occupying the axial sites and atoms N1, N2, O1 and O1a the equatorial sites. The axial bond lengths ($\approx 2.4 - 2.7 \text{ \AA}$) are significantly longer than the equatorial bond lengths ($1.9 - 2.0 \text{ \AA}$), as expected for a d^9 Cu^{II} ion exhibiting a Jahn-Teller distortion (see Table 2.2 for bond lengths). The structure is similar to a previously reported $[\text{Cu}_2(\text{H}_3\text{edte})_2][\text{ClO}_4]_2$ complex which contains perchlorate counterions instead of nitrates.⁴²

<i>Empirical formula</i>	<i>Cu₂C₂₀H₄₆N₆O₁₄</i>
Molar mass (g mol ⁻¹)	721.71
Crystal System	Monoclinic
Space Group	<i>P</i> 2 ₁ / <i>c</i>
<i>a</i> (Å)	8.9168(2)
<i>b</i> (Å)	16.6076(3)
<i>c</i> (Å)	9.7099(2)
<i>α</i> (deg)	90
<i>β</i> (deg)	96.868(2)
<i>γ</i> (deg)	90
<i>V</i> (Å ³)	1427.59(5)
<i>Z</i>	2
<i>T</i> (K)	100(2)
<i>λ</i> (Å)	0.71073
<i>ρ</i> _{calc} (g/cm ³)	1.679
<i>μ</i> (mm ⁻¹)	1.57
^a <i>R</i> ₁	0.0209
^b <i>wR</i> ₂	0.0513
Goodness of fit	1.059
F(000)	748
Reflections	2622
Parameters	199
Restraints	0

Table 2.1: Crystallographic data for **1**.

$${}^a R_1 = \frac{\sum ||F_o| - |F_c||}{\sum |F_o|}$$

$${}^b wR_2 = \frac{[\sum [w(F_o^2 - F_c^2)^2] - \sum [(F_o^2)^2]]^{\frac{1}{2}}}{\sum w F_o^2} \quad \text{where } w = 1/[\sigma^2(F_o^2) + (0.2P)^2] \text{ and } P = [F_o^2 + 2F_c^2]/3$$

Atoms	Distance (Å)
Cu1 – N1	2.0075(12)
Cu1 – N2	2.0267(12)
Cu1 – O1	1.9399(10)
Cu1 – O1a	1.9300(10)
Cu1 – O3	2.4018(11)
Cu1 – O4	2.7758(12)

Table 2.2: Selected bond distances in **1**.

2.3.3 Discussion of the $\{\text{LnCu}_3(\text{H}_2\text{edte})_3\}$ Series' Structure

The series $[\text{LnCu}_3(\text{H}_2\text{edte})_3(\text{NO}_3)][\text{NO}_3]_2$ where $\text{Ln} = \text{Pr}^{\text{III}}, \text{Nd}^{\text{III}}, \text{Eu}^{\text{III}}, \text{Gd}^{\text{III}}, \text{Tb}^{\text{III}}, \text{Dy}^{\text{III}}$, and Yb^{III} are all isostructural, crystallising in the triclinic space group $P-1$. The Er^{III} analogue crystallises in the monoclinic space group $P2_1/n$, however, the $\{\text{ErCu}_3(\text{H}_2\text{edte})_3\}$ molecule is isostructural with the rest of the series.

The unit cell of the triclinic analogues consists of two $\{\text{LnCu}_3\}$ molecules, two fully occupied lattice nitrates, two disordered lattice nitrates and a disordered MeOH molecule (Figure 2.5). The MeOH molecule (atoms C300 and O300) sits next to an inversion centre in the unit cell and is 50% positionally disordered. It is paired with a 50% occupied lattice nitrate (atoms N100, O100, O101 and O102) which sits next to the same inversion centre. The final nitrate (atoms N200, O200, O201 and O202) is also positionally disordered with an inversion centre sitting directly between atoms N200 and O200 giving it its 'odd' appearance (Figure 2.5).

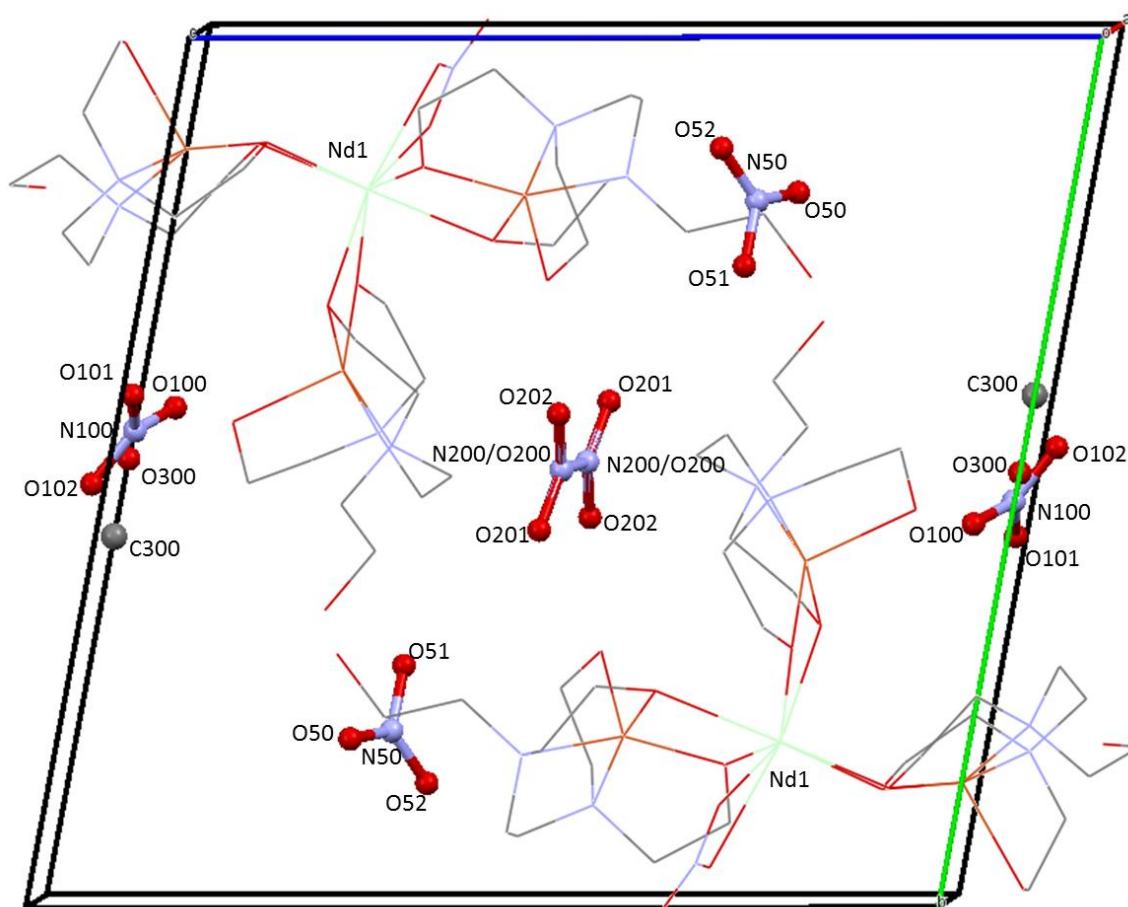


Figure 2.5: Unit cell of $[\text{NdCu}_3(\text{H}_2\text{edte})(\text{NO}_3)][\text{NO}_3]_2 \cdot 0.5\text{MeOH}$, representative of the unit cell for all triclinic analogues.

The unit cell for the Er^{III} analogue contains four $\{\text{ErCu}_3(\text{H}_2\text{edte})_3\}$ molecules, eight lattice nitrate counterions and four MeOH molecules. Unlike the triclinic structures, the counterions and lattice solvents are all fully occupied in their positions.

The $\{\text{LnCu}_3\}$ complex molecule consists of an 8-coordinate central lanthanide ion bound to three neutral $\{\text{CuH}_2\text{edte}\}$ metalloligand subunits and a bidentate nitrate ligand (Figure 2.6). The +3 charge of the lanthanide is balanced by the ligated nitrate and two lattice nitrates. The metalloligand subunits have a Cu^{II} ion chelated by a $\text{H}_2\text{edte}^{2-}$ ligand; adopting a square based pyramidal geometry. The ligand binds through both nitrogen donors and three of its four oxygen donor atoms. The two deprotonated arms of the ligand form alkoxo bridges between the central Ln^{III} ion and Cu^{II} subunit ion. Of the remaining protonated arms, one occupies the axial position on the Cu^{II} ion with the final arm extending out into the crystal lattice where it takes part in hydrogen bonding with lattice nitrates.

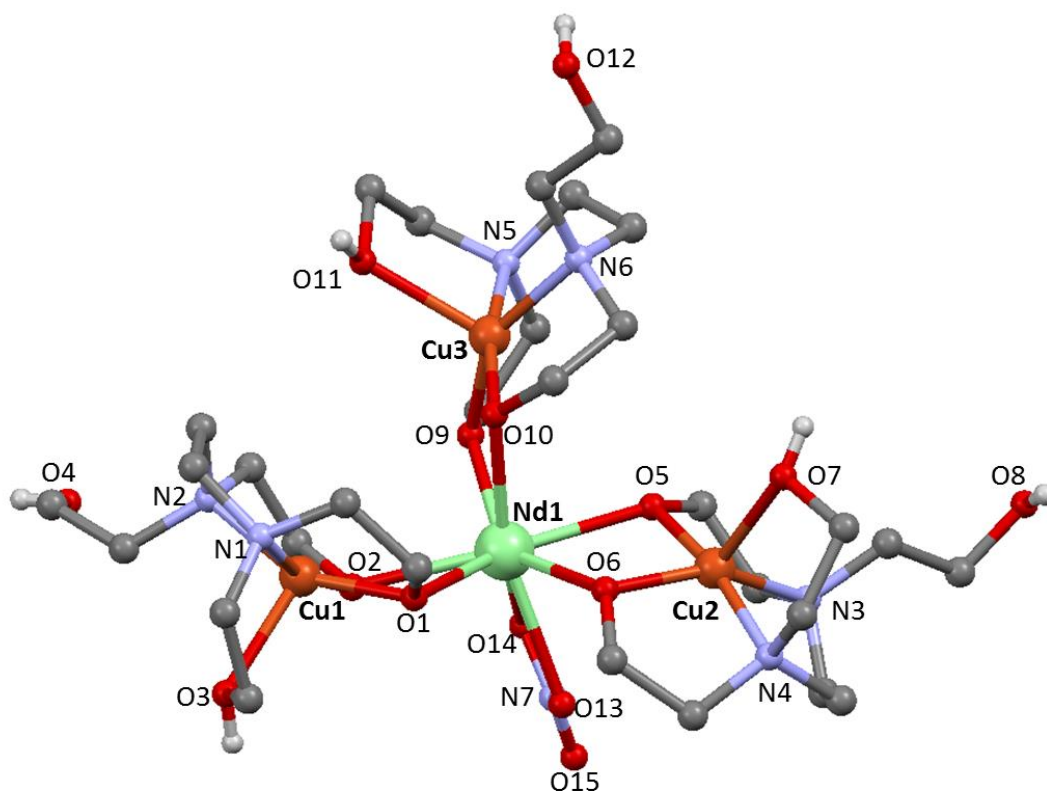


Figure 2.6: Molecular structure for **3**, representative of all series members. C-H protons have been omitted for clarity. Atom colours: Nd^{III} , Light green; Cu^{II} , orange; O, red; N, blue; C, grey; H white.

<i>Empirical formula</i>	<i>PrCu₃C_{30.5}H₆₈N₉O_{21.5}</i>	<i>NdCu₃C_{30.5}H₆₈N₉O_{21.5}</i>	<i>EuCu₃C_{30.5}H₆₈N₉O_{21.5}</i>	<i>GdCu₃C_{30.5}H₆₈N₉O_{21.5}</i>
Molar mass (g mol ⁻¹)	1236.47	1239.79	1247.52	1252.80
Crystal System	Triclinic	Triclinic	Triclinic	Triclinic
Space Group	<i>P-1</i>	<i>P-1</i>	<i>P-1</i>	<i>P-1</i>
<i>a</i> (Å)	8.9742(2)	8.9689(3)	8.9670(5)	8.9333(2)
<i>b</i> (Å)	16.0726(3)	16.0375(7)	16.0640(11)	15.9959(4)
<i>c</i> (Å)	16.4384(3)	16.3907(7)	16.3600(11)	16.2969(3)
α (deg)	78.244(2)	78.550(2)	78.392(5)	79.369 (2)
β (deg)	87.277(2)	86.983(3)	87.084(6)	86.275(2)
γ (deg)	82.562(2)	82.487(2)	82.617(5)	82.513(2)
V (Å ³)	2301.24(8)	2290.0(2)	2288.4(2)	2267.28(9)
Z	2	2	2	2
T (K)	100(2)	100(2)	100(2)	100(2)
λ (Å)	0.71073	0.71073	0.71073	0.71073
ρ_{calc} (g/cm ³)	1.783	1.797	1.807	1.834
μ (mm ⁻¹)	2.49	2.58	2.81	2.92
^a R ₁	0.0666	0.0555	0.055	0.0444
^b wR ₂	0.1181	0.1179	0.0967	0.0905
Goodness of fit	1.156	1.028	1.079	1.169
F(000)	1264	1266	1272	1274
Reflections	8440	8368	10405	8033
Parameters	590	590	557	587
Restraints	3	3	22	4

Table 2.3: Crystallographic data for complexes **2 - 5**.

$${}^aR_1 = \frac{\sum ||F_o| - |F_c||}{\sum |F_o|}$$

$${}^b wR_2 = \frac{[\sum [w(F_o^2 - F_c^2)^2] - \sum [(F_o^2)^2]]^{\frac{1}{2}}}{\sum [w(F_o^2 + (0.2P)^2)]^{\frac{1}{2}}} \quad \text{where} \quad w = 1/[\sigma^2(F_o^2) + (0.2P)^2] \quad \text{and} \quad P = [F_o^2 + 2F_c^2]/3$$

<i>Empirical formula</i>	<i>TbCu₃C_{30.5}H₆₈N₉O_{21.5}</i>	<i>DyCu₃C_{30.5}H₆₈N₉O_{21.5}</i>	<i>ErCu₃C_{30.5}H₆₈N₉O_{21.5}</i>	<i>YbCu₃C_{30.5}H₆₈N₉O_{21.5}</i>
Molar mass (g mol ⁻¹)	1254.48	1258.06	1262.82	1268.59
Crystal System	Triclinic	Triclinic	Monoclinic	Triclinic
Space Group	<i>P-1</i>	<i>P-1</i>	<i>P2₁/n</i>	<i>P-1</i>
<i>a</i> (Å)	8.9334(2)	8.9331(3)	8.8170(17)	8.9068(2)
<i>b</i> (Å)	16.0024(4)	15.9760(6)	41.419(8)	16.0181(4)
<i>c</i> (Å)	16.3048(4)	16.3223(6)	12.716(3)	16.2204(4)
α (deg)	78.9190(10)	79.003(2)	90	78.8190(10)
β (deg)	86.4920(10)	86.363(2)	90.183(3)	86.0550(10)
γ (deg)	82.839(2)	82.688(2)	90	83.102(2)
V (Å ³)	2267.91(10)	2266.24(14)	4643.7(11)	2251.35(6)
Z	2	2	4	2
T (K)	100(2)	100(2)	100(2)	100(2)
λ (Å)	0.71073	0.71073	0.71073	0.71073
ρ_{calc} (g/cm ³)	1.836	1.843	1.815	1.864
μ (mm ⁻¹)	3.02	3.11	3.232	3.545
^a R ₁	0.0549	0.0586	0.0551	0.0516
^b wR ₂	0.0832	0.1007	0.1163	0.0726
Goodness of fit	0.995	1.064	1.031	0.895
F(000)	1276	1278	2564	1286
Reflections	8346	8527	8529	8273
Parameters	617	589	596	542
Restraints	5	3	472	311

Table 2.4: Crystallographic data for complexes **6 - 9**

$${}^aR_1 = \frac{\sum ||F_o| - |F_c||}{\sum |F_o|}$$

$${}^b wR_2 = \frac{[\sum [w(F_o^2 - F_c^2)^2] - \sum [(F_o^2)^2]]^{\frac{1}{2}}}{\sum [w(F_o^2 - F_c^2)^2]} \quad \text{where} \quad w = 1/[\sigma^2(F_o^2) + (0.2P)^2] \quad \text{and} \quad P = [F_o^2 + 2F_c^2]/3$$

2.3.3.1 Torsion angles

An important structural feature of $\{\text{LnCu}_3\}$ complexes with respect to their magnetic properties is that of the torsion angle (θ) formed between Ln^{III} and Cu^{II} through the alkoxo bridges^{44,45,49} (Figure 2.7). Recent studies⁴⁴ of dinuclear $\{\text{Gd}^{\text{III}}\text{Cu}^{\text{II}}\}$ complexes using density functional theory (DFT) found that the torsion angle through $\text{Gd}^{\text{III}}\text{-O-O-Cu}^{\text{II}}$ was strongly correlated to the strength and sign of the coupling constant J . It was found that when θ is in the range: $140^\circ \leq \theta \leq 180^\circ$, ferromagnetic exchange is dominant; the strongest coupling observed as $\theta \approx 180^\circ$. As θ approaches 140° , the ferromagnetic exchange gradually weakens until there is a switch to antiferromagnetic at around $\theta \approx 140^\circ$. There are a number of theories which aim to rationalise this behaviour. One of these, (backed by DFT calculations⁴⁴), is that a superexchange mechanism exists between the $3d$ orbitals of Cu^{II} and the $4f$ orbitals of Gd^{III} . Direct $3d\text{-}4f$ overlap produces an antiferromagnetic $\text{Gd}^{\text{III}}\text{-Cu}^{\text{II}}$ interaction, whilst orthogonal overlap produces a ferromagnetic interaction. Both types of exchange co-exist, but depending on the torsion angle, one has a dominant contribution over the other. For planar structures ($\theta \approx 180^\circ$), of the seven possible $3d\text{-}4f$ orbital interactions there are only two non-orthogonal interactions; the remaining five interactions are considered orthogonal thus ferromagnetic exchange is observed. As the structure distorts and θ approaches 140° ; the number of non-orthogonal $3d\text{-}4f$ interactions increases until it exceeds the number of orthogonal interactions at which point antiferromagnetic exchange is observed.

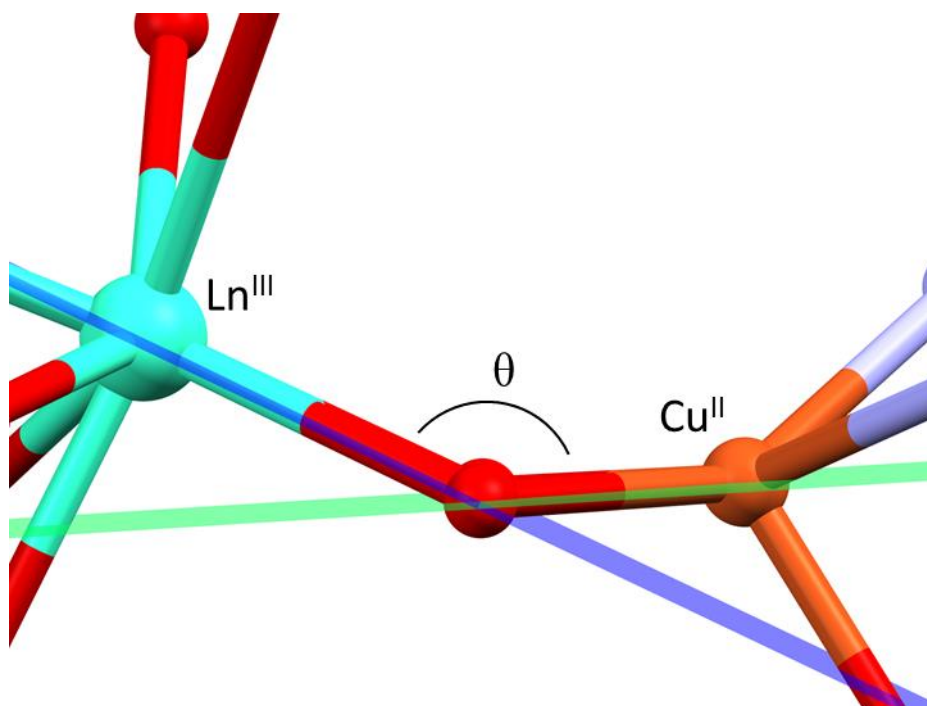


Figure 2.7: Representation of the $\text{Ln}^{\text{III}}\text{-O-O-Cu}^{\text{II}}$ torsion angle θ .

	2 (<i>Pr^{III}</i>)	3 (<i>Nd^{III}</i>)	4 (<i>Eu^{III}</i>)	5 (<i>Gd^{III}</i>)
Ln1-O1-O2-Cu1	152.05°	151.54°	152.26°	150.72°
Ln1-O5-O6-Cu2	164.95°	164.57°	165.13°	164.88°
Ln1-O9-O10-Cu3	165.62°	165.55°	166.01°	165.84°

Table 2.5: List of Ln-O-O-Cu torsion angles for complexes **2 – 5** with corresponding Ln^{III} ion in brackets.

	6 (<i>Tb^{III}</i>)	7 (<i>Dy^{III}</i>)	8 (<i>Er^{III}</i>)	9 (<i>Yb^{III}</i>)
Ln1-O1-O2-Cu1	150.98°	150.94°	150.45	149.97°
Ln1-O5-O6-Cu2	164.8°	165.04°	165.02	163.98°
Ln1-O9-O10-Cu3	166.11°	166.24°	167.06	166.79°

Table 2.6: List of Ln-O-O-Cu torsion angles for complexes **6 – 9** with corresponding Ln^{III} ion in brackets.

The torsion angles for the {LnCu₃} series are listed in Tables 2.5 and 2.6. The complexes all show θ to be in the ferromagnetic range, so for the lanthanides with greater than half filled 4*f* subshells, whose orbital moments are parallel to their spin moments (negative free ion spin orbit coupling constant), ferromagnetic exchange is expected. However, antiferromagnetic coupling is expected for the earlier lanthanides whose spin-orbit coupling constant is positive.⁴⁹

2.3.3.2 SHAPE Analysis

The coordination sphere of the central lanthanide was analysed using the programme SHAPE⁴³ to give insight into another structural property which also significantly affects the magnetic properties of 3*d*-4*f* complexes. The programme draws a geometric polyhedron around the lanthanide ion using the crystal field donor atoms as the vertices. The programme generates ‘continuous shape measurement values’ (ChSM) for each of the possible geometries for a certain coordination number (e.g. an 8-coordinate ion has 13 possible polyhedra), the closest ChSM value to zero indicates the closest matching polyhedron that describes the geometry.

	Square	Triangular	Biaugmented	Snub disphenoid
	D_{4d}	D_{2d}	C_{2v}	D_{2d}
	SAPR-8	TDD-8	BTPR-8	JSD-8
2 (Pr ^{III})	3.991	<u>2.755</u>	2.862	4.932
3 (Nd ^{III})	3.919	<u>2.664</u>	2.806	4.845
4 (Eu ^{III})	3.494	<u>2.434</u>	2.483	4.620
5 (Gd ^{III})	3.289	<u>2.313</u>	2.343	4.543
6 (Tb ^{III})	3.160	<u>2.252</u>	2.280	4.557
7 (Dy ^{III})	3.033	2.214	<u>2.197</u>	4.453
8 (Er ^{III})	2.354	2.590	<u>1.762</u>	4.695
9 (Yb ^{III})	2.586	2.143	<u>1.950</u>	4.463

Table 2.7: SHAPE summary for complexes **2 - 9**. Optimal ChSM value underlined.

The ChSM values in Table 2.7 show a trend toward the early Ln^{III} analogues favouring triangular dodecahedral (D_{2d}) geometry with a switch to biaugmented trigonal prismatic (C_{2v}) from Dy^{III} onwards. The relatively large ChSM values are indicative of significant distortion.

2.4 Magnetism

2.4.1 Static Magnetic Properties for $\{\text{PrCu}_3(\text{H}_2\text{edte})_3\}$ (2)

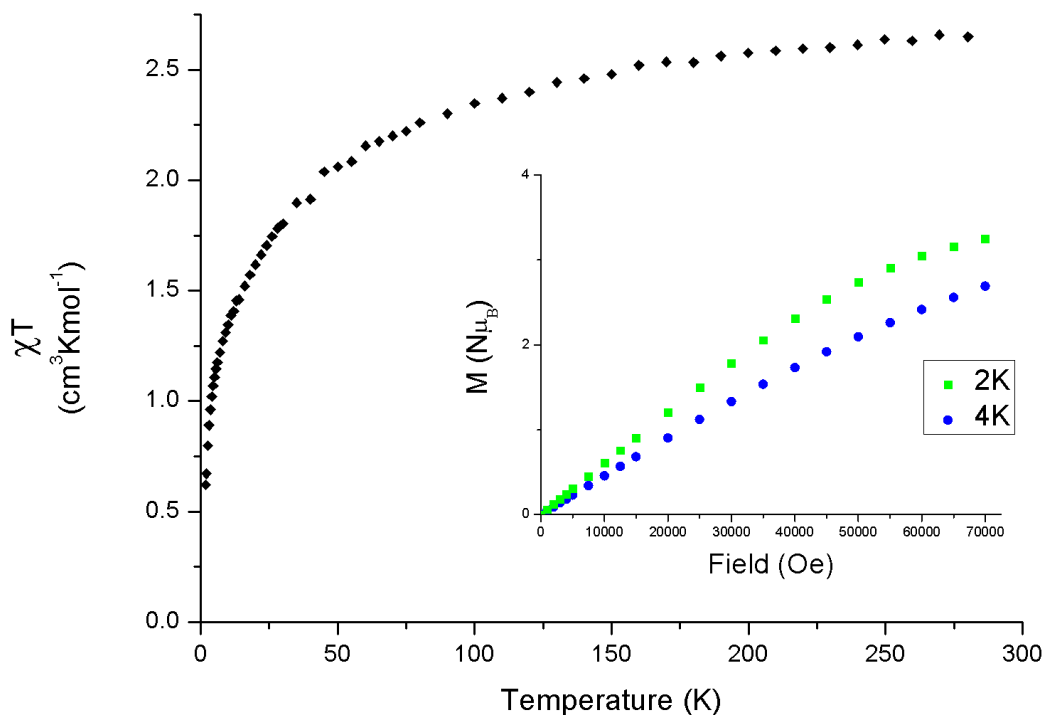


Figure 2.8: Dc magnetic susceptibility vs. temperature for **2** in a 1 kOe field. Inset; magnetisation vs. field at 2 and 4 K.

The temperature dependent magnetic susceptibility of a polycrystalline sample of **2** was measured in the temperature range 300 – 1.8 K under an applied dc field of 1 kOe (Figure 2.8). The room temperature χT value of $2.65 \text{ cm}^3 \text{ K mol}^{-1}$ agrees reasonably well with the calculated (see Equations 1.8 and 1.19) value of $2.83 \text{ cm}^3 \text{ K mol}^{-1}$ for a system of non-coupled spins; one Pr^{III} ion ($^3\text{H}_4$, $S = 1$, $L = 5$, $J = 4$, $g_J = 4/5$, $\chi T = 1.60 \text{ cm}^3 \text{ K mol}^{-1}$) and three Cu^{II} ions ($g_{\text{Cu}} = 2.1$, $s = 1/2$, $\chi T = 1.23$). As T is lowered, χT decreases down to a minimum of $0.62 \text{ cm}^3 \text{ K mol}^{-1}$ at 1.8 K. The decrease in χT is likely due to a combination of depopulation of M_{tot} sublevels, antiferromagnetic Pr^{III} - Cu^{II} exchange and possibly intermolecular antiferromagnetic interactions. It is however virtually impossible to unravel their individual contributions.

M vs. H data (inset Figure 2.8) were collected for **2** at 2 and 4 K in the range 0 – 70 kOe. Both complexes show a gradual increase in their magnetisation as the field is increased up to 70 kOe but do not show full saturation at the expected $M_{\text{sat}} = 6.35 N\mu_{\text{B}}$, even at 2 K. The profile of the M vs. H curves suggest the presence of closely spaced M_{tot} sublevels for **2**, with low lying states still populated at 70 kOe at both 2 and 4 K.

2.4.2 Dynamic Magnetic Properties of **2**

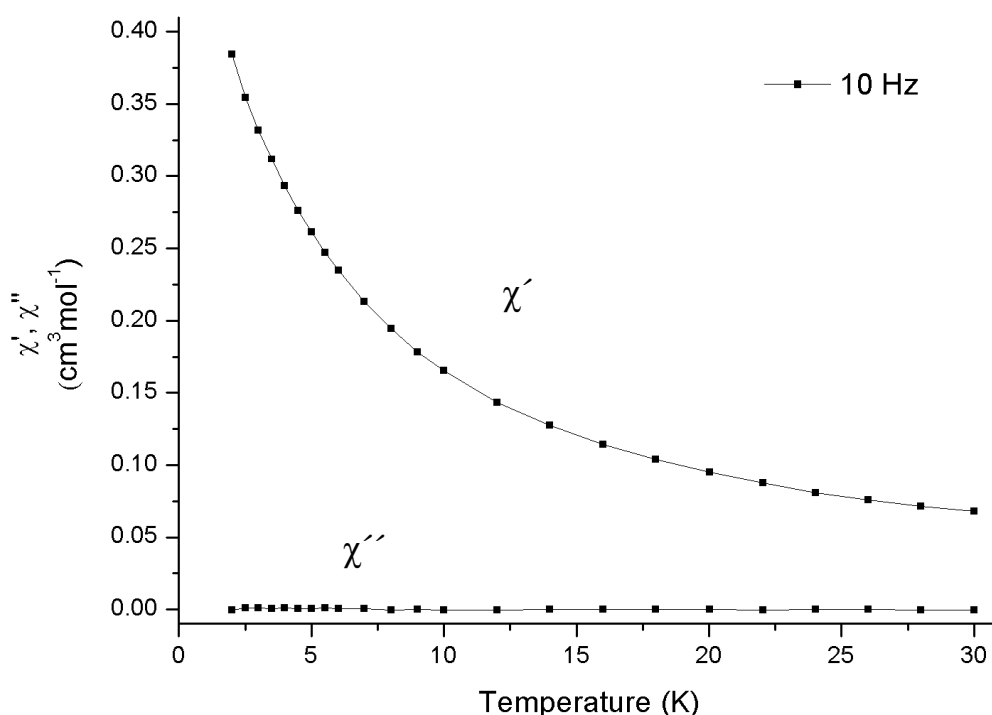


Figure 2.9: *Ac susceptibility measurements for 2 in zero applied dc field*

Ac susceptibility measurements were carried out for **2** to search for slow magnetic relaxation at low temperatures (Figure 2.9). The measurements were made in a 10 Hz ac field with no applied dc field, down to 1.8 K. **2** showed no significant increase in χ'' under these conditions, indicating the absence of slow relaxation under these conditions. Possible reasons for this could be that the crystal field around Pr^{III} is not stabilising the higher m_J sublevels relative to the lower ones, or that there is only a small energy gap between the ground and first excited states. The antiferromagnetic Pr^{III} - Cu^{II} exchange will also lead to an overall low value M_{tot} state for the complex.

2.4.3 Static Magnetic Properties for $\{\text{NdCu}_3(\text{H}_2\text{edte})_3\}$ (**3**)

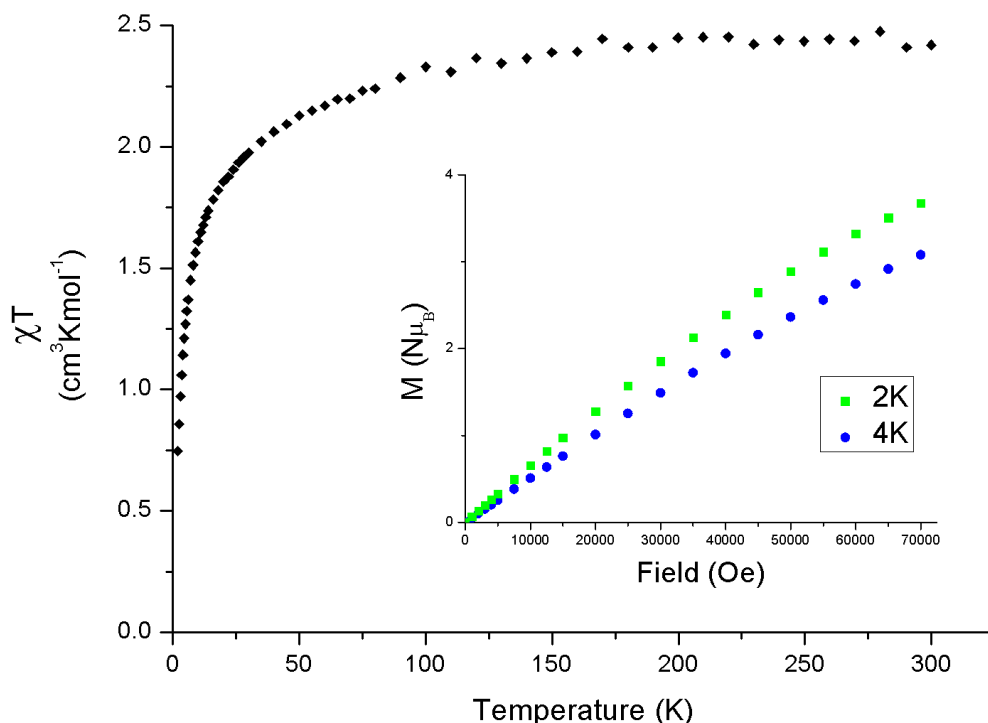


Figure 2.10: Dc magnetic susceptibility vs. temperature for **3** in a 1 kOe field. Inset; magnetisation vs. field at 2 and 4 K.

The temperature dependent magnetic susceptibility of a polycrystalline sample of **3** was measured in the temperature range 300 – 2 K under an applied dc field of 1 kOe (Figure 2.10). The room temperature χT value of $2.42 \text{ cm}^3 \text{K mol}^{-1}$ is in reasonable agreement with the calculated value of $2.87 \text{ cm}^3 \text{K mol}^{-1}$ for a system of non-interacting spins; one Nd^{III} ion ($^4\text{I}_{9/2}$, $S = 3/2$, $L = 6$, $J = 9/2$, $g_J = 8/11$) and three Cu^{II} ions ($g_{\text{Cu}} = 2.1$, $s = 1/2$). As T is lowered, χT decreases down to a minimum of $0.75 \text{ cm}^3 \text{K mol}^{-1}$ at 2 K. The decrease in χT is likely due to a combination of depopulation of excited M_{tot} sublevels, antiferromagnetic Nd^{III} - Cu^{II} exchange and possibly intermolecular antiferromagnetic interactions. It is however impossible to unravel their individual contributions.

Magnetisation vs. field data for **3** shows a gradual increase in magnetisation as the field is increased up to 70 kOe but without reaching full saturation, even at 2 K (inset Figure 2.10). The profile of the M vs. H curves suggest the presence of closely spaced M_{tot} sublevels for **2**, with low lying states still populated at 70 kOe at both 2 and 4 K.

2.4.4 Dynamic Magnetic Properties of **3**

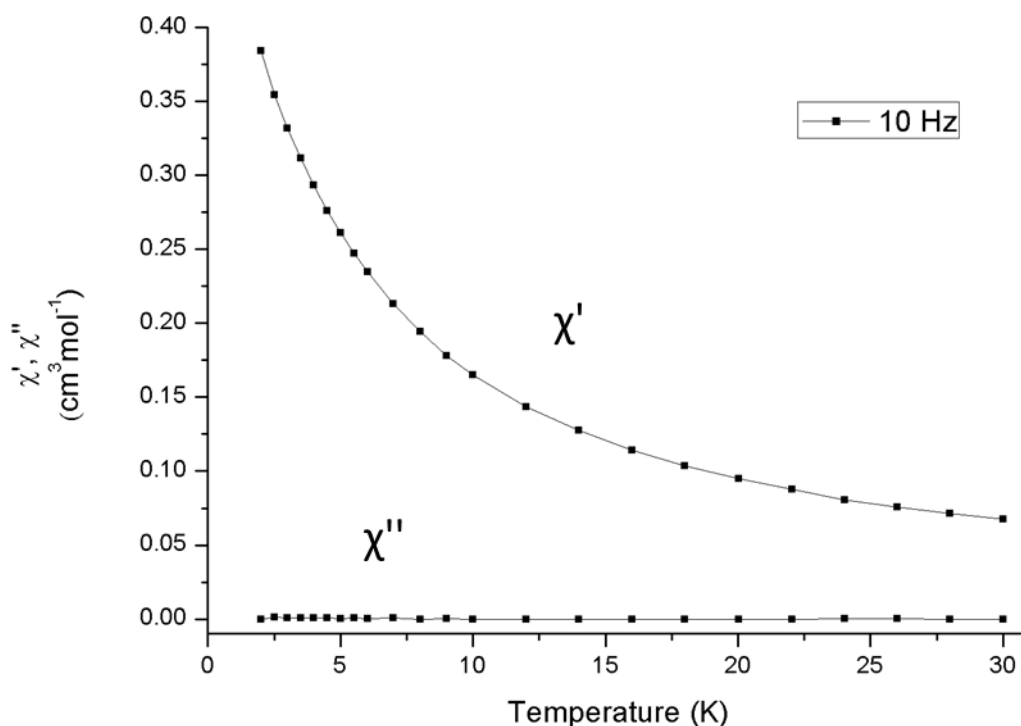


Figure 2.11: Ac susceptibility measurements for **3** in zero applied dc field.

Ac susceptibility measurements were made on **3** using a 10 Hz ac field with no applied dc field, down to 1.8 K (Figure 2.11). The complex showed no significant increase in χ'' under these conditions, indicating the absence of slow relaxation. Possible reasons for this could be that the crystal field around Nd^{III} is not stabilising the higher m_J sublevels relative to the lower ones, or that there is only a small energy gap between the ground and first excited states – similar to **2**. The antiferromagnetic Nd^{III} - Cu^{II} exchange will also lead to an overall low value M_{tot} state for the complex.

2.4.5 Magnetic Susceptibility Measurements for $\{\text{GdCu}_3(\text{H}_2\text{edte})_3\}$ (**5**)

The temperature dependent magnetic susceptibility of a polycrystalline sample of **5** was measured in a 1 kOe field in the temperature range 1.8 – 280 K (Figure 2.11). The measurements show χT gradually increasing as T decreases from 280 K to around 75 K whereby it increases much more rapidly up to a peak at $\chi T \approx 14.3 \text{ cm}^3 \text{ K mol}^{-1}$ at 3.5 K. This is then followed by a sharp downturn to $\chi T \approx 14.1 \text{ cm}^3 \text{ K mol}^{-1}$ at 1.8 K. The room temperature χT value of $9.4 \text{ cm}^3 \text{ K mol}^{-1}$ is consistent with a system of four non-interacting spins; one Gd^{III} ion ($^8\text{S}_{7/2}$, $s = 7/2$, $g_J = 2$) and three Cu^{II} ions ($g_{\text{Cu}} = 2.1$ $s = 1/2$). The increase in χT is due to ferromagnetic exchange between the Gd^{III} ion and three Cu^{II} ions; well documented^{39-41,49} for Gd – Cu systems and is expected for **5** due to the $\text{Gd}^{\text{III}}\text{-O-O-Cu}^{\text{II}}$ torsion angles^{44,45} being $> 140^\circ$ (see Table 5). The sharp downturn as T decreases below 3.5 K is possibly due to intermolecular antiferromagnetic interactions.

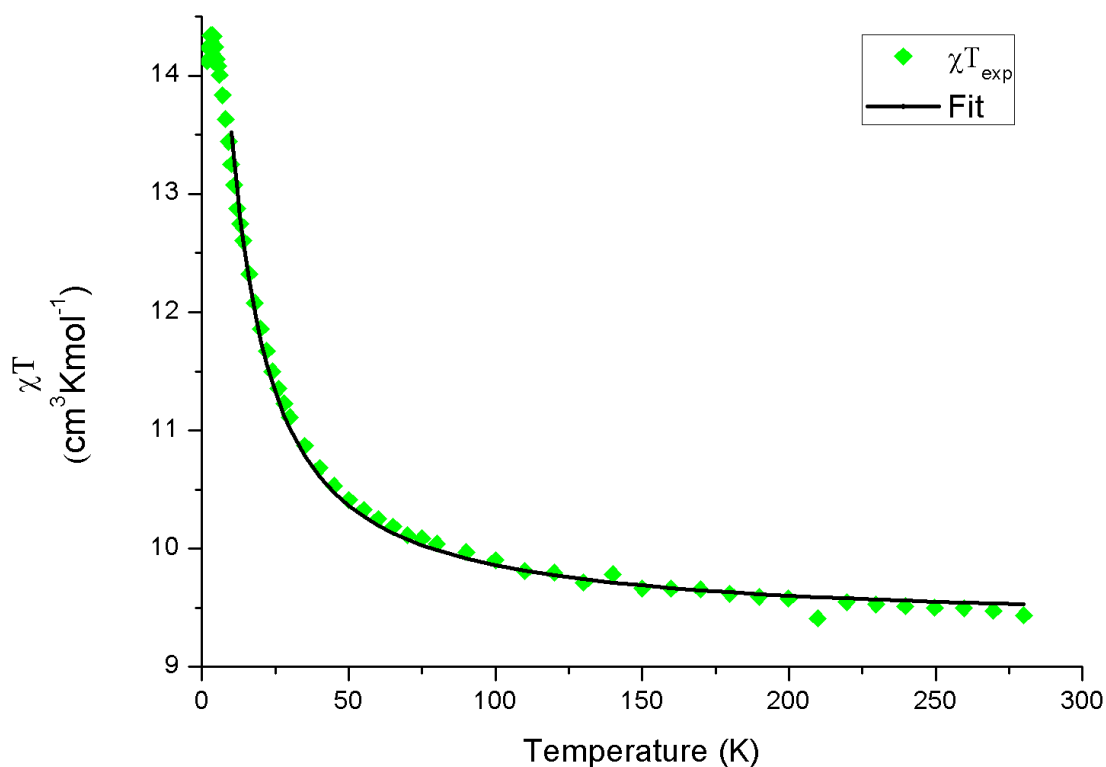


Figure 2.12: Variable temperature dc magnetic susceptibility for **5**. The green diamonds are the experimental χT data and the black line the calculated fit with $g = 2.04(3)$ and $J = 2.9(3) \text{ cm}^{-1}$ in the range 10 – 280 K.

With Gd^{III} being a spin only ion ($S_{\text{Gd}} = 7/2$), χT vs. T could be fit using a spin Hamiltonian with a single exchange parameter (here donated as J) describing the exchange interaction between S_{Gd} and three Cu_i^{II} spins ($s_i = 1/2$).

$$\mathcal{H} = -\mathcal{J} \sum_{i=1}^3 (\vec{S}_{\text{Gd}} \vec{s}_i) + g\mu_{\text{B}} \vec{H} (\vec{S}_{\text{Gd}} + \sum_{i=1}^3 \vec{s}_i)$$

Equation 2.1

The best fit model in the temperature range 10 K – 280 K gave $g = 2.04(3)$ and $J = 2.9(3) \text{ cm}^{-1}$. The value of g is reasonable as the spin only ion Gd^{III} has a $g = 2$ and Cu^{II} has a g value slightly larger than 2.

2.4.6 Magnetisation vs. Field Measurements for **5**

The parameters of $g = 2.04(3)$ and $J = 2.9(3) \text{ cm}^{-1}$ also provided a suitable fit for the magnetisation vs. field data for **5** (Figure 2.13). The magnetisation of the complex reaches a saturation value of $10 \text{ N}\mu_{\text{B}}$, consistent with an isotropic system with a ground state $S = 5$.

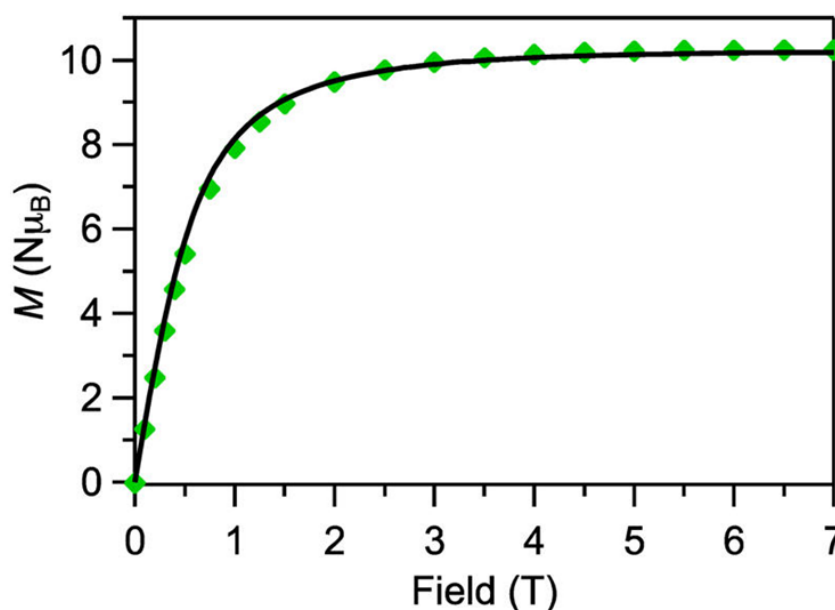


Figure 2.13: Magnetisation vs. field for **5**. The solid line corresponds to a data fit using the parameters $g = 2.04(3)$ and $J = 2.9(3) \text{ cm}^{-1}$.

2.4.7 Magnetic Susceptibility measurements for $\{\text{TbCu}_3\}$ (6) and $\{\text{DyCu}_3\}$ (7)

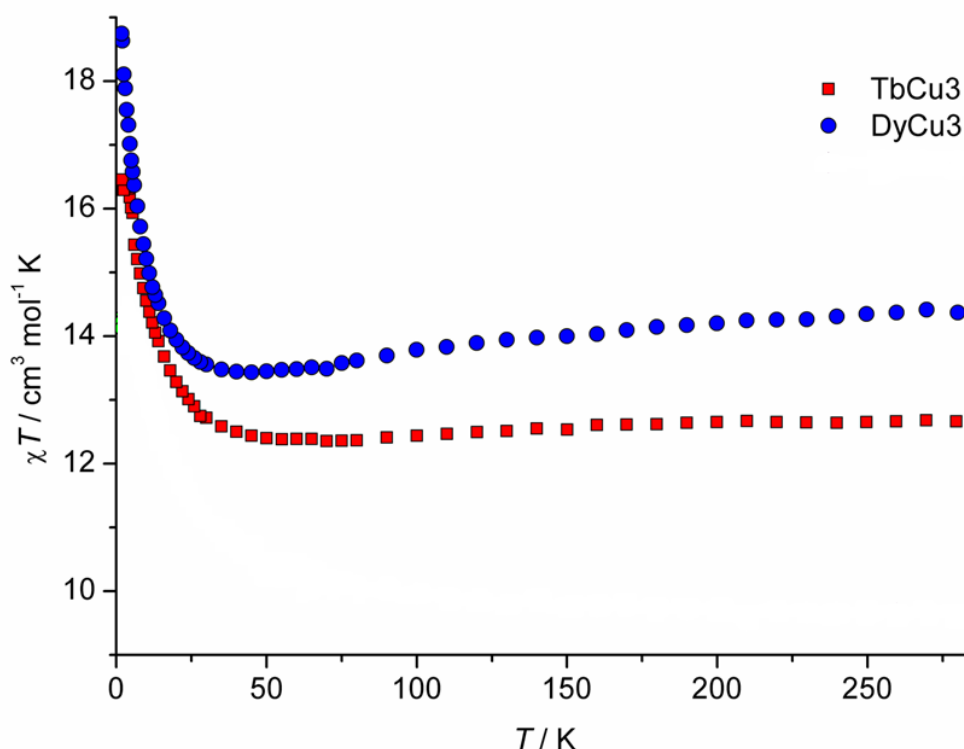


Figure 2.14: Variable temperature dc magnetic susceptibility for **6** (red squares), and **7** (blue circles).

The temperature dependent magnetic susceptibility of polycrystalline samples of **6** and **7** were measured in a 1 kOe field in the temperature range 1.8 – 280 K (Figure 2.14). For both complexes, χT gradually decreases as T decreases from 300 K down to ≈ 75 K for **6**, and ≈ 50 K for **7**, at which point χT plateaus. The high temperature χT value of $12.66 \text{ cm}^3 \text{ K mol}^{-1}$ for **6** is in relatively good agreement with the calculated χT value of $13.05 \text{ cm}^3 \text{ K mol}^{-1}$ for a system of non-interacting spins; one Tb^{III} ion (${}^7\text{F}_6$, $S = 3$, $L = 3$, $J = 6$, $g_J = 3/2$) and three Cu^{II} ions ($g_{\text{Cu}} = 2.1$, $s = 1/2$). For **7**, the high temperature χT value of $14.33 \text{ cm}^3 \text{ K mol}^{-1}$ is slightly lower than the calculated value of $15.40 \text{ cm}^3 \text{ K mol}^{-1}$ for a system of non-interacting spins; one Dy^{III} ion (${}^6\text{H}_{15/2}$, $S = 5/2$, $L = 5$, $J = 15/2$, $g_J = 4/3$) and three Cu^{II} ions ($g_{\text{Cu}} = 2.1$, $s = 1/2$). However, it appears that χT could still be increasing and would soon reach the calculated value at ≈ 300 K.

The gradual decrease in χT for both complexes as T decreases is consistent with depopulation of excited M_{tot} states which have a larger magnetic moment than the ground state. The eventual sharp increase in χT for both compounds is indicative of the predicted ferromagnetic exchange between $\text{Tb}^{\text{III}}/\text{Dy}^{\text{III}}$ and Cu^{II} (Table 2.6); ferromagnetic exchange

is well documented for $3d-4f$ systems containing Tb^{III} or Dy^{III} and Cu^{II} .^{1,19-38} The χT vs. T profiles for **6** and **7** were not able to be modelled due to the significant single ion anisotropies of these ions in conjunction with the low symmetry of the surrounding crystal field.⁴⁶

2.4.8 Magnetisation vs. Field Measurements for **6** and **7**

Magnetisation vs. field measurements were carried out at 2 and 4 K for **6**, and at 2, 4 and 6 K for **7**. Neither complex shows complete saturation of the magnetisation up to 70 kOe; indicative of strong magnetic anisotropy. The magnetisation data were fit using the effective Hamiltonian depicted in Equation 2.2. It was assumed that the thermal energy available was low enough (even at 6 K $\approx 4.2 \text{ cm}^{-1}$) for only the ground state of the systems to be considered. It was also assumed that the crystal field splitting of the Ln^{III} ions was axial enough that the levels in each m_J doublet could be considered degenerate. Finally, the effective model which allowed fitting of the data considered the ground m_J Ln^{III} doublet to be an effective $S' = 1/2$ system.

$$\mathcal{H} = -\sum_{i=1}^3 \mathcal{J}_{ixy} (\hat{S}'_x \hat{s}_{ix} + \hat{S}'_y \hat{s}_{iy}) - \sum_{i=1}^3 \mathcal{J}_{iz} \hat{S}'_z \hat{s}_{iz} + \mu_B \vec{H} (g_{xy} (\hat{S}'_x + \hat{S}'_y) + g_z \hat{S}'_z) + g_{\text{Cu}} \sum_{i=1}^3 \vec{s}_i$$

Equation 2.2

Where \mathcal{J}_{ixy} and \mathcal{J}_{iz} are the effective parameters describing the anisotropic exchange interactions between S' and the Cu^{II} $s_i = 1/2$ spins.

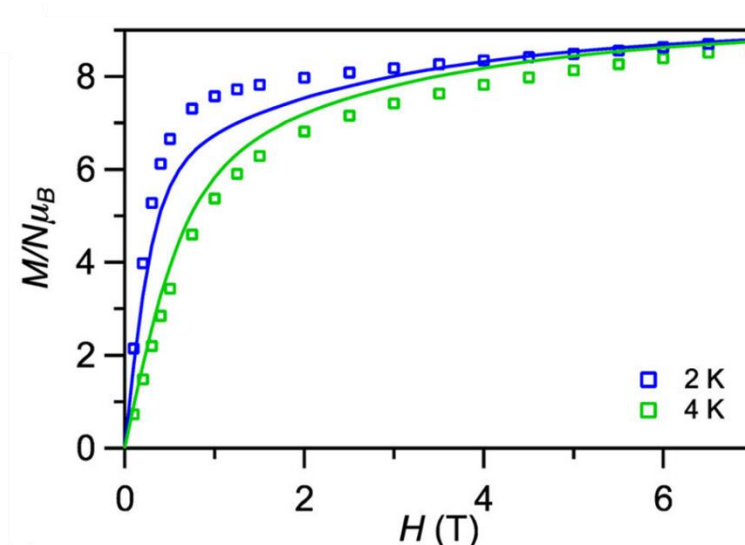


Figure 2.15: M vs. H curves for **6** at 2 K (blue squares) and 4 K (green squares). The solid lines are fits based on the effective model (Equation 2.2) with exchange parameters extracted from INS data (see Section 2.5.1).

For **6**, the best fit model of the magnetisation data (Figure 2.15), with the exchange parameters ($J_{xy} = 16.6 \text{ cm}^{-1}$, $J_z = 26.7 \text{ cm}^{-1}$) deduced from the INS data (Section 2.5.1), gave the g -values listed in Table 2.8.

g_{xy}	0(3)
g_z	18(2)
g_{Cu}	2.4(3)

Table 2.8: g -values from H vs. H data fit for **6**

The g_z value of 18(2) indicates that Tb^{III} 's $m_J = \pm 6$ state is the main contributor to the complex's ground doublet wavefunction; as deduced from Equation 2.3.¹⁷

$$g_z^{\text{max}} = 2|m_J^{\text{max}}|g_6$$

Equation 2.3

For Tb^{III} ($^7\text{F}_6$), $g_6 = 3/2$, and when the m_J^{max} value is set to ± 6 , the calculated value of $g_z = 18$. The transverse g_{xy} value is close to zero, within experimental error, indicating that its effect on the magnetisation is minimal.

For **7** (Figure 2.16), using the parameters from INS $J_{xy} = 13.1 \text{ cm}^{-1}$, $J_z = 27.7 \text{ cm}^{-1}$, the best fit model yielded the g -values depicted in Table 2.9.

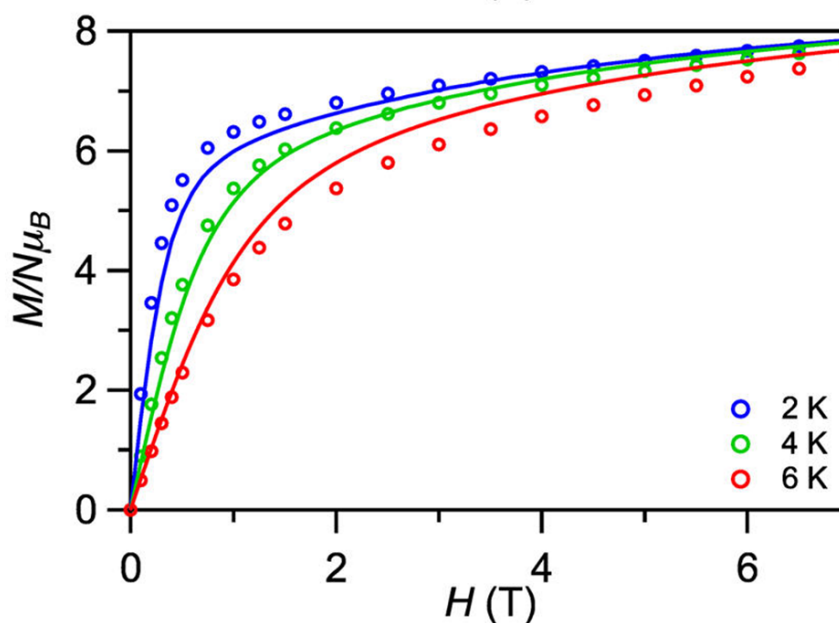


Figure 2.16: M vs. H curves for **7** at 2 K (blue circles), 4 K (green circles) and 6 K (red circles). The solid lines are fits based on the effective model (Equation 2.2) with exchange parameters extracted from INS data (see Section 2.5.2).

g_{xy}	0(1)
g_z	16.9(6)
g_{Cu}	2.2(1)

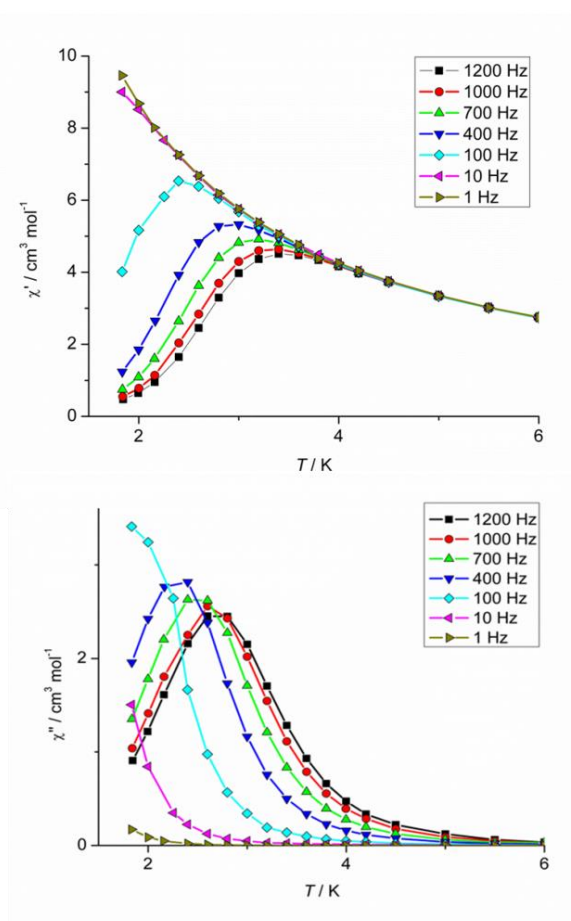
Table 2.9: g -values from M vs. H data fit for **7**.

Using Equation 2.3, we find that the $m_J = \pm 13/2$ state is the main contributor to the complex's ground doublet wavefunction. Again, the transverse g_{xy} value is close to zero and so has minimal effect on the compound's magnetisation.

2.4.9 Dynamic Magnetic Properties of $\{\text{TbCu}_3\}$ (**6**)

2.4.9.1 Ac Susceptibility

Ac susceptibility measurements were carried out to investigate whether **6** exhibited slow magnetic relaxation at low temperatures (Figure 2.17). In the absence of an applied dc field, there is a frequency dependent decrease in the in-phase magnetic susceptibility (χ'), with a concomitant increase in the out of phase magnetic susceptibility (χ'') signals.

**Figure 2.17:** Ac susceptibility measurements for **6** in zero applied dc field

The χ'' signals are well defined and have peaks within the temperature range of the measurement (down to 1.8 K). The χ'' data were modelled using an Arrhenius plot to give an estimated U_{eff} value of 17.3(4) K (12.0(3) cm^{-1}) with $\tau_0 = 2.2(3) \times 10^{-7}$ s. This is the third highest U_{eff} value in the literature for $\{\text{LnCu}\}$ complexes without an applied dc field. The highest, belongs to the cyclic tetranuclear $\{\text{Tb}_2\text{Cu}_2\}$ complex reported by Mzroniski *et al.*¹ ($U_{\text{eff}} = 21$ K), the second highest belonging to a macrocyclic $\{\text{TbCu}_3\}$ complex reported by Brooker *et al.*²⁶ ($U_{\text{eff}} = 19.5(5)$ K).

When an applied dc field of 1 kOe was used, again frequency dependent χ'' peaks were observed but at slightly higher temperatures (Figure 2.18). The Arrhenius analysis showed an increase in energy barrier of roughly 12% ($U_{\text{eff}} = 19.3(1)$ K, $\tau_0 = 1.4(1) \times 10^{-7}$ s). The small increase is indicative that QTM is not playing a dominant role in magnetic relaxation in **6**. This could be explained by the complex having a degenerate Kramer's ground state M_{tot} doublet instead of an Ising doublet.^{46,47}

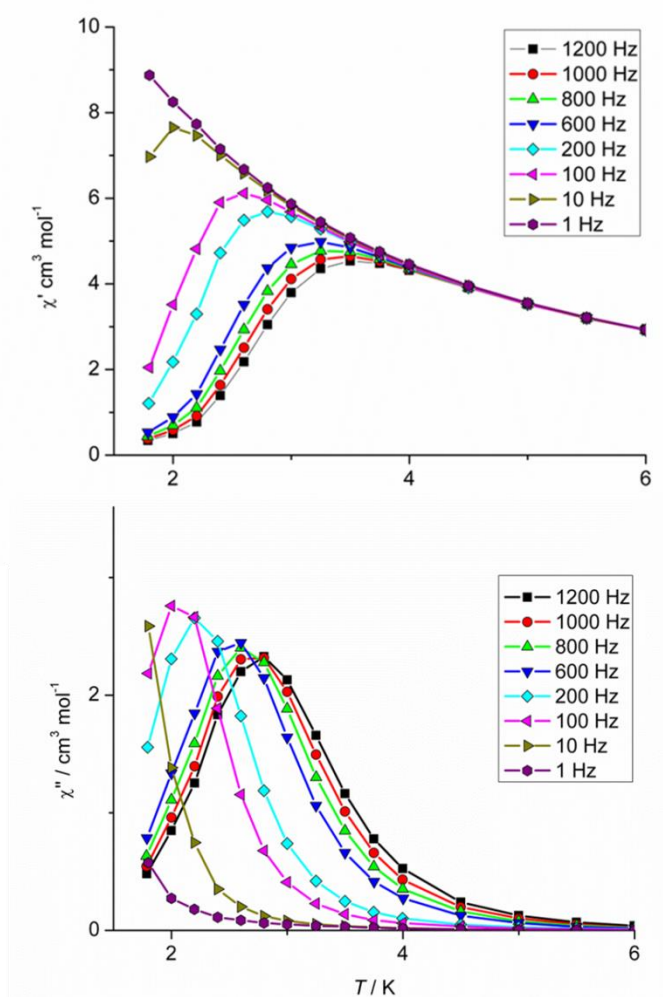


Figure 2.18: AC susceptibility measurements for **6** in a 1 kOe dc field

The $^7\text{F}_6$ Tb^{III} ion has an integer m_J value as a single ion, but coupling with three $s = 1/2$ Cu^{II} ions changes the nature of m_J states into M_{tot} states. The change from integer ($m_J = \pm 6$) to non-integer ($M_{\text{tot}} = 15/2$), means that QTM is formally forbidden due to an absence of time reversal symmetry as described by Kramer's theorem.⁴⁷

2.4.9.2 Magnetisation vs. Swept dc Field Scans

To investigate conclusively if **6** can be classed as a SMM, low temperature hysteresis measurements were made on an aligned single crystal (Figure 2.19). The results show that below 1 K the complex shows stepped, sweep rate dependent hysteresis curves and a non-zero remnant magnetisation at zero-field. The observation of these curves means that **6** is a confirmed SMM.

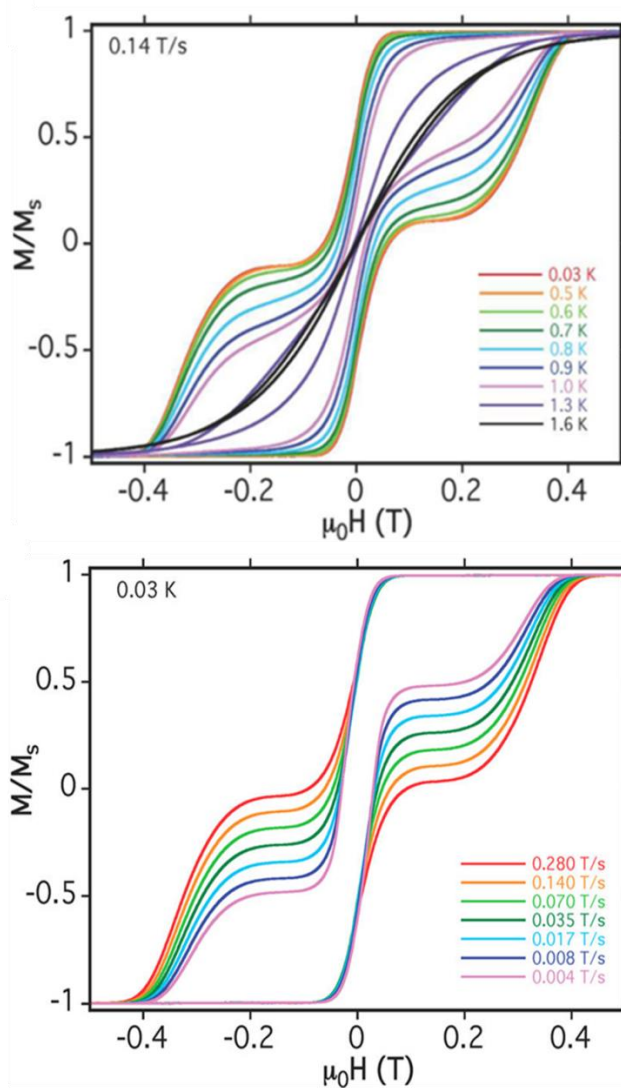


Figure 2.19: Magnetisation vs. Swept dc Field Scans for **6** with fixed scan rate and variable temperature (top) and fixed temperature and variable sweep rate (bottom)

2.4.10 Dynamic Magnetic Properties of $\{\text{DyCu}_3\}$ (7)

2.4.10.1 Ac Susceptibility

Ac susceptibility measurements were also made for **7** to search for slow magnetic relaxation (Figure 2.20). In zero applied dc field, the complex did not show any significant frequency dependent decrease in its χ' signals and only showed the onset of slow magnetic relaxation in its χ'' signals down to 1.8 K.

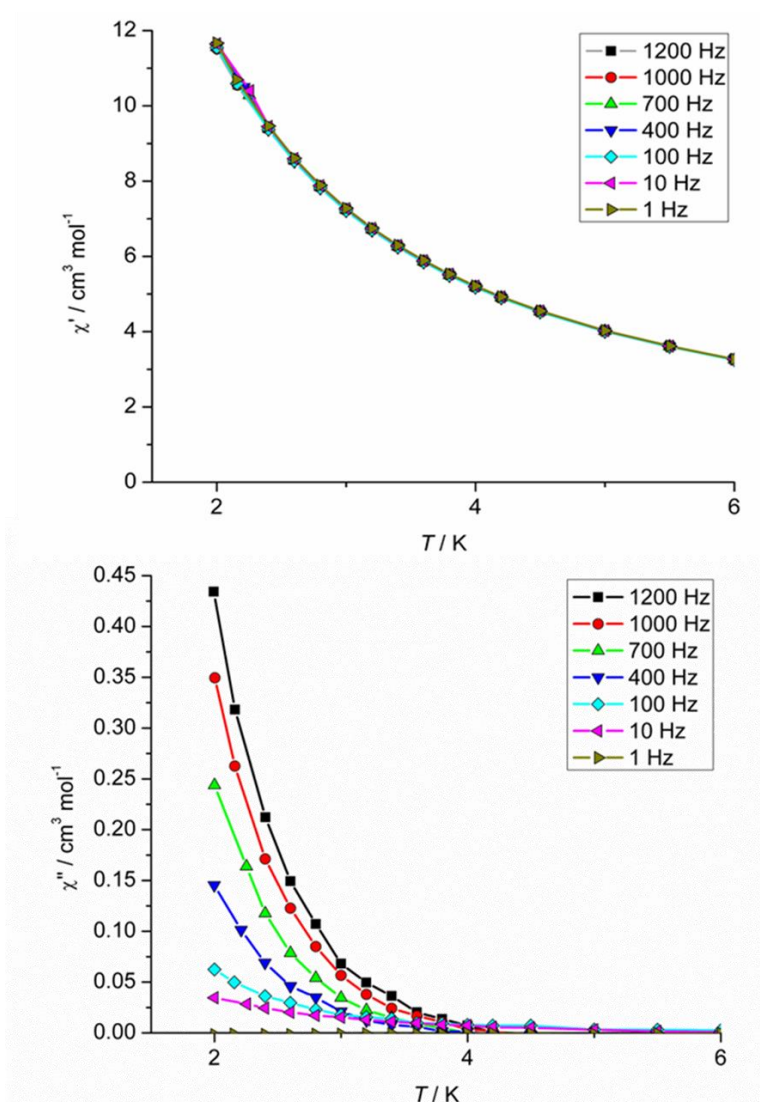


Figure 2.20: Ac susceptibility measurements for **7** in zero applied dc field

When a dc field of 1.5 kOe was applied, a frequency dependent decrease in the χ' signals and concomitant increase in the χ'' signals, with peaks above 1.8 K, was observed. An Arrhenius analysis using these peaks gave an estimated energy barrier as 16.2(4) K (11.2(3) cm^{-1}). The large increase in U_{eff} in the presence of the dc field is indicative of

QTM being a significant pathway to magnetic relaxation in **7**. The increased prevalence of QTM in **7** compared to **6** is due to the non-Kramer's nature of the M_{tot} ground state in **7** – coupling of the $m_J = \pm 13/2$ states with the three $\text{Cu}^{\text{II}} m_s = \pm 1/2$ states to give integer $M_{tot} = 8$. The integer M_{tot} state allows for time reversal symmetry therefore QTM is not suppressed.⁴⁷

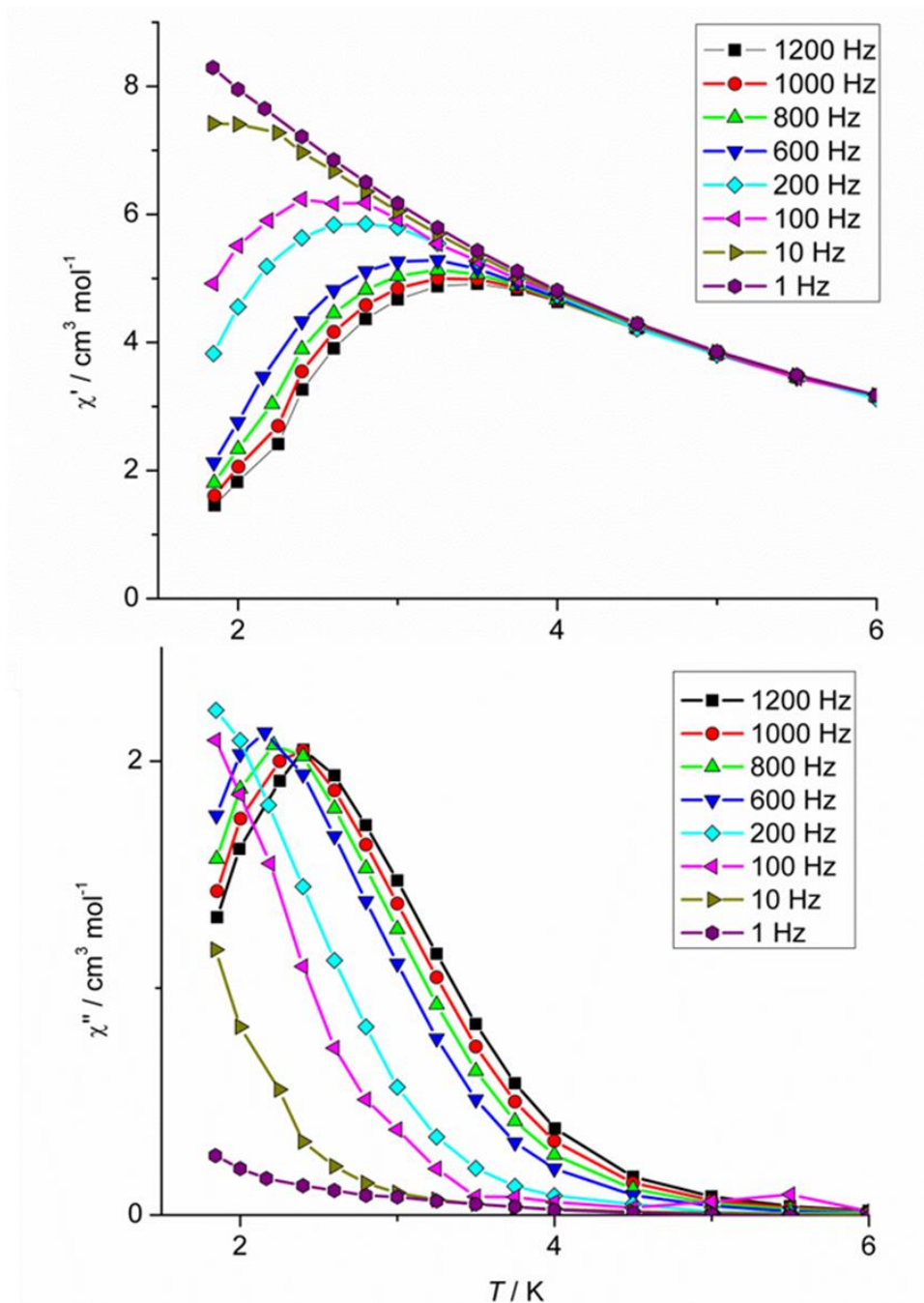


Figure 2 21: *Ac susceptibility measurements for 7 in a 1.5 kOe dc field*

2.4.10.2 Magnetisation vs. Swept dc Field Scans

Hysteresis measurements were also carried out for **7** under the same conditions as for **6**. The curves show very little temperature or sweep rate dependence, only a very small hysteresis at fields close to saturation with no remnant magnetisation at zero-field - butterfly hysteresis (Figure 2.22). This is further evidence that **7** does display slow relaxation of its magnetisation but exhibits very effective ground state QTM; consistent with the differences between the ac data collected with zero and then applied dc field for **7**.

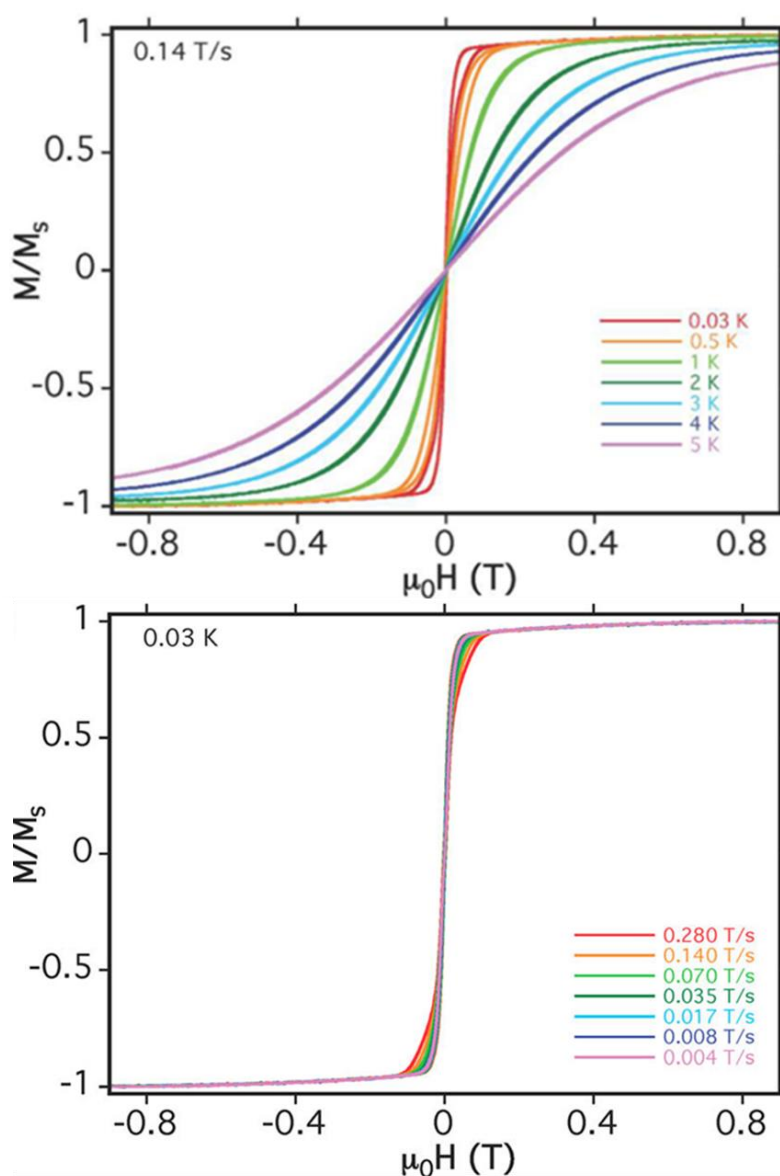


Figure 2.22: Magnetisation vs. Swept dc Field Scans for **7** with fixed scan rate and variable temperature (top) and fixed temperature and variable sweep rate (bottom)

2.5 Inelastic Neutron Scattering

Inelastic neutron scattering (INS) experiments were performed on polycrystalline samples of **6** and **7** to gain further insight into the $\text{Ln}^{\text{III}} - \text{Cu}^{\text{II}}$ exchange interactions and the crystal field splitting of the M_{tot} energy levels.⁵⁰ The experiments were performed on ≈ 2 g of non-deuterated **6** and ≈ 1 g non-deuterated **7** in the temperature range 1.4 K – 30 K on the time of flight spectrometer FOCUS at the Paul Scherrer Institute (PSI) in Switzerland. The data were collected and modelled by Dr Stefan Ochsenbein.

2.5.1 INS of $\{\text{TbCu}_3\}$ (**6**)

Compound **6** was analysed using two initial neutron wavelengths of 4.3 Å and 5.5 Å at 1.4, 10 and 30 K (Figure 2.23). At around 13 cm^{-1} there is a peak observed at all three temperatures (Peak II). There is also a shoulder peak next to the central elastic line at ≈ 7 cm^{-1} (Peak I). Both peaks decrease in intensity as the temperature is increased; indicative that the peaks are arising from electronic transitions from the ground state which becomes less populated as temperature increases. When 5.5 Å neutrons were used, a higher resolution spectrum was obtained and showed that Peak II is actually a split peak of multiple components.

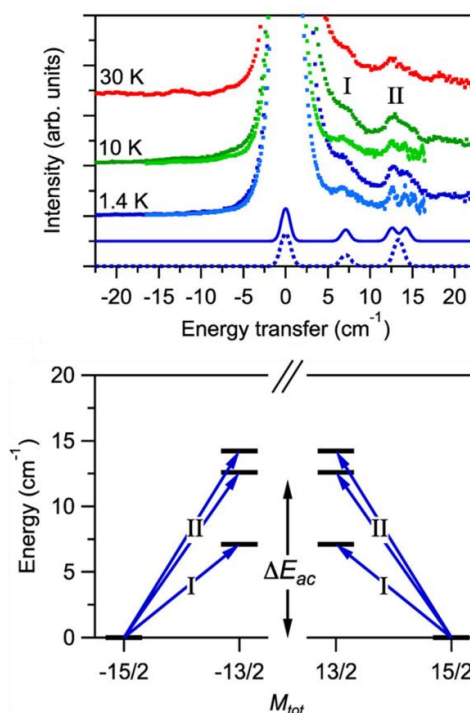


Figure 2.23: (Top) INS spectra of **6** at 1.4, 10, and 30 K with 4.3 Å neutrons and at 1.4 and 10 K with 5.5 Å neutrons (light blue and light green). (Bottom) Schematic of M_{tot} transitions with $\Delta E_{\text{ac}} = 12 \text{ cm}^{-1}$ for comparison

The peaks in the spectrum arise from excitations from the cluster ground state $M_{tot} = \pm 15/2$ to $M_{tot} = \pm 13/2$, in agreement with INS selection rules: $(\Delta M_{tot} = \pm 1, 0)$. The ground M_{tot} state of $\pm 15/2$ was assumed due to the ferromagnetic coupling in **6** which can be thought of as the parallel alignment of the main contributing $m_J = \pm 6$ state of Tb^{III} (Section 2.4.8) with the three Cu^{II} $s_i = 1/2$ spins. The excited $M_{tot} = \pm 13/2$ state therefore corresponds to the flipping of one of the Cu^{II} spins. There are three potential Cu^{II} spins which could flip, hence why there are three excited states within $M_{tot} = \pm 13/2$. However, the transitions to these three states cannot be assigned to the flipping of a specific Cu^{II} spin; rather, each state is a superposition of the three possible spin flipped states. Excitation II has an energy of $\approx 12 \text{ cm}^{-1}$, which correlates with the U_{eff} value of $12.0(3) \text{ cm}^{-1}$ obtained from the ac susceptibility measurements for **6**. This correlation suggests that thermal magnetic relaxation in **6** proceeds through an excited M_{tot} state whereby one of the Cu^{II} ion's spins has flipped. To try and model the spectra, an effective Hamiltonian was used (Equation 2.4):

$$\mathcal{H} = - \sum_{i=1}^3 \mathcal{J}_{ixy} (\hat{S}'_x \hat{s}_{ix} + \hat{S}'_y \hat{s}_{iy}) - \sum_{i=1}^3 \mathcal{J}_{iz} \hat{S}'_z \hat{s}_{iz}$$

Equation 2.4

Where J = exchange interaction parameters, \hat{S}' = effective spin = $1/2$ for Tb^{III} and $\hat{s}_i = 1/2$ for Cu^{II} . The equation is the same as the one used to model the magnetisation data for **6** and **7** but without the Zeeman terms. The three Tb^{III} - Cu^{II} exchange interactions in **6** are unrelated by symmetry so a maximum of six parameters could be used in this axial spin Hamiltonian. Due to the anisotropy of the Tb^{III} ion arising from the crystal field splitting of its m_J states, an isotropic model where $J_{xy} = J_z$ was deemed unreasonable. Instead, J_{xy} and J_z were used to describe all three interactions. The dotted line in Figure 2.23 shows the calculated fit for the spectrum at 1.4 K for **6** using the parameter values: $J_{xy} = 16.6(2) \text{ cm}^{-1}$ and $J_z = 26.7(2) \text{ cm}^{-1}$. The calculated fit using these J values is in reasonable agreement with the spectrum at 1.4 K, however, it does not effectively capture the splitting of Peak II. By varying the J parameters for the three different Tb^{III} - Cu^{II} exchange interactions, it was possible to model the splitting. The fit used a reduced number of parameters by assuming a constant ratio of J_z/J_{xy} and a symmetric variation of the three Tb^{III} - Cu^{II} exchange parameters so that: $J_{xy} - J_{zy} = J_{xy} - J_{zy}$. The fit with the best agreement yielded the values listed in Table 2.10.

J_{1xy}	16.6(2) cm ⁻¹
J_{2xy}	14.8(1) cm ⁻¹
J_{3xy}	18.4(1) cm ⁻¹
J_{1z}	26.7(6) cm ⁻¹
J_{2z}	23.8(5) cm ⁻¹
J_{3z}	29.6(6) cm ⁻¹
J_{iz}/J_{ixy}	1.61(3) cm ⁻¹

Table 2.10: List of parameters deduced from INS data for **6**

To elucidate an overall approximation of the strength of exchange coupling between Tb^{III} and Cu^{II}, and for a subsequent comparison with those in **5**, the J_z value was converted to J_{TbCu} following a method described by Dreiser *et. al.*⁴⁸ whereby: $J_z = 2|m_J| J_{\text{TbCu}}$. The method is analogous to the conversion of g_J to g_z . For Tb^{III}, $m_J = \pm 6$ and $J_z = 26.7(2)$ cm⁻¹, this gave a value of $J_{\text{TbCu}} = 2.2(7)$ cm⁻¹, which is comparable to the values for **5** (2.9(3) cm⁻¹) and **7** (2.1(7) cm⁻¹, see later). All three values are in accordance with those found in the literature for similar {LnCu} complexes, in the range 0.5 – 3 cm⁻¹.^{1,19-38}

2.5.2 INS of {DyCu₃} (**7**)

The experimental procedure for analysing **7** required a smaller sample size due to the large neutron absorption cross section of Dy^{III}. The nature of the Dy^{III} ion also prohibited the use of 5.5 Å neutrons whose flux is lower and sample absorption greater. INS spectra were therefore recorded for **7** using 4.3 Å neutrons at 1.4, 10 and 30 K (Figure 24). The spectra show peaks at ≈ 14 cm⁻¹ and ≈ 10 cm⁻¹ whose intensities decrease with increasing temperature (Figure 2.24). The decrease in intensity is again due to the transitions taking place from the cluster ground M_{tot} state which was assigned as $M_{\text{tot}} = \pm 8$ for **7**. Again, like for **6**, ferromagnetic coupling between the $m_J = \pm 13/2$ ground state of Dy^{III} (Section 2.4.8) and three $s_i = 1/2$ spins of Cu^{II} leads to the value of ± 8 . The excitation to $M_{\text{tot}} = \pm 7$ is a result of a Cu^{II} spin flip and has an energy value of ≈ 11.2 cm⁻¹ which is in good agreement with the U_{eff} value of 11.2(3) cm⁻¹ from the ac susceptibility measurements. Thermal relaxation in **7** appears to dominantly proceed through excitation I, again however, each transition cannot be thought of as corresponding to a specific Cu^{II} ion, rather each transition results in an excited state which corresponds to a superposition of the three possible spin flipped states.

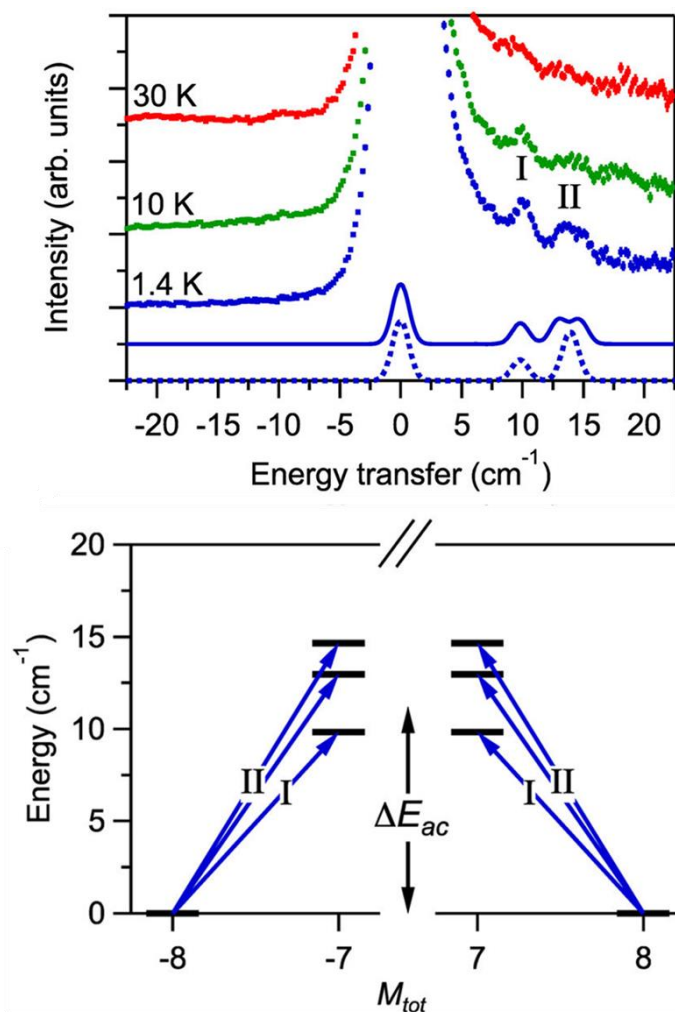


Figure 2.24: (Top) INS spectra of **7** at 1.4, 10, and 30 K with 4.3 Å neutrons. The dotted line represents the fit for the spectrum at 1.4 K using the parameters $J_{xy} = 13.1(1) \text{ cm}^{-1}$ and $J_z = 27.7 \text{ cm}^{-1}$. (Bottom) Schematic of M_{tot} transition with $\Delta E_{ac} = 11.2 \text{ cm}^{-1}$

Fitting of the INS data was carried out in a similar manner as for **6**. The dotted line in Figure 2.24 shows the fit for the spectrum at 1.4 K using the parameters $J_{xy} = 13.1(1) \text{ cm}^{-1}$ and $J_z = 27.7 \text{ cm}^{-1}$. Again, this model did not capture the split nature of Peak II and an adjustment of the parameters gave a new fit with the best fit parameter values listed in Table 2.11.

J_{1xy}	$12.5(2) \text{ cm}^{-1}$
J_{2xy}	$11.1(1) \text{ cm}^{-1}$
J_{3xy}	$13.9(1) \text{ cm}^{-1}$
J_{1z}	$27.5(8) \text{ cm}^{-1}$
J_{2z}	$24.4(6) \text{ cm}^{-1}$
J_{3z}	$30.6(7) \text{ cm}^{-1}$
J_{iz}/J_{ixy}	$2.20(5) \text{ cm}^{-1}$

Table 2.11: List of Parameters deduced from INS data for **7**.

Using the relation $J_z = 2 |m_J| J_{\text{DyCu}}$, with $\text{Dy}^{\text{III}} m_J = \pm 13/2$ and $J_z = 27.7(1) \text{ cm}^{-1}$, the overall exchange strength of $J_{\text{DyCu}} = 2.1(7) \text{ cm}^{-1}$ was calculated for **7**. This value is comparable to other DyCu SMMs found in the literature.³⁴⁻³⁸

2.6 Conclusions and Future Work

The ligand H_4edte was used to synthesise a new Cu^{II} dimer (**1**) which was subsequently used as reagent to synthesis eight new $[\text{LnCu}_3(\text{H}_2\text{edte})_3(\text{NO}_3)](\text{NO}_3)_2$ complexes where $\text{Ln} = \text{Pr}^{\text{III}}$ (**2**), Nd^{III} (**3**), Eu^{III} (**4**), Gd^{III} (**5**), Tb^{III} (**6**), Dy^{III} (**7**), Er^{III} (**8**), Yb^{III} (**9**). Magnetic susceptibility measurements were carried out for complexes **2**, **3**, **5**, **6** and **7**, showing dominant antiferromagnetic $\text{Ln}^{\text{III}}\text{-Cu}^{\text{II}}$ exchange in **2** and **3**, and dominant ferromagnetic exchange in **5-7**. Complex **6** was found to be a new SMM, confirmed by both ac-susceptibility and magnetisation hysteresis measurements. **6** was found to have a $U_{\text{eff}} = 17.3(4) \text{ K}$ ($12.0(3) \text{ cm}^{-1}$) from ac susceptibility measurements with zero applied dc field. When a 1 kOe dc field was applied, U_{eff} increased by 12 % to $19.3(1) \text{ K}$ ($13.4(1) \text{ cm}^{-1}$). Complex **7** only showed the onset of slow magnetic relaxation in ac susceptibility measurements with zero applied dc field. However, when a 1.5 kOe dc field was applied, **7** displayed a $U_{\text{eff}} = 16.2(4) \text{ K}$ ($11.2(3) \text{ cm}^{-1}$) – the large increase indicative that QTM plays a significant role in magnetic relaxation. This was reflected in the magnetisation *vs.* swept field hysteresis measurements, where **7** showed no remnant magnetisation at zero-field (butterfly hysteresis). The differences in behaviour were attributed to the Kramer's nature of the M_{tot} ground state of **6** suppressing QTM whereas the non-Kramer's nature of **7**'s did not. Excitations from the ground to the first excited M_{tot} states were observed for **6** and **7** using INS spectroscopy. The energy associated with these transitions was found to correlate well with the U_{eff} values found from ac susceptibility measurements for **6** and **7** – suggesting that magnetic relaxation in these complexes proceeds through Cu^{II} spin flips.

Interesting further work on the $\{\text{LnCu}_3(\text{H}_2\text{edte})_3\}$ series would involve synthesising analogous $\{\text{LnZn}^{\text{II}}_3(\text{H}_2\text{edte})_3\}$ complexes - substituting the Cu^{II} ions for diamagnetic Zn^{II} ions - in order to study the Ln^{III} single-ion contributions to the magnetic properties. Similarly, substitution of the paramagnetic central Ln^{III} ion for a diamagnetic ion such as Y^{III} or La^{III} would allow for the magnetic study of magnetically dilute samples of **6** and **7**. These dilute samples would show a further suppression of QTM and hence higher U_{eff} values. An important factor toward the magnetic properties of Ln^{III} containing complexes

is the geometry of the crystal field around the central Ln^{III} ion, therefore rational structural modifications toward more symmetric crystal fields would be an interesting avenue to explore. For example, replacement of the bidentate nitrate ion for either acetylacetonate, or another $\{\text{Cu}(\text{H}_2\text{edte})\}$ metalloligand subunit could push the symmetry closer to square antiprismatic (D_{4d}) – known to facilitate slow magnetic relaxation for ions such as Tb^{III} and Dy^{III} .

2.7 References

- (1) S. Osa, T. Kido, N. Matsumoto, N. Re, A. Pochaba, J. Mrozinski, *J. Am. Chem. Soc.* 126 (2004) 420 – 421.
- (2) A. Mishra, W. Wernsdorfer, K. A. Abboud, G. Christou, *J. Am. Chem. Soc.* 126 (2004) 15648-15649.
- (3) C. M. Zaleski, E. C. Depperman, J. W. Kampf, M. L. Kirk, V. L. Pecoraro, *Angew. Chem. Int. Ed.* 43 (2004) 3911-3914.
- (4) J. W. Sharples, D. Collison, *Coord. Chem. Rev.* 260 (2014) 1-20.
- (5) A. Saha, M. Thompson, K.A. Abboud, W. Wernsdorfer, G. Christou, *Inorg. Chem.* 50 (2011) 10476 – 10485.
- (6) M. N. Ahktar, V. Mereacre, G. Novitchi, J-P. Tuchagues, C. E. Anson, A. K. Powell, *Chem. Eur. J.* 15 (2009) 7278-7282.
- (7) C. Papatriantafyllopoulou, W. Wernsdorfer, K. A. Abboud, G. Christou, *Inorg. Chem.* 50 (2011) 421-423.
- (8) S. K. Langley, B. Moubaraki, K. S. Murray, *Dalton. Trans.* 39 (2010) 5066-5069.
- (9) M. Hołyńska, D. Premužić, I-R. Jeon, W. Wernsdorfer, R. Clérac, S. Dehnen, *Chem. Eur. J.* 17 (2011) 9605-9610.
- (10) G. Abbas, Y. Lan, V. Mereacre, W. Wernsdorfer, R. Clerac, G. Buth, M. T. Sougrati, F. Grandjean, J. Long, C. E. Anson, A. K. Powell, *Inorg. Chem.* 48 (2009) 9345-9355.
- (11) J.-L. Liu, J.-Y. Wu, Y.-C. Chen, V. Mereacre, A. K. Powell, L. Ungur, L. F. Chibotaru, X.-M. Chen, M.-L. Tong, *Angew. Chem. Int. Ed.* 53 (2014) 12966-12970.
- (12) S.-D. Jiang, S.-S. Liu, L.-N. Zhou, B.-W. Wang, Z.-M. Wang, S. Gao, *Inorg. Chem.* 51 (2012) 3079–3087.
- (13) S.K. Langley, N.F. Chilton, B. Moubaraki, K.S. Murray, *Inorg. Chem.* 52 (2013) 7183–7192.
- (14) S.K. Langley, N.F. Chilton, B. Moubaraki, K.S. Murray, *Chem. Commun.* 49 (2013) 6965–6967.
- (15) M. Towatari, K. Nishi, T. Fujinami, N. Matsumoto, Y. Sunatsuki, M. Kojima, N. Mochida, T. Ishida, N. Re, J. Mrozinski, *Inorg. Chem.* 52 (2013) 6160-6178.
- (16) K. Xiong, X. Wang, F. Jiang, Y. Gai, W. Xu, K. Su, X. Li, D. Yang, M. Hong, *Chem. Commun.* 48 (2012) 7456-7458.

- (17) F. J. Kettles, V. A. Milway, F. Tuna, R. Valiente, L. H. Thomas, W. Wernsdorfer, S. T. Ochsenbein, M. Murrie, *Inorg. Chem.* 53 (2014) 8970-8978.
- (18) G. J. Sopasis, A. B. Canaj, A. Philippidis, M. Siczek, T. Lis, J. R. O'Brien, M. M. Antonakis, S. A. Pergantis, C. J. Milios, *Inorg. Chem.* 51 (2012) 5911-5918.
- (19) M. Orfanoudaki, I. tamiolakis, M. Siczek, T. Lis, G. S. Armatas, S. A. Perlepes, C. J. Millios, *Dalton. Trans.* 40 (2011) 4793-4796.
- (20) T. Shiga, H. Miyasaka, M. Yamashita, M. Morimoto, M. Irie, *Dalton. Trans.* 40 (2011) 2275-2282.
- (21) T. Kajiwara, M. Nakano, K. Takahashi, S. Takaishi, M. Yamashita, *Chem. Eur. J.* 17 (2011) 196-205.
- (22) T. Kajiwara, K. Takahashi, T. Hiraizumi, M. Yamashita, *Polyhedron* 28 (2009) 1860-1863.
- (23) J-P. Costes, F. Dahan, W. Wernsdorfer, *Inorg. Chem.* 48 (2006) 5-7.
- (24) T. Hamamatsu, K. Yabe, M. Towatari, N. Matsumoto, N. Re, A. Pochaba, J. Mrozinski, *Bull. Chem. Soc. Jpn.* Vol. 80, (2007) 523-529.
- (25) T. Shimida, A. Okazawa, N. Kojima, S. Yoshii, H. Nojiri, T. Ishida, *Inorg. Chem.* 50 (2011) 10555-10557.
- (26) H. L. C. Feltham, R. Clerac, L. Ungur, L. F. Chibotaru, A. K. Powell, S. Brooker, *Inorg. Chem.* 52 (2013) 3236-3240.
- (27) X. Feng, W. Zhou, Y. Li, H. Ke, J. Tang, R. Clerac, Y. Wang, Z. Su, E. Wang, *Inorg. Chem.* 51 (2012) 2722-2724.
- (28) T. Kajiwara, K. Takahashi, T. Hiraizumi, S. Takaishi, M. Yamashita, *CrystEngComm.* 11 (2009) 2110-2116.
- (29) A. Borta, E. Jeanneau, Y. Chumakov, D. Luneau, L. Ungur, L. F. Chibotaru, W. Wernsdorfer, *New. J. Chem.* 35 (2011) 1270-1279.
- (30) J-P. Costes, M. Auchel, F. Dahan, V. Peyrou, S. Shova, W. Wernsdorfer, *Inorg. Chem.* 45, (2006) 1924-1934.
- (31) T. Kajiwara, M. Nakano, S. Takaishi, M. Yamashita, *Inorg. Chem.* 47 (2008) 8604-8606.
- (32) P. Zhang, L. Zhang, S-Y. Lin, J. Tang, *Inorg. Chem.* 52 (2013) 6595-6602.
- (33) N. Bridonneau, L-M. Chamoreau, P. P. Laine, W. Wernsdorfer, V. Marvaud, *Chem. Commun.* 49 (2013) 9476-9478.
- (34) J-P. Costes, S. Shova, W. Wernsdorfer, *Dalton. Trans.* (2008) 1843-1849.
- (35) C. Anson, G. Pilet, G. Chastanet, W. Wernsdorfer, J-F. Jacquot, D. Luneau, *Angew. Chem. Int. Ed.* 45 (2006) 4659-4662.

- (36) V. Baskar, K. Gopal, M. Helliwell, F. Tuna, W. Wernsdorfer, R. E. P. Winpenny, *Dalton. Trans.* 39 (2010) 4747-4750.
- (37) F. Mori, T. Nyui, T. Ishida, T. Nogami, K-Y. Choi, H. Nojiri, *J. Am. Chem. Soc.* 128 (2006) 1440-1441.
- (38) J.-L. Liu, Y-C. Chen, Q-W. Li, S. Gomez-Coca, D. Aravena, E. Ruiz, W-Q. Lin, J-D. Leng, M-L. Tong, *Chem. Commun.* 49 (2013) 6549-6551.
- (39) A. Bencini, C. Benelli, A. Caneschi, A. Dei, D. Gatteschi, *Inorg. Chem.* 25 (1986) 572-575.
- (40) A. Benelli, A. Caneschi, D. Gatteschi, O. Guillou, L. Pardi, *Inorg. Chem.* 29 (1990) 1750-1755.
- (41) A. Bencini, C. Benelli, A. Caneschi, R. L. Carlin, A. Dei, D. Gatteschi, *J. Am. Chem. Soc.* 107 (1985) 8128-8136.
- (42) A. S. de Sousa, M. A Fernandes, *Polyhedron* 21 (2002) 1883-1888.
- (43) M. Llunell, D. Casanova, J. Cirera, P. Alemany, S. Alvarez, 'SHAPE: Program for the Stereochemical Analysis of Molecular Fragments by Means of Continuous Shape Measures and Associated Tools', Version 2.1, 2013, Barcelona.
- (44) J. Cirera, E. Ruiz, *C. R. Chimie.* 11 (2008) 1227-1234.
- (45) J. P. Costes, F. Dahan, A. Dupuis, *Inorg. Chem.* 39 (2000) 5994-6000.
- (46) L. Ungur, L. F. Chibotaru, *Phys. Chem. Chem. Phys.* 13 (2011) 20086-20090.
- (47) S.D. Jiang, B.W. Wang, S. Gao, *Molecular Nanomagnets and Related Phenomena*, Chapter 2, pp 111-141.
- (48) J. Dreiser, K. S. Pederson, C. Piamonteze, S. Rusponi, Z. Salman, M. E. Ali, M. Schau-Magnussen, C. A. Thueson, S. Piligkos, H. WWeihe, H. Mutka, O. Waldmann, P. Oppeneer, J. Bendix, F. Nolting, H. Brune, *Chem. Sci.* 3 (2012) 1024-1032.
- (49) C. Benelli, D. Gatteschi, *Chem. Rev.* 102 (2002) 2369 – 2387.
- (50) R. Basler, C. Boskovic, G. Chaboussant, H. Güdel, M. Murrie, S. T. Ochsenbein, A. Sieber, *Chemphyschem.* 4 (2003) 910 – 926.
- (51) D. W. Bruce, D. O'Hare, R. I. Walton, *Molecular Materials*, Wiley (2010).
- (52) J. Tang, P. Zhang, *Lanthanide Single-Molecule Magnets*, Springer (2015).

3. Synthesis, Structure and Magnetic Properties of a $\{\text{LnCu}_3(\text{H}_2\text{pdte})_3\}$ Series

3.1 Introduction

In Chapter 2, the ligand H_4edte was used to synthesise a new $\{\text{LnCu}_3(\text{H}_2\text{edte})_3\}$ series where $\text{Ln}^{\text{III}} = \text{Pr}^{\text{III}}, \text{Nd}^{\text{III}}, \text{Eu}^{\text{III}}, \text{Gd}^{\text{III}}, \text{Tb}^{\text{III}}, \text{Dy}^{\text{III}}, \text{Er}^{\text{III}}, \text{Yb}^{\text{III}}$. Alternating current (ac) magnetic susceptibility measurements revealed that the Tb^{III} and Dy^{III} analogues exhibited slow relaxation of their magnetisation, with low temperature magnetisation vs. field hysteresis measurements confirming the Tb^{III} analogue as a single-molecule magnet (SMM).¹ In an attempt to increase the energy barrier to magnetic reorientation (U_{eff}) for these complexes, the H_4edte ligand was replaced with a closely related ligand; H_4pdte (Figure 3.1), which has a propylenediamine backbone compared to H_4edte 's ethylenediamine backbone.

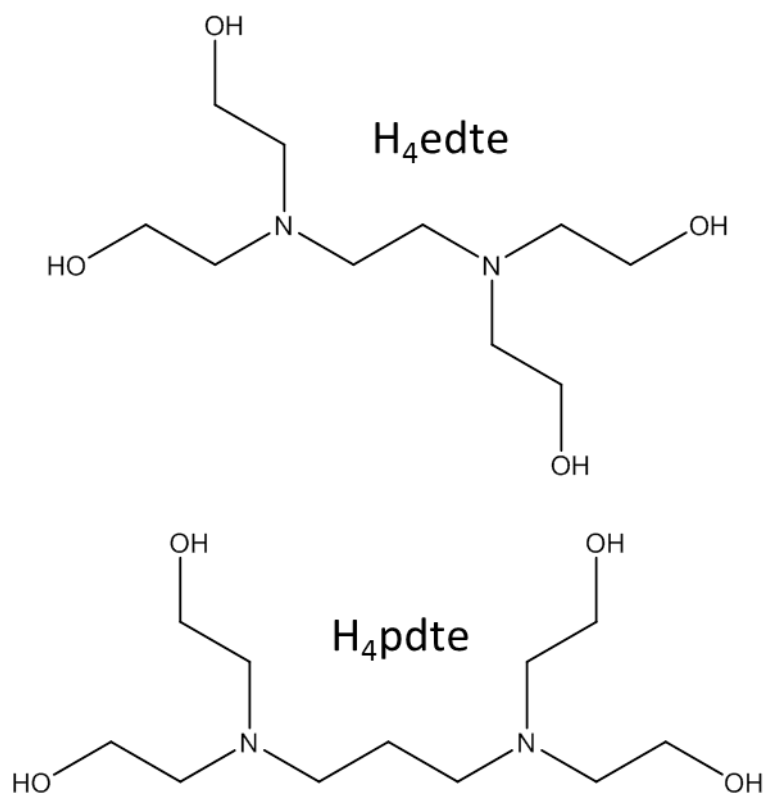


Figure 3.1: The ligand N,N,N',N' -tetrakis-(2-hydroxyethyl)-ethylenediamine (H_4edte) (top), and N,N,N',N' -tetrakis-(2-hydroxyethyl)-1,3-diaminopropane (H_4pdte) (bottom).

The added flexibility was predicted to change the coordination environment around the central Ln^{III} ion and potentially provide a more axially symmetric crystal field and/or facilitate stronger $3d$ - $4f$ magnetic exchange; both promoting an increase in magnitude of U_{eff} relative to the $\{\text{LnCu}_3(\text{H}_2\text{edte})_3\}$ ($\text{Ln}^{\text{III}} = \text{Tb}^{\text{III}}$ and Dy^{III}) complexes'.²⁻⁵ Brooker *et al.* conducted similar research; changing the ligand backbones of a family of macrocyclic $3d$ - $4f$ complexes to attempt to increase the magnitude of U_{eff} .⁶⁻¹⁰ In 2011 they reported the first example of a $3d$ - $4f$ macrocyclic SMM; $[\text{DyZn}_3(\text{L}^{\text{Pr}})(\text{NO}_3)_3(\text{MeOH})_3] \cdot 4\text{H}_2\text{O}$ (Figure 3.2).⁶ The complex was synthesised by metal ion templated cyclisation using a diamine and 1,4-diformyl-2,3-dihydroxybenzene. The macrocycle's ion pockets were designed so the harder $4f$ ion would take up the central position (hard $\{\text{O}_6\}$ donor set) with the three $3d$ ions in the three outer pockets (less hard $\{\text{N}_2\text{O}_2\}$ donor sets) bridging to the Ln^{III} through oxo-bridges.

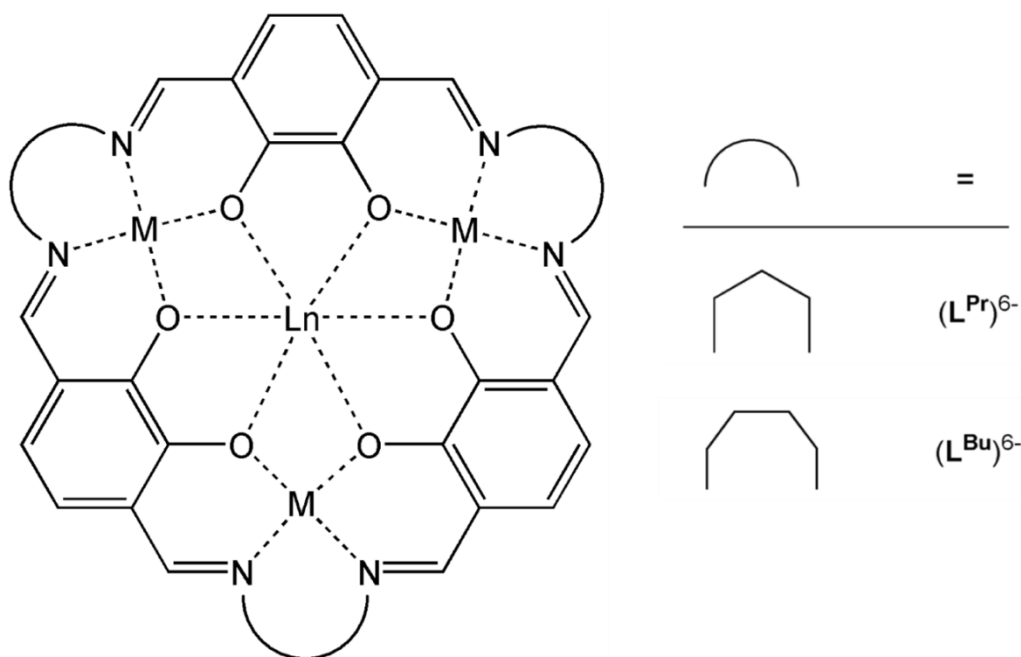


Figure 3.2: Schematic representation of the $\{\text{LnCu}_3\text{L}\}$ series. Figure adapted from reference 8.

The ring size was altered by changing the number of carbon atoms in the diamine starting material. Their first SMM, $\{\text{DyZn}_3(\text{L}^{\text{Pr}})\}$, showed slow relaxation in a 1.5 kOe dc field and had a $U_{\text{eff}} = 25.8$ K.⁶ They also found that the Er^{III} and Yb^{III} analogues behaved as field induced SMMs.^{6,7} They then replaced the Zn^{II} ions for Cu^{II} and found that the Tb^{III} analogue showed onset of slow relaxation in zero dc field down to 1.8 K (Figure 3.3).⁸ Of all the Ln^{III} ions successfully incorporated ($\text{Ln}^{\text{III}} = \text{La}^{\text{III}}, \text{Ce}^{\text{III}}, \text{Pr}^{\text{III}}, \text{Nd}^{\text{III}}, \text{Sm}^{\text{III}}, \text{Eu}^{\text{III}}, \text{Gd}^{\text{III}}$,

Dy^{III} , Tb^{III} , Ho^{III} , Er^{III} , Tm^{III} or Yb^{III}), only the Tb^{III} analogue showed onset of slow magnetic relaxation.⁹

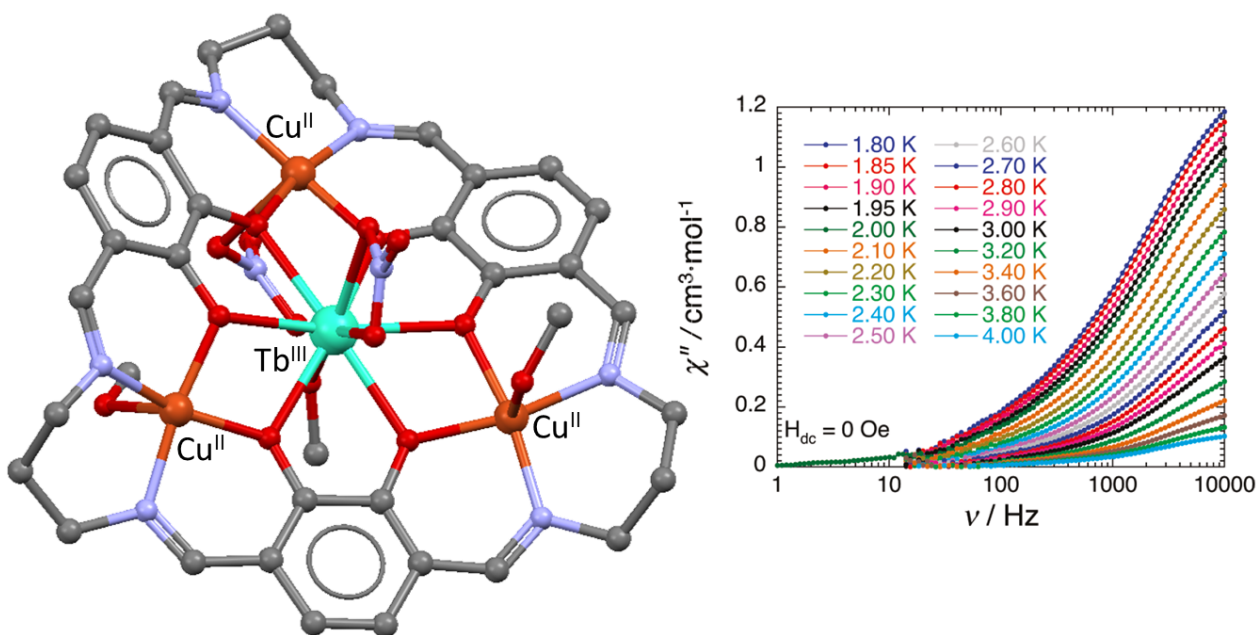


Figure 3.3: Structure of $\{\text{TbCu}_3(\text{L}^{\text{Pr}})\}$ (left) with out-of-phase ac susceptibility data (right).⁷ Atom colours: Tb^{III} , turquoise; Cu^{II} , orange; O, red; N, blue; C, grey. H-atoms and lattice solvent molecules are omitted.

When the diamine was modified; changing the propyl backbone for butyl, the complex $\{\text{TbCu}_3(\text{L}^{\text{Bu}})\}$ showed frequency dependent out-of-phase ac susceptibility peaks above 1.8 K in zero dc field with a $U_{\text{eff}} = 19.5 \text{ K}$ (Figure 4).¹⁰

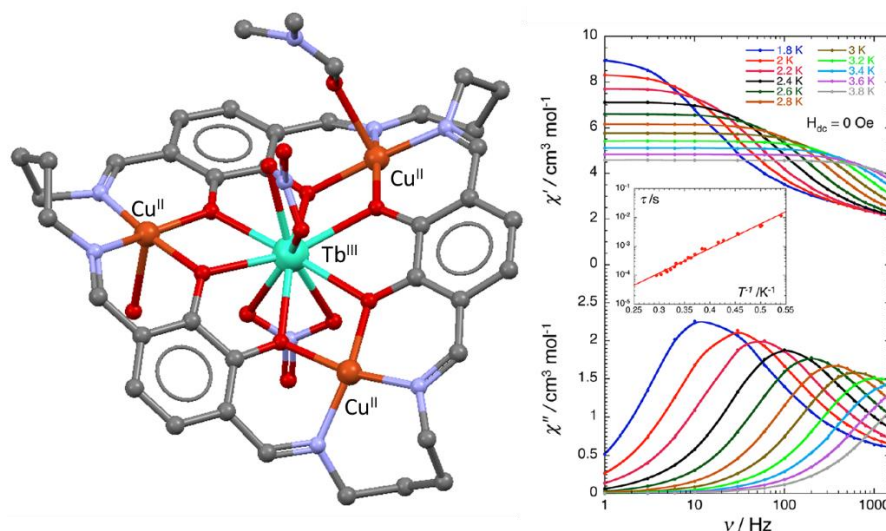


Figure 3.4: The complex $\{\text{TbCu}_3(\text{L}^{\text{Bu}})\}$ (left) with ac magnetic data in zero dc field (right).⁸ Atom colours: Tb^{III} , turquoise; Cu^{II} , orange; O, red; N, blue; C, grey.

The added carbon atoms resulted in more planar $\text{Tb}^{\text{III}}\text{-O-O-Cu}^{\text{II}}$ torsion angles compared to those in $\{\text{TbCu}_3(\text{L}^{\text{Pr}})\}$. The $\{\text{TbCu}_3(\text{L}^{\text{Bu}})\}$ complex having torsion angles 179.27° , 171.04° and 175.54° , and the $\{\text{TbCu}_3(\text{L}^{\text{Pr}})\}$ complex having 173.19° , 173.42° and 170.32° . This increase toward planarity (180°) resulted in stronger $\text{Tb}^{\text{III}}\text{-Cu}^{\text{II}}$ ferromagnetic interactions,¹¹⁻¹³ leading to a more energetically isolated ground state and hence a larger U_{eff} . The other major structural difference is the extra NO_3^- anion bound to Tb^{III} in $\{\text{TbCu}_3(\text{L}^{\text{Bu}})\}$ in an axial position; increasing the presence of axial negative electrostatic potential which in turn increased the energy gap between the ground and first excited states of the complex.²

As stated above, the ligand H_4pdte was used to synthesise an analogous series to that reported in Chapter 2, with the overall aim to study the differences in the structural and magnetic properties. In total, 10 new $\{\text{LnCu}_3(\text{H}_2\text{pdte})_3\}$ complexes ($\text{Ln} = \text{Y}^{\text{III}}, \text{Pr}^{\text{III}}, \text{Nd}^{\text{III}}, \text{Eu}^{\text{III}}, \text{Gd}^{\text{III}}, \text{Tb}^{\text{III}}, \text{Dy}^{\text{III}}, \text{Ho}^{\text{III}}, \text{Er}^{\text{III}}, \text{Yb}^{\text{III}}$) were synthesised, all of which were characterised by IR, CHN and single crystal X-ray diffraction, with the Gd^{III} , Tb^{III} and Dy^{III} analogues also characterised magnetically.

3.2 Experimental

3.2.1 Synthesis of *N,N,N',N'*-tetrakis-(2-hydroxyethyl)-1,3-diaminopropane (10)

The synthesis was adapted from the literature.¹⁴ Anhydrous K₂CO₃ (5.54 g, 40 mmol) was finely ground and added to 50 ml EtOH with vigorous stirring to form a suspension. 1,3-dibromopropane (4 ml, 40 mmol) was then added followed by diethanolamine (8.53 g, 81.13 mmol) and 30 ml EtOH. The reaction was heated at reflux for 64 hours then cooled to room temperature, 30 ml CHCl₃ was then added and the reaction stirred for a further 12 hours. The suspension was filtered and the white solid washed with 3 x 10 ml of CHCl₃. The solvents were then removed under vacuum to leave a pale yellow oil (weight ≈ 10 g). The crude oil was purified by loading 4 g onto a silica 60 column using a solvent system of 89% MeOH, 3% NH₃ (in MeOH solution) and 8% DCM. The *r_f* of H₄pdte was ≈ 0.34 on a silica TLC plate. The reaction products were traced on the plates using a permanganate stain which was prepared by adding K₂CO₃ (40 g) and KMnO₄ (6 g) to 600 ml deionised H₂O, followed by addition of 5 ml 0.1 M NaOH solution. The products showed up as brown spots on a purple background. The pure fractions were combined and eluent removed under vacuum to give a pale yellow oil: Yield; 30-50%. ESI-MS: *m/z* (%): 250 (100) [M⁺]; ¹H NMR (400MHz, [D₄]MeOH, 25°C): δ = 1.67 (br quint, 2H, CH₂CH₂CH₂), 2.59 (t, ³J = 5.8 Hz, 8H, NCH₂CH₂CH₂N), 2.65 (t, ³J = 5.8 Hz, 8H, HOCH₂CH₂), 3.62 ppm (t, ³J = 5.8 Hz, 8H, HOCH₂).

3.2.2 Synthesis of [Y^{III}(Cu^{II}H₂pdte)₃(NO₃)][NO₃]₂·0.5MeOH (11)

To a stirred solution of H₄pdte (0.13 g, 0.52 mmol) in MeOH (20 ml) was added Cu(NO₃)₂·3H₂O (0.07 g, 0.29 mmol), this was stirred at room temperature for 10 minutes then NEt₃ (0.19 ml, 1.36 mmol) was added. This solution was stirred for 15 minutes then Y(NO₃)₃·6H₂O (0.037 g, 0.097 mmol) and 10 ml MeOH were added and the reaction stirred for 7 hours at room temperature. The resulting deep blue solution was filtered then portions taken for vapour diffusion with Et₂O, forming blue plate-like crystals suitable for X-ray diffraction overnight. Yield: 58% (0.06 g) based on Y^{III}. Oven dried crystals (@60°C) analyse as **11**, (Y₁Cu₃C_{33.5}H₇₄N₉O_{21.5}), analysis (%) calc. (found): C 32.80 (32.73); H 6.08 (6.10); N 10.28 (10.16). Selected IR data (cm⁻¹): 3244 (br), 2958.90 (w), 2928.04 (w), 2870.17 (w), 2825.81 (w), 1444.73 (m), 1429.30 (m), 1383.01 (m), 1303.92

(s), 1163.11 (w), 1070.53 (s), 1018.45 (s), 985.66 (m), 950.94 (w), 904.64 (s), 827.49 (w), 752.26 (m), 738.76 (m), 619.17 (s).

3.2.3 Synthesis of $[Pr^{III}(Cu^{II}H_2pdte)_3(NO_3)][NO_3]_2 \cdot 0.5MeOH$ (12)

To a stirred solution of H₄pdte (0.13 g, 0.52 mmol) in MeOH (20 ml) was added Cu(NO₃)₂·3H₂O (0.07 g, 0.29 mmol), this was stirred at room temperature for 10 minutes then NEt₃ (0.19 ml, 1.36 mmol) was added. This solution was stirred for 15 minutes then Pr(NO₃)₃·6H₂O (0.044 g, 0.1 mmol) and 10 ml MeOH were added and the reaction stirred for 7 hours at room temperature. The resulting deep blue solution was filtered then portions taken for vapour diffusion with Et₂O, forming blue plate-like crystals suitable for X-ray diffraction overnight. Yield: 42% (0.05 g) based on Pr^{III}. Oven dried crystals (@60°C) analyse as **12**, (Pr₁Cu₃C_{33.5}H₇₄N₉O_{21.5}), analysis (%) calc. (found): C, 31.59 (31.42); H 5.85 (5.80); N 9.75 (9.68). Selected IR data (cm⁻¹): 3244(br), 2962.76 (w), 2914.54 (w), 2858.60 (w), 2831.6 (w), 1440.87 (m), 1429.30 (m), 1379.15 (m), 1294.28 (s), 1163.11 (w), 1068.6 (s), 1018.45 (s), 985.66 (m), 950.94 (w), 902.72 (s), 827.49 (w), 752.26 (m), 729.12 (m).

3.2.4 Synthesis of $[Nd^{III}(Cu^{II}H_2pdte)_3(NO_3)][NO_3]_2 \cdot 0.5MeOH$ (13)

To a stirred solution of H₄pdte (0.13 g, 0.52 mmol) in MeOH (20 ml) was added Cu(NO₃)₂·3H₂O (0.07 g, 0.29 mmol), this was stirred at room temperature for 10 minutes then NEt₃ (0.19 ml, 1.36 mmol) was added. This solution was stirred for 15 minutes then Nd(NO₃)₃·6H₂O (0.044 g, 0.1 mmol) and 10 ml MeOH were added and the reaction stirred for 7 hours at room temperature. The resulting deep blue solution was filtered then portions taken for vapour diffusion with Et₂O, forming blue plate-like crystals suitable for X-ray diffraction overnight. Yield: 35% (0.04 g) based on Nd^{III}. Oven dried crystals (@60°C) analyse as **13**, (Nd₁Cu₃C_{33.5}H₇₄N₉O_{21.5}), analysis (%) calc. (found): C 31.49 (31.30); H 5.79 (5.79); N 9.72 (9.60). Selected IR data (cm⁻¹): 3244(br), 2960.83 (w), 2914.54 (w), 2860.53 (w), 2831.60 (w), 1440.87 (m), 1429.30 (m), 1381.08 (m), 1294.28 (s), 1163.11 (w), 1070.53 (s), 1018.45 (s), 985.66 (m), 950.94 (w), 904.64 (s), 827.49 (w), 752.26 (m), 731.05.

3.2.5 Synthesis of [Eu^{III}(Cu^{II}H₂pdte)₃(NO₃)]/[NO₃]₂·0.5MeOH (14)

To a stirred solution of H₄pdte (0.13 g, 0.52 mmol) in MeOH (20 ml) was added Cu(NO₃)₂·3H₂O (0.07 g, 0.29 mmol), this was stirred at room temperature for 10 minutes then NEt₃ (0.19 ml, 1.36 mmol) was added. This solution was stirred for 15 minutes then EuCl₃·6H₂O (0.041 g, 0.091 mmol) and 10 ml MeOH were added and the reaction stirred for 7 hours at room temperature. The resulting deep blue solution was filtered then portions taken for vapour diffusion with Et₂O, forming blue plate-like crystals suitable for X-ray diffraction overnight. Yield: 19 % (0.02 g) based on Eu^{III}. Oven dried crystals (@60°C) analyse as **14**, (Eu₁Cu₃C_{33.5}H₇₄N₉O_{21.5}), analysis (%) calc. (found): C 31.08 (30.87) H 5.77 (5.73) N 9.75 (9.44). Selected IR data (cm⁻¹): 3240 (br), 2914.54 (w), 2866.32 (m), 2829.67 (w), 2681.14 (w), 1467.88 (m), 1442.80 (m), 1429.30 (m), 1381.08 (m), 1365.65 (m), 1296.21 (s), 1255.70 (m), 1163.11 (w), 1068.6 (s), 1031.95 (m), 1018.45 (s), 985.66 (m), 950.94 (w), 929.72 (w), 902.72 (s), 873.78 (m), 840.99 (w), 827.49 (m), 752.26 (m), 732.97 (m).

3.2.6 Synthesis of [Gd^{III}(Cu^{II}H₂pdte)₃(NO₃)]/[NO₃]₂·0.5MeOH (15)

To a stirred solution of H₄pdte (0.13 g, 0.52 mmol) in MeOH (20 ml) was added Cu(NO₃)₂·3H₂O (0.07 g, 0.29 mmol), this was stirred at room temperature for 10 minutes then NEt₃ (0.19 ml, 1.36 mmol) was added. This solution was stirred for 15 minutes then Gd(NO₃)₃·6H₂O (0.046 g, 0.097 mmol) and 10 ml MeOH were added and the reaction stirred for 7 hours at room temperature. The resulting deep blue solution was filtered then portions taken for vapour diffusion with Et₂O, forming blue plate-like crystals suitable for X-ray diffraction overnight. Yield: 66% (0.08 g) based on Gd^{III}. Oven dried crystals (@60°C) analyse as **15**, (Gd₁Cu₃C_{33.5}H₇₄N₉O_{21.5}), analysis (%) calc. (found): C, 31.07 (30.85); H 5.76 (5.71); N 9.74 (9.52). Selected IR data (cm⁻¹): 3244(br), 2958.90 (w), 2910.68 (w), 2866.32 (w), 2829.67 (w), 1442.8 (m), 1429.30 (m), 1381.08 (m), 1298.14 (s), 1163.11 (w), 1068.6 (s), 1018.45 (s), 985.66 (m), 950.94 (w), 904.64 (s), 827.49 (w), 752.26 (m), 734.9 (m), 619.17 (s).

3.2.7 Synthesis of $[\text{Tb}^{\text{III}}(\text{Cu}^{\text{II}}\text{H}_2\text{pdte})_3(\text{NO}_3)][\text{NO}_3]_2 \cdot 0.5\text{MeOH}$ (16)

To a stirred solution of H_4pdte (0.13 g, 0.52 mmol) in MeOH (20 ml) was added $\text{Cu}(\text{NO}_3)_2 \cdot 3\text{H}_2\text{O}$ (0.07 g, 0.29 mmol), this was stirred at room temperature for 10 minutes then NEt_3 (0.19 ml, 1.36 mmol) was added. This solution was stirred for 15 minutes then $\text{Tb}(\text{NO}_3)_3 \cdot 5\text{H}_2\text{O}$ (0.038 g, 0.097 mmol) and 10 ml MeOH were added and the reaction stirred for 7 hours at room temperature. The resulting deep blue solution was filtered then portions taken for vapour diffusion with Et_2O , forming blue plate-like crystals suitable for X-ray diffraction overnight. Yield: 61% (0.07 g) based on Tb^{III} . Oven dried crystals (@60°C) analyse as **16**, $(\text{Tb}_1\text{Cu}_3\text{C}_{33.5}\text{H}_{74}\text{N}_9\text{O}_{21.5})$, analysis (%) calc. (found): C 31.03 (30.77); H 5.75 (5.74); N 9.72 (9.54). Selected IR data (cm^{-1}): 3244(br), 2958.90 (w), 2928.04 (w), 2870.17 (w), 2825.81 (w), 1444.73 (m), 1429.30 (m), 1383.01 (m), 1303.92 (s), 1163.11 (w), 1070.53 (s), 1018.45 (s), 985.66 (m), 950.94 (w), 904.64 (s), 827.49 (w), 752.26 (m), 738.76 (m), 619.17 (s).

3.2.8 Synthesis of $[\text{Dy}^{\text{III}}(\text{Cu}^{\text{II}}\text{H}_2\text{pdte})_3(\text{NO}_3)][\text{NO}_3]_2 \cdot 0.5\text{MeOH}$ (17)

To a stirred solution of H_4pdte (0.13 g, 0.52 mmol) in MeOH (20 ml) was added $\text{Cu}(\text{NO}_3)_2 \cdot 3\text{H}_2\text{O}$ (0.07 g, 0.29 mmol), this was stirred at room temperature for 10 minutes then NEt_3 (0.19 ml, 1.36 mmol) was added. This solution was stirred for 15 minutes then $\text{Dy}(\text{NO}_3)_3 \cdot 5\text{H}_2\text{O}$ (0.046 g, 0.1 mmol) and 10 ml MeOH were added and the reaction stirred for 7 hours at room temperature. The resulting deep blue solution was filtered then portions taken for vapour diffusion with Et_2O , forming blue plate-like crystals suitable for X-ray diffraction overnight. Yield: 63% (0.07 g) based on Dy^{III} . Oven dried crystals (@60°C) analyse as **17**, $(\text{Dy}_1\text{Cu}_3\text{C}_{33.5}\text{H}_{74}\text{N}_9\text{O}_{21.5})$, analysis (%) calc. (found): C, 30.94 (30.43); H 5.73 (5.62); N 9.69 (9.50). Selected IR data (cm^{-1}): 3244 (br), 2956.97 (w), 2928.04 (w), 2870.17 (w), 2847.03 (w), 1442.80 (m), 1429.30 (m), 1381.08 (m), 1303.92 (s), 1163.11 (w), 1068.60 (s), 1018.45 (s), 985.66 (m), 950.94 (w), 904.64 (s), 827.49 (w), 752.26 (m), 736.83 (m).

3.2.9 Synthesis of $[\text{Ho}^{\text{III}}(\text{Cu}^{\text{II}}\text{H}_2\text{pdte})_3(\text{NO}_3)][\text{NO}_3]_2 \cdot 0.5\text{MeOH}$ (18)

To a stirred solution of H_4pdte (0.13 g, 0.52 mmol) in MeOH (20 ml) was added $\text{Cu}(\text{NO}_3)_2 \cdot 3\text{H}_2\text{O}$ (0.07 g, 0.29 mmol), this was stirred at room temperature for 10 minutes then NEt_3 (0.19 ml, 1.36 mmol) was added. This solution was stirred for 15 minutes then $\text{Ho}(\text{NO}_3)_3 \cdot 5\text{H}_2\text{O}$ (0.042 g, 0.095 mmol) and 10 ml MeOH were added and the reaction stirred for 7 hours at room temperature. The resulting deep blue solution was filtered then portions taken for vapour diffusion with Et_2O , forming blue plate-like crystals suitable for X-ray diffraction overnight. Yield: 88% (0.10 g) based on Ho^{III} . Oven dried crystals (@60°C) analyse as **18**, ($\text{Ho}_1\text{Cu}_3\text{C}_{33.5}\text{H}_{74}\text{N}_9\text{O}_{21.5}$), analysis (%) calc. (found): C, 30.90 (30.67); H 5.73 (5.68); N 9.67 (9.43). Selected IR data (cm^{-1}): 3244(br), 2958.90 (w), 2912.61 (w), 2872.10 (w), 2825.81 (w), 1442.80 (m), 1429.30 (m), 1381.08 (m), 1301.99 (s), 1163.11 (w), 1068.60 (s), 1018.45 (s), 987.59 (m), 950.94 (w), 904.64 (s), 827.49 (w), 752.26 (m), 736.83 (m).

3.2.10 Synthesis of $[\text{Er}^{\text{III}}(\text{Cu}^{\text{II}}\text{H}_2\text{pdte})_3(\text{NO}_3)][\text{NO}_3]_2 \cdot 0.5\text{MeOH}$ (19)

To a stirred solution of H_4pdte (0.13 g, 0.52 mmol) in MeOH (20 ml) was added $\text{Cu}(\text{NO}_3)_2 \cdot 3\text{H}_2\text{O}$ (0.07 g, 0.29 mmol), this was stirred at room temperature for 10 minutes then NEt_3 (0.19 ml, 1.36 mmol) was added. This solution was stirred for 15 minutes then $\text{Er}(\text{NO}_3)_3 \cdot 5\text{H}_2\text{O}$ (0.045 g, 0.1 mmol) and 10 ml MeOH were added and the reaction stirred for 7 hours at room temperature. The resulting deep blue solution was filtered then portions taken for vapour diffusion with Et_2O , forming blue plate-like crystals suitable for X-ray diffraction overnight. Yield: 53% (0.06 g) based on Er^{III} . Oven dried crystals (@60°C) analyse as **19**, ($\text{Er}_1\text{Cu}_3\text{C}_{33.5}\text{H}_{74}\text{N}_9\text{O}_{21.5}$), analysis (%) calc. (found): C 30.84 (30.96); H 5.72 (5.71); N 9.66 (9.44). Selected IR data (cm^{-1}): 3244(br), 2958.90 (w), 2914.54 (w), 2872.10 (w), 2825.81 (w), 1442.80 (m), 1429.30 (m), 1381.08 (m), 1303.92 (s), 1163.11 (w), 1068.6 (s), 1018.45 (s), 987.59 (m), 950.94 (w), 904.64 (s), 827.49 (w), 752.26 (m), 729.12 (m), 619.17 (s).

3.2.11 Synthesis of [Yb^{III}(Cu^{II}H₂L²)₃(NO₃)][(NO₃)₂·0.5MeOH] (20)

To a stirred solution of H₄pdte (0.13 g, 0.52 mmol) in MeOH (20 ml) was added Cu(NO₃)₂·3H₂O (0.07 g, 0.29 mmol), this was stirred at room temperature for 10 minutes then NEt₃ (0.19 ml, 1.36 mmol) was added. This solution was stirred for 15 minutes then Yb(NO₃)₃·5H₂O (0.041 g, 0.091 mmol) and 10 ml MeOH were added and the reaction stirred for 7 hours at room temperature. The resulting deep blue solution was filtered then portions taken for vapour diffusion with Et₂O, forming blue plate-like crystals suitable for X-ray diffraction overnight. Yield: 59% (0.07 g) based on Yb^{III}. Oven dried crystals (@60°C) analyse as **20**, (Yb₁Cu₃C_{33.5}H₇₄N₉O_{21.5}), analysis (%) calc. (found): C 30.62 (30.30); H 5.61 (5.61); N 9.74 (9.41). Selected IR data (cm⁻¹): 3244(br), 2956.97 (w), 2914.54 (w), 2872.10 (w), 2825.81 (w), 1442.80 (m), 1429.30 (m), 1381.08 (m), 1305.85 (s), 1163.11 (w), 1068.6 (s), 1018.45 (s), 987.59 (m), 952.87 (w), 904.64 (s), 827.49 (w), 752.26 (m), 740.69 (m), 731.05 (s).

3.3 Results and Discussion

3.3.1 Synthesis

The method used to synthesise H₄pdte was adapted from a previously reported procedure.¹⁴ The procedure was a 64 hour reflux of 1,3-dibromopropane, diethanolamine and K₂CO₃ in the ratio 1:2:2 in EtOH. The resulting crude suspension was then filtered to remove the white solid which was thoroughly washed with DCM. The remaining solvent was then removed under vacuum at 70°C to give a pale yellow crude oil. Thin layer chromatography of the crude showed the product H₄pdte at around $r_f \approx 0.34$, with unreacted diethanolamine showing up just below with $r_f \approx 0.3$. The crude oil was purified using column chromatography using Silica 60 gel. Initially, the reported solvent system of MeOH 8%, DCM 89%, NH₃ (in MeOH) 3% was used. This system however did not achieve as pure a final product compared to MeOH 89%, DCM 8% and NH₃ (in MeOH) 3%. The adapted ratios maintained a better separation of H₄pdte from unreacted diethanolamine. A possible reason for this could be the high vapour pressure of DCM and the difficulty in keeping a uniform ratio of solvents throughout the purification. Switching to a higher concentration of MeOH resulted in some dissolution of the silica gel, however, this did not have a significant impact on the purity of the final product. After removing the eluent under

vacuum, the ligand could be extracted with DCM, leaving behind any silica impurities. The purified ligand was successfully characterised with ^1H NMR (Figure 3.5) and ESI-MS.

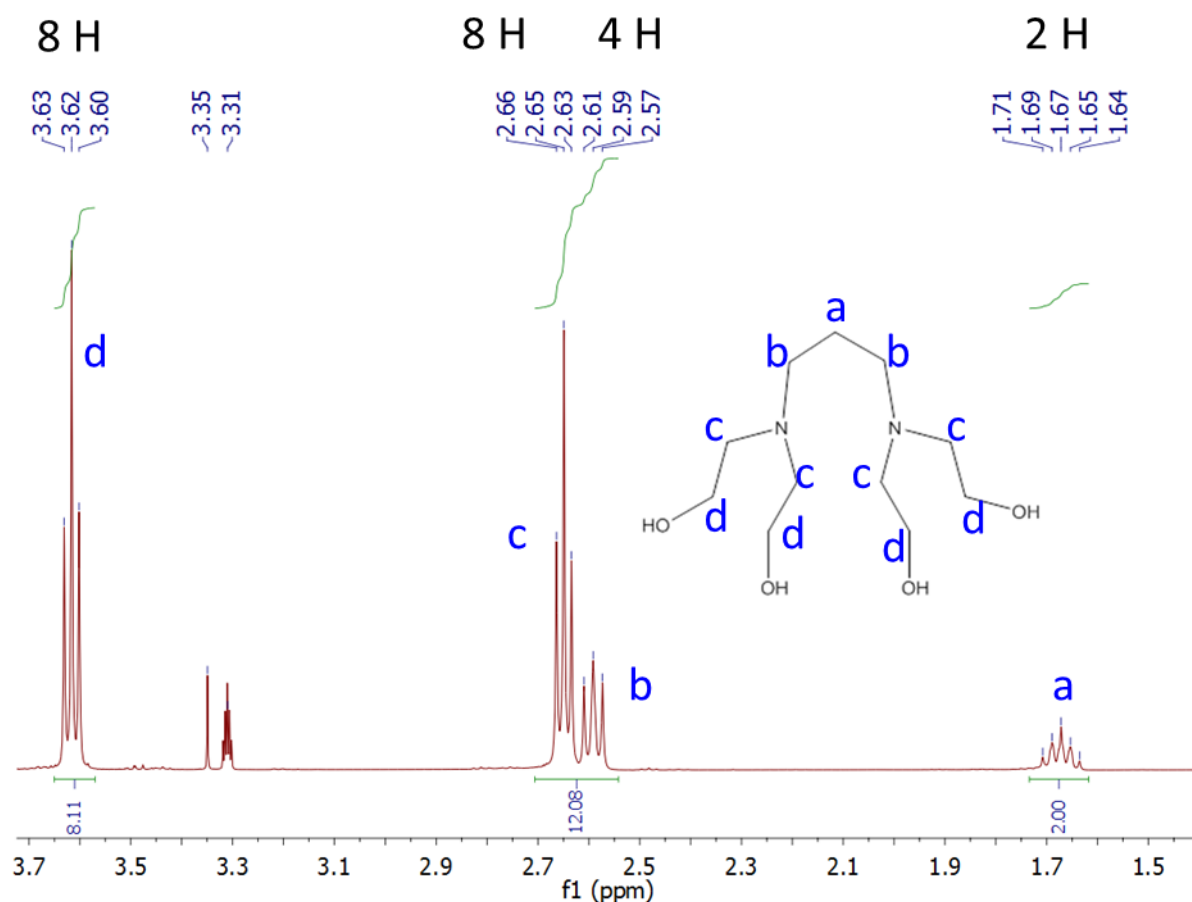


Figure 3.5: ^1H NMR spectrum of purified H_4pdte in $[\text{d}_4]\text{MeOD}$. Peaks at 3.31 and 3.35 ppm correspond to residual MeOH solvent.¹⁵

The series $[\text{LnCu}_3(\text{H}_2\text{pdte})_3(\text{NO}_3)][\text{NO}_3]_2 \cdot 0.5\text{MeOH}$, where $\text{Ln} = \text{Y}^{\text{III}}, \text{Pr}^{\text{III}}, \text{Nd}^{\text{III}}, \text{Gd}^{\text{III}}, \text{Tb}^{\text{III}}, \text{Dy}^{\text{III}}, \text{Ho}^{\text{III}}, \text{Er}^{\text{III}}, \text{Yb}^{\text{III}}$, can be synthesised in a one pot reaction by mixing H_4pdte , NEt_3 , $\text{Cu}(\text{NO}_3)_2 \cdot 3\text{H}_2\text{O}$ and $\text{Ln}(\text{NO}_3)_3 \cdot x\text{H}_2\text{O}$ in the ratio 0.52 : 1.36 : 0.21 : 0.09 in MeOH . The Eu^{III} analogue followed the same procedure except EuCl_3 was used instead of $\text{Eu}(\text{NO}_3)_3$. Single crystals of each of the analogues were obtained overnight by vapour diffusing the mother liquor with Et_2O .

3.3.2 Discussion of the $\{\text{LnCu}_3(\text{H}_2\text{pdte})_3\}$ Series' Structure

The series $[\text{LnCu}_3(\text{H}_2\text{edte})_3(\text{NO}_3)][\text{NO}_3]_2$ where $\text{Ln} = \text{Y}^{\text{III}}$ (11), Pr^{III} (12), Nd^{III} (13), Eu^{III} (14), Gd^{III} (15), Tb^{III} (16), Dy^{III} (17), Ho^{III} (18), Er^{III} (19) and Yb^{III} (20) are all isostructural, crystallising in the triclinic space group $P-1$. The unit cell consists of two $\{\text{LnCu}_3\}$ molecules, two fully occupied NO_3^- anions, two positionally disordered NO_3^- anions and a disordered MeOH solvent of crystallisation (Figure 3.6). Atoms N300, O300, O301 and O302 make up the fully occupied nitrate. Atoms N2000, O2001, O201 and O202 make up a positionally disordered nitrate which lies directly on an inversion centre. The inversion centre lies in the middle of the bond between N2000 and O2001, giving it its 'odd' appearance. The final nitrate, N100, O500, O501 and O502 is 50:50 positionally disordered with a solvent MeOH (C600 & O600), the pair lie adjacent to an inversion centre. The unit cell structure for the $\{\text{LnCu}_3(\text{H}_2\text{pdte})_3\}$ series is analogous to the $\{\text{LnCu}_3(\text{H}_2\text{edte})_3\}$ series' (Section 2.3.3).

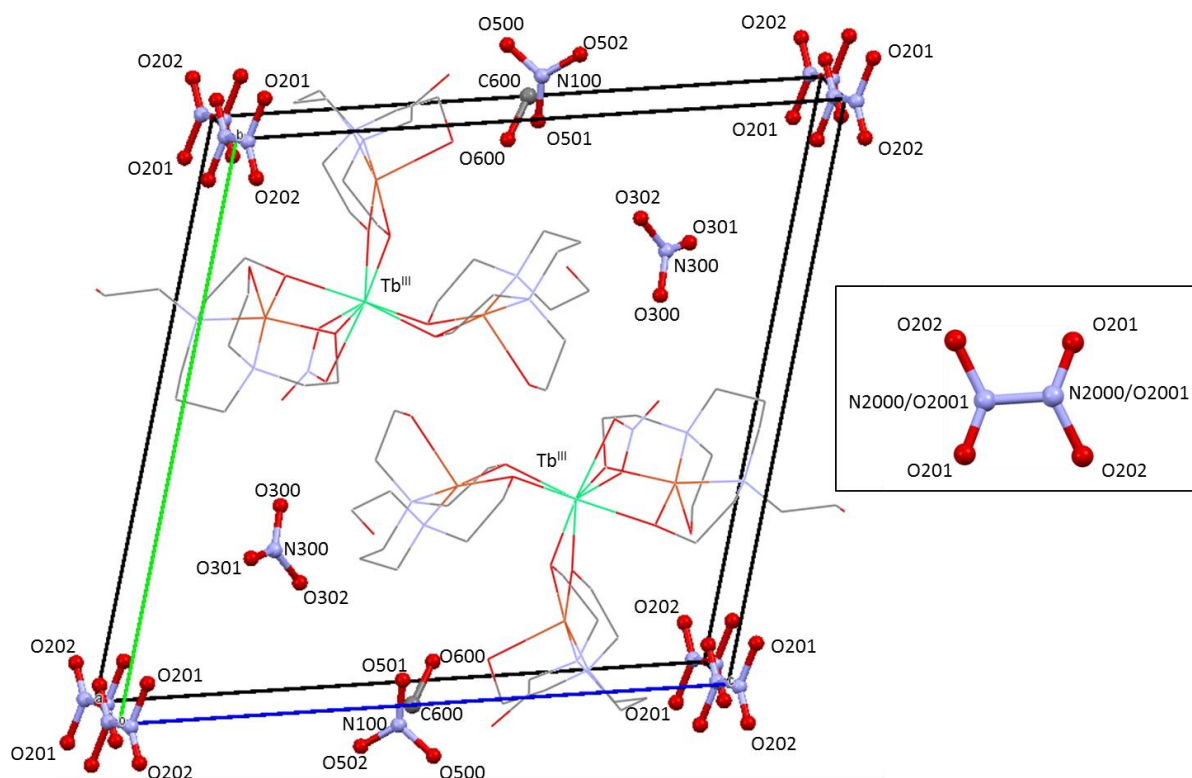


Figure 3.6: Unit cell of $[\text{TbCu}_3(\text{H}_2\text{pdte})_3(\text{NO}_3)][\text{NO}_3]_2 \cdot 0.5\text{MeOH}$, representative of the unit cell for all analogues. Inset depicts nitrate anion at corners of unit cell.

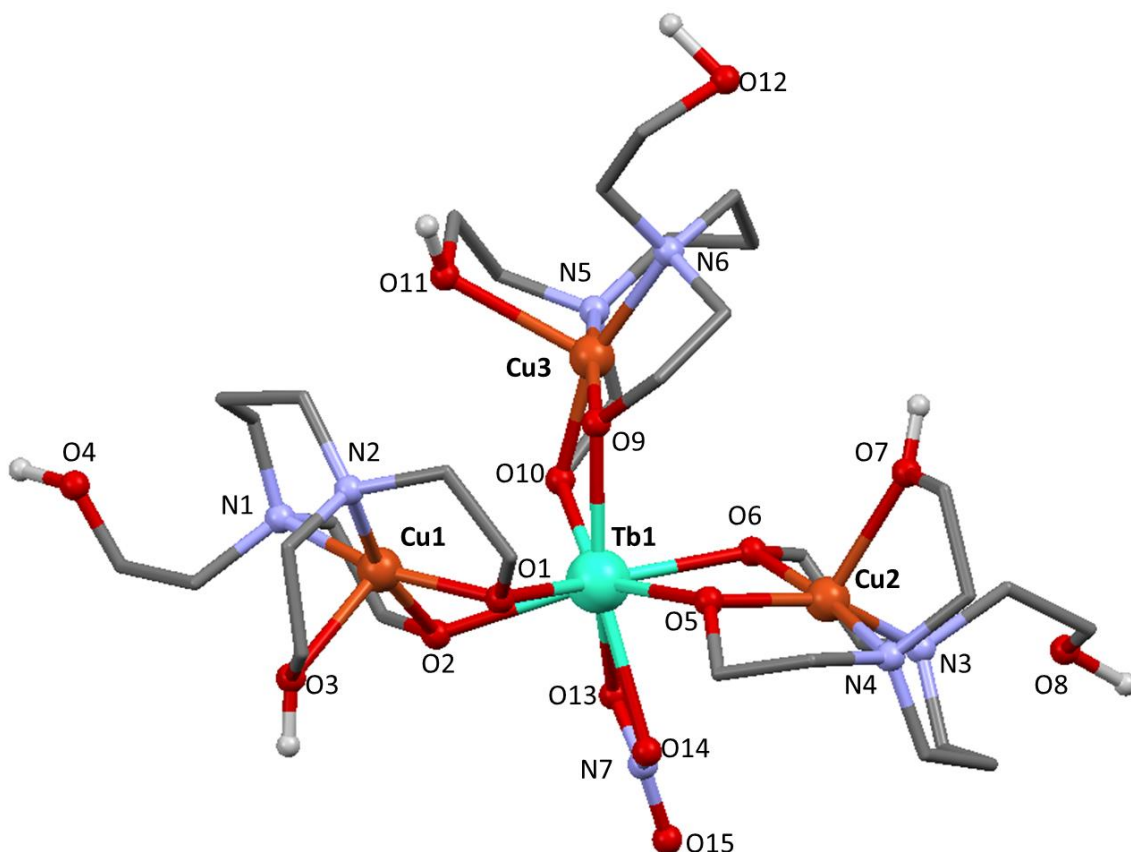


Figure 3.7: *Molecular structure for $\{\text{TbCu}_3(\text{H}_2\text{pdte})_3\}$, representative of all series members. C-H protons have been omitted for clarity. Atom colours: Light green, Tb^{III} ; orange, Cu^{II} ; red, O; blue, N; grey, C; white, H.*

The $\{\text{LnCu}_3(\text{H}_2\text{pdte})_3\}$ complex molecule consists of an 8-coordinate central lanthanide ion bound to three neutral $\{\text{Cu}(\text{H}_2\text{pdte})\}$ metalloligand subunits and a bidentate nitrate ligand. The +3 charge of the lanthanide is balanced by the ligand nitrate and two lattice nitrates. The metalloligand subunits have a Cu^{II} ion chelated by a $\text{H}_2\text{pdte}^{2-}$ ligand; adopting a square based pyramidal geometry. The ligand binds through both nitrogen donors and three of its four oxygen donor atoms. The two deprotonated arms of the ligand form alkoxo-bridges between the central Ln^{III} ion and Cu^{II} subunit ion. Of the remaining protonated arms, one occupies the axial position on the Cu^{II} ion with the final arm extending out into the crystal lattice where it takes part in hydrogen bonding with lattice nitrates.

<i>Empirical formula</i>	<i>YCu₃C_{33.5}H₇₄N₉O_{21.5}</i>	<i>PrCu₃C_{33.5}H₇₄N₉O_{21.5}</i>	<i>NdCu₃C_{33.5}H₇₄N₉O_{21.5}</i>	<i>EuCu₃C_{33.5}H₇₄N₉O_{21.5}</i>	<i>GdCu₃C_{33.5}H₇₄N₉O_{21.5}</i>
Molar mass (gmol ⁻¹)	1226.54	1277.74	1281.88	1289.6	1294.89
Crystal System	<i>P</i> -1	<i>P</i> -1	<i>P</i> -1	<i>P</i> -1	<i>P</i> -1
Space Group	Triclinic	Triclinic	Triclinic	Triclinic	Triclinic
a (Å)	9.3244(11)	9.180(2)	9.1861(11)	9.1555(9)	9.0967(9)
b (Å)	16.056(2)	16.253(3)	16.266(2)	16.2678(17)	16.5402(18)
c (Å)	16.626(2)	16.862(3)	16.8604(19)	16.7309(18)	16.6530(18)
α (deg)	74.776(3)	74.452(4)	74.603(3)	75.187(2)	76.420(3)
β (deg)	84.565(3)	84.816(4)	84.844(3)	84.881(2)	84.938(3)
γ (deg)	84.374(3)	81.325(4)	81.375(3)	82.023(2)	81.399(3)
V (Å ³)	2384.0(3)	2392.8(4)	2398.1(3)	2382.0(3)	2404.5(3)
Z	2	2	2	2	2
T (K)	100	100	100	100	100
λ (Å)	0.71073	0.71073	0.71073	0.71073	0.71073
ρ _{calc} (g/cm ³)	1.708	1.763	1.769	1.798	1.788
μ (mm ⁻¹)	2.613	2.402	2.464	2.707	2.757
^a R ₁	0.0734	0.1065	0.0532	0.0471	0.0520
^b wR ₂	0.1588	0.2330	0.1185	0.1061	0.1196
Goodness of fit	0.949	1.051	0.907	0.894	0.909
F(000)	1272	1312	1314	1320	1322
Reflections	8412	8202	8753	8709	8777
Parameters	580	556	572	571	561
Restraints	449	629	37	418	370

Table 3.1: Crystallographic data for complexes **11-15**.

$${}^aR_1 = \sum ||F_o| - |F_c|| / \sum |F_o|$$

$${}^b wR_2 = [\sum [w(F_o^2 - F_c^2)^2] - \sum [(F_o^2)^2]]^{\frac{1}{2}} \quad \text{where} \quad w = 1/[\sigma^2(F_o^2) + (0.2P)^2] \quad \text{and} \quad P = [F_o^2 + 2F_c^2]/3$$

<i>Empirical formula</i>	<i>TbCu₃C_{33.5}H₇₄N₉O_{21.5}</i>	<i>DyCu₃C_{33.5}H₇₄N₉O_{21.5}</i>	<i>HoCu₃C_{33.5}H₇₄N₉O_{21.5}</i>	<i>ErCu₃C_{33.5}H₇₄N₉O_{21.5}</i>	<i>YbCu₃C_{33.5}H₇₄N₉O_{21.5}</i>
Molar mass (gmol ⁻¹)	1296.56	1300.14	1302.57	1304.9	1310.68
Crystal System	Triclinic	Triclinic	Triclinic	Triclinic	Triclinic

Space Group	<i>P</i> -1				
a (Å)	9.3485(2)	9.3068(2)	9.3411(17)	9.3225(5)	9.3150(6)
b (Å)	16.1128(4)	16.1268(4)	16.067(3)	16.0795(9)	16.0901(13)
c (Å)	16.6576(4)	16.6433(4)	16.620(3)	16.6348(10)	16.6170(13)
α (deg)	75.2580(10)	75.1850(10)	74.839(4)	74.6752(16)	74.510(4)
β (deg)	84.3110(10)	84.479(2)	84.480(4)	84.6520(16)	85.133(4)
γ (deg)	84.2360(10)	84.054(2)	84.411(4)	84.4603(17)	84.841(4)
V (Å ³)	2407.21(6)	2395.62(6)	2389.7(4)	2387.72(14)	2385.56(19)
Z	2	2	2	2	2
T (K)	100	100	100	100	100
λ (Å)	0.71073	0.71073	0.71073	0.71073	0.71073
ρ _{calc} (g/cm ³)	1.789	1.802	1.809	1.814	1.824
μ (mm ⁻¹)	2.845	2.942	3.042	3.145	3.349
^a R ₁	0.0405	0.0432	0.0795	0.0429	0.0494
^b wR ₂	0.0778	0.0761	0.1741	0.1107	0.1123
Goodness of fit	0.910	0.963	0.919	0.982	0.877
F(000)	1324	1326	1328	1330	1334
Reflections	8818	8788	8716	9428	8410
Parameters	582	584	575	583	593
Restraints	427	447	435	432	444

Table 3.2: Crystallographic data for complexes **16 - 20**

$${}^aR_1 = \frac{\sum ||F_o| - |F_c||}{\sum |F_o|}$$

$${}^b wR_2 = \frac{[\sum [w(F_o^2 - F_c^2)^2] - \sum [(F_o^2)^2]]^{\frac{1}{2}}}{\sum [w(F_o^2 + (0.2P)^2)]} \quad \text{where } w = 1/[\sigma^2(F_o^2) + (0.2P)^2] \quad \text{and } P = [F_o^2 + 2F_c^2]/3$$

3.3.2.1 Torsion Angles

As mentioned in Chapter 2 (Section 2.3.3.1), the $\text{Ln}^{\text{III}}\text{-O-O-Cu}^{\text{II}}$ torsion angle (θ , Figure 3.8) has a significant impact on the $\text{Ln}^{\text{III}}\text{-Cu}^{\text{II}}$ magnetic exchange.¹¹⁻¹³ When θ is in the range $140 - 180^\circ$ ferromagnetic exchange is likely to be observed; the strongest exchange as θ approaches 180° . As θ decreases, the exchange gradually weakens until there is a switch to antiferromagnetic as θ approaches 140° . In accordance with a superexchange mechanism between the $3d$ Cu^{II} orbitals and $4f$ Ln^{III} orbitals, complexes with planar ($\theta = 180^\circ$) structures have a higher number of orthogonal $3d\text{-}4f$ (ferromagnetic) interactions compared to directly overlapping (antiferromagnetic) interactions. As the structure distorts ($\theta < 180^\circ$), the number of orthogonal $3d\text{-}4f$ interactions decreases as the number of directly overlapping interactions increases; eventually leading to dominant antiferromagnetic exchange.

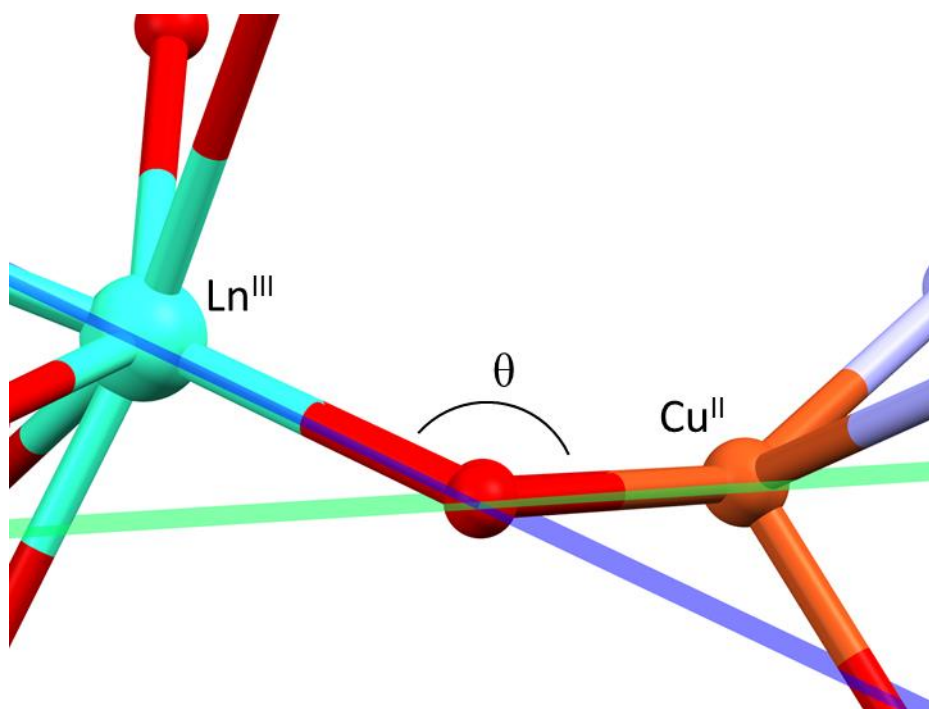


Figure 3.8: Representation of the torsion angle θ between the central Ln^{III} and Cu^{II} ions.

The torsion angles for the series are listed in Tables 3.3 & 3.4. Only two out of the three angles for each complex lie well in the ferromagnetic range, with one (Ln1-O1-O2-Cu1) lying at the edge of the range. In comparison, the $\{\text{LnCu}_3(\text{H}_2\text{edte})_3\}$ series has all angles for each complex in the ferromagnetic range (Section 2.3.3.1). Therefore the structural distortion caused by the added carbon atom is unfortunately likely to decrease the $\text{Ln}^{\text{III}} - \text{Cu}^{\text{II}}$ exchange strength. This is in contrast to the macrocyclic series reported by Brooker *et*

al. where added flexibility resulted in a more planar $\text{Ln}^{\text{III}} - \text{Cu}^{\text{II}}$ arrangement and stronger exchange.^{8,10}

	11	12	13	14	15
Ln1-O1-O2-Cu1	139.92°	142.83°	143.25°	145.21°	151.68°
Ln1-O5-O6-Cu2	163.41°	159.36°	159.51°	160.18°	161.06°
Ln1-O9-O10-Cu3	164.59°	163.98°	163.52°	164.8°	165.78°

Table 3.3: Torsion angles for complexes 11 - 15

	16	17	18	19	20
Ln1-O1-O2-Cu1	138.64°	139.61°	140.36°	139.43°	139.93°
Ln1-O5-O6-Cu2	163.86°	163.41°	163.67°	163.05°	162.23°
Ln1-O9-O10-Cu3	163.38°	163.78°	164.07°	164.22°	165.07°

Table 3.4: Torsion angles for complexes 16 - 20

3.3.2.2 SHAPE Analysis

Continuous SHAPE measurements¹⁶ were performed to analyse the central Ln^{III} geometry (Table 3.5). All analogues show a closest match to biaugmented trigonal prismatic geometry (C_{2v}) with triangular dodecahedral (D_{2d}) a close second. The relatively high ChSM values and small variations between geometries indicate significantly distorted Ln^{III} coordination spheres. Comparing the values between the $\{\text{LnCu}_3(\text{H}_2\text{pdte})_3\}$ series and $\{\text{LnCu}_3(\text{H}_2\text{edte})_3\}$ series (Tables 3.5 and 3.6), the former have slightly higher ChSM values overall. Also, all of the $\{\text{LnCu}_3(\text{H}_2\text{pdte})_3\}$ analogues are best described by C_{2v} symmetry whereas the $\{\text{LnCu}_3(\text{H}_2\text{edte})_3\}$ analogues **2 - 6** ($\text{Pr}^{\text{III}} - \text{Tb}^{\text{III}}$) are best described by the more symmetric D_{2d} point group and complexes **7 - 9** ($\text{Dy}^{\text{III}} - \text{Yb}^{\text{III}}$) by C_{2v} (Section 2.3.3.2). The lower symmetry for the $\{\text{LnCu}_3(\text{H}_2\text{pdte})_3\}$ series will increase the significance of transversal magnetic anisotropy relative to the $\{\text{LnCu}_3(\text{H}_2\text{edte})_3\}$ series.¹⁷ Non-zero transversal anisotropy causes a mixing of m_J states of the same size (i.e. $\pm m_J$) which results in a higher probability of QTM occurring and hence an overall lowering of U_{eff} .^{18,19}

	Square	Triangular	Biaugmented	Biaugmented
	D_{4d}	D_{2d}	C_{2v}	C_{2v}
	SAPR-8	TDD-8	BTPR-8	JBTPR-8
11 (Y^{III})	3.021	2.547	<u>2.215</u>	2.831
12 (Pr^{III})	4.464	3.663	<u>3.481</u>	4.064
13 (Nd^{III})	4.179	3.468	<u>3.257</u>	3.941
14 (Eu^{III})	3.594	3.095	<u>2.811</u>	3.493
15 (Gd^{III})	3.308	2.840	<u>2.473</u>	3.235
16 (Tb^{III})	3.148	2.529	<u>2.326</u>	3.006
17 (Dy^{III})	3.167	2.581	<u>2.306</u>	2.953
18 (Ho^{III})	3.118	2.576	<u>2.244</u>	2.835
19 (Er^{III})	3.009	2.569	<u>2.166</u>	2.774
20 (Yb^{III})	2.961	2.609	<u>2.083</u>	2.664

Table 3.5: ChSM values for complexes **11** to **20**, with the lowest ChSM value for each are underlined. All complexes show a closest match to Biaugmented trigonal prismatic (C_{2v}) geometry.

	Square	Triangular	Biaugmented
	D_{4d}	D_{2d}	C_{2v}
	SAPR-8	TDD-8	BTPR-8
2 (Pr^{III})	3.991	<u>2.755</u>	2.862
3 (Nd^{III})	3.919	<u>2.664</u>	2.806
4 (Eu^{III})	3.494	<u>2.434</u>	2.483
5 (Gd^{III})	3.289	<u>2.313</u>	2.343
6 (Tb^{III})	3.160	<u>2.252</u>	2.280
7 (Dy^{III})	3.033	2.214	<u>2.197</u>
8 (Er^{III})	2.354	2.590	<u>1.762</u>
9 (Yb^{III})	2.586	2.143	<u>1.950</u>

Table 3.6: ChSM values for $\{\text{LnCu}_3(\text{H}_2\text{edte})_3\}$ series where $\text{Ln} = \text{Pr}^{\text{III}}$ (**2**), Nd^{III} (**3**), Eu^{III} (**4**), Gd^{III} (**5**), Tb^{III} (**6**), Dy^{III} (**7**), Er^{III} (**8**) and Yb^{III} (**9**). Lowest ChSM values are underlined.

SHAPE analyses of the Cu^{II} ions were also carried out and compared to the respective $\{\text{LnCu}_3(\text{H}_2\text{edte})_3\}$ analogues', the results for the Gd^{III} , Tb^{III} and Dy^{III} analogues are shown in Table 3.7. As expected considering the greater Ln^{III} distortion, the Cu^{II} crystal fields are

in general more distorted for the {LnCu₃(H₂pdte)₃} series – a direct result of the added flexibility of the H₂pdte²⁻ ligand relative to H₂edte²⁻.

	5 (Gd^{III})	15	6 (Tb^{III})	16	7 (Dy^{III})	17
Cu1	<u>1.442</u>	2.115	<u>1.456</u>	1.485	1.534	<u>1.307</u>
Cu2	<u>1.704</u>	1.79	<u>1.450</u>	1.924	<u>1.472</u>	1.942
Cu3	<u>1.599</u>	2.091	<u>1.563</u>	1.877	<u>1.602</u>	1.805

Table 7: *ChSM* values for square based pyramidal geometry for the Gd^{III}, Tb^{III} and Dy^{III} analogues of both series.

3.4 Magnetism

3.4.1 Static Magnetic Properties of $\{\text{GdCu}_3(\text{H}_2\text{pdt})_3\}$ (**15**)

The temperature dependent magnetic susceptibility of **15** was measured in a 1 kOe field in the temperature range 1.8 – 280 K (Figure 3.9). The χT value of $\approx 9.8 \text{ cm}^3 \text{ K mol}^{-1}$ at 280 K is in reasonable agreement with the calculated value of $9.12 \text{ cm}^3 \text{ K mol}^{-1}$ for a spin only system of non-interacting spins; one Gd^{III} ion ($s = 7/2$, $g_J = 2$) and three Cu^{II} ions ($s = 1/2$, $g = 2.1$).

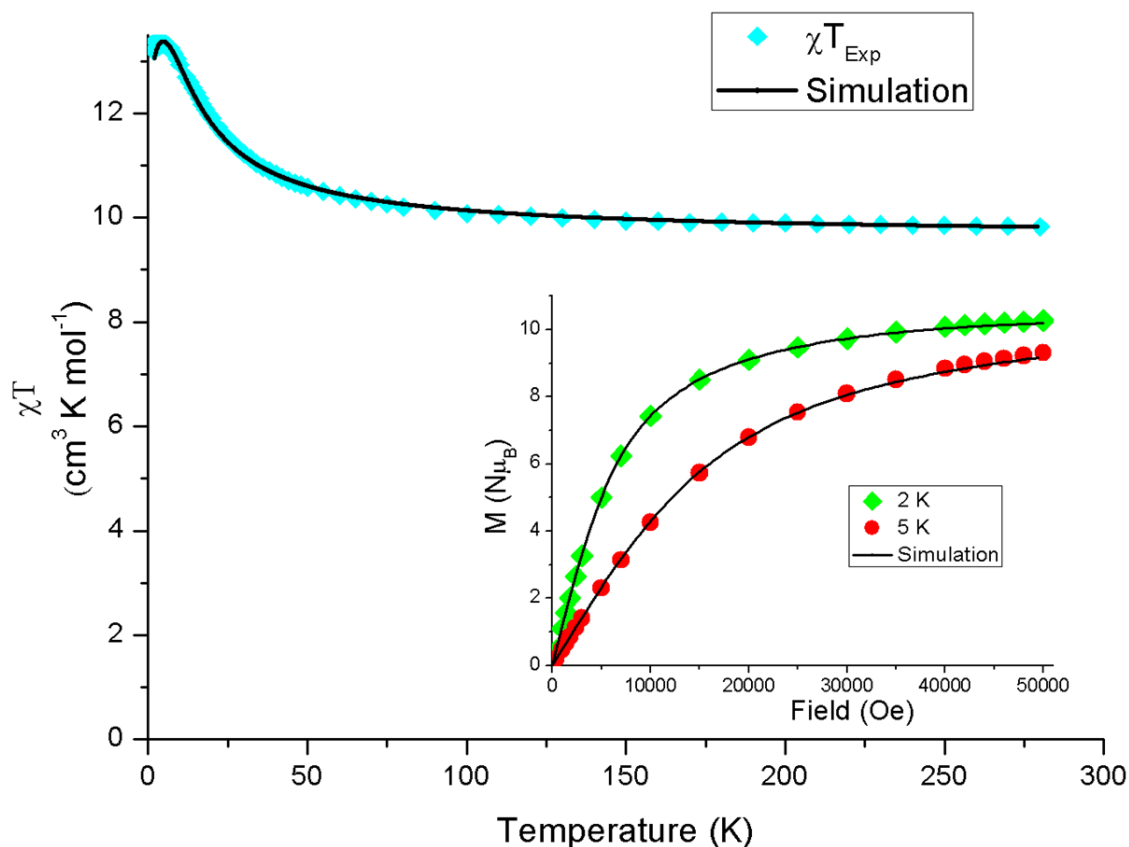


Figure 3.9: Dc magnetic susceptibility vs. temperature for **15** in a 1000 Oe dc field (light blue diamonds). Inset; M vs. H at 2 K (green diamonds) and 5 K (red circles) for **15**. Black lines represent data simulation using $g = 2.07$, $J_1 = 2.09 \text{ cm}^{-1}$ and $J_2 = -0.07 \text{ cm}^{-1}$.

Simulation calculated using the programme FIT-MART.²⁰

As T is lowered, χT steadily increases up to a maximum of $\chi T_{\text{max}} \approx 13.3 \text{ cm}^3 \text{ K mol}^{-1}$ at 5 K, indicative of ferromagnetic $\text{Gd}^{\text{III}}\text{-Cu}^{\text{II}}$ exchange. This is followed by a sharp downturn reaching a value of $\chi T \approx 12.7 \text{ cm}^3 \text{ K mol}^{-1}$ at 1.8 K. Magnetisation vs. field data for **15** was

collected at 2 and 5 K up to fields of 50 kOe (inset Figure 3.9). At 2 K, the magnetisation reaches $\approx 10.27 \text{ N}\mu_{\text{B}}$ at 50 kOe, indicating that the $S = 5$ state of the molecule is occupied under these conditions ($M_{\text{sat}} = gM_s$ for $g \approx 2$ and $M_s = 5$). A simulation of the χT vs. T and M vs. H data was calculated using the programme FIT-MART,²⁰ firstly using a one J model in the temperature range 280 – 10 K to compare with the fit for $\{\text{GdCu}_3(\text{H}_2\text{edte})_3\}$ (5). The one J model however could not adequately account for both the χT vs. T and M vs. H data, therefore a two J model (Figure 3.10) was adopted using the spin only Hamiltonian shown in Equation 3.1.

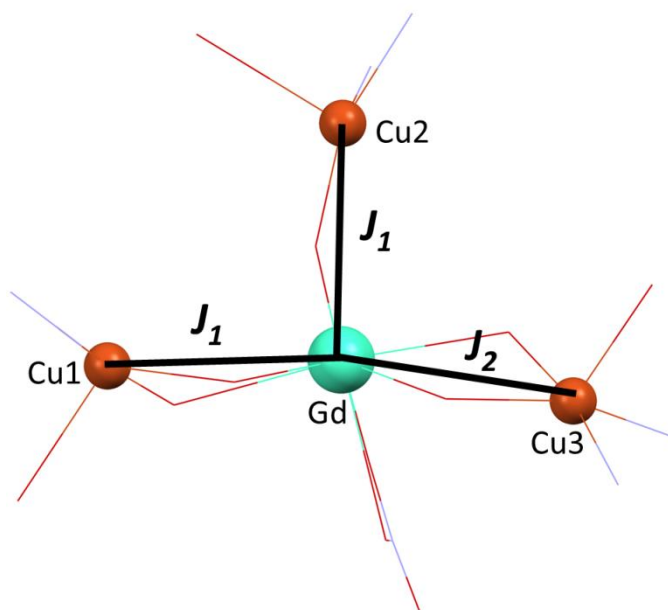


Figure 3.10: Illustration of two J model used to simulate the χT vs. T and M vs. H data for 15.

$$\hat{H} = -2J_1(\vec{S}_{\text{Gd}} \cdot \vec{S}_{\text{Cu}_1} + \vec{S}_{\text{Gd}} \cdot \vec{S}_{\text{Cu}_2}) - 2J_2(\vec{S}_{\text{Gd}} \cdot \vec{S}_{\text{Cu}_3}) + g\mu_B\vec{H} \left(\vec{S}_{\text{Gd}} + \sum_{i=1}^3 \vec{S}_{\text{Cu}_i} \right)$$

Equation 3.1

A simulation using $J_1 = 2.09 \text{ cm}^{-1}$ and $J_2 = -0.07 \text{ cm}^{-1}$ (negative J values indicate antiferromagnetic exchange) with an isotropic g -value of 2.07 gave a good correlation with the data (Figure 3.9). The magnitude of g is sensible considering that for the respective single ions; $g_{\text{Gd}} = 2$ and $g_{\text{Cu}} = 2.1$ (FIT-MART only uses one g -value for the whole system). The magnitudes of the exchange parameters are similar to those found for previously reported $\text{Gd}^{\text{III}}\text{-Cu}^{\text{II}}$ complexes.²¹⁻²⁴ The nature of the exchange interactions are concurrent with the expected exchange interactions due to the $\text{Gd}^{\text{III}}\text{-O-O-Cu}^{\text{II}}$ torsion angles θ (Section

3.3.2.1); θ angles in the $\approx 140 - 180^\circ$ range are expected to facilitate ferromagnetic $\text{Gd}^{\text{III}}\text{-Cu}^{\text{II}}$ exchange, with angles between $\approx 150 - 140^\circ$ resulting in borderline ferromagnetic/antiferromagnetic exchange.¹¹⁻¹³ The θ angles in **15** are 165.78° , 161.06° and 151.68° , therefore a ferromagnetic J_1 and a weakly antiferromagnetic J_2 appears reasonable. The ground state of **15** was calculated by FIT-MART as $S = 4$, with the $S = 5$ excited state lying only $\approx 0.35 \text{ cm}^{-1}$ above in energy. Therefore the downturn in the χT vs. T data below 5 K is at least partly due to the $S = 4$ state becoming dominantly populated over the $S = 5$ state, it could also be due to intermolecular antiferromagnetic interactions. The static magnetic data of **5** (Figure 3.11, with results from the one J model used in Section 2.4.5) was revisited using the two J model; however the low temperature ($< 10 \text{ K}$) χT vs. T data could not be adequately simulated.

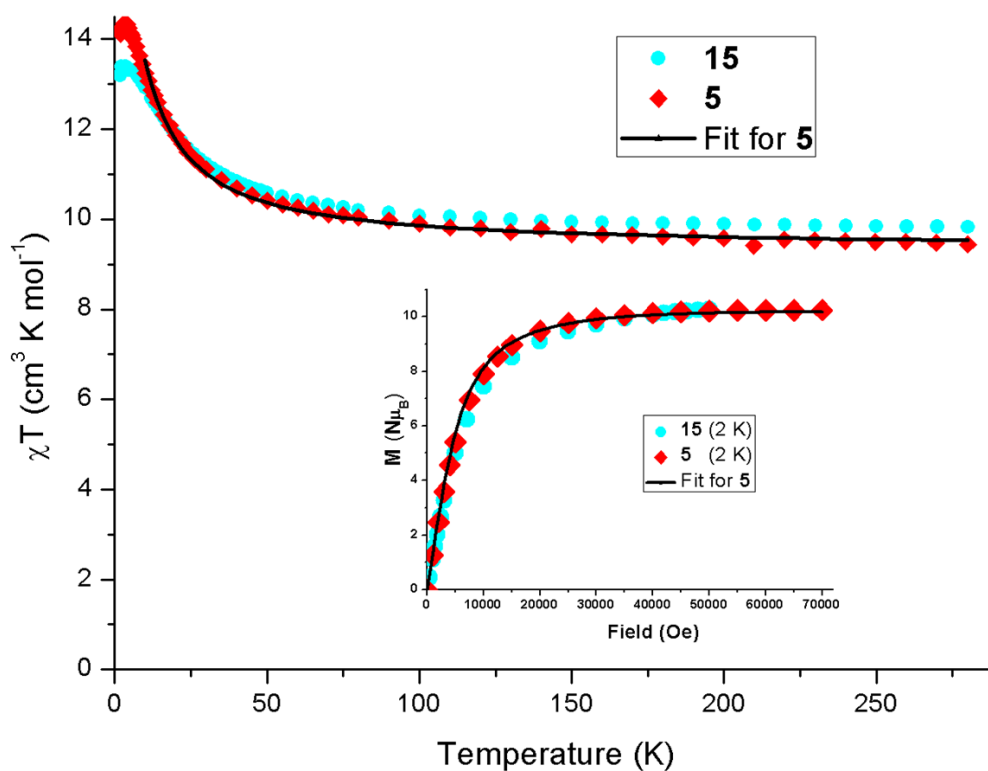


Figure 3.11: Comparison of dc susceptibility and M vs. H data (2 K) for **5** (red diamonds) and **15** (light blue circles). The fit calculated for **5** using a one J model in Chapter 2 (Section 2.4.5) is shown as a black line which gave $J = 2.9(3) \text{ cm}^{-1}$, $g = 2.0(4)$ and a ground state $S = 5$.

When a combination of antiferromagnetic and ferromagnetic exchange constants were used, the simulated χT values were too low between 1.8 - 5 K, and using only ferromagnetic exchange constants resulted in no downturn to 1.8 K. The torsion angles (Table 3.8) used to rationalise the χT data for **15** suggest that for **5** there should perhaps be two stronger

Gd^{III}-Cu^{II} ferromagnetic interactions and one stronger antiferromagnetic interaction compared to **15**, however this could not be shown by simulation.

5	15
150.72°	151.68°
164.88°	161.06°
165.84°	165.78°

Table 3.8: Torsion angles in **5** and **15**. Angles in the 140-180° range are expected to facilitate ferromagnetic Gd^{III} – Cu^{II} exchange with a transition to antiferromagnetic at $\approx 140 - 150^\circ$.¹¹⁻¹³

Intermolecular interactions are likely to be stronger in **5** compared to **15** due to the former having the shortest ion-ion distances in the crystal lattice (Table 3.9). However, further work would be needed to show whether these interactions are ferromagnetic or antiferromagnetic. This would include synthesising magnetically dilute samples of **5** and **15** and comparing their magnetic data with the respective non-dilute complexes’.

	5	15
Gd···Gd	8.52 Å	8.57 Å
Gd···Cu	6.06 Å	7.95 Å
Cu···Cu	4.75 Å	5.32 Å

Table 3.9: Shortest intermolecular ion-ion distances in **5** and **15**.

In summary, the differences in static magnetic properties cannot be rationalised just by considering the torsion angles and predicted 3d-4f exchange. Further work is needed to investigate the differences in intermolecular interactions by measuring the magnetic properties of magnetically dilute samples of **5** and **15**. A more complex model with more *J* variables (up to six) could be used to simulate/fit the magnetic data, however the simulation/fit would be less meaningful due to the increased number of parameters. Ideally DFT calculations should be performed on both complexes to calculate which orbitals are interacting and what the nature of the magnetic exchange interactions are.

3.4.2 Static Magnetic Properties of $\{\text{TbCu}_3(\text{H}_2\text{pdte})_3\}$ (16)

The temperature dependent magnetic susceptibility of **16** was measured in a 1 kOe field in the temperature range 1.8 – 300 K (Figure 3.12). The room temperature χT value of $\approx 13.65 \text{ cm}^3 \text{ K mol}^{-1}$ is reasonable compared to the calculated value of $13.05 \text{ cm}^3 \text{ K mol}^{-1}$ for a system of non-interacting spins; one Tb^{III} ion ($^7\text{F}_6$, $S = 3$, $L = 3$, $J = 6$, $g_J = 3/2$) and three Cu^{II} ions ($s = 1/2$, $g = 2.1$).

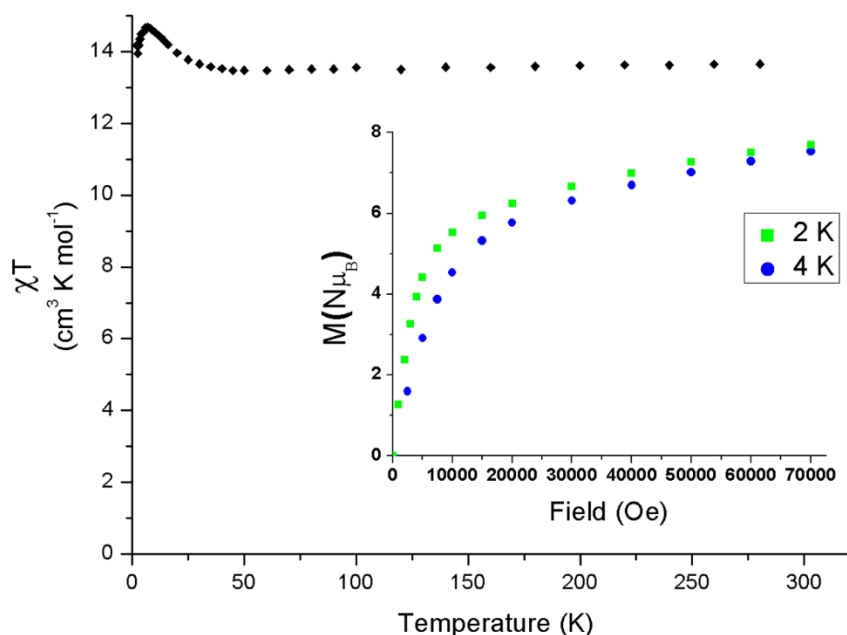


Figure 3.12: Dc magnetic susceptibility vs. temperature for **16** in a 1 kOe dc field. Inset; magnetisation vs. field at 2 and 4K.

On lowering the temperature, χT stays roughly constant, reaching a minimum of $13.47 \text{ cm}^3 \text{ K mol}^{-1}$ at 45 K, followed by a sharp upturn; reaching a χT_{max} of $14.7 \text{ cm}^3 \text{ K mol}^{-1}$ at $\approx 7 \text{ K}$ indicative of ferromagnetic Tb^{III} - Cu^{II} exchange. The same upturn was observed in $\{\text{TbCu}_3(\text{H}_2\text{edte})_3\}$ (**6**). Ln^{III} - Cu^{II} ferromagnetic exchange is expected for Ln^{III} ions with $f > 7$ due to their negative spin-orbit coupling constant.¹¹ A negative spin-orbit coupling constant has the effect of cooperatively aligning the Ln^{III} ion's orbital and spin moments, therefore, if the spins of the Ln^{III} ion and Cu^{II} ion were initially ferromagnetic then the resultant interaction is ferromagnetic for $f > 7$ Ln^{III} ions and antiferromagnetic for $f < 7$ Ln^{III} ions - assuming the spin-spin interaction is unaltered throughout the series (Figure 3.13).²⁵

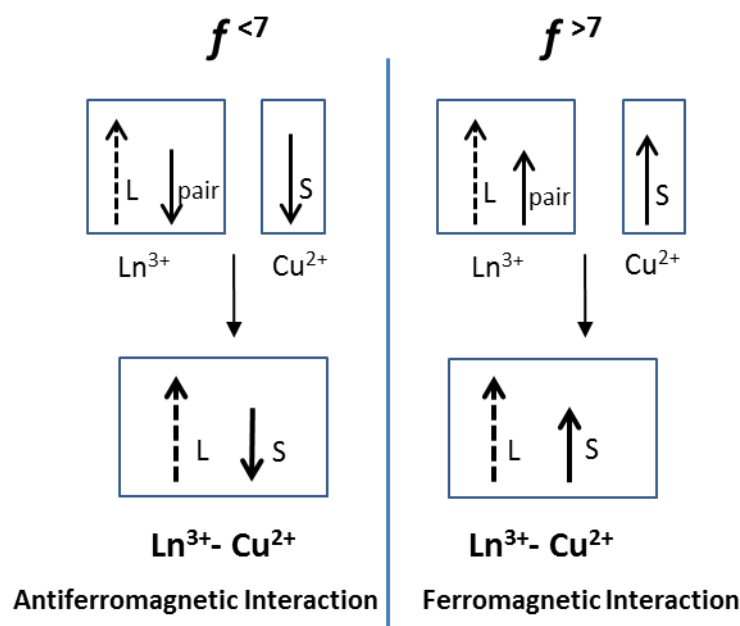


Figure 3.13: Schematic representation of magnetic interactions of Ln^{III} and Cu^{II} ions depending on f -electron count. It is assumed that the spin-spin interaction is unaltered throughout the series. Adapted from ref. 11.

Between 7 – 1.8 K there is a downturn in χT for **16**, reaching $14.18 \text{ cm}^3 \text{ K mol}^{-1}$ at 1.8 K, no downturn was observed for **6**. This could be due to the presence of $\text{Tb}^{\text{III}}\text{-Cu}^{\text{II}}$ antiferromagnetic exchange in **16** which is not present in **6**. Considering the $\text{Tb}^{\text{III}}\text{-O-O-Cu}^{\text{II}}$ torsion angles (Table 3.10), **16** has two angles which are clearly in the ferromagnetic range ($\approx 140\text{-}180^\circ$) and one on the edge of the antiferromagnetic range ($< \approx 140^\circ$), whereas **6** has all three in the ferromagnetic range. Having an antiferromagnetic interaction will result in cancellation of Cu^{II} spins and consequentially a ground state with a smaller magnetic moment compared to **6** (Figure 3.14). The downturn could also be due in part to intermolecular antiferromagnetic interactions.

6	16
150.98°	138.64°
164.80°	163.86°
166.11°	163.38°

Table 3.10: Comparison of the torsion angles between **6** and **16**.

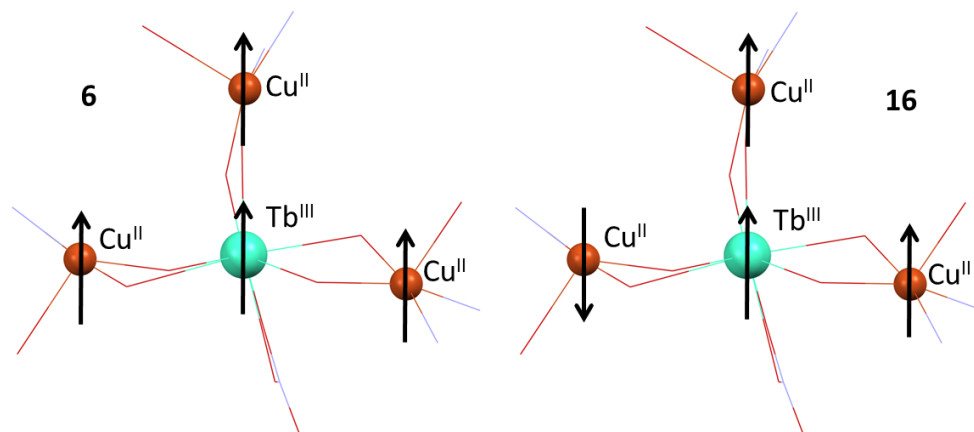


Figure 3.14: Schematic representation of the magnetic moments of the constituent ions of **6** (left) and **16** (right). In **6**, all moments are aligned ferromagnetically, leading to a ground state with a higher magnetic moment compared to **16** where two of the Cu^{II} spins effectively cancel.

Magnetisation vs. dc field measurements at 2 and 4 K were made for **16** (Figure 3.15). Even at 2 K, the magnetisation does not reach the expected saturation value of $12 N\mu_{\text{B}}$, as expected for a molecule with strong magnetic anisotropy. Comparing the M vs. H data to **6** (Figure 3.15), it appears that the magnetisation of **6** will eventually saturate at a higher value compared to **16**. This could indicate that the ground Tb^{III} m_J sublevel for **16** is ± 5 instead of ± 6 , the latter shown by INS as the Tb^{III} ground state in **6**. However, without measuring to higher fields, it is impossible to say if they will saturate at different values. Further work, such as INS measurements could be used to conclusively prove the ground m_J state of Tb^{III} .

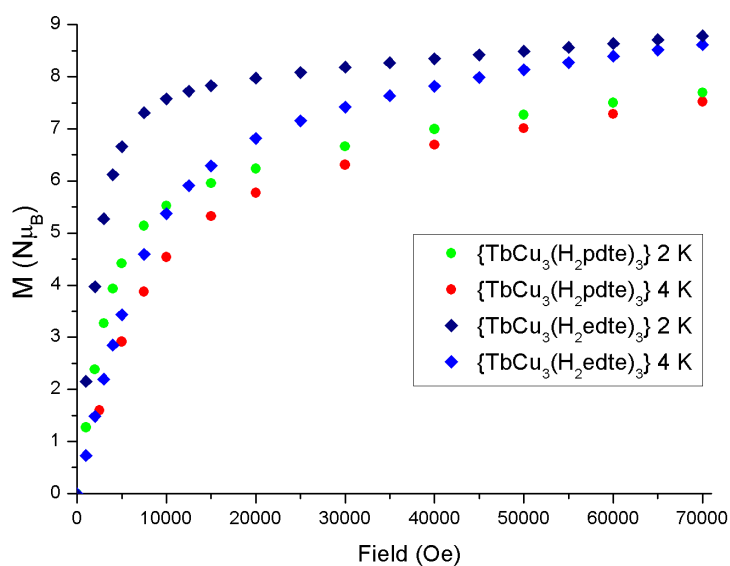


Figure 3.15: Comparison of M vs. H curves at 2 and 4 K for **16** and **6**.

3.4.3 Dynamic Magnetic Properties of **16**

Ac susceptibility measurements were carried out to investigate if **16** exhibited slow magnetic relaxation at low temperatures. Measurements were made down to 2 K at 957 Hz firstly without an applied dc field (data not shown) and then with a 1000 Oe dc field (Figure 3.16).

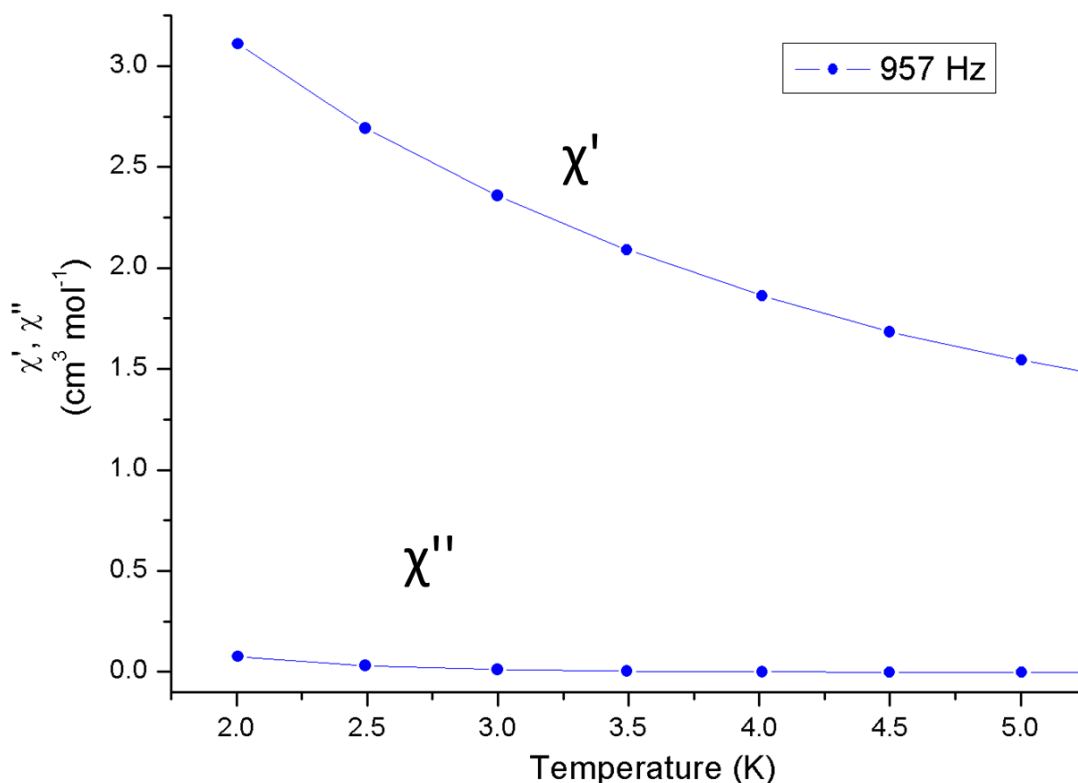


Figure 3.16: Ac susceptibility measurements at 957 Hz for **16** in a 1 kOe dc field with in-phase susceptibility (upper) and out-of-phase susceptibility (lower).

Either with, or without a dc field, there was no significant increase in χ'' or decrease in χ' down to 1.8 K – indicative of no slow relaxation. In contrast, **6** showed well defined χ'' maxima above 2 K with zero applied dc field, with a 12% increase in U_{eff} when the dc field was applied (Section 2.4.9).

The ac data clearly shows that **6** exhibits slow relaxation due to a significant energy barrier to magnetic relaxation in zero dc field, whereas **16** does not. A possible explanation for the better performance of **6** comes from considering the differences in magnetic exchange interactions and the results of the INS experiments on **6** which showed that the energy required to flip one Cu^{II} spin correlated with the energy barrier to relaxation. This suggests that complexes with Cu^{II} spins which are harder to flip would have larger energy barriers.

In **6**, all $\text{Tb}^{\text{III}} - \text{Cu}^{\text{II}}$ exchange interactions are ferromagnetic; evidenced by INS (Section 2.5.1) and the torsion angles.¹¹⁻¹³ In **16** however, one of the torsion angles is at the edge of the ferromagnetic range. This could mean that one exchange interaction is either weakly antiferromagnetic or weakly ferromagnetic,¹² in either case, the energy required to flip a Cu^{II} spin in **16** would be less compared to **6**. If the interaction is ferromagnetic, the weakness of the exchange interaction with this Cu^{II} ion could act as a ‘weak link’ to relaxation. If the exchange interaction is antiferromagnetic, it would still be easier to flip a Cu^{II} spin in **16** due to the diminished intrinsic field experienced by the Cu^{II} spins.²⁶ In **6**, all three Cu^{II} spins are aligned together; intrinsically reinforcing each other. However, when only 2/3 spins are co-aligned, the intrinsic field is diminished and there would be less energy required to flip one of the remaining spins. Another contributing factor to the performance difference could be due to the slightly more distorted ligand field in **16**. An increased distortion away from axially will reduce energy gaps between the lowest lying M_{tot} states.²⁷⁻²⁹ Also, the shift from D_{2d} (**6**) to the less symmetric C_{2v} (**16**) would result in greater transverse magnetic anisotropy in **16** and a resulting increase in QTM.³⁰

3.4.4 Static Magnetic Properties of $\{\text{DyCu}_3(\text{H}_2\text{pdte})_3\}$ (**17**)

Temperature dependent magnetic susceptibility was measured for **17** in the range 2 – 300 K in a 1 kOe dc field (Figure 3.17). The room temperature χT value of $16.2 \text{ cm}^3 \text{ K mol}^{-1}$ is reasonable compared to the calculated value of $15.4 \text{ cm}^3 \text{ K mol}^{-1}$ for four non-interacting ions: one Dy^{III} ion (${}^6\text{H}_{15/2}$, $S = 5/2$, $L = 5$, $J = 15/2$, $g_J = 4/3$) and three Cu^{II} ions ($s = 1/2$, $g = 2.1$).

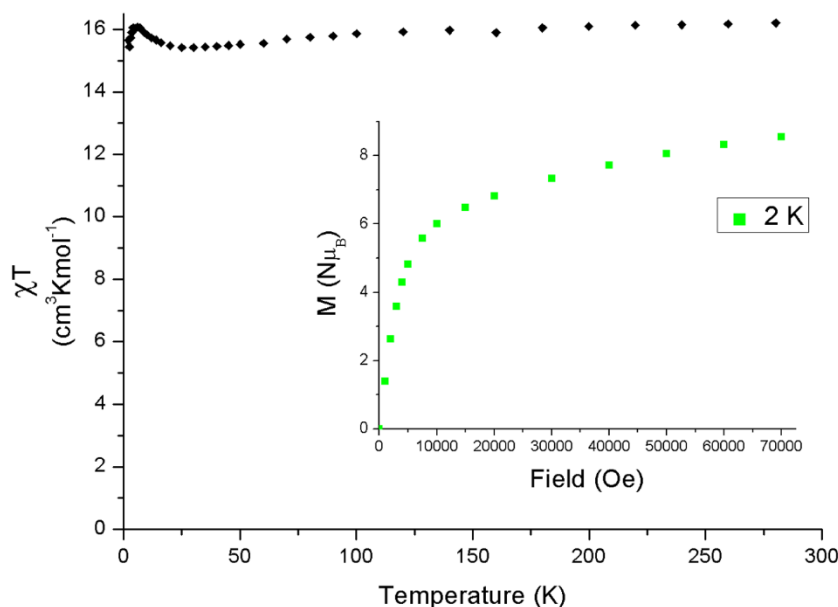


Figure 3.17: Dc magnetic susceptibility vs. temperature for **17** in a 1 kOe dc field. Inset; magnetisation vs. field at 2 K.

As the temperature decreases down to 30 K, χT decreases gradually down to $15.4 \text{ cm}^3 \text{ K mol}^{-1}$ due to depopulation of excited M_{tot} states. On further cooling there is an upturn in χT , reaching a χT_{max} of $16.1 \text{ cm}^3 \text{ K mol}^{-1}$ at 6 K, indicative of ferromagnetic $\text{Dy}^{\text{III}}\text{-Cu}^{\text{II}}$ exchange. Ferromagnetic $\text{Dy}^{\text{III}}\text{-Cu}^{\text{II}}$ exchange was also observed in $\{\text{DyCu}_3(\text{H}_2\text{edte})_3\}$ (**7**) and is expected for $\text{Dy}^{\text{III}}\text{-Cu}^{\text{II}}$ ion pairings with $\text{Dy}^{\text{III}}\text{-O-O-Cu}^{\text{II}}$ torsion angles between $140\text{-}180^\circ$ (Table 3.11 for θ angles). Cooling further to 1.8 K, χT decreases for **17** down to a minimum of $15.6 \text{ cm}^3 \text{ K mol}^{-1}$; no downturn was observed for **7**. The downturn is probably due to the presence of antiferromagnetic $\text{Dy}^{\text{III}}\text{-Cu}^{\text{II}}$ interactions (Figure 3.18) – whereas for **7** the $\text{Dy}^{\text{III}}\text{-Cu}^{\text{II}}$ exchange interactions were all shown to be ferromagnetic by INS (Section 2.5.2).

7	17
150.94°	139.61°
165.04°	163.41°
166.24°	163.78°

Table 3.11: Comparison of the torsion angles between **7** and **17**.

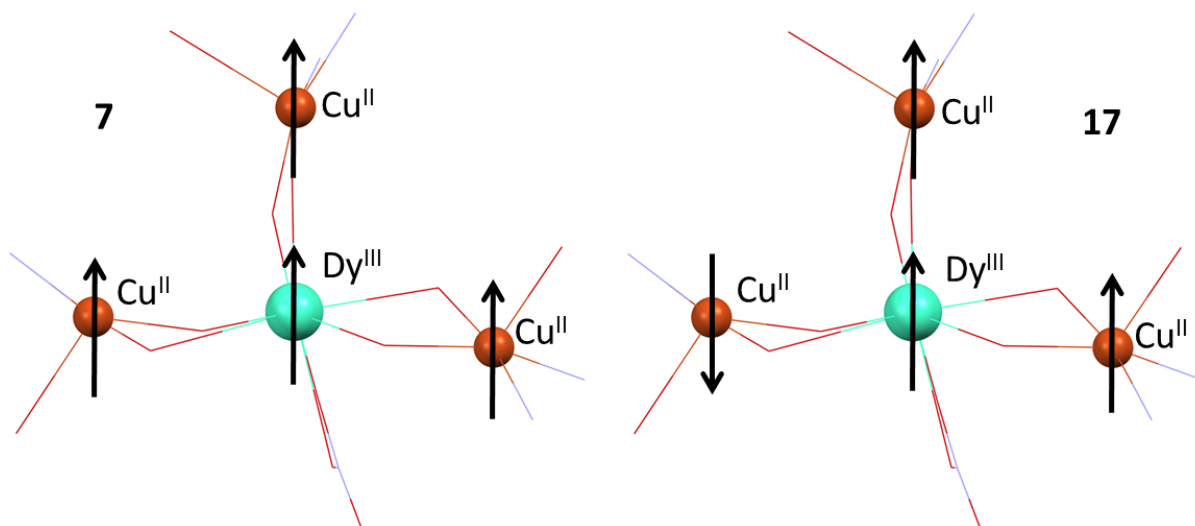


Figure 3.18: Schematic representation of the magnetic moments of the constituent ions of **7** (left) and **17** (right). In **6** all moments are aligned ferromagnetically, leading to a ground state with a higher magnetic moment compared to **16** where two of the Cu^{II} spins effectively cancel.

Magnetisation vs. field at 2 K was measured for **17** up to fields of 70 kOe (inset Figure 3.17). The magnetisation reaches $8.5 \text{ N}\mu_{\text{B}}$ at 70 kOe but does not saturate at the expected $13 \text{ N}\mu_{\text{B}}$; indicative of significant magnetic anisotropy. Comparing the M vs. H measurements for **7** and **17** (Figure 3.19), the magnetisation of **17** is slightly higher at 70 kOe. One possible reason could be that the ground Dy^{III} m_J sublevel in **17** is $15/2$ instead of $13/2$, the latter shown by INS as the ground Dy^{III} sublevel in **7**. The higher m_J value would eventually result in a higher saturation magnetisation for **17**, however, INS measurements would be needed to verify this.

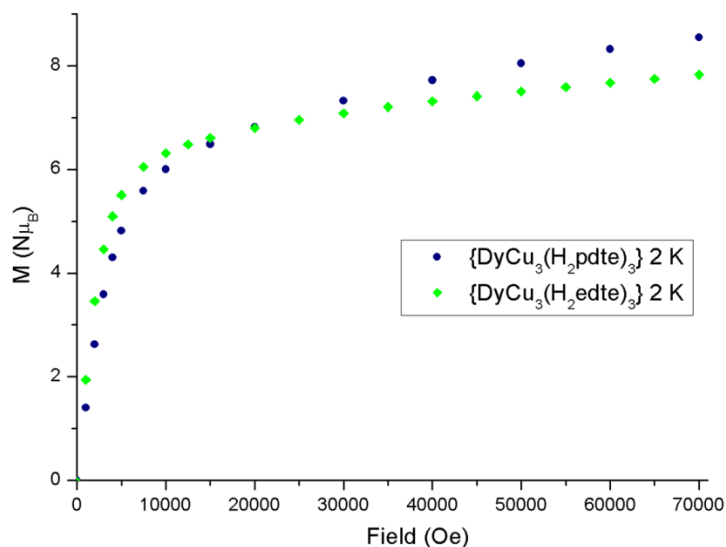


Figure 3.19: Comparison of M vs. H curves at 2 K for **7** and **17**.

3.4.5 Dynamic Magnetic Properties of **17**

Ac susceptibility measurements were carried out to investigate if **17** exhibited slow magnetic relaxation at low temperatures. Measurements were made down to 2 K at 957 Hz firstly without an applied dc field (data not shown) and then with a 1 kOe dc field (Figure 3.20).

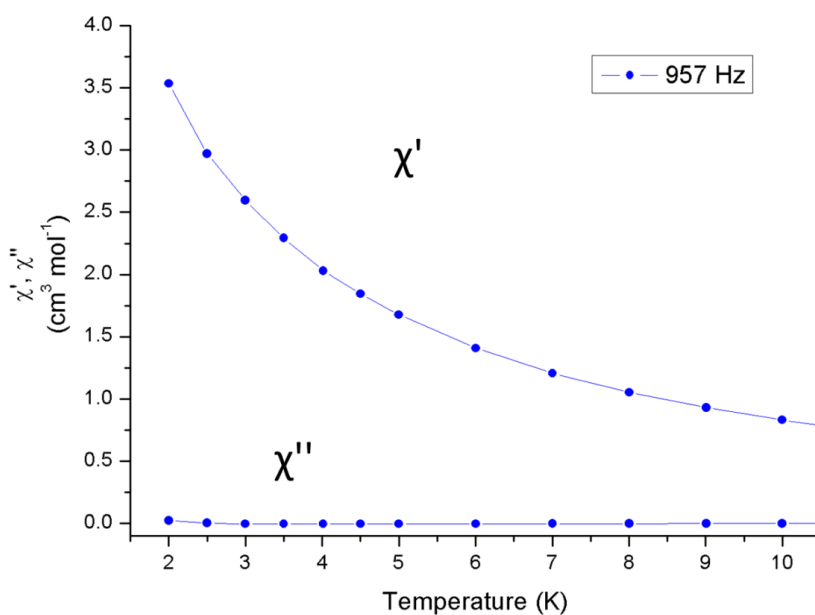


Figure 3.20: Ac susceptibility measurements at 957 Hz for **17** in a 1 kOe dc field with in-phase (upper) and out-of-phase (bottom) susceptibility.

Either with, or without a dc field, there was no significant increase in χ'' or decrease in χ' down to 1.8 K – indicative of no slow relaxation. Complex **7** only showed the onset of χ'' signals without an applied dc field but showed well defined χ'' maxima above 2 K when the dc field was applied. As for the Tb^{III} analogues (Section 3.4.2), the difference in behaviour between the Dy^{III} analogues can be accounted for by weakened $\text{Dy}^{\text{III}} - \text{Cu}^{\text{II}}$ exchange resulting in a lower energy barrier to flip a Cu^{II} spin - which was correlated to the magnitude of U_{eff} by INS for the $\{\text{LnCu}_3(\text{H}_2\text{edte})_3\}$ series (Section 2.5.2).

3.5 Conclusions and Future Work

The ligand H_4pdte was successfully synthesised and utilised to form ten new $\{\text{LnCu}_3(\text{H}_2\text{edte})_3\}$ complexes ($\text{Ln} = \text{Y}^{\text{III}}$ (**11**), Pr^{III} (**12**), Nd^{III} (**13**), Eu^{III} (**14**), Gd^{III} (**15**), Tb^{III} (**16**), Dy^{III} (**17**), Ho^{III} (**18**), Er^{III} (**19**) and Yb^{III} (**20**)) analogous to the related $\{\text{LnCu}_3(\text{H}_2\text{edte})_3\}$ series. The ten new complexes were characterised using single crystal X-ray diffraction, CHN and IR. At the time of writing there were no examples in the CSD of any complex containing the H_xpdte ligand ($x = 0-4$). The crystal structures show that each analogue crystallises in the triclinic space group $P-1$, and share a similar unit cell structure to the $\{\text{LnCu}_3(\text{H}_2\text{edte})_3\}$ series'. Complexes **15**, **16** and **17** were also characterised magnetically and their data compared to their respective $\{\text{LnCu}_3(\text{H}_2\text{edte})_3\}$ analogues (**5**, **6** and **7** respectively). The χT vs. T and M vs. H data for **15** were simulated using a two J model which gave a ground $S = 4$ state with a 1st excited $S = 5$ state only 0.35 cm^{-1} above, $g = 2.07$, $J_1 = 2.09 \text{ cm}^{-1}$ and $J_2 = -0.07 \text{ cm}^{-1}$. The results are comparable to the fit for the static magnetic properties of **5** (Section 2.4.5) – ground state $S = 5$, $g = 2.0(4)$ and $J = 2.0(4) \text{ cm}^{-1}$. Unfortunately the one J model could not provide an acceptable simulation for the static magnetic properties of **15**, and the two J model could not accurately simulate the low temperature χT data ($< 10 \text{ K}$) for **5**. To provide a more accurate comparison of **5** and **15**, further work is needed to find a model with more J parameters (up to six). Intermolecular interactions also need to be investigated by measuring the magnetic properties of magnetically dilute samples of **5** and **15**. Ideally DFT calculations should be performed on both complexes to calculate which orbitals are interacting and what the nature of the magnetic exchange interactions are.

Complexes **16** and **17** both exhibited a decrease in χT at low temperatures ($< 6 \text{ K}$), whereas **6** and **7** did not; indicative of the presence of antiferromagnetic $\text{Ln}^{\text{III}}-\text{Cu}^{\text{II}}$ exchange in **16** and **17**. Comparison of the M vs. H data for **16** and **6** suggested that the ground Tb^{III} m_J

sublevel in **16** could be ± 5 instead of ± 6 (as seen in **6**), however INS measurements would be needed to conclusively prove this. Conversely, the comparison of **17** and **7** suggested that the ground Dy^{III} m_J sublevel could be $15/2$ instead of $13/2$ (as seen in **7**). Again however INS measurements would be needed for proof. Ac-susceptibility measurements showed no out-of-phase signals for **16** or **17**, indicating that neither are SMMs – in contrast to **6** and **7**. Overall, $\text{H}_2\text{pdte}^{2-}$ induced a more distorted central Ln^{III} local crystal field and reduced the $\text{Ln}^{\text{III}}\text{-O-O-Cu}^{\text{II}}$ torsion angles relative to the $\{\text{LnCu}_3(\text{H}_2\text{edte})_3\}$ series.

3.6 References

- (1) F. J. Kettles, V. A. Milway, F. Tuna, R. Valiente, L. H. Thomas, W. Wernsdorfer, S. T. Ochsenbein, M. Murrie, *Inorg. Chem.* 53 (2014) 8970-8978.
- (2) J.D. Rinehart, J.R. Long, *Chem. Sci.* 2 (2011) 2078–2085.
- (3) J. J. Baldoví, J. M. Clemente-Juan, E. Coronado, Y. Duan, A. Gaita-Arino, C. Giménez-Saiz, *Inorg. Chem.* 53 (2014) 9976–9980.
- (4) J. J. Baldoví, S. Cardona-Serra, J. M. Clemente-Juan, E. Coronado, A. Gaita-Arino, A. Palií, *Inorg. Chem.* 51 (2012) 12565-12574.
- (5) L. R. Piquer, E. C. Sañudo, *Dalton Trans.* 44 (2015) 8771–8780.
- (6) H. L. C. Feltham, Y. Lan, F. Klöwer, L. Ungur, L. F. Chibotaru, A. K. Powell, S. Brooker, *Chem. Eur. J.* 17 (2011) 4362-4365.
- (7) H. L. C. Feltham, F. Klöwer, S. A. Cameron, Y. Lan, M. Tropiano, S. Faulkner, A. K. Powell, S. Brooker, *Dalton Trans.* 40 (2011) 11425-11432.
- (8) H. L. C. Feltham, R. Clerac, A. K. Powell, S. Brooker, *Inorg. Chem.* 50 (2011) 4232-4234.
- (9) H. L. C. Feltham, R. Clerac, L. Ungur, V. Vieru, L. F. Chibotaru, A. K. Powell, S. Brooker, *Inorg. Chem.* 51 (2012) 10603-10612.
- (10) H. L. C. Feltham, R. Clerac, L. Ungur, L. F. Chibotaru, A. K. Powell, S. Brooker, *Inorg. Chem.* 52 (2013) 3236-3240.
- (11) C. Benelli, D. Gatteschi, *Chem. Rev.* 102 (2002) 2369 – 2387.
- (12) J. Cirera, E. Ruiz, *C. R. Chimie.* 11 (2008) 1227-1234.
- (13) J. P. Costes, F. Dahan, A. Dupuis, *Inorg. Chem.* 39 (2000) 5994-6000.
- (14) B. Spingler, P.M. Antoni, *Chem. Eur. J.* 13 (2007) 6617 – 6622.
- (15) H. E. Gottlieb, V. Kotlyar, A. Nudelman, *J. Org. Chem.* 62 (1997) 7512 – 7515.
- (16) M. Llunell, D. Casanova, J. Cirera, P. Alemany, S. Alvarez, ‘SHAPE: Program for the Stereochemical Analysis of Molecular Fragments by Means of Continuous Shape Measures and Associated Tools’, Version 2.1, 2013, Barcelona.
- (17) L. Ungur, L. F. Chibotaru, *Phys. Chem. Chem. Phys.* 13 (2011) 20086-20090.
- (18) J. Tang, P. Zhang, *Lanthanide Single-Molecule Magnets*, Springer (2015).
- (19) D. Gatteschi, R. Sessoli and J. Villain, *Molecular Nanomagnets*, Oxford University Press, (2006).
- (20) L. Engelhardt, S. C. Garland, C. Rainey, R. A. Freeman, *Physic Procedia* 53 (2014) 39-45.

- (21) I. Ramade, O. Kahn, Y. Jeannin, F. Robert, *Inorg. Chem.* 36 (1997) 930-936.
- (22) M. Ryazanov, V. Nikiforov, F. Lloret, M. Julve, N. Kuzmina, A. Gleizes, *Inorg. Chem.* 41 (2002) 1816-1823.
- (23) C. Brewer, G. Brewer, W. R. Scheidt, M. Shang, E. E. Carpenter, *Inorg. Chim. Acta* 313 (2001) 65-70.
- (24) M. Sasaki, H. Horiuchi, M. Kumagai, M. Sakamoto, H. Sakiyama, Y. Nishida, Y. Sadaoka, M. Ohba, H. Okawa, *Chem. Lett.* (1998) 911-912.
- (25) M. L. Kahn, C. Mathoniere, O. Kahn, *Inorg. Chem.* 38 (1999) 3692-3697.
- (26) S. Blundell, *Magnetism in Condensed Matter* (2001), Oxford University Press, ISBN: 978-0-19-850591-4
- (27) H. L. C. Feltham, S. Brooker, *Coord. Chem. Rev.* 276 (2014) 1-33.
- (28) N. Ishikawa, M. Sugita, T. Ishikawa, S. Koshihara, Y. Kaizu, *J. Am. Chem. Soc.* 125 (2003) 8694-8695.
- (29) N. Ishikawa, M. Sugita, T. Ishikawa, S. Koshihara and Y. Kaizu, *J. Phys. Chem. B* 108 (2004) 11265-11271.
- (30) D. Gatteschi, R. Sessoli, *Angew. Chem. Int. Ed.* 42 (2003) 268-297.

4. Synthesis, Structure and Magnetic Properties of a {Ln₄Zn₂} Series with H₄edte

4.1 Introduction

The use of Zn^{II} in 3d-4f single-molecule magnet (SMM) research is usually as a diamagnetic substitute for paramagnetic 3d ions in 3d-4f complexes so that the magnetic properties of only the 4f component can be studied.¹ This is of particular use in complexes with only one Ln^{III} ion as it enables the direct study of the Stark sublevel energies of the Ln^{III} ion without the added complication of 3d-4f exchange. Most research toward the synthesis of 3d-4f SMMs is directed at inclusion of paramagnetic 3d ions,²⁻⁴ especially those exhibiting high ground state spin and uniaxial magnetic anisotropy such as Mn^{III}. Combining these types of 3d ions with Ln^{III} ions (such as Tb^{III} and Dy^{III}) has resulted in a number of new SMMs. However, alignment of anisotropy axes has to be perfect otherwise the overall complex magnetocrystalline anisotropy quickly diminishes.^{5,6} Using Zn^{II} ions which have no magnetic moment or magnetic anisotropy avoids this complication. A more important factor which determines the magnitude of the magnetic anisotropy in Ln^{III} containing species is the crystal field of the Ln^{III} ion.⁷⁻¹⁰ It is well known that for single Ln^{III} ions with oblate 4f-electron density (Tb^{III}, Dy^{III}, Ho^{III}, Pr^{III} and Nd^{III}), large uniaxial magnetic anisotropy can be generated in axial crystal fields, with square antiprismatic (SAP) crystal fields^{10,11} being a good example. Therefore ligands capable of generating such geometries have received much interest; a good example being acac ligands in the synthesis of Dy^{III} single-ion magnets (SIMs).^{8,12-14} An application of Zn^{II} with this respect is to use it as part of a metalloligand subunit with appropriate geometry which can form potentially generate axially symmetric crystal fields around a central Ln^{III} ion.¹⁵ Another consideration is to design crystal fields with high symmetry such as $C_{\infty v}$, $D_{\infty h}$, S_8 , D_{4d} , D_{5h} or D_{6d} which theoretically block quantum tunnelling of the magnetisation (QTM).⁹ These high symmetry crystal fields eliminate higher order terms in the crystal field Hamiltonian for Ln^{III} species which causes the wavefunctions of different spin states to overlap – promoting QTM. A good example of this is a {DyZn₂} complex synthesised by Tong *et al.*¹⁶ which had a central Dy^{III} ion with approximate D_{5h} crystal field symmetry (Figure 4.1). The complex, full formula [Zn₂DyL₂(MeOH)][NO₃]·3MeOH·H₂O (where L = 2,2',2''-(((nitrioltris(ethane-2,1-diyl))tris(azanediyl))tris(methylene))tris-(4-bromophenol)) exhibited a large energy barrier to magnetic reorientation (U_{eff}) of 305 cm⁻¹ in zero applied

dc field. Interestingly, when the coordinating MeOH ligand was lost, U_{eff} became negligible due to a change to quasi- O_h local symmetry around Dy^{III} .

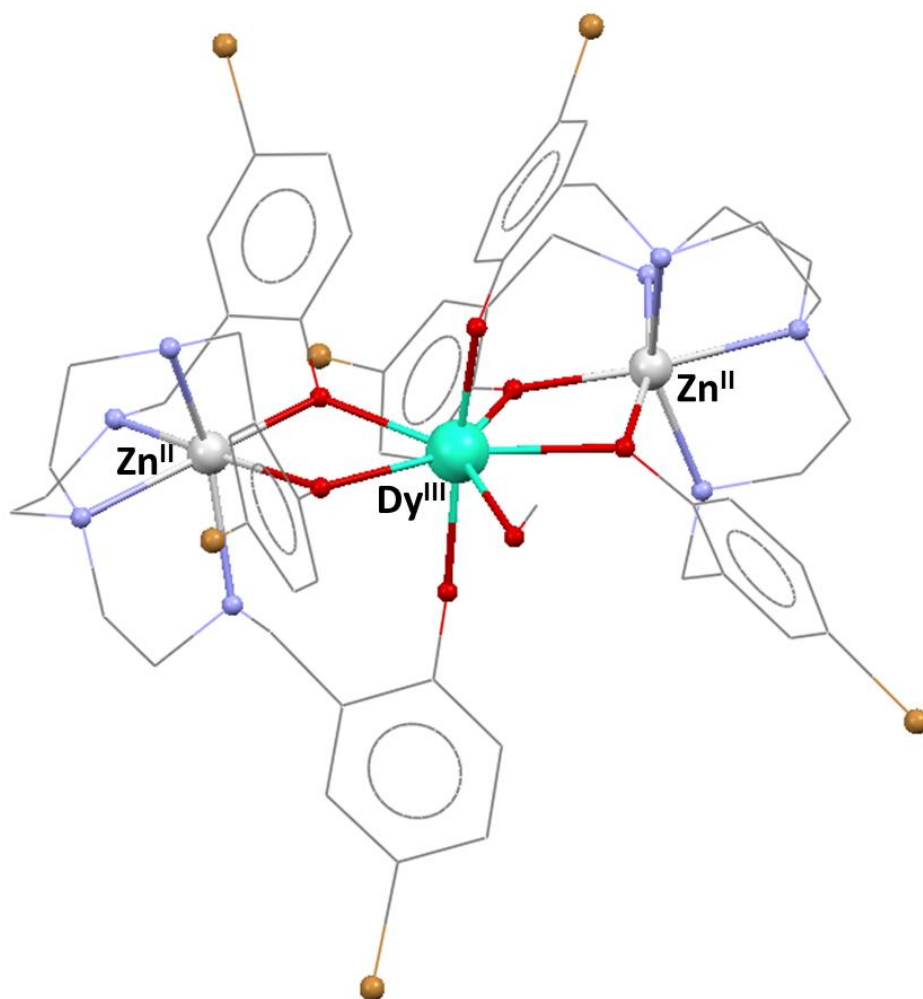


Figure 4.1: The molecular structure of Tong *et al.*'s $\{Dy^{III}Zn^{II}_2\}$ SIM with coordinated MeOH. The Zn^{II} ions form metalloligand subunits which coordinate to the central Dy^{III} ion – generating the local D_{5h} crystal field symmetry. Atom colours: Dy^{III} , turquoise; Br, orange; O, red; N, blue; C, grey; Zn^{II} , silver. CSD ref. code: HIBMAI.

The majority of Zn^{II} -4f nanomagnets are so called SIMs as they only contain one Ln^{III} ion.¹⁷⁻²³ As well as Dy^{III} ,¹⁵⁻¹⁸ there are also examples of Zn^{II} -4f nanomagnets with Tb^{III} ,¹⁹ Er^{III} ,^{20,21} Yb^{III} ,^{21,22} and interestingly Ce^{III} .²³ There are also Zn^{II} -4f SMMs reported with more than one Ln^{III} ion,²⁴⁻²⁹ however, these are far fewer compared to Zn^{II} -4f SIMs. Dy^{III} is the predominant ion, with examples of $\{Dy_6Zn_6\}$ ²⁴ $\{Dy^{III}_3Zn^{II}\}$ ²⁵ and $\{Dy^{III}_2Zn^{II}_2\}$ ²⁶⁻²⁹ structural motifs and a $\{Dy^{III}_2Zn^{II}_2\}$ cubane.³⁰ There are also field induced $\{Tb^{III}_2Zn^{II}_2\}$ ²⁷ and $\{Yb^{III}_2Zn^{II}_2\}$ ³¹ SMMs reported.

The work detailed in this chapter was conducted to synthesise new Zn^{II}-Ln^{III} molecular nanomagnets with the ligand H₄edte. It was assumed that the Zn^{II} ion would be chelated by the ligand to form metalloligand subunits which would bind to either one or multiple Ln^{III} centres. The result was a new 7-membered family of {Ln^{III}₄Zn^{II}₂} complexes where Ln^{III} = Eu^{III}, Gd^{III}, Tb^{III}, Dy^{III}, Ho^{III}, Er^{III} and Yb^{III}. Crystal structures for all but the Ho^{III} analogue are presented. Magnetic data was collected for the Gd^{III} and Dy^{III} analogues, the latter displaying the onset of slow magnetic relaxation in ac-susceptibility measurements down to 1.8 K both with and without an applied dc field.

4.2 Experimental

4.2.1 Synthesis of [Eu^{III}₄Zn^{II}₂(OH)₂(H₂edte)₄(NO₃)₂Cl₂(MeOH)₂][NO₃]₂ (**21**)

To a stirred solution of H₄edte (0.13 g, 0.55 mmol) and NEt₃ (0.14 ml, 1 mmol) in 30 ml MeOH was added Zn(NO₃)₂·6H₂O (0.19 g, 0.64 mmol). The reaction was heated to 90°C for two hours then EuCl₃·6H₂O (0.10 g, 0.27 mmol) was added and the reaction heated for a further 4 hours. The reaction was then allowed to cool to room temperature and filtered to isolate a white precipitate of **21**, yield = 35% (0.05 g). The mother liquor was placed in a loosely capped vial for slow evaporation, from which small colourless plates of **21** suitable for X-ray diffraction formed over the next few weeks. A suitable match of CHN data for the precipitate could not be obtained, nor could a match be obtained for the crystals; this is discussed in section 4.3.1. IR spectra of the precipitate and crystals were a match; precipitate selected IR data (cm⁻¹): 3568.43 (w), 3475.84 (w), 3300 (br), 2964.69 (w), 2856.67 (w), 2710.08 (w), 1629.90 (w), 1456.30 (m), 1365.65 (m), 1329.00 (m), 1301.99 (s), 1259.56 (m), 1236.41 (w), 1176.62 (w), 1157.33 (w), 1143.83 (w), 1124.54 (w), 1070.53 (s), 1035.81 (m), 1012.66 (m), 995.30 (w), 977.94 (w), 914.29 (m), 923.93 (m), 887.28 (m), 875.71 (m), 827.49 (w), 817.85 (w), 717.54 (m), 611.45 (m)

4.2.2 Synthesis of [Gd^{III}₄Zn^{II}₂(OH)₂(H₂edte)₄(NO₃)₂Cl₂(MeOH)₂][NO₃]₂ (22)

To a stirred solution of H₄edte (0.13 g, 0.55 mmol) and NEt₃ (0.14 ml, 1 mmol) in 30 ml MeOH was added ZnCl₂ (0.09 g, 0.66 mmol). The reaction was heated to 90°C for two hours then Gd(NO₃)₃·6H₂O (0.11 g, 0.25 mmol) was added and the reaction heated for a further 4 hours. The reaction was then allowed to cool to room temperature and filtered. The mother liquor was placed in a loosely capped vial for slow evaporation, from which small colourless plates of **22** suitable for X-ray diffraction formed over the next few weeks. Precipitate of **22** can be synthesised in the same manner but instead using H₄edte (0.12 g, 0.50 mmol), NEt₃ (0.14 ml, 1 mmol), ZnCl₂ (0.03 g, 0.22 mmol) and Gd(NO₃)₃·6H₂O (0.22 g, 0.5 mmol), yield = 43% (0.1 g). Analysis of crystals and precipitate are a good match. Crystals are hygroscopic, analysing as **22**·4.5H₂O (Gd₄Zn₂C₄₂H₁₀₇N₁₂O_{36.5}Cl₂), analysis (%) calc. (found): C 22.98 (22.64) H 4.91 (4.55) N 7.66 (7.39). Selected IR data (cm⁻¹): 3570.36 (w), 3475.84 (w), 3300 (br), 2964.69 (w), 2893.32 (w), 2858.60 (w), 2712.01 (w), 1631.83 (w), 1456.30 (m), 1365.65 (m), 1301.99 (s), 1261.49 (m), 1176.62 (w), 1157.33 (w), 1143.83 (w), 1124.54 (w), 1070.53 (s), 1035.81 (m), 1012.66 (m), 995.30 (w), 977.94 (w), 923.93 (m), 914.29 (m), 887.28 (m), 875.71 (m), 827.49 (w), 817.85 (w), 719.47 (m), 611.45 (m).

4.2.3 Synthesis of [Tb^{III}₄Zn^{II}₂(OH)₂(H₂edte)₄(NO₃)₂Cl₂(MeOH)₂][NO₃]₂ (23)

To a stirred solution of H₄edte (0.13 g, 0.55 mmol) and NEt₃ (0.14 ml, 1 mmol) in 30 ml MeOH was added ZnCl₂ (0.09 g, 0.66 mmol). The reaction was heated to 90°C for two hours then Tb(NO₃)₃·5H₂O (0.11 g, 0.25 mmol) was added and the reaction heated for a further 4 hours. The reaction was then allowed to cool to room temperature and filtered. The mother liquor was placed in a loosely capped vial for slow evaporation, from which small colourless plates of **23** suitable for X-ray diffraction formed over the next few days. Precipitate of **23** can be synthesised in a similar manner to the crystals but instead using H₄edte (0.12 g, 0.50 mmol), NEt₃ (0.14 ml, 1 mmol), ZnCl₂ (0.03 g, 0.22 mmol) and Tb(NO₃)₃·5H₂O (0.22 g, 0.5 mmol), yield = 79 % (0.19 g). A suitable CHN match was not obtained for the crystals (see section 4.3.1), IR data for crystals and precipitate were a match. Precipitate is hygroscopic, analysing as **23**·5.5H₂O (Tb₄Zn₂C₄₂H₁₀₉N₁₂O_{37.5}Cl₂), analysis (%) calc. (found): C 22.73 (22.33) H 4.95 (4.55) N 7.57 (7.37). Selected IR data

(cm⁻¹): 3566.50 (w), 3479.70 (w), 3300 (br), 2966.62 (w), 2891.39 (w), 2862.46 (w), 1626.05 (w), 1471.74 (m), 1458.23 (m), 1367.58 (m), 1330.93 (m), 1303.92 (s), 1261.49 (m), 1236.14 (w), 1157.33 (w), 1143.83 (w), 1126.47 (w), 1070.53 (s), 1055.10 (s), 1012.66 (m), 995.30 (w), 977.94 (w), 925.86 (m), 916.22 (m), 902.72 (m), 895.00 (m), 887.28 (m), 875.71 (m), 827.49 (w), 817.85 (w), 732.33 (m), 613.38 (m).

4.2.4 Synthesis of [Dy^{III}₄Zn^{II}₂(OH)₂(H₂edte)₄(NO₃)₂Cl₂(MeOH)₂][NO₃]₂ (24)

To a stirred solution of H₄edte (0.13 g, 0.55 mmol) and NEt₃ (0.14 ml, 1 mmol) in 30 ml MeOH was added ZnCl₂ (0.09 g, 0.66 mmol). The reaction was heated to 90°C for two hours then Dy(NO₃)₃·xH₂O (0.11g, 0.25 mmol) was added and the reaction heated for a further 6 hours. The reaction was then allowed to cool to room temperature and filtered. The mother liquor was placed in a loosely capped vial for slow evaporation, from which small colourless plates of **24** suitable for X-ray diffraction formed over the next few days. Precipitate of **24** can be synthesised in a similar manner, but instead using H₄edte (0.12 g, 0.50 mmol), NEt₃ (0.14 ml, 1 mmol), ZnCl₂ (0.03 g, 0.22 mmol) and Dy(NO₃)₃·xH₂O (0.22 g, 0.5 mmol), yield = 47% (0.11 g). A suitable CHN match was not obtained for the crystals. IR data of precipitate and crystals were a match. Precipitate is hygroscopic, analysing as **24**·6.50H₂O, (Dy₄Zn₂C₄₂H₁₁₂N₁₂O_{39.5}Cl₂), analysis (%) calc. (found): C 22.34 (21.91) H 4.99 (4.56) N 7.25 (7.44). Selected IR data (cm⁻¹): 3564.57 (w), 3483.56 (w), 3300 (br), 2964.69 (w), 2893.32 (w), 2862.46 (w), 2712.01 (w), 1635.69 (w), 1458.23 (m), 1367.58 (m), 1305.85 (s), 1261.49 (m), 1234.48 (w), 1157.33 (w), 1143.83 (w), 1126.47 (w), 1072.46 (s), 1055.1 (s), 1039.67 (m), 1012.66 (m), 995.3.0 (w), 977.94 (w), 918.15 (m), 896.93 (m), 887.28 (m), 877.64 (m), 827.49 (w), 817.85 (w), 725.26 (m), 617.24 (m).

4.2.5 Synthesis of [Ho^{III}₄Zn^{II}₂(H₂edte)₄(NO₃)₂Cl₂(MeOH)₂(OH)₂][NO₃]₂ (25)

To a stirred solution of H₄edte (0.12 g, 0.50 mmol) and NEt₃ (0.14 ml, 1 mmol) in 30 ml MeOH was added ZnCl₂ (0.03 g, 0.22 mmol). The reaction was heated to 90°C for two hours then Ho(NO₃)₃·5H₂O (0.22 g, 0.50 mmol) was added and the reaction heated for a further 6 hours. The reaction was then allowed to cool to room temperature and filtered to isolate a pink precipitate of **25**, yield = 78% (0.19 g). The mother liquor was placed in a

loosely capped vial, from which no crystals of **25** were isolated. Precipitate is hygroscopic, analysing as **25**·7H₂O (Ho₄Zn₂C₄₂H₁₁₂N₁₂O₃₉Cl₂), analysis (%) calc. (found): C 22.22 (21.73) H 4.97 (4.54) N 7.40 (7.20). Selected IR data (cm⁻¹): 3364.57 (w), 3485.49 (w), 3300 (br), 2966.62 (w), 2895.25 (w), 2862.46 (w), 2712.01 (w), 2362.88 (w), 2332.02 (w), 1635.69 (w), 1464.02 (m), 1367.58 (m), 1305.85 (s), 1261.49 (m), 1159.26 (w), 1143.83 (w), 1126.47 (w), 1072.46 (s), 1055.10 (s), 1039.67 (m), 1012.66 (m), 976.01 (w), 920.08 (m), 900.79 (m), 887.28 (m), 827.49 (w), 815.92 (w), 734.90 (m), 617.24 (m).

4.2.6 Synthesis of [Er^{III}₄Zn^{II}₂(H₂edte)₄(NO₃)₂Cl₂(MeOH)₂(OH)₂][NO₃]₂ (**26**)

To a stirred solution of H₄edte (0.13 g, 0.55 mmol) and NEt₃ (0.14 ml, 1 mmol) in 30 ml MeOH was added ZnCl₂ (0.03g, 0.66 mmol). The reaction was heated to 90°C for two hours then Er(NO₃)₃·5H₂O (0.11g, 0.25 mmol) was added and the reaction heated for a further 4 hours. The reaction was then allowed to cool to room temperature and filtered. The mother liquor was placed in a loosely capped vial for slow evaporation, from which small light pink plates of **26** suitable for X-ray diffraction formed over the next few weeks. Precipitate of **26** can be synthesised in a similar manner but instead using H₄edte (0.12 g, 0.50 mmol), NEt₃ (0.14 ml, 1 mmol), ZnCl₂ (0.03 g, 0.22 mmol) and Er(NO₃)₃·5H₂O (0.22 g, 0.5 mmol), yield = 39 % (0.09 g). A suitable CHN match of the crystals could not be obtained. IR data for crystals and precipitate were a match. Precipitate is hygroscopic, analysing as **26**·6.5H₂O (Er₄Zn₂C₄₂H₁₁₁N₁₂O_{38.5}Cl₂), analysis (%) calc. (found): C 22.22 (21.72) H 4.97 (4.46) N 7.40 (7.52). Selected IR data (cm⁻¹): 3564.57 (w), 3485.49 (w), 3290 (br), 2951.19 (w), 2897.18 (w), 2862.46 (w), 2715.86 (w), 2343.59 (w), 1631.83 (w), 1464.02 (m), 1367.58 (m), 1305.85 (s), 1261.49 (m), 1159.26 (w), 1143.83 (w), 1126.47 (w), 1072.46 (s), 1055.10 (s), 1041.60 (m), 1012.66 (m), 995.30 (w), 977.94 (w), 922.00 (m), 900.79 (m), 887.287 (m), 827.49 (w), 815.92 (w), 736.83 (m), 717.54 (m), 667.39 (m), 619.17 (m).

4.2.7 Synthesis of [Yb^{III}₄Zn^{II}₂(OH)₂(H₂edte)₄(NO₃)₂Cl₂(MeOH)₂][NO₃]₂ (27)

To a stirred solution of H₄edte (0.13 g, 0.55 mmol) and NEt₃ (0.14 ml, 1 mmol) in 30 ml MeOH was added ZnCl₂ (0.03 g, 0.22 mmol). The reaction was heated to 90°C for two hours then Yb(NO₃)₃·5H₂O (0.22 g, 0.5 mmol) was added and the reaction heated for a further 4 hours. The reaction was then allowed to cool to room temperature and filtered to isolate a white precipitate of **27**, yield = 30% (0.08 g). The mother liquor was placed in a loosely capped vial for slow evaporation, from which small colourless plates of **27** suitable for X-ray diffraction formed over the next few weeks. A suitable CHN match for the crystals could not be obtained, IR data of the crystals and precipitate were a match. Precipitate is hygroscopic, analysing as **27**·7H₂O (Yb₄Zn₂C₄₂H₁₁₂N₁₂O₃₉Cl₂), analysis (%) calc. (found): C 21.87 (21.32) H 4.91 (4.36) N 7.29 (7.35). Selected IR data (cm⁻¹): 3560.71 (w), 3495.13 (w), 3300 (br), 2953.12 (w), 2899.11 (w), 2862.46 (w), 1631.83 (w), 1460.16 (m), 1369.50 (m), 1307.78 (s), 1261.41 (m), 1159.26 (w), 1143.83 (w), 1126.47 (w), 1074.39 (s), 1055.10 (s), 1041.60 (s), 1014.59 (m), 979.87 (w), 923.93 (m), 902.72 (m), 887.28 (m), 827.49 (w), 815.92 (w), 740.69 (m), 621.1 (m).

4.3 Results and Discussion

4.3.1 Synthesis

All {Ln₄Zn₂} series members, where Ln^{III} = Eu^{III} (**21**), Gd^{III} (**22**), Tb^{III} (**23**), Dy^{III} (**24**), Ho^{III} (**25**), Er^{III} (**26**) and Yb^{III} (**27**) were synthesised in one pot reactions using H₄edte, NEt₃ as base and simple metal salts with MeOH as solvent. Reacting H₄edte, NEt₃, ZnCl₂ and Ln(NO₃)₃·xH₂O in the molar ratio 0.55 : 1 : 0.66 : 0.25 produced single crystals for the Gd^{III}, Tb^{III}, Dy^{III} and Er^{III} analogues. Using the same reagents but in the molar ratios 0.5 : 1 : 0.22 : 0.5 produced precipitates of the Gd^{III}, Tb^{III}, Dy^{III}, Ho^{III}, Er^{III} and Yb^{III} analogues as well as single crystals of **27**. All crystals were grown by slow evaporation at room temperature of the MeOH mother liquor. Crystals of **21** were synthesised by reacting H₄edte, NEt₃, Zn(NO₃)₂·6H₂O and EuCl₃·6H₂O in the ratio 0.55:1:0.66:0.25 and again

allowing the mother liquor to evaporate at room temperature. Excluding **21**, CHN analysis of the precipitates of all compounds were a good match with the general formula obtained from single crystal X-ray diffraction. However, analysis of batches of single crystals only yielded a good match for $\{\text{Gd}_4\text{Zn}_2\}$. Batches of crystals harvested from the slowly evaporating mother liquors contained crystals of two morphologies; small colourless plates and non-single colourless crystallites. To reduce the percentage of non-single crystallites, batches were harvested shortly after crystalline solid began to appear. Analysis of multiple plates (> 10) per batch showed no discrepancy between unit cells of the plate-like crystals; matching those of the respective final structures. The crystallites could be separated from the plates under the microscope by hand, however, CHN analyses of these manually purified batches were still not a satisfactory match. Attempts to recrystallise the precipitates by slow evaporation of MeOH solutions of different starting concentrations were unsuccessful. Vapour diffusion of MeOH solutions of the complexes (of different starting concentrations) with Et_2O or THF were also unsuccessful. Single crystals of the Ho^{III} analogue were not isolated, however a pink precipitate which analyses as $\{\text{Ho}_4\text{Zn}_2\}$ by CHN, IR and PXRD (see Section 4.3.3) was obtained when the ratios 0.5 : 1 : 0.22 : 0.5 ($\text{H}_4\text{edte} : \text{NEt}_3 : \text{Ho}(\text{NO}_3)_3 : \text{ZnCl}_2$) were used. Attempts to synthesise the Y^{III} , La^{III} , Pr^{III} and Nd^{III} analogues were unfortunately unsuccessful. In each case an intractable gel was obtained from which no solid could be isolated.

4.3.2 Discussion of the $\{Ln^{III}_4Zn^{II}_2\}$ Series' Crystal Structure

The series $[Ln^{III}_4Zn^{II}_2(H_2edte)_4(NO_3)_2Cl_2(MeOH)_2(OH)_2][NO_3]_2$, where $Ln = Eu^{III}, Gd^{III}, Tb^{III}, Dy^{III}, Er^{III}$ and Yb^{III} , are all isostructural and crystallise in the monoclinic space group $P2_1/c$. The $\{Ln_4Zn_2\}$ molecule is best described as an incomplete face-fused dicubane with added Zn^{II} 'wings'. The $\{Ln_4Zn_2\}$ molecule is centrosymmetric, with an inversion centre between $Ln1$ and $Ln1a$ ($a = -x, 1-y, -z$) (see Figure 4.2).

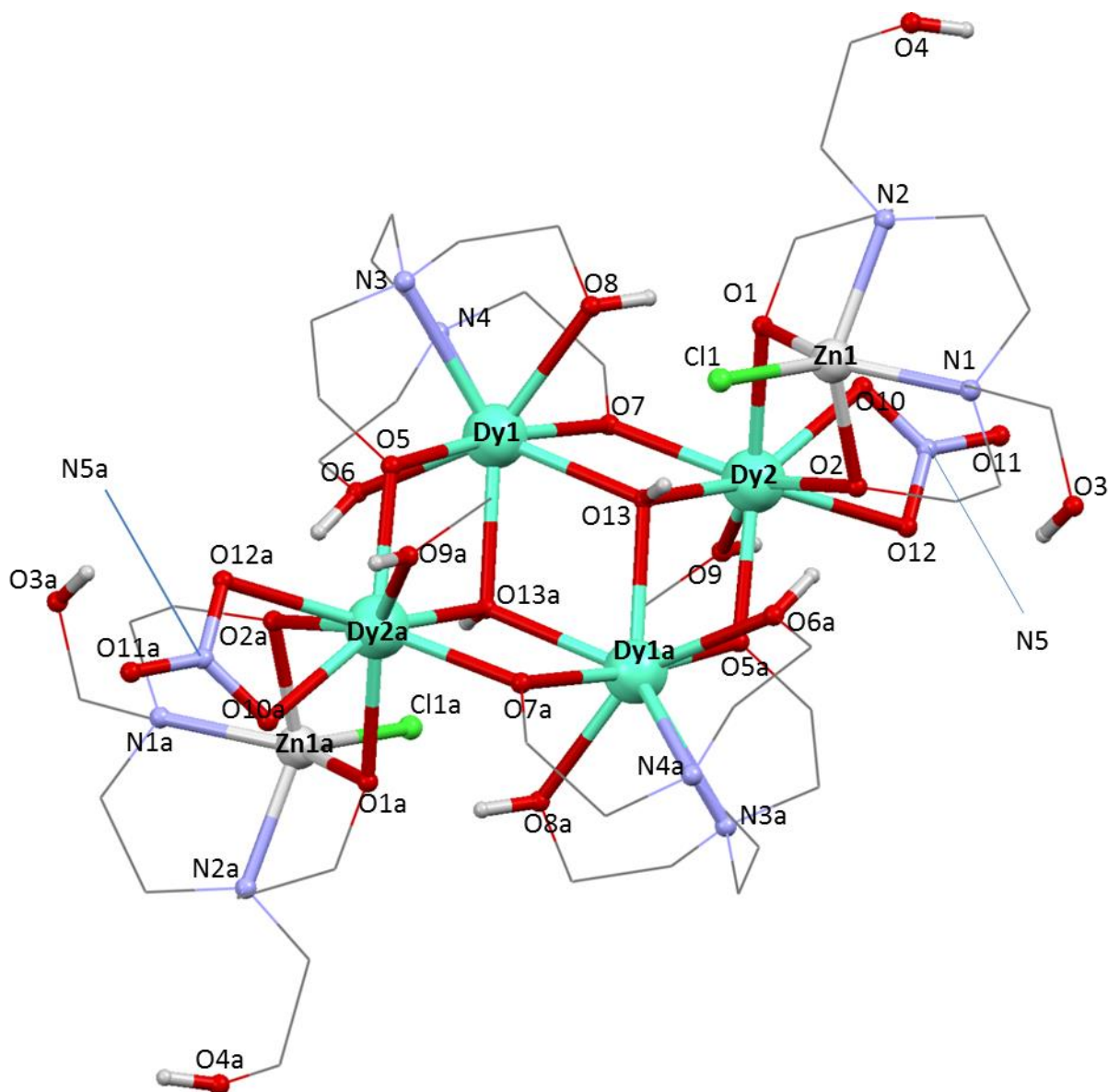


Figure 4.2: Molecular structure for $\{Dy_4Zn_2\}$, representative of entire series. C-H protons and lattice nitrates omitted. Atom colours: Light green, Dy^{III} ; silver, Zn^{II} ; red, O; blue, N; grey, C; green, Cl; and white, H. Symmetry relation; $a = (-x, 1-y, -z)$.

The 16+ charge of the metal ions is balanced by four H₂edte²⁻ ligands (-8), two chloride ions (-2), two OH⁻ groups (-2) and four nitrate ions; two as ligands and two in the lattice (-4). The asymmetric unit contains half of the {Ln₄Zn₂} complex molecule and two half occupied lattice nitrates, both nitrates lying adjacent to inversion centres. There are two distinct Ln^{III} environments (Ln1-2) within the asymmetric unit and one Zn^{II} environment (Zn1). Ln1 is chelated by a H₂edte²⁻ ligand and bridges to its symmetry equivalent Ln1a through two symmetry equivalent μ₃ hydroxyl groups (O13(H)). The four Ln^{III} ions sit in a plane, with the hydroxyl groups positioned just above and below (Figure 4.3). See Tables 4.2-4.4 for Ln-donor atom bond lengths and Table 4.5 for M-O-M (M = Ln^{III} or Zn^{II}) bond angles. For Ln1, the H₂edte²⁻ ligand acts as a {N₂O₄} donor set, with deprotonated alkoxo arms bridging to Ln2 through O5 and O7. The remaining arms, with atoms O6 and O8 remain protonated, forming hydrogen bonds to the alkoxo-arms of the H₂edte²⁻ ligand chelating Zn1 (O1 and O2). For all analogues, Ln1 is 8-coordinate and adopts a square antiprismatic (SAP) geometry as determined by SHAPE³² (see Table 4.1).

<i>Atom</i>	<i>Square antiprism D_{4d}</i>
Eu1	5.032
Eu2	2.005
Gd1	4.881
Gd2	1.923
Tb1	4.710
Tb2	1.778
Dy1	4.301
Dy2	1.823
Er1	4.537
Er2	1.774
Yb1	4.705
Yb2	1.676

Table 4.1: *ChSM values for closest matching geometry for both Ln^{III} ions in each complex.*

Both ions in all complexes are square antiprismatic with Ln1 more distorted than Ln2.

Ln2 is also 8-coordinate, SHAPE measurements show Ln2 in all analogues to be SAP and to be less distorted compared to Ln1. Ln2 bridges to Zn1 through O1 and O2, with a bidentate nitrate (O10 and O11) and a MeOH ligand (O9) completing Ln2's ligand field. Zn1 is 5-coordinate, with square based pyramidal coordination geometry and is chelated by a H₂edte²⁻ ligand. The ligand acts as a {N₂O₂} donor set, bridging Zn1 and Ln2 through O1 and O2, the remaining arms (O3 and O4) retaining their protons and extend into the lattice as unbound hydroxyethyl arms. Finally, Cl1 occupies the axial site on Zn1 and acts as a hydrogen bond acceptor to the hydroxyl group O13(H). There are two other intramolecular

hydrogen bonds between the protonated hydroxyethyl arms of the H_2edte^{2-} ligand on Ln1 and the deprotonated alkoxo arms of the H_2edte^{2-} ligand on Zn1 (see Figure 4.3).

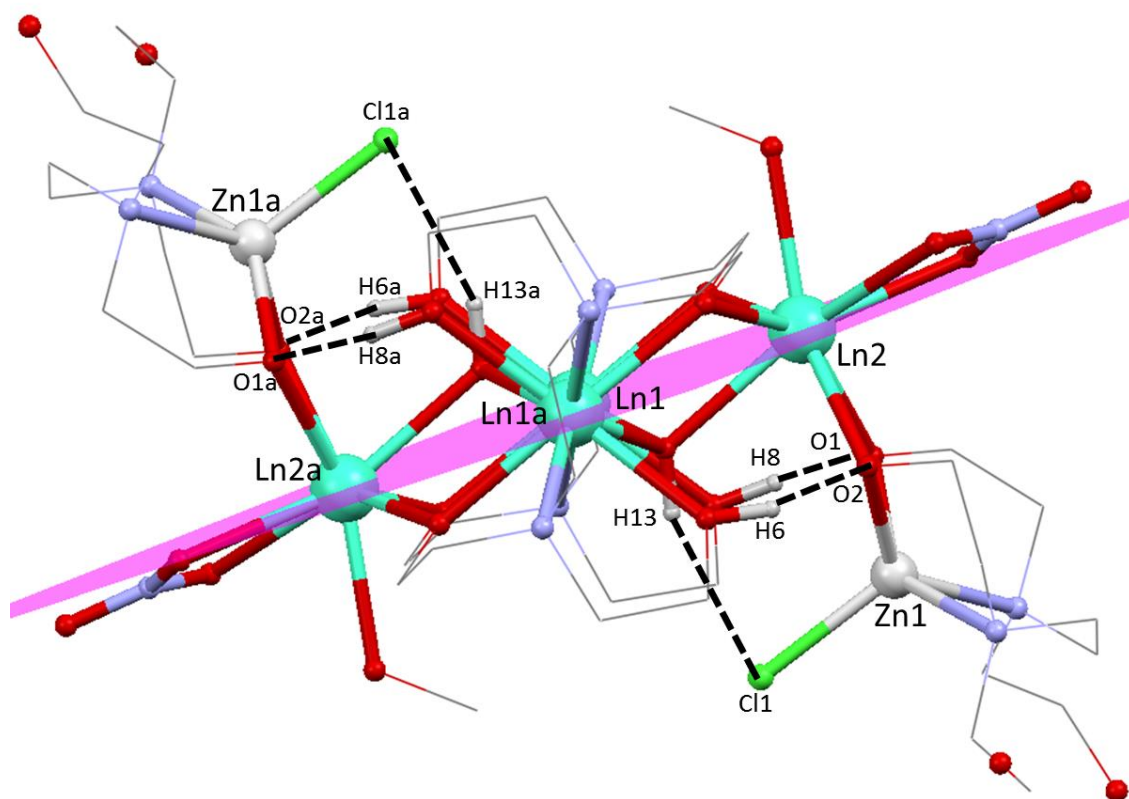


Figure 4.3: Molecular structure of $\{Ln_4Zn_2\}$ series depicting intramolecular H-bonding interactions (black dashed lines) and the plane of Ln^{III} ions (magenta plane). Only protons involved in intramolecular H-bonds are shown. Atom colours: Light green, Ln^{III} ; silver, Zn^{II} ; red, O; blue, N; grey, C; green, Cl; and white, H.

Bond	Distance (Å)	Bond	Distance (Å)	Bond	Distance (Å)	Bond	Distance (Å)
Eu1-O5	2.330(12)	Eu2-O1	2.443(13)	Gd1-O5	2.314(5)	Gd2-O1	2.429(5)
Eu1-O6	2.417(14)	Eu2-O2	2.425(12)	Gd1-O6	2.379(5)	Gd2-O2	2.406(5)
Eu1-O7	2.333(13)	Eu2-O5a	2.319(13)	Gd1-O7	2.303(5)	Gd2-O5a	2.293(5)
Eu1-O8	2.426(13)	Eu2-O7	2.306(13)	Gd1-O8	2.372(5)	Gd2-O7	2.281(5)
Eu1-O13	2.461(13)	Eu2-O9	2.478(13)	Gd1-O13	2.433(5)	Gd2-O9	2.456(6)
Eu1-O13a	2.453(13)	Eu2-O10	2.517(14)	Gd1-O13a	2.433(5)	Gd2-O10	2.517(5)
Eu1-N3	2.648(15)	Eu2-O12	2.527(12)	Gd1-N3	2.640(6)	Gd2-O11	2.515(7)
Eu1-N4	2.649(16)	Eu2-O13	2.410(13)	Gd1-N4	2.623(6)	Gd2-O13	2.427(5)

Table 4.2: Selected bond lengths in complexes **21** and **22**. $a = (-x, 1-y, -z)$

Bond	Distance (Å)	Bond	Distance (Å)	Bond	Distance (Å)	Bond	Distance (Å)
Tb1-O5	2.302(8)	Tb2-O1	2.411(8)	Dy1-O5	2.276(9)	Dy2-O1	2.387(10)
Tb1-O6	2.385(9)	Tb2-O2	2.382(8)	Dy1-O6	2.394(11)	Dy2-O2	2.371(10)
Tb1-O7	2.295(8)	Tb2-O5a	2.278(9)	Dy1-O7	2.277(9)	Dy2-O5a	2.253(9)
Tb1-O8	2.377(9)	Tb2-O7	2.261(8)	Dy1-O8	2.407(11)	Dy2-O7	2.257(9)
Tb1-O13	2.418(8)	Tb2-O9	2.445(9)	Dy1-O13	2.396(8)	Dy2-O9	2.416(11)
Tb1-O13a	2.404(8)	Tb2-O10	2.501(9)	Dy1-O13a	2.411(9)	Dy2-O10	2.486(11)
Tb1-N3	2.624(10)	Tb2-O11	2.520(10)	Dy1-N3	2.604(11)	Dy2-O11	2.496(11)
Tb1-N4	2.612(10)	Tb2-O13	2.417(8)	Dy1-N4	2.630(11)	Dy2-O13	2.402(9)

Table 4.3: Selected bond lengths in complexes **23** and **24**. $a = (-x, 1-y, -z)$

Bond	Distance (Å)	Bond	Distance (Å)	Bond	Distance (Å)	Bond	Distance (Å)
Er1-O5	2.263(7)	Er2-O1	2.367(8)	Yb1-O5	2.266(8)	Yb2-O1	2.324(8)
Er1-O6	2.318(8)	Er2-O2	2.384(8)	Yb1-O6	2.315(8)	Yb2-O2	2.350(8)
Er1-O7	2.279(8)	Er2-O5a	2.220(8)	Yb1-O7	2.242(7)	Yb2-O5a	2.212(8)
Er1-O8	2.333(8)	Er2-O7	2.225(8)	Yb1-O8	2.321(8)	Yb2-O7	2.220(8)
Er1-O13	2.394(7)	Er2-O9	2.394(10)	Yb1-O13	2.387(7)	Yb2-O9	2.394(9)
Er1-O13a	2.366(7)	Er2-O10	2.476(10)	Yb1-O13a	2.354(7)	Yb2-O10	2.464(8)
Er1-N3	2.591(10)	Er2-O12	2.471(9)	Yb1-N3	2.608(10)	Yb2-O11	2.474(9)
Er1-N4	2.610(9)	Er2-O13	2.396(7)	Yb1-N4	2.599(10)	Yb2-O13	2.387(7)

Table 4.4: Selected bond lengths in complexes **26** and **27**. $a = (-x, 1-y, -z)$.

	21	22	23	24	26	27
Ln1-O5-Ln2a	111.0(5)	111.55(19)	111.4(3)	112.4(4)	112.7(3)	112.9(3)
Ln1-O7-Ln2	111.5(4)	114.2(4)	112.2(3)	112.1(4)	111.7(3)	111.9(3)
Ln1-O13-Ln1a	111.4(9)	113.23(19)	113.2(3)	113.3(3)	113.8(3)	114.1(3)
Ln1a-O13-Ln2	104.1(5)	103.86(17)	102.9(3)	103.2(3)	103.1(3)	103.3(3)
Ln1-O13-Ln2	103.7(5)	103.22(18)	103.4(3)	102.9(3)	102.4(3)	102.3(3)
Ln2-O1-Zn1	100.7(5)	101.2(2)	101.3(3)	101.9(4)	103.7(3)	103.6(3)
Ln2-O2-Zn1	103.4(5)	103.5(2)	103.8(3)	103.8(4)	101.6(3)	101.5(3)

Table 4.5: Selected bond angles in complexes **21-24**, **26** and **27**.

<i>Empirical formula</i>	<i>Eu₄Zn₂C₄₂H₉₈N₁₂O₃₂Cl₂</i>	<i>Gd₄Zn₂C₄₂H₉₈N₁₂O₃₂Cl₂</i>	<i>Tb₄Zn₂C₄₂H₉₈N₁₂O₃₂Cl₂</i>
Molar mass (gmol ⁻¹)	2092.81	2113.97	2127.60
Crystal System	Monoclinic	Monoclinic	Monoclinic
Space Group	<i>P2₁/c</i>	<i>P2₁/c</i>	<i>P2₁/c</i>
a (Å)	13.100(5)	13.0261(3)	12.9896(18)
b (Å)	15.890(6)	15.8688(3)	15.867(2)
c (Å)	17.484(6)	17.3336(5)	17.352(2)
α (deg)	90	90	90
β (deg)	97.166(8)	97.3150(10)	96.942(4)
γ (deg)	90	90	90
V (Å ³)	3611(2)	3553.84(10)	3550.1(5)
Z	2	2	2
T (K)	100	100	100
λ (Å)	0.71073	0.71073	0.71073
ρ _{calc} (g/cm ³)	1.984	1.964	1.990
μ (mm ⁻¹)	4.242	4.507	4.759
^a R ₁	0.0869	0.0375	0.0600
^b wR ₂	0.2099	0.0810	0.0111
Goodness of fit	1.046	0.925	1.075
F(000)	2072	2080	2088
Reflections	6300	7276	7218
Parameters	443	420	434
Restraints	600	20	33

Table 4.6: Crystallographic data for complexes **23**, **24** and **25**.

$${}^aR_1 = \frac{\sum ||F_o| - |F_c||}{\sum |F_o|}$$

$${}^b wR_2 = \left[\frac{\sum [w(F_o^2 - F_c^2)^2]}{\sum [(F_o^2)]} \right]^{\frac{1}{2}} \quad \text{where} \quad w = 1/[\sigma^2(F_o^2) + (0.2P)^2] \quad \text{and} \quad P = [F_o^2 + 2F_c^2]/3$$

<i>Empirical formula</i>	<i>Dy₄Zn₂C₄₂H₉₈N₁₂O₃₂Cl₂</i>	<i>Er₄Zn₂C₄₂H₉₈N₁₂O₃₂Cl₂</i>	<i>Yb₄Zn₂C₄₂H₉₈N₁₂O₃₂Cl₂</i>
Molar mass (g mol ⁻¹)	2134.97	2154.01	2177.13
Crystal System	Monoclinic	Monoclinic	Monoclinic
Space Group	<i>P2₁/c</i>	<i>P2₁/c</i>	<i>P2₁/c</i>
a (Å)	12.962(2)	12.9048(18)	12.868(3)
b (Å)	15.893(3)	15.818(2)	15.757(4)
c (Å)	17.240(3)	17.185(2)	17.229(4)
α (deg)	90	90	90
β (deg)	96.792(4)	96.816(4)	96.648(5)
γ (deg)	90	90	90
V (Å ³)	3526.5(6)	3483.2(5)	3469.8(7)
Z	2	2	2
T (K)	100	100	100
λ (Å)	0.71073	0.71073	0.71073
ρ _{calc} (g/cm ³)	2.010	2.053	2.083
μ (mm ⁻¹)	5.019	5.609	6.186
^a R ₁	0.0670	0.0574	0.0538
^b wR ₂	0.1482	0.1227	0.0947
Goodness of fit	0.886	0.950	0.922
F(000)	2096	2112	2128
Reflections	6941	7074	7106
Parameters	415	428	436
Restraints	30	25	18

Table 4.7: Crystallographic data for complexes **26**, **28** and **29**.

$${}^aR_1 = \frac{\sum ||F_o| - |F_c||}{\sum |F_o|}$$

$${}^b wR_2 = \frac{[\sum [w(F_o^2 - F_c^2)^2] - \sum [(F_o^2)^2]]^{\frac{1}{2}}}{\sum [w(F_o^2 + 2F_c^2)]} \quad \text{where } w = 1/[\sigma^2(F_o^2) + (0.2P)^2] \quad \text{and } P = [F_o^2 + 2F_c^2]/3$$

4.3.3 Powder Diffraction Data

Powder X-ray diffraction data were collected for samples of ground single crystals and precipitates of $\{\text{Gd}_4\text{Zn}_2\}$ (**22**) and $\{\text{Dy}_4\text{Zn}_2\}$ (**24**) and compared to the respective calculated patterns from single crystal X-ray data. These data are plotted for **22** and **24** in Figures 4.5 and 4.6 respectively.

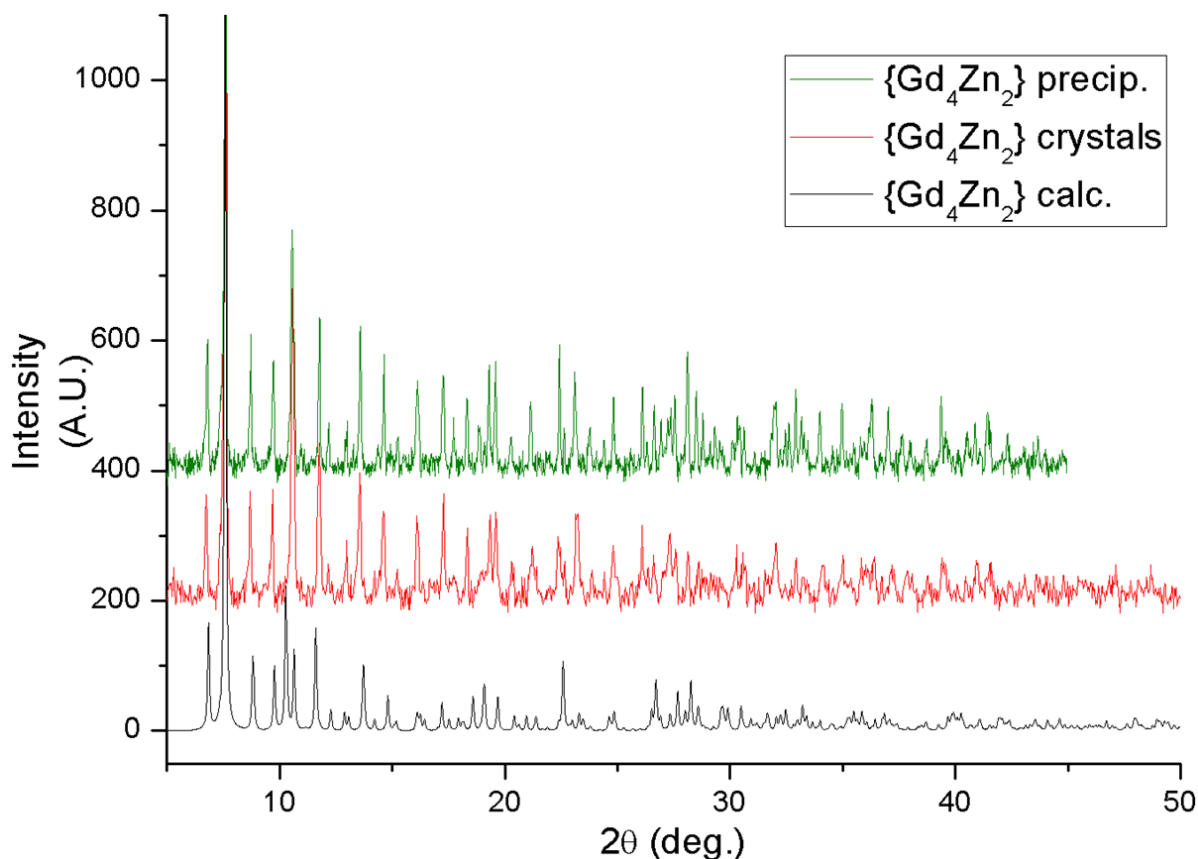


Figure 4.4: Powder X-ray patterns for $\{\text{Gd}_4\text{Zn}_2\}$: calculated, black line; crystals, red line and precipitate, green line. The spectrum for the precipitate of $\{\text{Gd}_4\text{Zn}_2\}$ was collected to $2\theta = 45^\circ$.

There is a good correlation between the powder patterns of the crystals and precipitate of **22**, indicating that they are of the same structural phase. There are discrepancies however between the calculated pattern and experimental patterns. IR confirms that the crystals and precipitate are the same material; CHN reveals that both the crystals and precipitate are hygroscopic – analysing as hydrated forms of the single crystal structure. The discrepancies between the calculated and experimental patterns could be due to the hygroscopic nature of **22** causing structural changes.

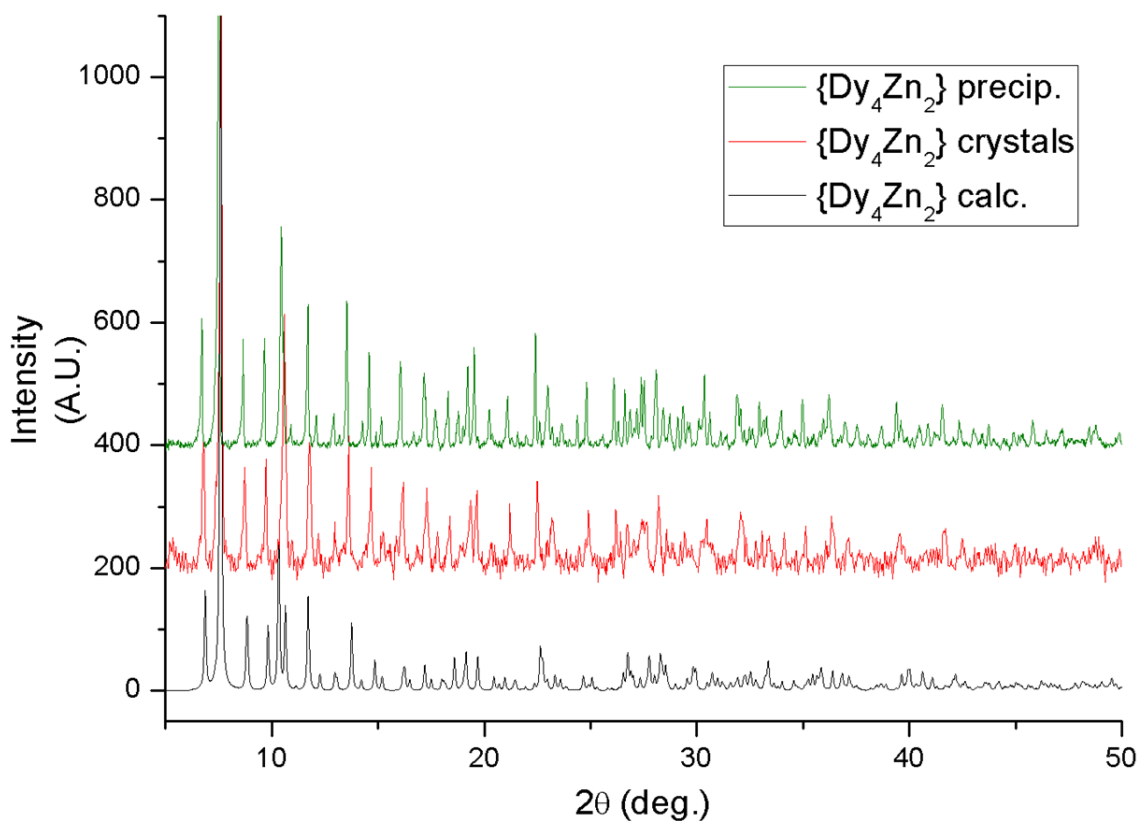


Figure 4.5: Powder X-ray patterns for $\{\text{Dy}_4\text{Zn}_2\}$: calculated, black line; crystals, red line and precipitate, green line.

For $\{\text{Dy}_4\text{Zn}_2\}$ (**24**), there are good correlations between the precipitate and crystal diffraction patterns, indicating they are of the same structural phase. IR confirms they are the same material and CHN of the precipitate shows that it is hygroscopic. An acceptable CHN match was not obtained for the crystals, the closest analysing as **24**·4H₂O with a max difference between calculated and found values of 0.6%. Assuming the ground crystals to also be hygroscopic, as for **22**, the hygroscopic nature of the ground crystals and precipitate could again have resulted in the discrepancies of the powder and calculated patterns.

Precipitates of the other analogues, excluding $\{\text{Eu}_4\text{Zn}_2\}$ were also collected and are plotted in Figure 4.7, the data show a good correlation between each analogue. Single crystals of the $\{\text{Ho}_4\text{Zn}_2\}$ analogue were unfortunately not obtained, however, comparing the powder pattern of the $\{\text{Ho}_4\text{Zn}_2\}$ precipitate to those of the other precipitates suggests that it shares a common structure and phase. IR data also matches those of the other precipitates and CHN results suggest a hydrated version of the $\{\text{Ln}_4\text{Zn}_2\}$ structure – together these suggest that the $\{\text{Ho}_4\text{Zn}_2\}$ has been isolated.

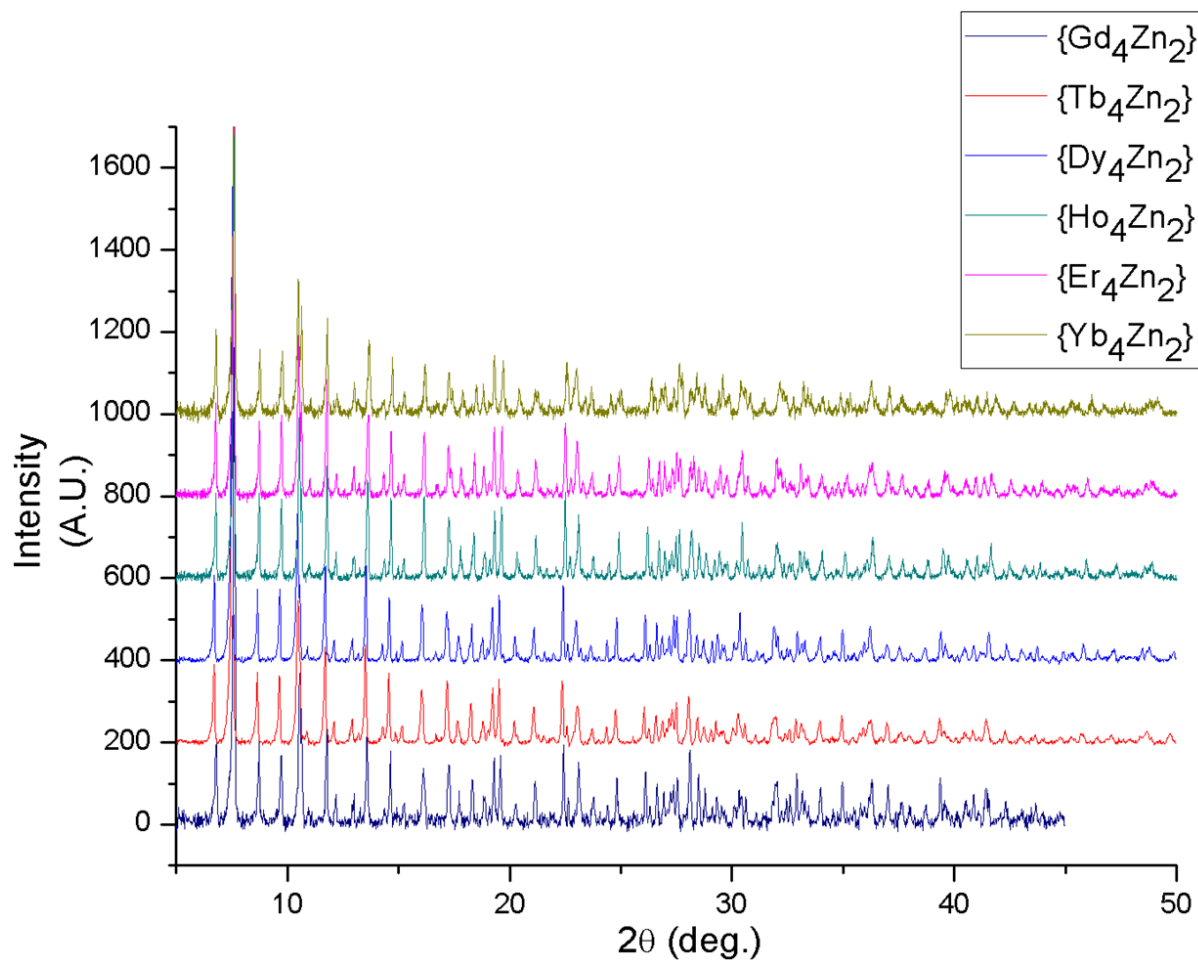


Figure 4.6: Powder X-ray patterns of precipitates of $\{Ln_4Zn_2\}$ series 22-27. The spectrum for the precipitate of $\{Gd_4Zn_2\}$ was collected to $2\theta = 45^\circ$.

4.4 Magnetism

4.4.1 Static magnetic properties of $\{\text{Gd}_4\text{Zn}_2\}$ (**22**)

The temperature dependent magnetic susceptibility of a polycrystalline sample of **22** was measured in the temperature range 1.8 – 300 K under an applied dc field of 1 kOe (Figure 4.7). The room temperature χT value of $31.85 \text{ cm}^3 \text{ K mol}^{-1}$ is in good agreement with the calculated value of $31.50 \text{ cm}^3 \text{ K mol}^{-1}$ for four non-interacting Gd^{III} ions ($^8\text{S}_{7/2}$, $S = 7/2$, $g_J = 2$, $L = 0$), Zn^{II} (d^{10}) is diamagnetic so will have no contribution to the paramagnetic susceptibility.

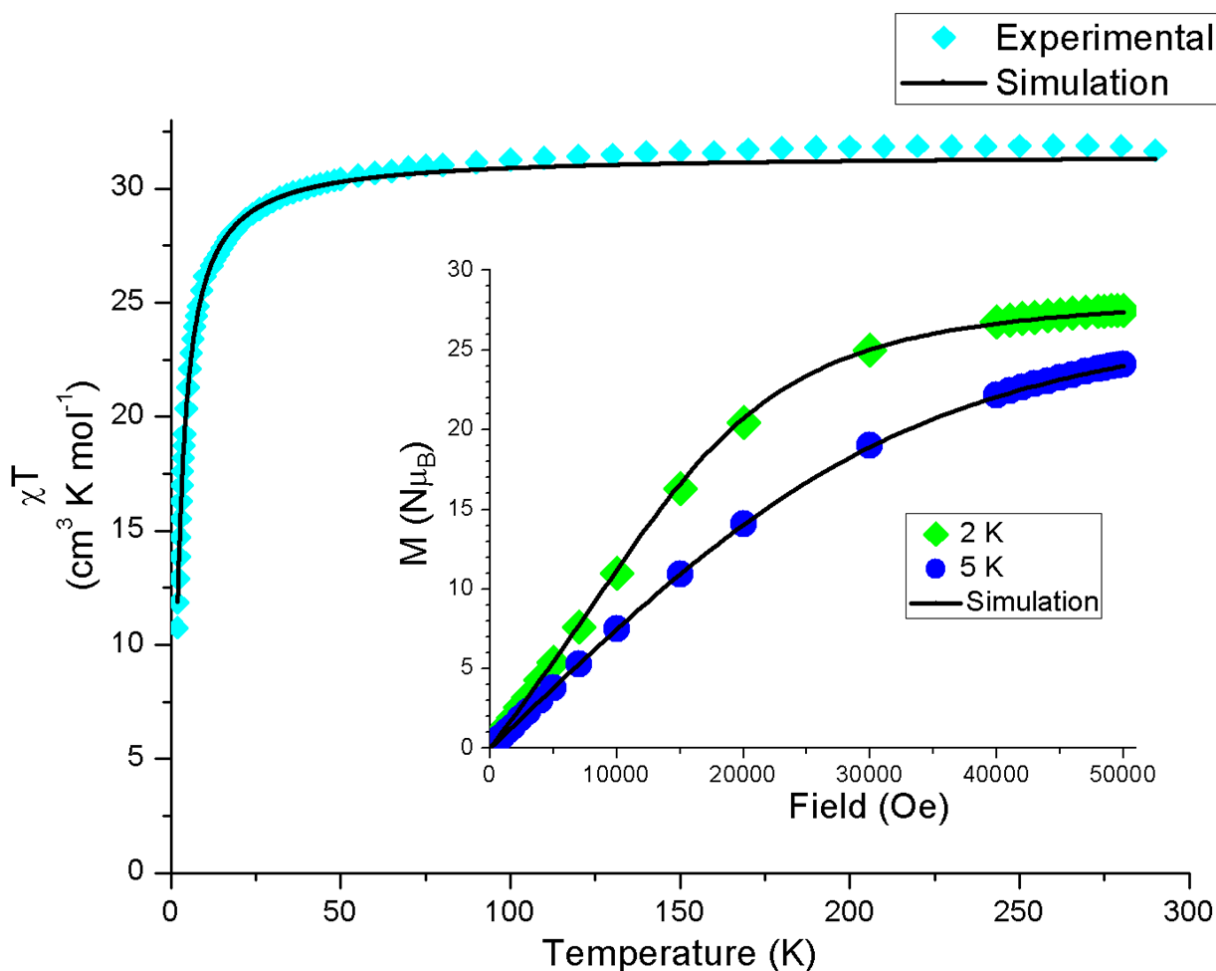


Figure 4.7: Temperature dependent magnetic susceptibility and magnetisation vs. field for **22**. The solid lines are from the 2 J simulation model.

As T is lowered, χT stays roughly constant down to ≈ 50 K where it then decreases sharply down to a minimum of $10.74 \text{ cm}^3 \text{ K mol}^{-1}$ at 1.8 K. The χT curve is indicative of antiferromagnetic coupling between Gd^{III} ions, however, the downturn could also be due in part to intermolecular antiferromagnetic interactions. Magnetisation vs. field was also measured for **22** at 2 and 5 K in fields up to 50 kOe (inset Figure 4.7). At 2 K the magnetisation reaches $27.50 \text{ N}\mu_{\text{B}}$ at 50 kOe, which is close to the expected saturation value of $28 \text{ N}\mu_{\text{B}}$ for four co-aligned Gd^{III} spins ($S = 14$, $g = 2$, $M_{\text{sat}} = gS$). At 5 K the magnetisation reaches $24.1 \text{ N}\mu_{\text{B}}$ at 50 kOe but is still increasing, indicative that the $S = 14$ state is not fully occupied under these conditions. The ground state of **22** is actually $S = 0$ (Figure 4.8) due to dominant $\text{Gd}^{\text{III}}\text{-Gd}^{\text{III}}$ antiferromagnetic interactions (see below), with low lying excited states with higher spin becoming populated as the field H is increased (Figure 4.9).

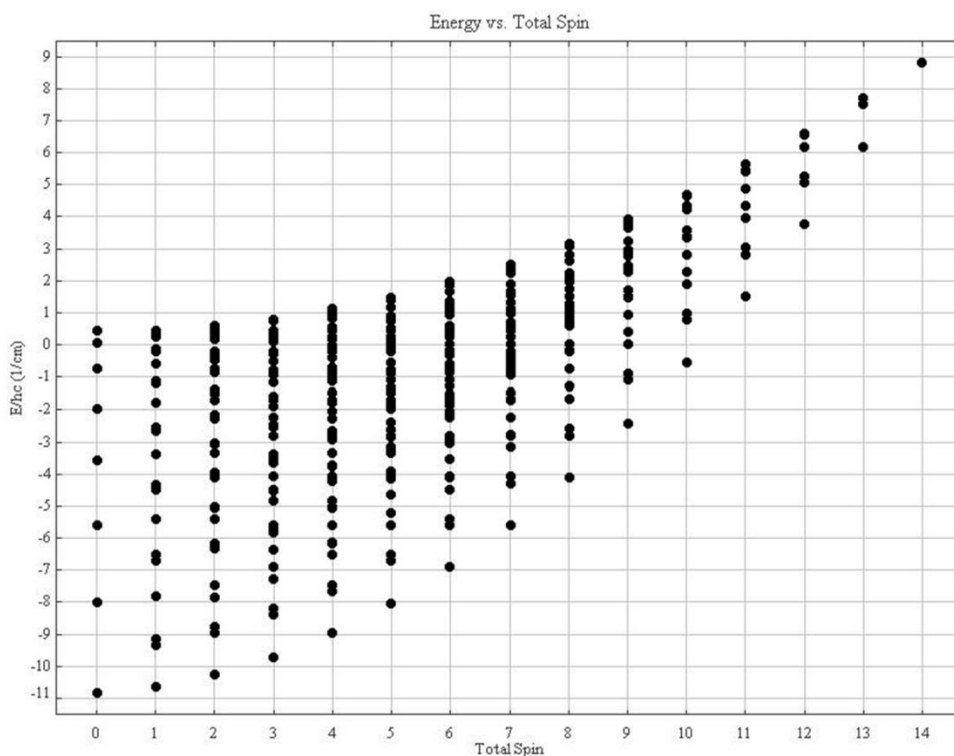


Figure 4.8: Distribution of spin states of **22**. The lowest energy state is $S = 0$ (bottom left) and the highest $S = 14$ (top right).

The $S = 14$ state, which is highest in energy, is split by the magnetic field into $m_s = \pm 14$ states (Figure 4.9), at some point as H is increased the $m_s = -14$ state becomes the lowest in energy and becomes increasingly populated as H increases – accounting for the high field magnetisation values of $\approx 28 \text{ N}\mu_{\text{B}}$ for **22** representative of a $S = 14$ state.

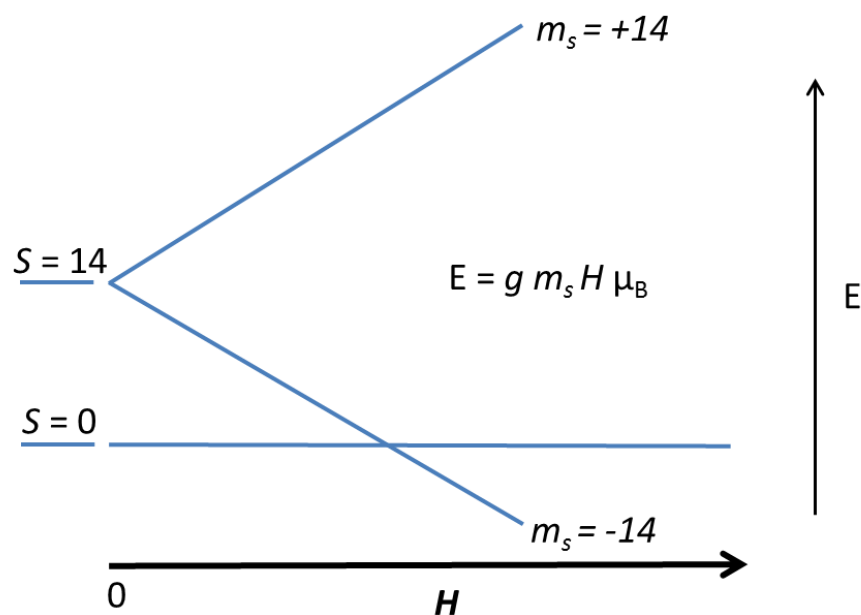


Figure 4.9: Schematic energy diagram of the Zeeman splitting of the $S = 14$ state in the magnetic field into $m_s = \pm 14$ states, spin states between $S = 0$ and $S = 14$ have been omitted for clarity. The $m_s = -14$ state eventually becomes lower in energy than the ground $S = 0$ state as the field is increased; accounting for the field induced magnetisation behaviour of **22**.

Due to the spin only nature of Gd^{III} , a simulation of the magnetisation and susceptibility data could be calculated using the programme FITMART³³ and a spin only Hamiltonian. For simplicity, the data was initially simulated using a single isotropic J value and a fixed g value of 2, the Hamiltonian is shown in Equation 4.1:

$$\hat{H} = -2J(s_1 \cdot s_2 + s_2 \cdot s_3 + s_3 \cdot s_4 + s_4 \cdot s_1 + s_2 \cdot s_4) + g\mu_B \vec{H} \sum_{i=1}^4 s_i$$

Equation 4.1

In this Hamiltonian a positive J signifies ferromagnetic exchange. Using this single J model, an antiferromagnetic exchange value of -0.06 cm^{-1} gave the best simulation for both the χT vs. T and M vs. H data with an average root mean square (RMS) error of 0.77 between the simulation and experimental data. This weak antiferromagnetic exchange is in agreement with reported values for similar $\{\text{Gd}_4\}$ structural motifs.³⁴⁻³⁶ The data was then simulated using a two J model (J and J' , see Figure 4.10) to account for the different exchange pathways. The Hamiltonian is shown in Equation 4.2.

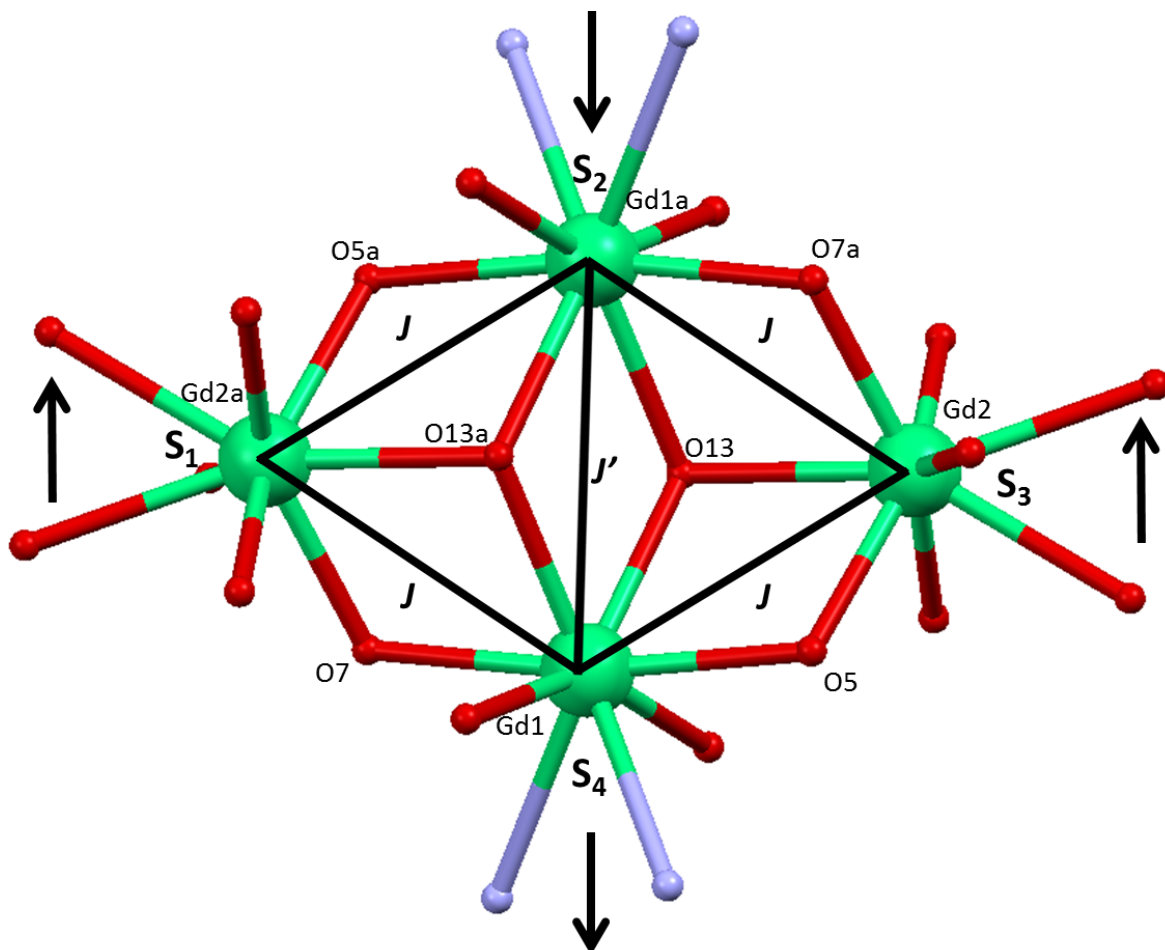


Figure 4.10: Magnetic model used for simulated fit of $\{Gd_4Zn_2\}$ data.

$$\hat{H} = -2J(s_1 \cdot s_2 + s_2 \cdot s_3 + s_3 \cdot s_4 + s_4 \cdot s_1) - 2J' s_2 \cdot s_4 + g\mu_B \vec{H} \sum_{i=1}^4 s_i$$

Equation 4.2

Again a positive J represents ferromagnetic exchange in Equation 2. The best simulation was found when $J = -0.065 \text{ cm}^{-1}$ and $J' = +0.01 \text{ cm}^{-1}$ which gave an RMS between the simulation and experiment of 0.36 – almost half of the RMS for the single J model. This is concurrent with an overall $S = 0$ ground state for **22**. Ideally, a model with three J values should be used considering the structure of **22**, however, simulating three variables would give a less meaningful result compared to the two J model. The weak ferromagnetic exchange between the crystallographic Gd1 ions (Figure 4.10) is in agreement with an empirical relation derived by Zhang *et al.*³⁷ that correlates the average Gd^{III}-O-Gd^{III} bond angles with observed Gd^{III}-Gd^{III} magnetic exchange. They found that Gd^{III}-O-Gd^{III} angles above 110.9° resulted in ferromagnetic exchange with only one exception out of the

twenty-one complexes surveyed. The relation they derived, shown in Equation 4.3, calculates an expected J_{calc} value using the Gd^{III}-O-Gd^{III} bond angle (φ).

$$J_{calc} = 0.0123\varphi - 1.364$$

Equation 4.3

In Equation 4.3, a negative J_{calc} corresponds to antiferromagnetic exchange with the factor 2 accounted for. The relevant Gd-O-Gd average bond angles in **22** and their corresponding J_{calc} values are tabulated in Table 4.8.

Bond	Average angle	J_{calc}
Gd1-O -Gd1a	113.2(2) ^o	+0.028 cm ⁻¹
Gd1-O-Gd2	108.3(3)	-0.032 cm ⁻¹

Table 4.8

The J_{calc} values are concurrent with the simulation values from the two J model of $J = -0.065$ cm⁻¹ (Gd1-Gd2) and $J' = +0.01$ cm⁻¹ (Gd1-Gd1a). The empirical relation predicts both the sign of exchange and that the antiferromagnetic exchange is larger in magnitude. Overall, the complex displays an $S = 0$ ground state which agrees with the simulated and empirically calculated J values – antiferromagnetic exchange being dominant overall.

4.4.2 Static Magnetic Properties of $\{Dy_4Zn_2\}$ (24)

The temperature dependent magnetic susceptibility of **24** was measured in the temperature range 1.8 – 300 K under an applied dc field of 1 kOe (Figure 4.11). The room temperature χT value of $57.14 \text{ cm}^3 \text{ K mol}^{-1}$ is in good agreement with the calculated value of $56.67 \text{ cm}^3 \text{ K mol}^{-1}$ for four non-interacting Dy^{III} ions (${}^6H_{15/2}$, $S = 5/2$, $L = 5$, $J = 15/2$, $g_J = 4/3$), Zn^{II} (d^{10}) is diamagnetic so will have no contribution to the paramagnetic susceptibility.

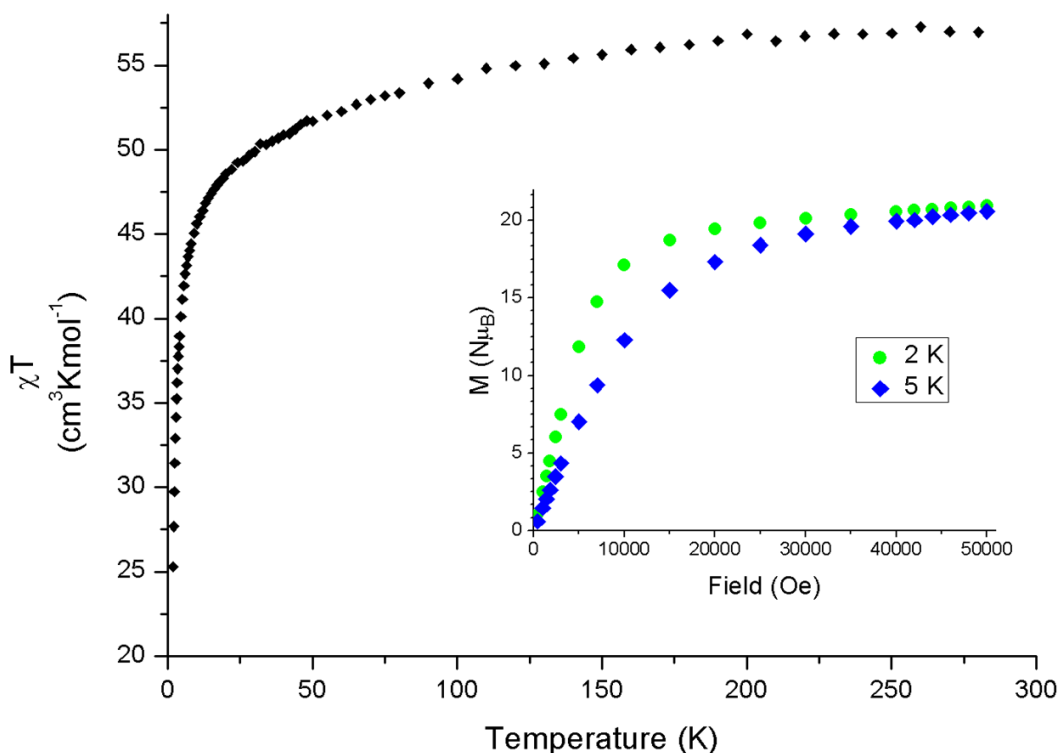


Figure 4.11: Temperature dependent magnetic susceptibility and M vs. H for **24** (inset).

As T is lowered, χT gradually decreases down to $\approx 50 \text{ K}$ where it then decreases sharply down to a minimum of $25.38 \text{ cm}^3 \text{ K mol}^{-1}$ at 1.8 K . The decrease is most likely due to thermal depopulation of excited Stark sublevels on Dy^{III} which arise due to the splitting of the ${}^6H_{15/2}$ ground state by the ligand field rather than weak antiferromagnetic Dy^{III} - Dy^{III} exchange (≈ 100 's cm^{-1} compared to $< 1 \text{ cm}^{-1}$).⁹ Another possible contributing factor to the downturn could be weak intermolecular antiferromagnetic interactions at low temperature. Magnetisation vs. field data were collected at 2 and 5 K up to fields of 50 kOe (inset Figure 4.11). The magnetisation rapidly increases at low fields followed by a gradual increase, eventually reaching $20.93 \text{ N}\mu_B$ at 2 K and $20.57 \text{ N}\mu_B$ at 5 K. These values are around half of the calculated saturation magnetisation (M_{sat}) value of $40 \text{ N}\mu_B$ for four Dy^{III} ions ($M_{sat} =$

$N g_J J$, $N = 4$, $g_J = 4/3$, $J = 15/2$). This discrepancy is well documented in systems containing Dy^{III} ions and is due to their significant magnetic anisotropy and/or the presence of low lying excited states.³⁸⁻⁴³

4.4.3 Dynamic Magnetic Properties of **24**

Ac susceptibility measurements were used to determine if **24** exhibited slow relaxation of its magnetisation. In the absence of an applied dc field, **24** shows onset of frequency dependent out-of-phase susceptibility with a concomitant decrease in the in-phase susceptibility down to 1.8 K.

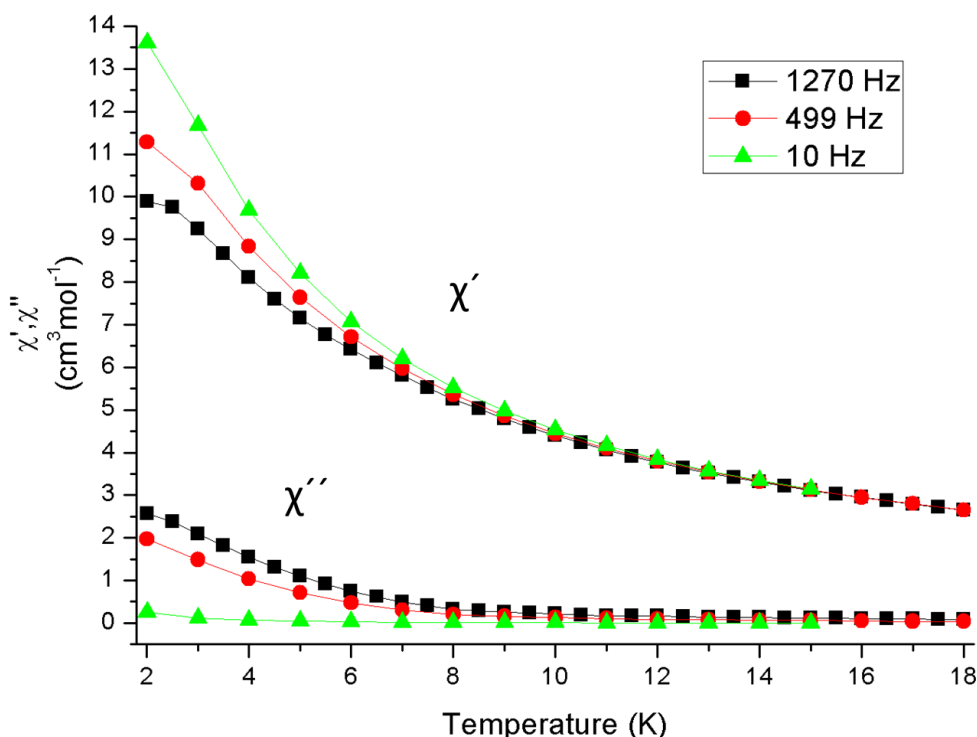


Figure 4.12: Ac susceptibility measurements for **24** in zero applied dc field.

Because no maxima are observed in χ'' , an energy barrier (U_{eff}) cannot be calculated using the conventional Arrhenius method.⁴⁵ Instead, another method reported by Bartolomé *et al.*⁴⁶ which assumes only one relaxation mechanism of Debye type with one energy barrier

and one time constant can be used to estimate U_{eff} . The relation is presented in Equation 4.4:

$$\ln(\chi''/\chi') = \ln(\omega\tau_0) + (E_a/k_B T)$$

(where $\omega = 2\pi\nu$)

Equation 4.4

From this relation, a plot of $\ln(\chi''/\chi')$ vs. $(1/T)$ gives a straight line for each frequency, from which the gradient = E_a/k_B and intercept = $\ln(\omega\tau_0)$ can be extracted. The plot for **24** is shown in Figure 4.13, with the data at 10 Hz omitted due to the almost negligible increase in χ'' or decrease in χ' down to 1.8 K. The results of the linear fits are presented in Table 4.9.

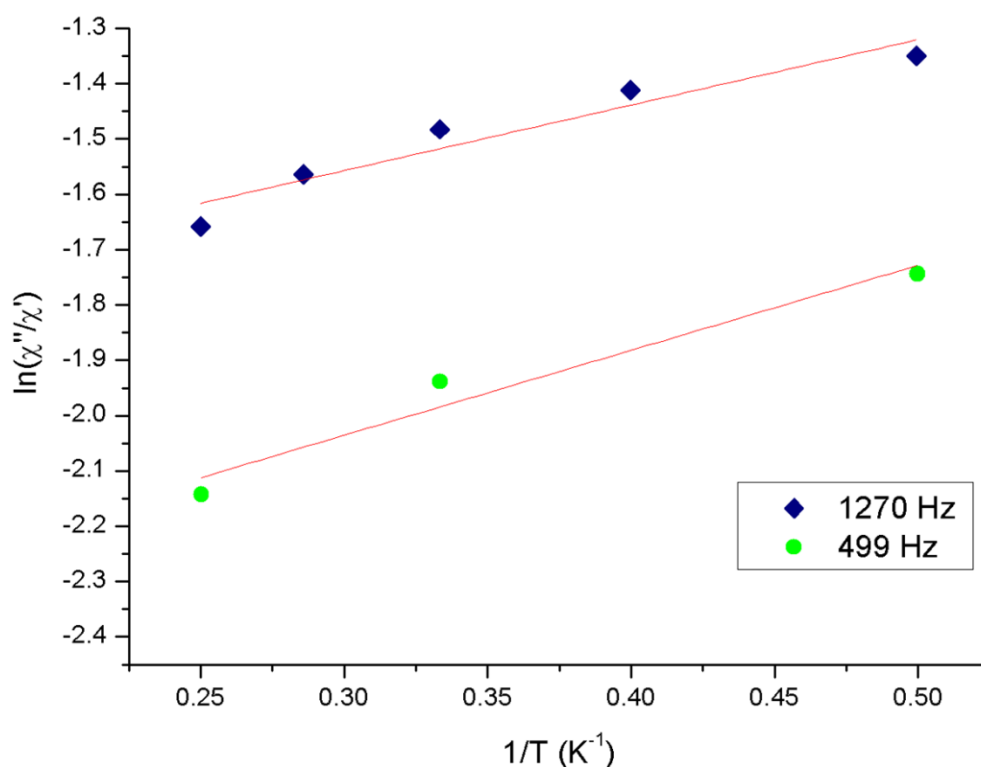


Figure 4.13: Plot of $\ln(\chi''/\chi')$ vs. $(1/T)$ for **24** in zero applied dc field. The red lines represent the linear fits of the data collected at 1270 Hz (blue diamonds) and 499 Hz (green circles) between 5-1.8 K.

	$U_{\text{eff}}(\text{K})$	$\tau_0(\text{s})$
1270 Hz	1.2 ± 0.2	$3.2 \times 10^{-5} \pm 1.2 \times 10^{-5}$
499 Hz	1.5 ± 0.3	$1.7 \times 10^{-5} \pm 5.8 \times 10^{-6}$

Table 4.9: Summary of linear fits of $\ln(\chi''/\chi')$ vs. $(1/T)$ for **26** in zero field.

The estimates for U_{eff} are within error range of each other; taking an average value of $\approx 1.35 \pm 0.25 \text{ K}$ ($0.95 \pm 0.18 \text{ cm}^{-1}$) in zero applied dc field which is concurrent with similar reported $\{\text{Dy}_4\}$ structures.^{34,38,39} The τ_0 values are also within error range of each other, taking an average gives $\tau_0 = 2.45 \times 10^{-5} \pm 0.9 \times 10^{-6} \text{ (s)}$ which is also in agreement with reported values for similar $\{\text{Dy}_4\}$ structures.³⁸⁻⁴¹ It should be noted however that the U_{eff} and τ_0 values reported here were calculated using only a limited number of data points, especially in the case of the 499 Hz data. A more accurate estimate would require more χ'' and χ' data points to be measured below 5 K. Ac susceptibility was also measured in an applied field of 2 kOe in an effort to reduce QTM which is known to be prevalent in complexes containing Dy^{III} ions in low symmetry crystal fields.⁸ The data are shown in Figure 4.14.

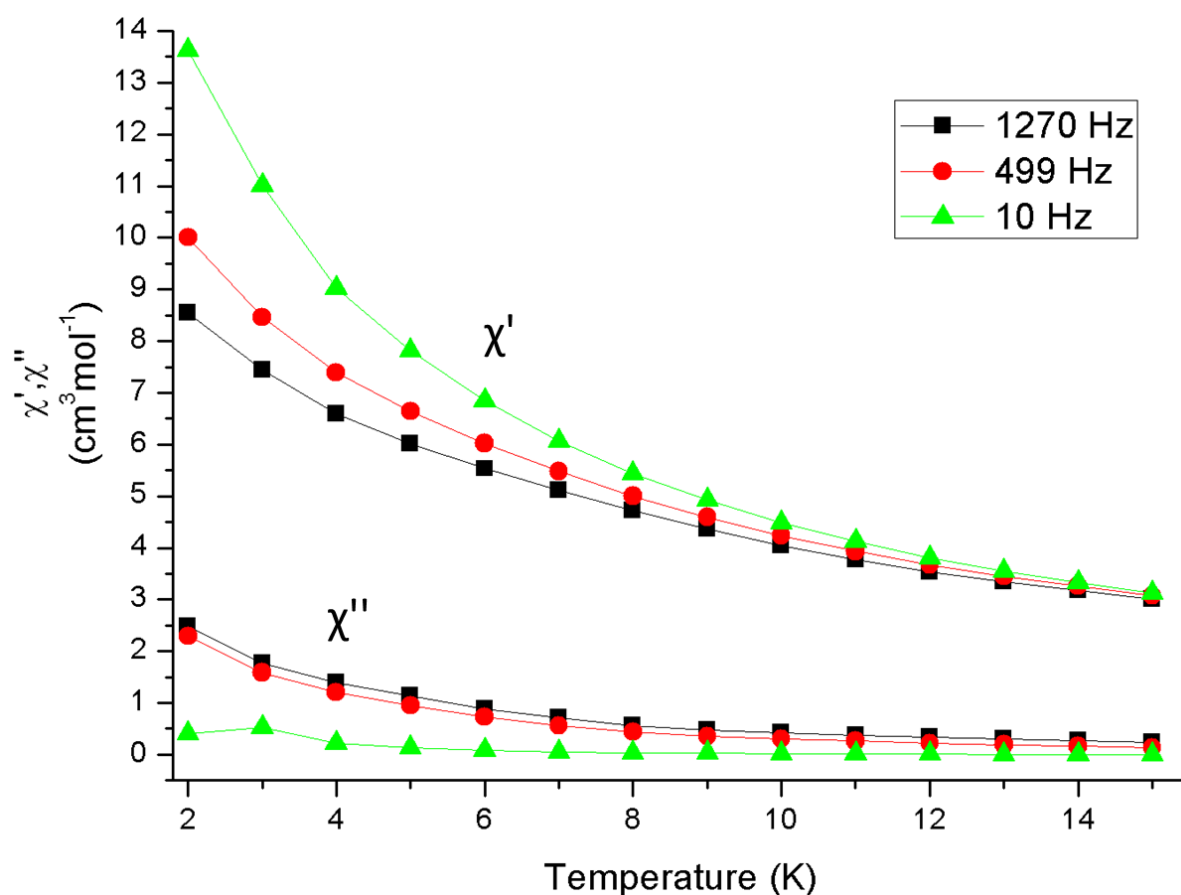


Figure 4.14: Ac susceptibility measurements for **24** in 2 kOe applied field.

The profiles of χ'' and χ' are very similar to those measured in zero applied field, indicative that QTM is perhaps not as prevalent as thermally activated relaxation which has been observed in similar $\{\text{Dy}_4\}$ structures.^{34,39} A plot of $\ln(\chi''/\chi')$ vs. $(1/T)$ was used to estimate U_{eff} , the results of which are given in Figure 4.15 and Table 4.10. It should be noted that the χ'' data point at 1.8 K and 10 Hz is thought to be an anomaly. Three measurements of χ'' were taken at 10 Hz and 1.8 K, the average of which is the reported data point. The three

values are all of similar magnitude so a stray datum is not the cause of the observed reduction. Where maxima in χ'' are not observed at the higher field frequencies, it is not possible for there to be maxima observed at lower frequencies in the same temperature window.

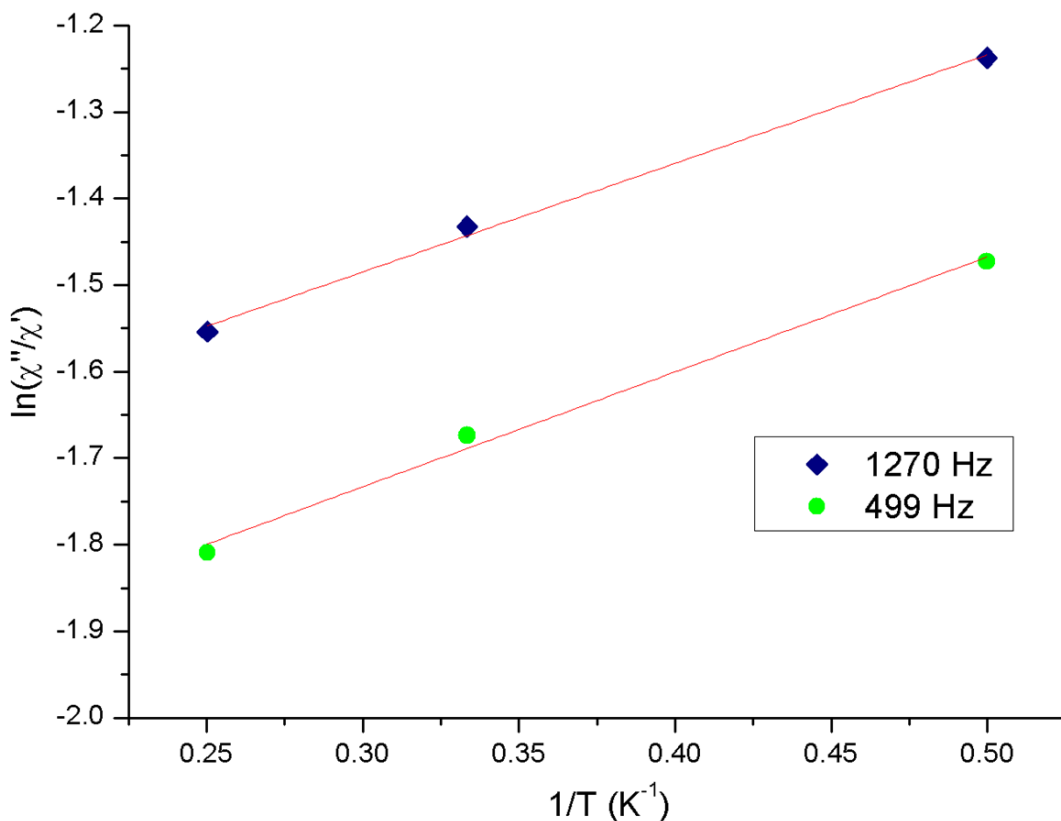


Figure 4.15: Plot of $\ln(\chi''/\chi')$ vs. $(1/T)$ for **24** in 2 kOe applied dc field. The red lines represent the linear fits of the data collected at 1270 Hz (blue diamonds) and 499 Hz (green circles) between 5-1.8 K.

	U_{eff} (K)	τ_0 (s)
1270 Hz	1.3 ± 0.1	$1.9 \times 10^{-5} \pm 5.3 \times 10^{-7}$
499 Hz	1.3 ± 0.1	$3.8 \times 10^{-5} \pm 1.5 \times 10^{-6}$

Table 4.10: Summary of linear fits of $\ln(\chi''/\chi')$ vs. $(1/T)$ for **24** in 2 kOe applied field. The gradient values represent the estimated U_{eff} in Kelvin.

The U_{eff} values estimated from both frequencies are 1.3 ± 0.1 K (0.9 ± 0.1 cm⁻¹), which are similar to the estimated values in zero applied field. The τ_0 values do not lie within error boundary of each other, however, each is within the expected range of between 10^{-5} and

10⁻¹⁰ s for a SMM.¹⁻³ Again, the estimates of U_{eff} and τ_0 are only calculated using a very small data set and more accurate values representative of the actual value of **24** would require more χ'' and χ' measurements below 5 K. The low estimated U_{eff} values for **24** could be due to a number of factors, namely: poor separation of Stark sublevels on Dy^{III} caused by a distorted local Dy^{III} crystal field, non-aligned magnetic anisotropy axes of Dy^{III} and/or intermolecular interactions facilitated by hydrogen bonding.

4.5 Conclusions and Future Work

Seven new isostructural {Ln₄Zn₂} complexes have been synthesised, where Ln = Eu^{III} (**21**), Gd^{III} (**22**), Tb^{III} (**23**), Dy^{III} (**24**), Ho^{III} (**25**), Er^{III} (**26**) and Yb^{III} (**27**). Attempts to synthesise the La^{III}, Ce^{III}, Pr^{III} and Nd^{III} analogues were unfortunately unsuccessful. Magnetic measurements carried out on **22** show that there are weak exchange interactions between Gd^{III} centres. Using a two J model, the temperature dependent dc susceptibility and magnetisation *vs.* field data were simulated giving $J = -0.065 \text{ cm}^{-1}$ between Gd1 and Gd2, and $J' = +0.01 \text{ cm}^{-1}$ between Gd1-Gd1, leading to an overall antiferromagnetic spin ground state. Magnetic measurements for **24** revealed that the complex does show slow relaxation of its magnetisation at low temperatures, however with a relatively small energy barrier of $U_{eff} \approx 1.3 \text{ K}$ both with and without an applied field of 2 kOe. The low energy barrier could be due in part to the significant distortion from ideal SAP geometry around the Dy^{III} ions.

Future work with the {Ln₄Zn₂} series would be to measure the magnetic properties of the {Tb₄Zn₂} analogue to search for slow relaxation of its magnetisation. The Tb^{III} analogue will likely exhibit a smaller U_{eff} barrier compared to Dy^{III} however; Tb^{III} based systems are much more sensitive to perturbations from local ideal SAP symmetry which induce QTM.⁹ To help increase U_{eff} for both the Tb^{III} and Dy^{III} analogues, subtle structural modifications could be investigated. A starting point could be to replace the ZnCl₂ starting material with either ZnBr₂ or ZnI₂ to try and exchange the chloride ligand on Zn1 for another halide. The change in hydrogen bonding strength (and distance) between the C11 and the μ_3 O13(H) would likely change the crystal field of both Ln^{III} ions, however, the exact outcome is difficult to predict. If the bidentate nitrate ion coordinated to Ln2 could be replaced with a β -diketonate ligand, it is likely that Ln2 would be closer to ideal SAP geometry. Optical studies of the Eu^{III} and Tb^{III} analogues would be an interesting route to pursue as these ions

exhibit strong emission in the near-IR (620 nm) and green (550 nm) regions of the electromagnetic spectrum respectively. Their strong emission at these wavelengths makes them ideal for luminescent probes used for biological imaging. The addition of sensitising ligands to the $\{Ln_4Zn_2\}$ molecule, such as β -diketonate ligands, would also be advantageous toward their optical properties.⁴⁷

4.6 References

- (1) H. L. C. Feltham, S. Brooker, *Coord. Chem. Rev.* 276 (2014) 1–33.
- (2) R. Sessoli, A. K. Powell, *Coord. Chem. Rev.* 253 (2009) 2328–2341.
- (3) L. R. Piquer, E. C. Sañudo, *Dalton Trans.* 44 (2015) 8771–8780.
- (4) M. Andruh, J.-P. Costes, C. Diaz, S. Gao, *Inorg. Chem.* 48 (2009) 3342–3359.
- (5) E. Ruiz, J. Cirera, J. Cano, S. Alvarez, C. Loose, J. Kortus, *Chem. Commun.* (2008) 52–54.
- (6) X. F. Liao, J. H. Jia, J. D. Leng, J. L. Liu, F. S. Guo, M. L. Tong, *Chem. Eur. J.* 19 (2013) 12254–12258.
- (7) L. Sorace, C. Benelli, D. Gatteschi, *Chem. Soc. Rev.* 40 (2011) 3092–3104.
- (8) P. Zhang, Y.N. Guoa, J. Tang, *Coord. Chem. Rev.* 257 (2013) 1728–1763.
- (9) J. Tang, P. Zhang, *Lanthanide Single-Molecule Magnets*, Springer (2015).
- (10) J.D. Rinehart, J.R. Long, *Chem. Sci.* 2 (2011) 2078–2085.
- (11) N. Ishikawa, M. Sugita, T. Ishikawa, S.-Y. Koshihara, Y. Kaizu, *J. Am. Chem. Soc.* 125 (2003) 8694–8695.
- (12) S.-D. Jiang, B.-W. Wang, G. Su, Z.-M. Wang, S. Gao, *Angew. Chem. Int. Ed.* 49 (2010) 7448–7451.
- (13) Y. Bi, Y.-N. Guo, L. Zhao, Y. Guo, S.-Y. Lin, S.-D. Jiang, J. Tang, B.-W. Wang, S. Gao, *Chem. Eur. J.* 17 (2011) 12476–12481.
- (14) G.-J. Chen, Y.-N. Guo, J.-L. Tian, J. Tang, W. Gu, X. Liu, S.-P. Yan, P. Cheng, D.-Z. Liao, *Chem. Eur. J.* 18 (2012) 2484–2487.
- (15) I. Oyarzabal, J. Ruiz, J. M. Seco, M. Evangelisti, A. Camon, E. Ruiz, D. Aravena, E. Colacio, *Chem. Eur. J.* 20 (2014) 14262 – 14269.
- (16) J.-L. Liu, Y.-C. Chen, Y.-Z. Zheng, W.-Q. Lin, Liviu Ungur, W. Wernsdorfer, L. F. Chibotaru, M. –L. Tong, *Chem. Sci.* 4 (2013) 3310–3316.
- (17) H. L. C. Feltham, Y. Lan, F. Klöwer, L. Ungur, L. F. Chibotaru, A. K. Powell, S. Brooker, *Chem. Eur. J.* 17 (2011) 4362–4365.
- (18) A. Watanabe, A. Yamashita, M. Nakano, T. Yamamura, T. Kajiwara, *Chem. Eur. J.* 17 (2011) 7428–7432.
- (19) K. Yamashita, R. Miyazaki, Y. Kataoka, T. Nakanishi, Y. Hasegawa, M. Nakano, T. Yamamura, T. Kajiwara, *Dalton Trans.* 42 (2013) 1987–1990.
- (20) A. Yamashita, A. Watanabe, S. Akine, T. Nabeshima, M. Nakano, T. Yamamura, T. Kajiwara, *Angew. Chem. Int. Ed.* 50 (2011) 4016–4019.
- (21) H.L.C. Feltham, F. Klöwer, S.A. Cameron, D.S. Larsen, Y. Lan, M. Tropicano, S. Faulkner, A.K. Powell, S. Brooker, *Dalton Trans.* 40 (2011) 11425–11432.

- (22) H.L.C. Feltham, Y. Lan, F. Klöwer, L. Ungur, L.F. Chibotaru, A.K. Powell, S. Brooker, *Chem. Eur. J.* 17 (2011) 4362-4365.
- (23) S. Hino, M. Maeda, K. Yamashita, Y. Kataoka, M. Nakano, T. Yamamura, H. Nojiri, M. Kofu, O. Yamamuro, T. Kajiwara, *Dalton Trans.* 42 (2013) 2683-2686.
- (24) A. S. Dinca, J. Vallejo, S. Shova, F. Lloret, M. Julve, M. Andruh, *Polyhedron* 65 (2013) 238-243.
- (25) K. Su, F. Jiang, J. Qian, M. Wu, K. Xiong, Y. Gai, M. Hong, *Inorg. Chem.* 52 (2013) 3780–3786.
- (26) S. Titos-Padilla, J. Ruiz, J. M. Herrera, E. K. Brechin, W. Wernsdorfer, F. Lloret, E. Colacio, *Inorg. Chem.* 52 (2013) 9620-9626.
- (27) K. Ehama, Y. Ohmichi, S. Sakamoto, T. Fujinami, N. Matsumoto, N. Mochida, T. Ishida, Y. Sunatsuki, M. Tsuchimoto, N. Re, *Inorg. Chem.* 52 (2013) 12828-12841.
- (28) S. M. T. Abtab, M. C. Majee, M. Maity, J. Titiš, R. Boča, M. Chaudhury, *Inorg. Chem.* 53 (2014) 1295-1306.
- (29) C. E. Burrow, T. J. Burchell, P.-H. Lin, F. Habib, W. Wernsdorfer, R. Clerac, M. Murugesu, *Inorg. Chem.* 48 (2009) 8051-8053.
- (30) W.-R. Yu, G.-H. Lee, E.-C. Yang, *Dalton Trans.* 42 (2013) 3941–3949.
- (31) J. Ruiz, G. Lorusso, M. Evangelisti, E. K. Brechin, S. J. A. Pope, E. Colacio, *Inorg. Chem.* 53 (2014) 3586-3594.
- (32) M. Llunell, D. Casanova, J. Cirera, P. Alemany, S. Alvarez, 'SHAPE: Program for the Stereochemical Analysis of Molecular Fragments by Means of Continuous Shape Measures and Associated Tools', Version 2.1, 2013, Barcelona.
- (33) L. Engelhardt, S. C. Garland, C. Rainey, R. A. Freeman, *Physic Procedia* 53 (2014) 39-45.
- (34) J. A. Sheikh, A. Adhikary, S. Konar, *New J. Chem.* 38 (2014) 3006-3014
- (35) S. K. Langley, N. F. Chilton, I. A. Gass, B. Moubaraki, K. S. Murray, *Dalton Trans.* 40 (2011) 12656–12659.
- (36) P.-F. Yan, P.-H. Lin, F. Habib, T. Aharen, M. Murugesu, Z.-P. Deng, G.-M. Li, W.-B. Sun, *Inorg. Chem.* 50 (2011) 7059-7065.
- (37) S. Xiang, S. Hu, T. Sheng, R. Fu, X. Wu, X. Zhang, *J. Am. Chem. Soc.* 129 (2007) 15144-15146.
- (38) G. Abbas, G. E. Kostakis, Y. Lan, A. K. Powell, *Polyhedron*, 41 (2012) 1–6.
- (39) K. C. Mondal, G. E. Kostakis, Y. Lan, A. K. Powell, *Polyhedron*, 66 (2013) 268-273.
- (40) G. Abbas, Y. Lan, G. E. Kostakis, W. Wernsdorfer, C. E. Anson, A. K. Powell, *Inorg. Chem.* 49 (2010) 8067–8072.

- (41) P.-H. Lin, T. J. Burchell, L. Ungur, L. F. Chibotaru, W. Wernsdorfer, M. Murugesu, *Angew. Chem. Int. Ed.* 48 (2009) 9489–9492.
- (42) Y.-Z. Zheng, Y. Lan, C. E. Anson, A. K. Powell, *Inorg. Chem.* 47 (2008) 10813-10815.
- (43) W.-B. Sun, B.-L. Han, P.-H. Lin, H.-F. Li, P. Chen, Y.-M. Tian, M. Murugesu, P.-F. Yan, *Dalton Trans.* 42 (2013) 13397–13403.
- (44) D. W. Bruce, D. O'Hare, R. I. Walton, *Molecular Materials*, Wiley (2010).
- (45) J. Bartolomé, G. Filoti, V. Kuncser, G. Schinteie, V. Meracre, C. E. Anson, A. K. Powell, D. Prodius, C. Turta, *Phys. Rev. B* 80 (2009) 014430.
- (46) J.-C. G. Bunzli, C. Piguet, *Chem. Soc. Rev.* 34 (2005) 1048-1077.

5. Monometallic complexes of 4f ions with H₄edte

5.1 Introduction

The ligand H₄edte is capable of chelating single 3d metal ions (Chapter 6); therefore, experimental work was undertaken to synthesise mononuclear 4f complexes and study their magnetic properties. Mononuclear 4f complexes have been one of the hottest topics in molecular nanomagnet research since the discovery in 2003 that a complex containing only a single lanthanide ion exhibited magnetic bistability with an energy barrier to magnetic reorientation (U_{eff}) one order of magnitude larger than any 3d polynuclear complex.¹⁻³ Research into this type of molecular nanomagnet, coined a single-ion magnet (SIM), quickly gathered momentum; with the vast majority of research concentrated on 4f ions. The reason being, certain Ln^{III} ions have both large ground state spin and large unquenched orbital angular momentum, the latter leading to strong magnetic anisotropy due to the strong angular dependence of the 4f orbitals. In contrast to 3d ions, the lanthanides have much stronger spin-orbit coupling compared to crystal field splitting, which leads to more pronounced magnetic anisotropy relative to 3d ions. Ions such as Tb^{III} and Dy^{III} are particularly prevalent in SIM research due to their ability, under axial crystal field geometries, to exhibit strong uniaxial magnetic anisotropy with a large separation between their ground and first excited m_J states; vital for magnetic bistability.^{4,5}

There have been a number of different SIMs reported using different ligands such as nitronyl nitroxide radicals,^{6,7} macrocyclic and Schiff base ligands.⁸⁻¹¹ However, the three most predominant areas of SIM research are considered to be the {LnPc₂} (where Pc = phthalocyanine) family,¹ LnPOMs^{12,13} and Dy-β-diketonates.¹⁴⁻¹⁶ The latter family has a complex with the highest U_{eff} outside of the {LnPc₂} family. Research into the Dy-β-diketonates began when the seemingly modest [Dy(acac)₃(H₂O)₂] (acac = acetylacetonate) was found to exhibit slow relaxation of the magnetisation.¹⁴ The molecule itself consists of an 8-coordinate Dy^{III} ion in a distorted square antiprismatic geometry, corresponding roughly to D_{4d} symmetry (Figure 5.1).

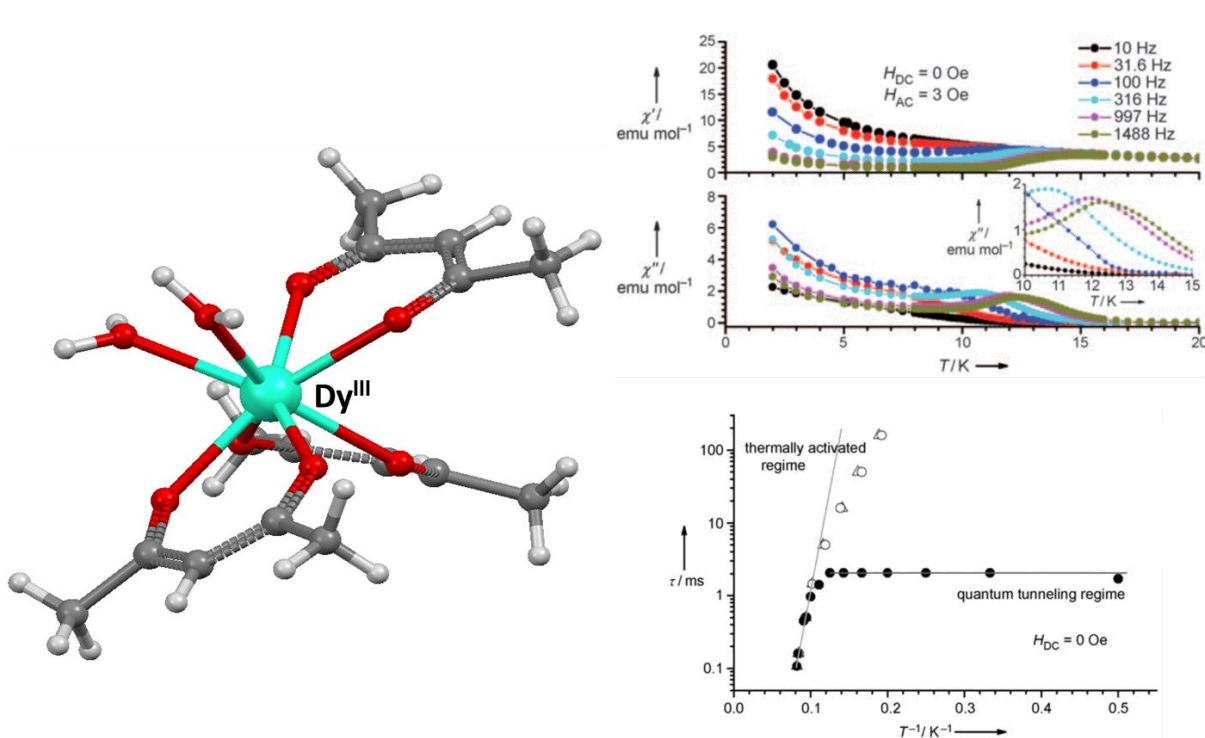


Figure 5.1: Molecular structure (left) of $[Dy(acac)_3(H_2O)_2]$. Atom colours: grey, C; red, O; white, H; turquoise, Dy^{III} . Magnetic data (right) adapted from ref. 6.

Ac susceptibility measurements for $[Dy(acac)_3(H_2O)_2]$ showed that the complex had a $U_{eff} = 66$ K. The Arrhenius analysis also indicated that below 8 K, magnetic relaxation became thermally independent and proceeded through quantum tunnelling of the magnetisation (QTM) alone. The prevalence of QTM for a single Dy^{III} was considered peculiar as Dy^{III} is a Kramer's ion: the odd number of electrons should lead to an absence of time reversal symmetry and should theoretically block QTM.¹⁷ However, they found, using computational methods that the distortions from ideal D_{4d} symmetry resulted in significant transversal anisotropy, a consequence of which is a higher probability of QTM. By synthesising magnetically dilute sample of the Dy^{III} analogue with the isostructural Y^{III} analogue in 1:20 and 1:50 ratios, and repeating the ac measurements under an additional dc field, they were able to effectively block QTM.

Work on $[Dy(acac)_3(H_2O)_2]$ prompted further research into β -diketonate ligands in an effort to study the effect of crystal field manipulations on the dynamic magnetic properties.^{15,16} Interestingly, by replacing the water ligands with capping bipyridyl type ligands, larger U_{eff} values were generated. Indeed, the highest U_{eff} of the non-phthalocyanine type SIMs belongs to such a complex.¹⁶ In 2012 Laio *et al.* reported the complexes $[Dy(acac)_3dpq]$ and $[Dy(acac)_3dppz]$, $dpq =$ dipyridylquinoxaline and $dppz =$

dipyridylphenazine (Figure 5.2). Both complexes had central 8-coordinate Dy^{III} ions in distorted square antiprismatic (D_{4d}) ligand fields.

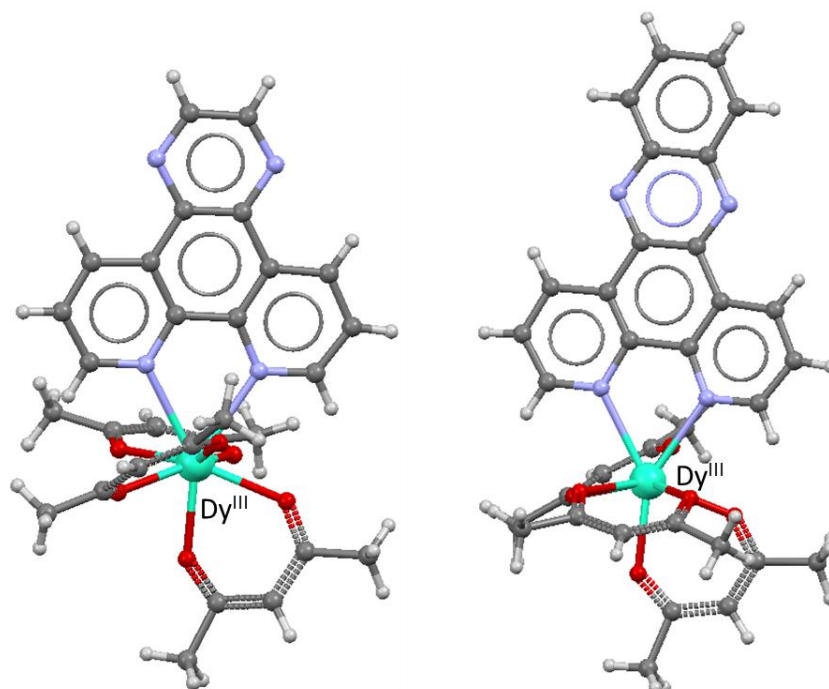


Figure 5.2: Molecular structures of $[Dy(acac)_3dpq]$ (left) and $[Dy(acac)_3dppz]$ (right). Atom colours: grey, C; blue, N; red, O; white, H; turquoise, Dy^{III}.

For the two complexes, the reported effective energy barriers were $U_{\text{eff}} = 136$ K for the dpq analogue and $U_{\text{eff}} = 187$ K for the dppz analogue. They also reported that QTM was faster in the dpq analogue and attributed this to the structure having a larger shift from ideal D_{4d} symmetry. Hysteresis was also observed below 2 K for the dppz analogue; however, there was no remnant magnetisation at zero-field due to fast QTM between the ground m_J states of Dy^{III}.

There is only one example in the literature of H₄edte chelating a lanthanide ion (Figure 5.3). The complex is not a SIM but is instead a trinuclear SMM.¹⁹ The complex was made by solvothermally heating (100°C, 3 days) Dy(NO₃)₃·6H₂O, LiOH and H₄edte in a 1 : 0.8 : 2 ratio in EtOH. The complex exhibited frequency dependent out-of-phase (χ'') peaks as well as temperature and sweep rate dependent hysteresis loops; confirming its classification as a SIM. The ac data indicated a two-step relaxation process, possibly due to two different Dy^{III} environments.

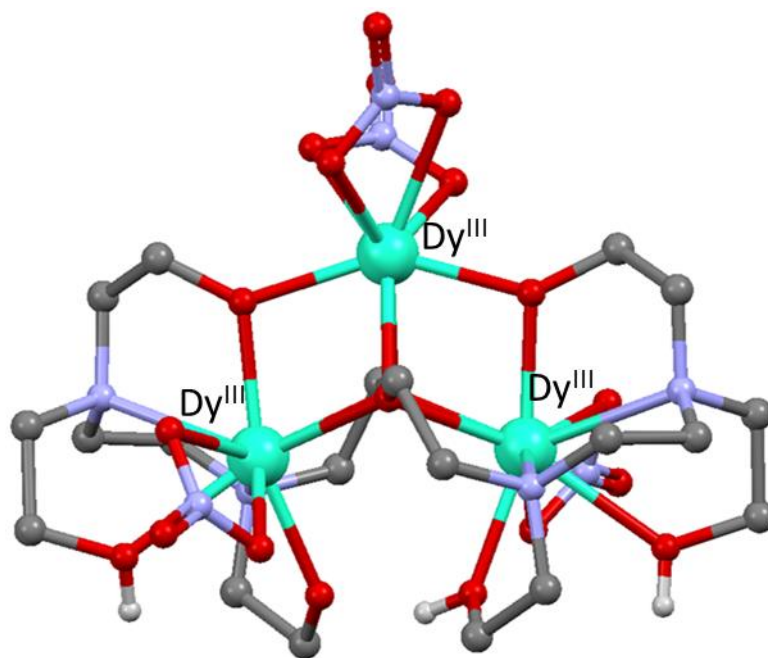


Figure 5.3: Molecule of $[Dy_3(Hedte)(H_2edte)(NO_3)_4]$ with H atoms omitted. Atom colours: grey, C; blue, N; red, O; turquoise, Dy^{III}.

The nine new compounds presented in this chapter were synthesised in high-yielding one pot reactions and the magnetic properties of the Tb^{III} and Dy^{III} analogues studied; revealing onset of slow relaxation down to 1.8 K in the Dy^{III} analogue. Single crystal X-ray diffraction shows that the complexes are of distorted D_{4d} symmetry with 10-coordinate central 4f ions. At the time of writing there were only two reported 10-coordinate SIMs.²⁰

5.2 Experimental

5.2.1 Synthesis of [Y^{III}(H₄edte)(NO₃)₂][NO₃] (28)

To a stirred solution of H₄edte (0.12 g, 0.5 mmol), in MeCN 20 ml was added Y(NO₃)₃·6H₂O (0.2 g, 0.5 mmol), the reaction was heated for 6 hours at 80°C then stirred at room temperature overnight. A white precipitate was collected, washed with MeCN and air dried, weight = 0.158 g, yield = 56.3% based on Y. Colourless block-like crystals of **28** were grown over a few days by dissolving 0.09 g precipitate in 5 ml MeOH and vapour diffusing with Et₂O. Crystals analyse as **28**, (YC₁₀H₂₄N₄O₁₃), analysis (%) calc (found) C 23.49 (23.70) H 4.70 (4.82) N 13.70 (13.65). Selected IR data (cm⁻¹): 3280 (br), 2997.48 (w), 2947.33 (w), 2926.11 (w), 2858.60 (w), 1494.88 (m), 1479.45 (m), 1454.38 (m), 1423.51 (m), 1402.30 (m), 1384.94 (m), 1369.50 (m), 1340.57 (m), 1305.85 (s), 1280.78 (s), 1257.63 (m), 1240.27 (m), 1230.63 (m), 1170.83 (w), 1155.40 (w), 1136.11 (w), 1112.96 (w), 1093.67 (m), 1076.32 (m), 1057.03 (s), 1033.88 (s), 1022.31 (m), 1014.59 (m), 999.16 (m), 922 (m), 916.22 (m), 908.50 (s), 893.07 (m), 877.64 (w), 819.77 (m), 813.99 (m), 758.05 (w), 748.41 (m), 738.46 (m), 688.61 (m), 669.32 (m), 603.74 (m). IR and CHN data for the crystals matches those of the precipitate.

5.2.2 Synthesis of [La^{III}(H₄edte)(NO₃)₂][NO₃] (29)

To a stirred solution of H₄edte (0.12 g, 0.5 mmol), in MeCN 20 ml was added La(NO₃)₃·6H₂O (0.23g, 0.5 mmol), the reaction was heated for 6 hours at 80°C then stirred at room temperature overnight. A white precipitate was collected, washed with MeCN and air dried, weight = 0.20 g, yield = 73.7% yield based on La. Colourless block-like crystals of **29** were grown over a few days by dissolving 0.09 g precipitate in 5 ml MeOH and vapour diffusing with Et₂O. Crystals analyse as **29**, (LaC₁₀H₂₄N₄O₁₃), analysis (%) calc. (found) C 21.40 (21.36), H 4.31 (4.32), N 12.48 (12.23). Selected IR data (cm⁻¹): 3250 (br), 2999.41 (w), 2918.40 (w), 2850.88 (w), 1491.02 (w), 1460.16 (w), 1452.45 (m), 1440.87 (m), 1402.30 (m), 1367.58 (m), 1340.57 (m), 1288.49 (s), 1274.99 (s), 1238.34 (m), 1232.55 (m), 1168.90 (w), 1138.04 (w), 1111.03 (m), 1093.67 (m), 1076.32 (m), 1055.10 (s), 1028.09 (s), 1010.73 (m), 995.3 (m), 900.79 (s), 883.43 (m), 871.85 (m), 815.92 (m), 752.26 (m), 731.05 (m), 686.68 (m), 621.10 (m). IR and CHN data for the crystals matches those of the precipitate.

5.2.3 Synthesis of [Pr^{III}(H₄edte)(NO₃)₂][NO₃] (30)

To a stirred solution of H₄edte (0.11 g, 0.46 mmol) in 20 ml MeCN was added Pr(NO₃)₃·6H₂O (0.22 g, 0.5 mmol), the reaction was heated for 6 hours at 80°C then stirred at room temperature overnight. A light green precipitate was collected, washed with MeCN and air dried, weight = 0.21 g, yield = 74.6% based on Pr. Green block-like crystals of **30** were grown over a few days by dissolving 0.09 g precipitate in 5 ml MeOH and vapour diffusing with Et₂O. Crystals analyse as **30**, (LaC₁₀H₂₄N₄O₁₃), analysis (%) calc (found) C 21.36 (21.14), H 4.30 (4.26), N 12.45 (12.09). Selected IR data (cm⁻¹): 3248 (br), 2978.19 (w), 2943.47 (w), 2920.32 (w), 2868.24 (w), 2852.81 (w), 1491.02 (m), 1475.59 (m), 1452.45 (m), 1440.87 (m), 1402.30 (m), 1367.58 (m), 1340.57 (m), 1290.42 (s), 1274.99 (s), 1230.63 (m), 1168.90 (w), 1151.54 (w), 1138.04 (w), 1111.03 (m), 1076.32 (m), 1055.1 (s), 1030.02 (s), 1010.73 (m), 997.23 (m), 902.72 (m), 885.36 (m), 873.78 (m), 815.92 (m), 752.26 (m), 732.97 (m), 686.68 (m), 621.1 (m). IR and CHN data for the crystals matches those of the precipitate.

5.2.4 Synthesis of [Nd^{III}(H₄edte)(NO₃)₂][NO₃] (31)

To a stirred solution of H₄edte (0.11 g, 0.46 mmol) in 20 ml MeCN was added Nd(NO₃)₃·6H₂O (0.23 g, 0.5 mmol), the reaction was heated for 6 hours at 80°C then stirred at room temperature overnight. A light purple precipitate was collected, washed with MeCN and air dried, weight = 0.199 g, yield = 70% based on Nd. Light purple block like crystals of **31** were grown by dissolving 0.09 g of precipitate in 5ml MeOH and vapour diffusing with Et₂O. Crystals analyse as **31**, (NdC₁₀H₂₄N₄O₁₃), analysis (%) calc (found) C 21.19 (21.15), H 4.27 (4.26), N 12.36 (12.08). Selected IR data (cm⁻¹): 3260 (br), 3001.34 (w), 2980.12 (w), 2943.47 (w), 2922.25 (w), 2852.81 (w), 1492.95 (m), 1477.52 (m), 1462.09 (m), 1452.45 (m), 1442.80 (m), 1402.30 (m), 1365.65 (m), 1340.57 (m), 1292.35 (s), 1276.92 (s), 1230.63 (m), 1168.902 (w), 1151.54 (w), 1138.04 (w), 1112.96 (w), 1093.67 (w), 1076.32 (m), 1070.53 (m), 1055.1(s), 1030.02 (s), 1010.73 (m), 997.23 (m), 910.43 (m), 902.72 (m), 887.28 (m), 873.78 (m), 815.92 (m), 754.19 (m), 734.9 (w), 686.68 (m). IR and CHN data for the crystals matches those of the precipitate.

5.2.5 Synthesis of [Gd^{III}(H₄edte)(NO₃)₂][NO₃] (32)

To a stirred solution of H₄edte (0.11 g, 0.46 mmol) in 20ml MeCN was added Gd(NO₃)₃·6H₂O (0.24 g, 0.5 mmol), the reaction was heated for 6 hours at 80°C then stirred at room temperature overnight. A white precipitate was collected, washed with MeCN and air dried, weight = 0.166 g, yield = 57% based on Gd. Colourless block-like crystals of **32** can be grown by dissolving 0.09 g of precipitate in 5 ml MeOH and vapour diffusing with Et₂O. Crystals analyse as **32**, (GdC₁₀H₂₄N₄O₁₃), analysis (%) calc (found) C 20.72 (20.69), H 4.14 (4.15), N 12.08 (11.95). Selected IR data (cm⁻¹): 3270 (br), 3005.20 (w), 2995.55 (w), 2983.98 (w), 2945.40 (w), 2924.18 (w), 2872.10 (w), 2856.67 (w), 1494.88 (m), 1477.52 (m), 1454.38 (m), 1442.80 (m), 1402.30 (m), 1367.58 (m), 1359.86 (m), 1340.57 (m), 1303.92 (s), 1276.92 (s), 1257.63 (m), 1240.27 (m), 1230.63 (m), 1170.83 (w), 1153.47 (w), 1136.11 (w), 1112.96 (w), 1093.67 (w), 1078.24 (m), 1072.46 (m), 1057.03 (s), 1031.95 (s), 1022.31 (m), 1012.66 (m), 997.23 (m), 906.57 (m), 889.21 (m), 875.71 (m), 819.77 (m), 813.99 (m), 756.12 (m), 744.55 (m), 736.83 (m), 690.54 (w), 624.96 (m), 601.81 (m). IR and CHN data for the crystals matches those of the precipitate.

5.2.6 Synthesis of [Tb^{III}(H₄edte)(NO₃)₂][NO₃] (33)

To a stirred solution of H₄edte (0.11 g, 0.46 mmol) in 20ml MeCN was added Tb(NO₃)₃·5H₂O (0.226g, 0.52 mmol), the reaction was stirred at room temperature for 6 hours then filtered and placed in a loosely capped vial. Large colourless block-like crystals suitable for X-ray diffraction formed over 5 days. Repeating the reaction but with heating at 80°C produces a white precipitate which was air dried, weight = 0.208 g, yield = 72% based on Tb. Crystals of **33** can also be grown by dissolving 0.09 g precipitate in 5ml MeOH and vapour diffusing with Et₂O. Crystals from slow evaporation and vapour diffusion analyse as **33**, (TbC₁₀H₂₄N₄O₁₃), analysis (%) calc. (found): C 20.66 (20.96), H 4.16 (4.24), N 12.04 (11.85). Selected IR data (cm⁻¹): 3273 (br), 3007.12 (w), 2995.55 (w), 2945.40 (w), 2924.18 (w), 2874.03 (w), 2856.67 (w), 1494.88 (m), 1477.52 (m), 1454.38 (m), 1402.30 (m), 1367.58 (m), 1359.86 (m), 1340.57 (m), 1303.92 (s), 1278.85 (m), 1257.63 (m), 1230.63 (m), 1170.83 (w), 1153.47 (w), 1136.11 (m), 1112.96 (m), 1093.67 (m), 1074.39 (m), 1057.03 (s), 1033.88 (m), 1022.31 (m), 1012.66 (m), 999.16 (m), 922 (m), 914.29 (m), 906.57 (m), 891.14 (m), 877.64 (m), 819.77 (m), 813.99 (m), 758.05 (m),

746.48 (m), 738.76 (m), 690.54 (m), 626.89 (m), 601.81 (m). IR and CHN data for the crystals obtained by slow evaporation and vapour diffusion match those of the precipitate.

5.2.7 Synthesis of [Dy^{III}(H₄edte)(NO₃)₂][NO₃] (34)

To a stirred solution of H₄edte (0.11 g, 0.46 mmol), in 20 ml MeCN was added Dy(NO₃)₃·5H₂O (0.22 g, 0.5 mmol), the reaction was heated for 6 hours at 80°C then stirred at room temperature overnight. A white precipitate was collected, washed with MeCN and air dried, weight = 0.18 g, yield = 61.5% yield based on Dy. Colourless block-like crystals of **34** were grown by dissolving 0.09 g of precipitate in 5ml MeOH and vapour diffusing with Et₂O. Crystals analyse as **34**, (DyC₁₀H₂₄N₄O₁₃), analysis (%) calc (found) C 20.53 (20.60), H 4.10 (4.13), N 11.97 (11.86). Selected IR data (cm⁻¹): 3270 (br), 3007.12 (w), 2997.48 (w), 2987.84 (w), 2947.33 (w), 2926.11 (w), 2874.03 (w), 2858.60 (w), 1496.81 (m), 1477.52 (m), 1454.38 (m), 1402.30 (m), 1367.58 (m), 1340.57 (m), 1305.85 (s), 1278.58 (s), 1257.63 (m), 1240.27 (m), 1230.63 (m), 1107.83 (w), 1153.47 (w), 1136.11 (w), 1112.96 (w), 1093.67 (w), 1074.39 (m), 1057.03 (s), 1033.88 (s), 1024.24 (m), 1012.66 (m), 999.16 (m), 922 (m), 914.29 (m), 906.57 (m), 891.14 (m), 877.64 (m), 819.77 (m), 813.99 (m), 758.05 (m), 746.48 (m), 738.76 (m), 690.54 (w), 626.89 (m), 603.74 (m). IR and CHN data for the crystals matches those of the precipitate.

5.2.8 Synthesis of [Ho^{III}(H₄edte)(NO₃)₂][NO₃] (35)

To a stirred solution of H₄edte (0.11g, 0.46 mmol), in MeCN 20ml was added Ho(NO₃)₃·5H₂O (0.22 g, 0.5 mmol), the reaction was heated for 6 hours at 80°C then stirred at room temperature overnight. A light pink precipitate was collected, washed with MeCN and air dried, weight = 0.22 g, yield = 74.2% yield based on Ho. Crystals of **35** can be grown by mixing 0.09 g precipitate in 5 ml MeOH, filtering the remaining solid and vapour diffusing the solution with Et₂O. Small light pink crystals suitable for single crystal X-ray diffraction form over a few weeks along with colourless crystals. Due to the small yield and difficult separation, CHN and IR data were only collected for the precipitate. Precipitate analyses as **35**, (HoC₁₀H₂₄N₄O₁₃), (%) calc. (found): C 20.45 (20.49), H 4.12 (4.12), N 11.93 (11.60). Selected IR data (cm⁻¹): 3076 (br), 2916.47 (w), 2862.46 (w), 2762.16 (w), 2686.93 (w), 1687.77 (w), 1473.66 (m), 1429.30 (m), 1404 .22 (m), 1334.78

(m), 1294.28 (s), 1257.63 (m), 1172.76 (w), 1147.68 (m), 1109.11 (w), 1089.82 (m), 1062.81 (s), 1031.95 (m), 1018.45 (w), 1003.02 (w), 912.36 (m), 898.86 (m), 875.71 (w), 817.85 (w), 754.19 (m), 740.69 (w), 688.61 (w), 671.25 (w), 623.03 (w), 605.67 (w).

5.2.9 Synthesis of [Er^{III}(H₄edte)(NO₃)₂][NO₃] (36)

To a stirred solution of H₄edte (0.11 g, 0.46 mmol) in 20 ml MeCN was added Er(NO₃)₃·5H₂O (0.22 g, 0.5 mmol), the reaction was stirred at room temperature for 6 hours then filtered and placed in a loosely capped vial. Large pink crystals suitable for X-ray diffraction formed overnight, these were oven dried overnight at 60°C, weight = 0.048 g, Yield = 32% based on Er. Crystals appear to be hygroscopic, analysing as **36**·1.5H₂O, (ErC₁₀H₂₇N₄O_{14.5}), analysis (%) calc. (found): C 19.62 (19.82), H 4.36 (4.32), N 11.44 (11.14). Selected IR data (cm⁻¹): 3095 (br), 3009.05 (w), 2987.84 (w), 2962.76 (w), 2920.32 (w), 2854.74 (w), 2681.14 (w), 1641.48 (w), 1487.17 (m), 1471.74 (m), 1433.16 (m), 1390.72 (m), 1361.79 (m), 1323.21 (s), 1294.28 (s), 1247.99 (m), 1236.41 (m), 1174.69 (w), 1147.68 (m), 1116.32 (w), 1074.39 (m), 1057.03 (m), 1030.02 (m), 1008.80 (m), 910.43 (m), 896.93 (m), 873.78 (m), 860.28 (w), 819.77 (m), 813.99 (m), 754.19 (m), 746.48 (m), 721.4 (m), 707.9 (m), 613.38 (m).

5.3 Results and Discussion

5.3.1 Synthesis

The series [Ln(H₄edte)(NO₃)₂][NO₃] where Ln = Y^{III} (**28**), La^{III} (**29**), Pr^{III} (**30**), Nd^{III} (**31**), Gd^{III} (**32**), Tb^{III} (**33**), Dy^{III} (**34**), Ho^{III} (**35**), Er^{III} (**36**) were synthesised by reacting the nitrate salt of the respective lanthanide ion with H₄edte in a roughly 1:1 ratio in MeCN. The reactions were heated to 80°C for 6 hours followed by cooling to room temperature and stirring overnight. For compounds **28-35**, a precipitate forms which can be recrystallised into block-like crystals suitable for single crystal X-ray diffraction. In the case of **36** however, only very small amounts of precipitate formed; a better yield was achieved by collecting the single crystals formed after the reaction was conducted at room temperature. Crystals of **36** appear to be hygroscopic; repeated CHN analysis consistently indicated the presence of water even after oven drying at 60°C. Single crystals of **33** were obtained using two methods; first by slow evaporation of the mother liquor and second by vapour diffusion of re-dissolved precipitate. Crystals from both methods and the precipitate were of the same composition judging by CHN and IR data. For **35**, a precipitate readily forms when the reaction is heated; however, it shows poor solubility in MeOH compared to the other analogues'. Crystals could be grown by saturating 5 ml of MeOH with precipitate and vapour diffusing the solution with Et₂O. However, only a small amount of crystals of **35** formed along with a much larger crop of colourless crystals. The two crystal types were hard to separate due to the similarity in appearance so only the precipitate was analysed by IR and CHN.

When the synthesis was performed under basic conditions (1-4 equivalents of base w.r.t. H₄edte), there was little to no precipitate obtained and crystals did not form by slow evaporation or vapour diffusion of the mother liquor with Et₂O or THF. Isolation of monomeric lanthanide compounds using other salts such as acetate, acetylacetonate and chloride in a 1:1 ratio with H₄edte was also unsuccessful. Reaction of EuCl₃ and H₄edte in a 1:1 ratio did not yield the europium monomer, even with an excess of NaNO₃ as a nitrate source. No monomeric complexes containing cerium were successfully isolated. Syntheses of promethium, samarium, thulium or lutetium monomers were not attempted.

5.3.2 Discussion of the {Ln(H₄edte)} Series' Structure

The series [Ln(H₄edte)(NO₃)₂][NO₃] Ln = Y^{III} (28), La^{III} (29), Pr^{III} (30), Nd^{III} (31), Gd^{III} (32), Tb^{III} (33), Dy^{III} (34), Ho^{III} (35), Er^{III} (36) are all isostructural (Figure 5.4) and crystallise in the monoclinic space group $P2_1/n$. The asymmetric unit of the series contains one {Ln} complex molecule and one lattice nitrate anion, the unit cell consists of four {Ln} molecules and four lattice nitrate anions.

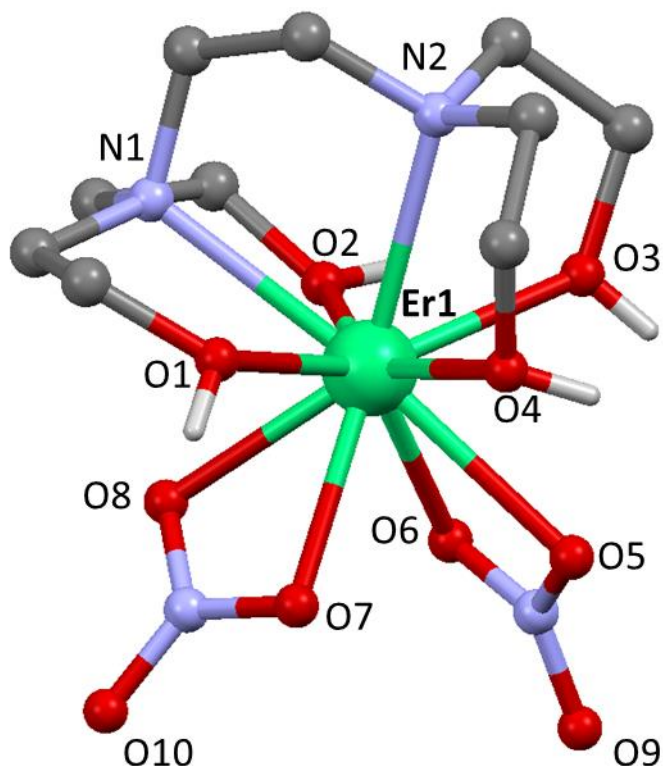


Figure 5.4: Molecular structure of [Er(H₄edte)(NO₃)₂][NO₃], used as representative of the series structure, H atoms on carbons and lattice nitrate have been omitted for clarity. Atom colours: grey, C; blue, N; red, O; white, H; green, Er^{III}.

<i>Empirical formula</i>	<i>Y₁C₁₀H₂₄N₅O₁₃</i>	<i>La₁C₁₀H₂₄N₅O₁₃</i>	<i>Pr₁C₁₀H₂₄N₅O₁₃</i>	<i>Nd₁C₁₀H₂₄N₅O₁₃</i>
Molar mass (g mol ⁻¹)	511.23	561.23	562.42	566.57
Crystal System	Monoclinic	Monoclinic	Monoclinic	Monoclinic
Space Group	<i>P</i> ₂₁ / <i>n</i>	<i>P</i> ₂₁ / <i>n</i>	<i>P</i> ₂₁ / <i>n</i>	<i>P</i> ₂₁ / <i>n</i>
<i>a</i> (Å)	8.3903(9)	8.5522(8)	8.4838(12)	8.4567(14)
<i>b</i> (Å)	15.5108(18)	15.6896(15)	15.656(2)	15.635(3)
<i>c</i> (Å)	14.0995(16)	14.2784(13)	14.2310(18)	14.209(2)
<i>α</i> (deg)	90	90	90	90
<i>β</i> (deg)	96.477(3)	96.590(2)	96.538(3)	96.559(4)
<i>γ</i> (deg)	90	90	90	90
<i>V</i> (Å ³)	1823.2(2)	1903.23(17)	1877.9(2)	1866.4(3)
<i>Z</i>	4	4	4	4
<i>T</i> (K)	100	100	100	100
<i>λ</i> (Å)	0.71073	0.71073	0.71073	0.71073
<i>ρ</i> _{calc} (g/cm ³)	1.862	1.959	1.989	2.016
<i>μ</i> (mm ⁻¹)	3.280	2.322	2.673	2.861
^a <i>R</i> ₁	0.0656	0.0368	0.0370	0.0458
^b <i>wR</i> ₂	0.1099	0.0931	0.0919	0.1140
Goodness of fit	0.9913	1.1005	0.9678	0.9747
F(000)	1048	1120	1128	1132
Reflections	3203	3177	3209	3297
Parameters	271	262	262	262
Restraints	4	4	6	12

Table 5.1: Crystallographic data for complexes **28** - **31**.

$${}^a R_1 = \sum ||F_o| - |F_c|| / \sum |F_o|$$

$${}^b wR_2 = [\sum [w(F_o^2 - F_c^2)^2] - \sum [(F_o^2)^2]]^{1/2} \quad \text{where} \quad w = 1/[\sigma^2(F_o^2) + (0.2P)^2] \quad \text{and} \quad P = [F_o^2 + 2F_c^2]/3$$

<i>Empirical formula</i>	<i>Gd₁C₁₀H₂₄N₅O₁₃</i>	<i>Tb₁C₁₀H₂₄N₅O₁₃</i>	<i>Dy₁C₁₀H₂₄N₅O₁₃</i>	<i>Ho₁C₁₀H₂₄N₅O₁₃</i>	<i>Er₁C₁₀H₂₄N₅O₁₃</i>
Molar mass (g mol ⁻¹)	579.58	581.25	584.83	587.26	589.59
Crystal System	Monoclinic	Monoclinic	Monoclinic	Monoclinic	Monoclinic

Space Group	<i>P</i> ₂₁ / <i>n</i>				
<i>a</i> (Å)	8.4207(8)	8.39610(10)	8.3986(12)	8.3885(8)	8.37170(10)
<i>b</i> (Å)	15.5891(14)	15.5415(2)	15.535(2)	15.5228(15)	15.4996(2)
<i>c</i> (Å)	14.1601(13)	14.11330(10)	14.120(2)	14.1106(13)	14.0949(2)
α (deg)	90	90	90	90	90
β (deg)	96.574(5)	96.5410(10)	96.595(3)	96.5047(19)	96.5680(10)
γ (deg)	90	90	90	90	90
<i>V</i> (Å ³)	1846.6(3)	1829.628(13)	1830.0(3)	1825.56(17)	1816.92(3)
<i>Z</i>	4	4	4	4	4
<i>T</i> (K)	100	100	100	100	100
λ (Å)	0.71073	0.71073	0.71073	0.71073	0.71073
ρ_{calc} (g/cm ³)	2.085	2.110	2.123	2.137	2.155
μ (mm ⁻¹)	3.672	3.946	4.164	4.415	4.700
^a <i>R</i> ₁	0.0297	0.0168	0.0269	0.0292	0.0186
^b <i>wR</i> ₂	0.0634	0.0247	0.0699	0.0677	0.0263
Goodness of fit	0.9821	1.0750	1.001	0.9121	0.9889
F(000)	1148	1152	1156	1160	1164
Reflections	4215	4202	4195	3858	4147
Parameters	274	275	274	274	275
Restraints	4	4	4	4	4

Table 5.2: Crystallographic data for complexes **32 - 36**.

$${}^a R_1 = \frac{\sum ||F_o| - |F_c||}{\sum |F_o|}$$

$${}^b wR_2 = \frac{[\sum [w(F_o^2 - F_c^2)^2] - \sum [(F_o^2)^2]]^{\frac{1}{2}}}{\sum [w(F_o^2 + 2F_c^2)]^{\frac{1}{2}}}$$
 where $w = 1/[\sigma^2(F_o^2) + (0.2P)^2]$ and $P = [F_o^2 + 2F_c^2]/3$

The structure of the {Ln} complex molecule consists of a 10-coordinate central ion chelated by one H₄edte ligand and two bidentate nitrates. The +3 charge of the central ion is balanced by the two nitrate ligands and the remaining lattice nitrate anion. H₄edte provides an {N₂O₄} donor set with all oxygen donors remaining protonated. The average bond lengths (Tables 5.3-5.5) between H₄edte and the central ion correlate well with ionic radii of the central ion: {La} having the longest average bond length (largest ionic radius) and {Er} having the shortest average bond length (smallest ionic radius).²¹

Bond	Distance (Å)	Bond	Distance (Å)	Bond	Distance (Å)
Y1-O1	2.438(3)	La1-O1	2.575(2)	Pr1-O1	2.528(3)
Y1-O2	2.424(3)	La1-O2	2.573(2)	Pr1-O2	2.534(4)
Y1-O3	2.413(4)	La1-O3	2.559(3)	Pr1-O3	2.500(3)
Y1-O4	2.391(4)	La1-O4	2.546(2)	Pr1-O4	2.524(4)
Y1-O5	2.614(4)	La1-O5	2.641(2)	Pr1-O5	2.621(4)
Y1-O6	2.438(4)	La1-O6	2.576(2)	Pr1-O6	2.538(4)
Y1-O7	2.472(4)	La1-O7	2.600(2)	Pr1-O7	2.561(3)
Y1-O8	2.438(4)	La1-O8	2.599(2)	Pr1-O8	2.553(3)
Y1-N1	2.634(4)	La1-N1	2.730(3)	Pr1-N1	2.702(4)
Y1-N2	2.612(4)	La1-N2	2.745(3)	Pr1-N2	2.697(4)
Average	2.416(4)	Average	2.563(3)	Average	2.521(4)

Table 5.3: Ligand to metal bond lengths for complexes 28 - 30.

Bond	Distance (Å)	Bond	Distance (Å)	Bond	Distance (Å)
Nd1-O1	2.513(4)	Gd1-O1	2.459(2)	Tb1-O1	2.459(2)
Nd1-O2	2.506(4)	Gd1-O2	2.480(2)	Tb1-O2	2.439(2)
Nd1-O3	2.484(3)	Gd1-O3	2.439(2)	Tb1-O3	2.442(2)
Nd1-O4	2.506(4)	Gd1-O4	2.462(2)	Tb1-O4	2.413(2)
Nd1-O5	2.616(4)	Gd1-O5	2.612(2)	Tb1-O5	2.605(2)
Nd1-O6	2.521(4)	Gd1-O6	2.477(2)	Tb1-O6	2.459(2)
Nd1-O7	2.540(4)	Gd1-O7	2.504(2)	Tb1-O7	2.493(2)
Nd1-O8	2.533(4)	Gd1-O8	2.481(2)	Tb1-O8	2.453(2)
Nd1-N1	2.682(5)	Gd1-N1	2.655(3)	Tb1-N1	2.641(2)
Nd1-N2	2.684(5)	Gd1-N2	2.639(3)	Tb1-N2	2.622(2)
Average	2.505(5)	Average	2.460(3)	Average	2.438(2)

Table 5.4: Ligand to metal bond lengths for complexes 31-33

Bond	Distance (Å)	Bond	Distance (Å)	Bond	Distance (Å)
Dy1-O1	2.426(3)	Ho1-O1	2.445(2)	Er1-O1	2.426(2)
Dy1-O2	2.452(3)	Ho1-O2	2.417(3)	Er1-O2	2.404(2)
Dy1-O3	2.410(3)	Ho1-O3	2.423(2)	Er1-O3	2.413(2)
Dy1-O4	2.436(3)	Ho1-O4	2.400(2)	Er1-O4	2.384(2)
Dy1-O5	2.610(3)	Ho1-O5	2.436(2)	Er1-O5	2.625(2)
Dy1-O6	2.458(3)	Ho1-O6	2.440(2)	Er1-O6	2.426(2)
Dy1-O7	2.487(3)	Ho1-O7	2.476(2)	Er1-O7	2.463(2)
Dy1-O8	2.445(3)	Ho1-O8	2.436(2)	Er1-O8	2.421(2)
Dy1-N1	2.630(3)	Ho1-N1	2.626(3)	Er1-N1	2.621(2)
Dy1-N2	2.614(3)	Ho1-N2	2.606(3)	Er1-N2	2.595(2)
Average	2.430(3)	Average	2.421(3)	Average	2.407(2)

Table 5.5: Ligand to metal bond lengths for complexes 34-36

The series packs in rows running parallel with the crystallographic *a*-axis in a head to tail arrangement. Within the chains, short contacts exist between the C-H protons of the ethylenediamine backbone and the unbound oxygen atoms of the ligand nitrates (Figure 5.5). Between the chains, packing is facilitated by the lattice nitrate acting as a H-bond acceptor for protonated ligand oxygen atoms (Figure 5.6).

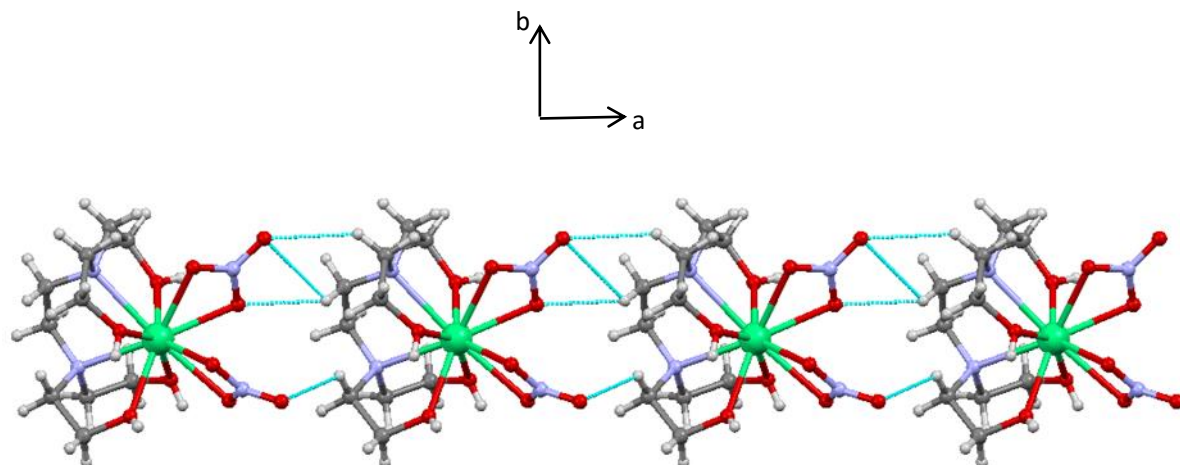


Figure 5.5: *Crystal packing of 36 (representative of entire series), viewed down the crystallographic c-axis; shows intra-chain short contacts (blue lines) along the a-axis.*

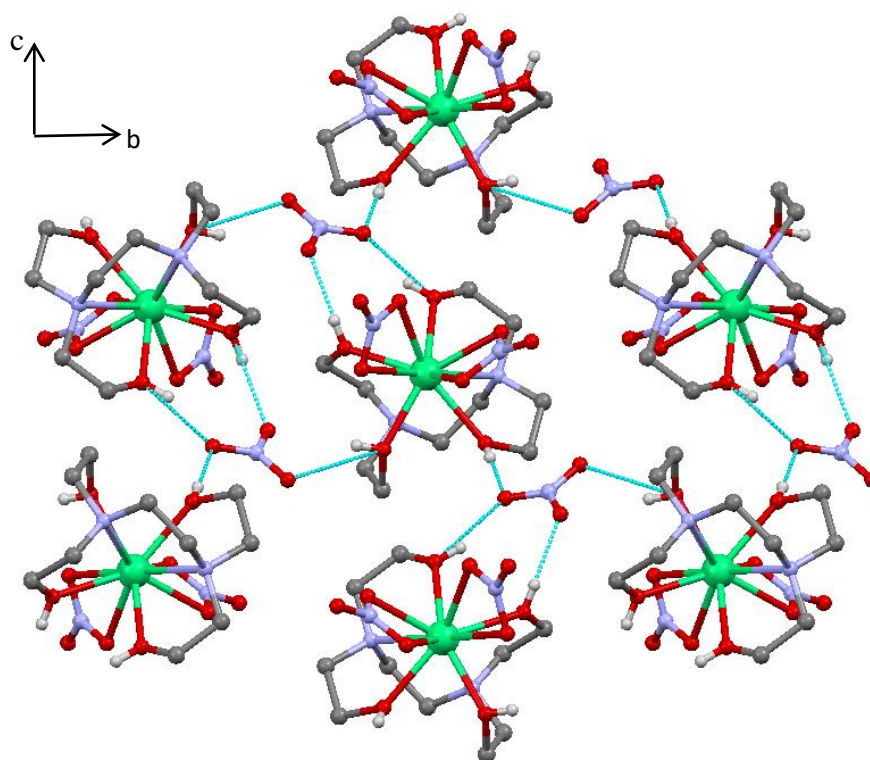


Figure 5.6: *Crystal packing of 36 (representative of entire series), viewed down the crystallographic a-axis; shows inter-chain H-bonding (blue lines).*

The central lanthanide geometry was analysed in detail as deviations from ideal geometry have significant effects on the magnetic properties of the complexes.¹⁴⁻¹⁶ Firstly, the

programme SHAPE was used to analyse the Ln^{III} coordination sphere geometry.²² The programme uses the atoms bound to the central ion as vertices to form a geometric polyhedron around the ion. The programme generates ‘continuous shape measurement’ (ChSM) values for all of the possible polyhedra for a particular coordination number; for example, a 10-coordinate central ion can make 13 different polyhedra. The geometry with the lowest ChSM value corresponds to the closest match, a value of zero would indicate a perfect match i.e. zero distortion from the ideal dimensions of that polyhedron. The ChSM values for the series are relatively high compared to the literature,^{2,3} indicative of significant distortion from ideal D_{4d} symmetry. The ChSM values for the β -diketonates range between 0.54-0.75, with [Dy(acac)₃(H₂O)₂] having the highest at 2.016, the only 10-coordinate SIM has a ChSM value of 2.13.²⁰

The two geometries with the lowest ChSM values are bicapped square antiprismatic *J17* (D_{4d}) and sphenocoronal *J87* (C_{2v}), see Table 5.6. Compounds **29** - **31** are closest to sphenocoronal geometry with the remaining closest to bicapped square antiprismatic; the difference between the two geometries is however quite small.

	<i>Bicapped square antiprismatic (J17)</i>	<i>Sphenocoronal (J87)</i>
28 (Y ^{III})	<u>2.991</u>	3.216
29 (La ^{III})	3.675	<u>3.610</u>
30 (Pr ^{III})	3.508	<u>3.471</u>
31 (Nd ^{III})	3.432	<u>3.420</u>
32 (Gd ^{III})	<u>3.173</u>	3.280
33 (Tb ^{III})	<u>3.118</u>	3.269
34 (Dy ^{III})	<u>3.071</u>	3.225
35 (Ho ^{III})	<u>2.994</u>	3.203
36 (Er ^{III})	<u>2.899</u>	3.168

Table 5.6: ChSM values for the series with optimal geometry underlined

As well as SHAPE measurements, the distortion of the Ln^{III} ions can be seen in a few other ways: the first is if we draw two mean planes through the atoms {N2, O1, O2, O8} and {O3, O4, O6, O7} (referred to herein as basal planes, Figure 5.7); in ideal D_{4d} symmetry these planes should be parallel, however, we can see that they are offset by a dihedral angle. The dihedral angles decrease in the order **29** > **30** > **31** > **32** > **28** > **33** > **34** > **35** > **36** which roughly correlates to the trend in decreasing ChSM values.

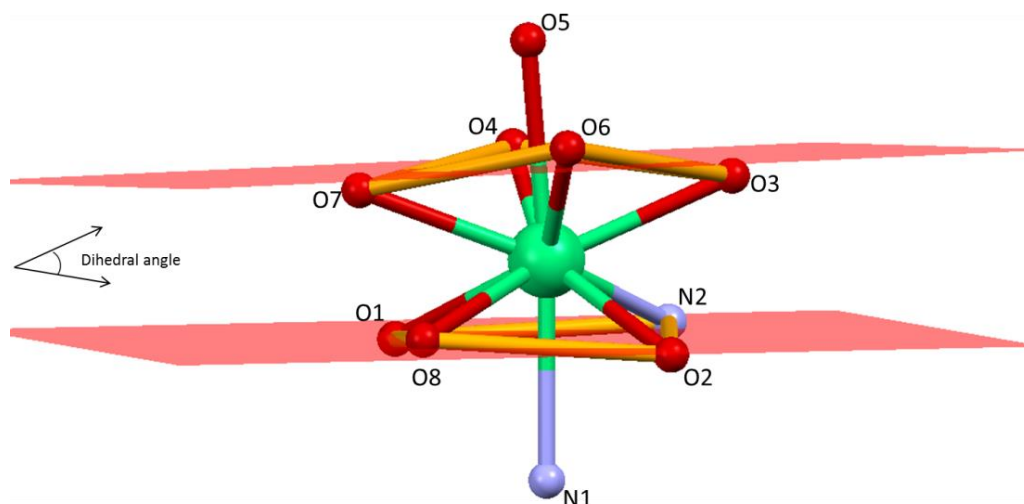


Figure 5.7: Mean planes drawn through {O3, O4, O6, O7} (top plane) and {N2, O1, O2, O8} (bottom plane).

<i>Complex</i>	<i>Dihedral angle</i>
28 (Y ^{III})	3.07°
29 (La ^{III})	3.71°
30 (Pr ^{III})	3.49°
31 (Nd ^{III})	3.43°
32 (Gd ^{III})	3.20°
33 (Tb ^{III})	3.06°
34 (Dy ^{III})	3.04°
35 (Ho ^{III})	2.89°
36 (Er ^{III})	2.96°

Table 5.7: List of dihedral angles. An angle of zero would represent parallel alignment.

Another distortion is observed in the basal planes of the structure: the atoms in the planes {N2, O1, O2, O8} and {O3, O4, O6, O7} should occupy the corners of a square, but instead they form distorted trapezoids (Figure 5.8). These trapezoids are offset by a skew angle Φ which in ideal D_{4d} symmetry should be 45°. The skew angles were calculated by measuring the torsion angles between each of the corner atoms by using the centroids of the planes as reference (the centroid being the mid-point between the four corner atoms of the individual trapezoid). Changes in the skew angle induces transverse anisotropy and leads to a higher probability of QTM.²⁴

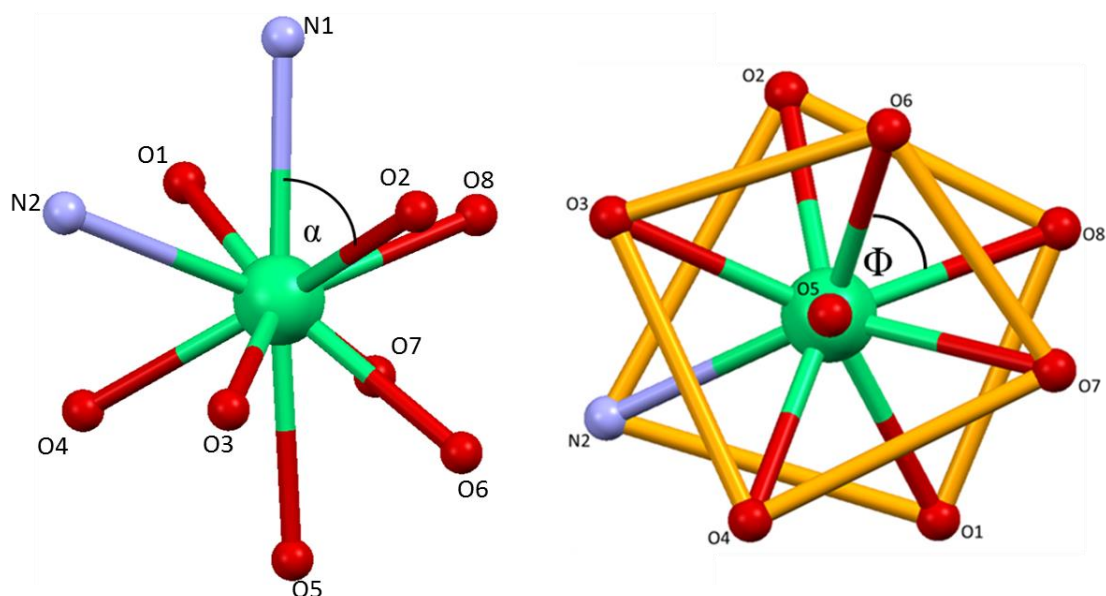


Figure 5.8: Depictions of the α angle (left) and skew angle Φ between distorted trapezoids (right).

Complex	Skew angle Φ
28 (Y ^{III})	40.6°
29 (La ^{III})	40.2°
30 (Pr ^{III})	40.3°
31 (Nd ^{III})	40.3°
32 (Gd ^{III})	40.4°
33 (Tb ^{III})	40.5°
34 (Dy ^{III})	40.5°
35 (Ho ^{III})	40.5°
36 (Er ^{III})	40.6°

Table 5.8: List of skew angle distortions. 45° is the ideal angle for D_{4d} symmetry.

As well as the skew angle Φ , the α angle²³ (Figure 5.8) has significant effects on 4f SIM magnetic performance. The ‘magic angle’ of 54.74° represents the mathematical ideal for a square antiprism, angles larger than this indicate tetragonal compression of the crystal field along the C_4 axis. Tetragonal compression can increase the axial magnetic anisotropy for ‘oblate’ ions such as Tb^{III} and Dy^{III}, as observed in {LnPc₂}.¹⁷

The average α angles for the series, listed in Table 5.9, are all above 54.74° indicating tetragonal compression of the crystal field.

<i>Complex</i>	<i>Average α</i>
27 (Y ^{III})	64.6°
28 (La ^{III})	64.8°
29 (Pr ^{III})	64.9°
30 (Nd ^{III})	64.8°
31 (Gd ^{III})	64.7°
32 (Tb ^{III})	64.7°
33 (Dy ^{III})	64.6°
34 (Ho ^{III})	64.7°
35 (Er ^{III})	64.5°

Table 5.9: List of average α angles.

5.4 Magnetism

5.4.1 Static Magnetic Properties of {Tb(H₄edte)} (33)

The temperature dependent χT product of **33** was measured for a polycrystalline sample in a 1 kOe dc field between 2 – 300 K (Figure 5.9). The room temperature χT value of 11.80 cm³ K mol⁻¹ is in good agreement with the calculated value of 11.76 cm³ K mol⁻¹ for a single Tb^{III} ion (⁷F₆, $S = 3$, $L = 3$, $J = 6$, $g_J = 3/2$).

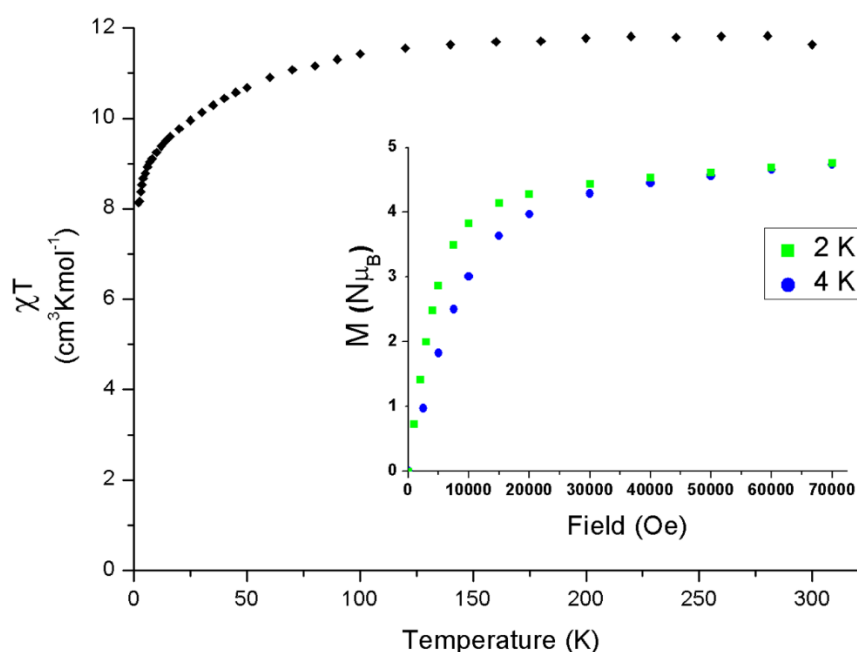


Figure 5.9: Temperature dependent magnetic susceptibility and magnetisation vs. field for **33** (inset).

As T decreases, χT also gradually decreases, reaching a minimum of 8.14 cm³ K mol⁻¹ at 2 K. The gradual decrease in χT is due to depopulation of excited Stark sublevels and also possibly intermolecular antiferromagnetic interactions at low temperatures.

Field dependency of the magnetisation of **33** was measured at 2 and 4 K in the range 0 – 70 kOe (inset Figure 5.9). The magnetisation increases up to 4.73 N μ_B at 70 kOe but does not reach the expected saturation value of 9 N μ_B for a free Tb^{III} ion - indicative of significant magnetic anisotropy.

5.4.2 Dynamic Magnetic Properties of **33**

Ac susceptibility measurements were made down to 1.8 K to see if **33** showed slow magnetic relaxation. To increase the chances of observing slow relaxation, the measurements were made in a relatively high frequency ac field (957 Hz) and with an applied 1 kOe dc field.

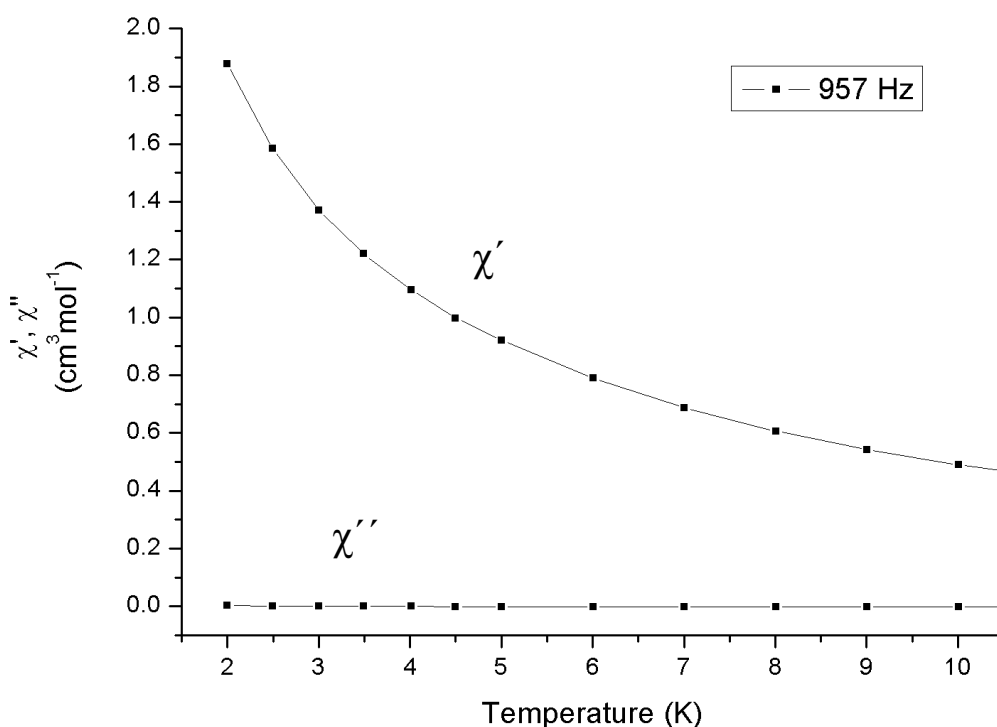


Figure 5.10: Ac susceptibility measurements for **33** with a 1 kOe applied dc field.

However, even under these conditions, there was no out-of-phase susceptibility and no deviation in the in-phase susceptibility down to 1.8 K. The lack of slow relaxation is

probably due to the highly distorted Tb^{III} crystal field.⁵ For Tb^{III}, a non-Kramer's ion with an integer number of electrons (f^8), the ground m_J doublet's degeneracy can be easily removed with small distortions from ideal D_{4d} symmetry which results in fast QTM.

5.4.3 Static Magnetic Properties of {Dy(H₄edte)} (34)

The temperature dependent χT product of **34** was measured for a polycrystalline sample in a 1 kOe dc field between 2 – 300 K (Figure 5.11). **34** has a room temperature χT value of 14.20 cm³ K mol⁻¹ which is in good agreement with the calculated value of 14.15 cm³ K mol⁻¹ for a single Dy^{III} ion ($^6H_{15/2}$, $S = 5/2$, $L = 5$, $J = 15/2$, $g_J = 4/3$).

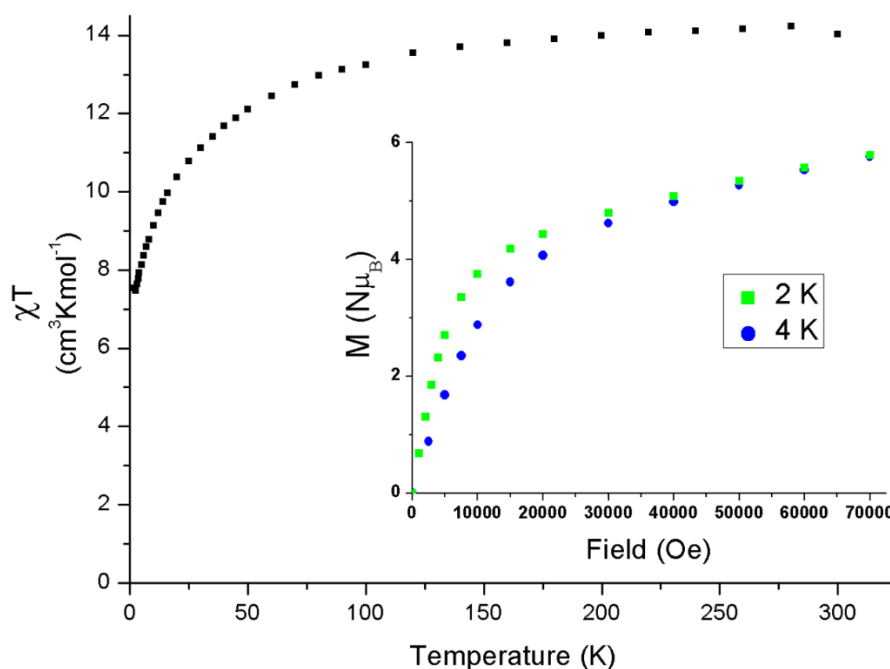


Figure 5.11: Temperature dependent magnetic susceptibility and magnetisation vs. field (inset) for **34**

χT decreases gradually as T is lowered, reaching a minimum of 7.53 cm³ K mol⁻¹ at 2 K. The gradual decrease in χT is due to depopulation of excited Stark sublevels and possibly due to intermolecular antiferromagnetic interactions at low temperatures.

Field dependency of the magnetisation of **33** was measured at 2 and 4 K in the range 0 – 70 kOe. The magnetisation increases up to 5.75 N μ_B at 70 kOe but does not reach the expected saturation value of 10 N μ_B for a free Dy^{III} ion - indicative of significant magnetic anisotropy.

5.4.4 Dynamic Magnetic Properties of 33

The ac data for **34** was also collected in the presence of a 1 kOe field in order to suppress QTM which is prevalent for single Dy^{III} ions in low symmetry crystal fields. The results show a frequency dependent decrease in χ' with a concomitant increase in χ'' .

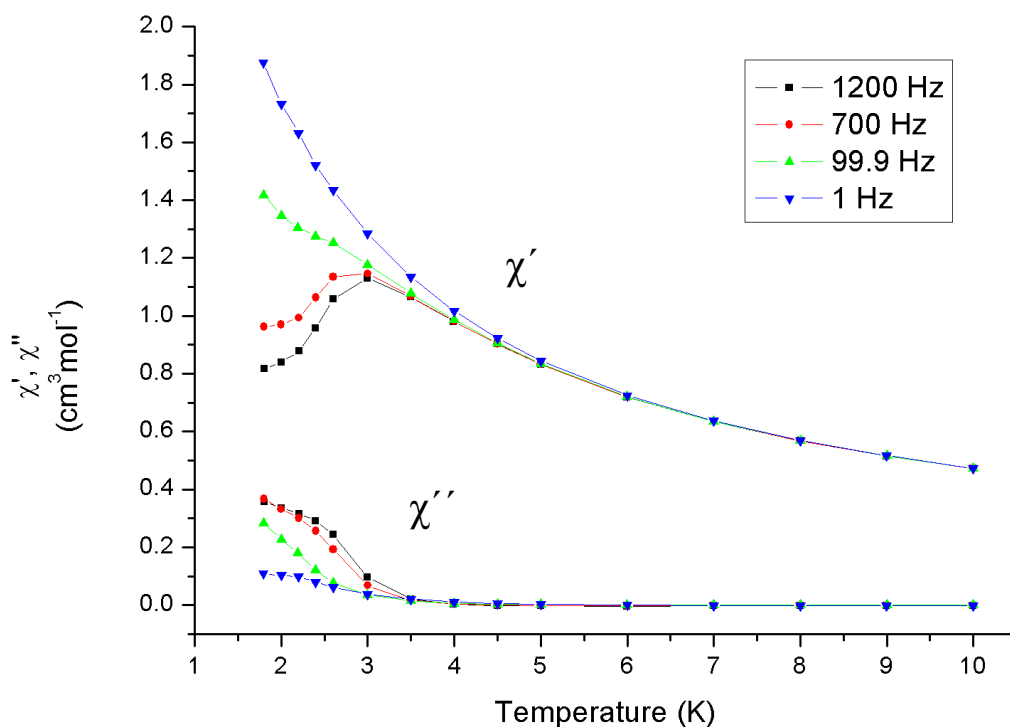


Figure 5.12: Ac susceptibility measurements for 33 with a 1 kOe applied dc field.

The χ'' data only shows onset of slow relaxation of the magnetisation down to 1.8 K, making an Arrhenius analysis to extract an energy barrier impossible. The signals themselves may have a double hump feature; similar to those reported [Dy(acac)₃(H₂O)₂]; indicative that QTM was not fully suppressed by the dc field. The transverse anisotropy in **34** is expected to be higher than in [Dy(acac)₃(H₂O)₂] due to greater distortions from ideal D_{4d} symmetry.

5.5 Conclusions and Future Work

The aim to synthesise Ln^{III} monomeric complexes using the ligand H₄edte was successful with the analogues Ln^{III} = Y^{III}, La^{III}, Pr^{III}, Nd^{III}, Gd^{III}, Tb^{III}, Dy^{III}, Ho^{III}, Er^{III} being isolated and characterised using CHN, IR and single crystal X-ray crystallography. The Tb^{III} and Dy^{III} monomers were also magnetically characterised; the Tb^{III} analogue showed no slow relaxation of the magnetisation in ac measurements, even in the presence of a dc field. The Dy^{III} analogue on the other hand showed the onset of slow magnetic relaxation, but due to the highly distorted crystal field and the resulting prevalence of QTM, the U_{eff} value was very low and could not be estimated using an Arrhenius analysis. Although attempts were made to synthesise monomeric complexes using different counter ions (chloride, acetate, acac), further work would certainly involve trying other counterions which could perhaps enforce a more axial and/or less distorted D_{4d} crystal field thus improving the magnetic performance.

5.6 References

- (1) N. Ishikawa, M. Sugita, T. Ishikawa, S.-Y. Koshihara, Y. Kaizu, *J. Am. Chem. Soc.* 125 (2003) 8694-8695.
- (2) H.L.C. Feltham, S. Brooker, *Coord. Chem. Rev.* 276 (2014) 1-33.
- (3) D.N. Woodruff, R.E.P. Winpenny, R. Layfield, *Chem. Rev.* 113 (2013) 5110–5148.
- (4) J.D. Rinehart, J.R. Long, *Chem. Sci.* 2 (2011) 2078–2085.
- (5) S.D. Jiang, B.W. Wang, S. Gao, *Molecular Nanomagnets and Related Phenomena*, Chapter 2, pp 111-141.
- (6) X.-L. Wang, L.-C. Li, D.-Z. Liao, *Inorg. Chem.* 49 (2010) 4735-4737.
- (7) N. Zhou, Y. Ma, C. Wang, G.F. Xu, J.-K. Tang, J.-X. Xu, S.-P. Yan, P. Cheng, L.-C. Lia, D.-Z. Liao, *Dalton Trans.* (2009) 8489-8492.
- (8) A. Yamashita, A. Watanabe, S. Akine, T. Nabeshima, M. Nakano, T. Yamamura, T. Kajiwarra, *Angew. Chem. Int. Ed.* 50 (2011) 4016-4019.
- (9) H. L. C. Feltham, Y. Lan, F. Klçwer, L. Ungur, L. F. Chibotaru, A. K. Powell, S. Brooker, *Chem. Eur. J.* 17 (2011) 4362-4365.
- (10) M.-E. Boulon, G. Cucinotta, J. Luzon, C. Degl’Innocenti, M. Perfetti, K. Bernot, G. Calvez, A. Caneschi, R. Sessoli, *Angew. Chem. Int. Ed.* 52 (2013) 350-354.
- (11) G. Cucinotta, M. Perfetti, J. Luzon, M. Etienne, P.-E. Car, A. Caneschi, G. Calvez, K. Bernot, R. Sessoli, *Angew. Chem. Int. Ed.* 51 (2012) 1606-1610.
- (12) M. A. AlDamen, J. M. Clemente-Juan, E. Coronado, C.M. Gastaldo, A. Gaita-Arino, *J. Am. Chem. Soc.* 130 (2008) 8874-8875.
- (13) M. A. AlDamen, S. Cardona-Serra, J. M. Clemente-Juan, E. Coronado, A. Gaita-Arino, C. Marti-Gastaldo, F. Luis, O. Montero, *Inorg. Chem.* 48 (2009) 3467-3479.
- (14) S.-D. Jiang, B.-W. Wang, G. Su, Z.-M. Wang, S. Gao, *Angew. Chem. Int. Ed.* 49 (2010) 7448-7451.
- (15) Y. Bi, Y.-N. Guo, L. Zhao, Y. Guo, S.-Y. Lin, S.-D. Jiang, J. Tang, B.-W. Wang, S. Gao, *Chem. Eur. J.* 17 (2011) 12476-12481.
- (16) G.-J. Chen, Y.-N. Guo, J.-L. Tian, J. Tang, W. Gu, X. Liu, S.-P. Yan, P. Cheng, D.-Z. Liao, *Chem. Eur. J.* 18 (2012) 2484-2487.
- (17) J. Tang, P. Zhang, *Lanthanide Single Molecule Magnets*, Springer, (2015).
- (18) A. Bhunia, M.T. Gamer, L. Ungur, L.F. Chibotaru, A.K. Powell, Y. Lan, P.W. Roesky, F. Menges, C. Riehn, G. Niedner-Schatteburg, *Inorg. Chem.* 51 (2012) 9589-9597.

- (19) Y.X. Wang, W. Shi, H. Li, Y. Song, L. Fang, Y. Lan, A.K. Powell, W. Wernsdorfer, L. Ungur, L.F. Chibotaru, M. Shen, P. Cheng, *Chem. Sci.* 3 (2012) 3366–3370.
- (20) V.E. Campbell, R. Guillot, E. Riviere, P.T. Brun, W. Wernsdorfer T. Mallah, *Inorg. Chem.* 52 (2013) 5194–5200.
- (21) P.W. Atkins, T.L. Overton, J.P. Rourke, M.T. Weller, F.A. Armstrong, *Inorganic Chemistry* 6th edition Oxford University Press 2014.
- (22) M. Llunell, D. Casanova, J. Cirera, P. Alemany, S. Alvarez, ‘SHAPE: Program for the Stereochemical Analysis of Molecular Fragments by Means of Continuous Shape Measures and Associated Tools’, Version 2.1, 2013, Barcelona.
- (23) P. Zhang, Y.N. Guoa, J. Tang, *Coord. Chem. Rev.* 257 (2013) 1728–1763.
- (24) L. Sorace, C. Benelli, D. Gatteschi, *Chem. Soc. Rev.* 40 (2011) 3092–3104.
- (25) S. Takamatsu, T. Ishikawa, S-Y. Koshihara, N. Ishikawa, *Inorg. Chem.* 46 (2007) 7250-7252.

6. 3d Metal Complexes with H₄edte

6.1 Introduction

The majority of complexes synthesised using H₄edte contain 1st row transition metals,¹⁻¹³ the most prevalent being manganese.¹⁻⁵ A search of the CSD found {Mn₃}, {Mn₄}, {Mn₆}, {Mn₈}, {Mn₁₀}, {Mn₁₂}, {Mn₁₈} complexes and a {Mn₂₀} complex, the latter being the largest complex containing the ligand¹ (Figure 6.1). Unfortunately, none of these complexes were confirmed as SMMs.

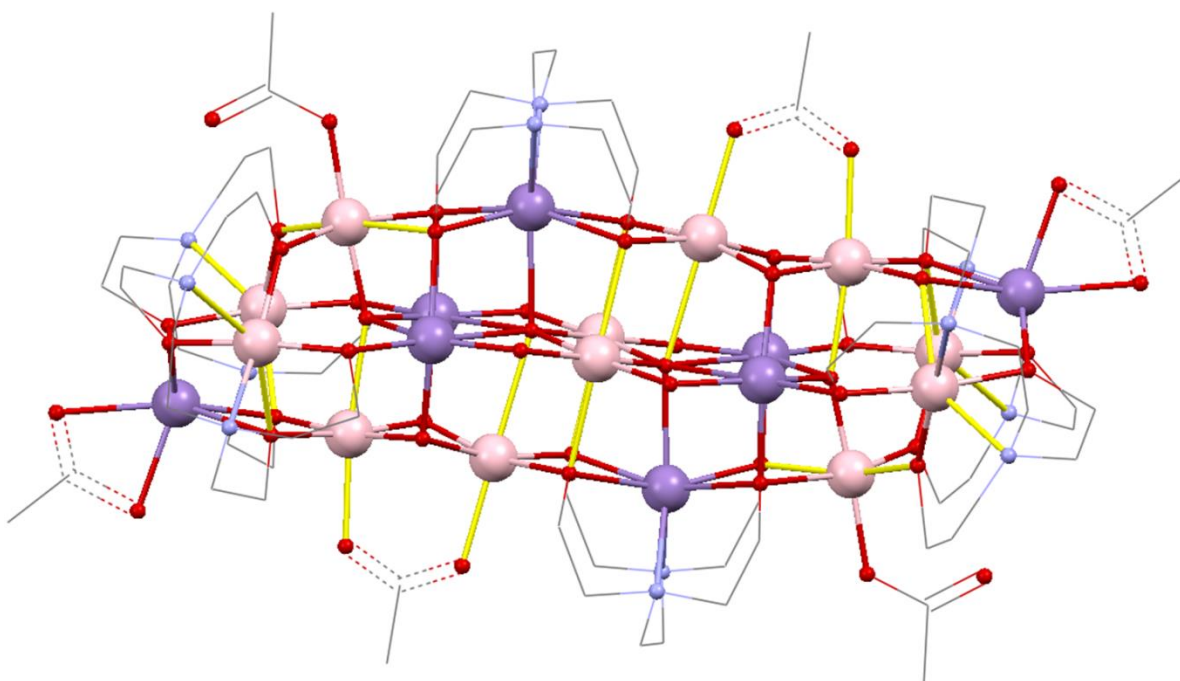


Figure 6.1: Molecular structure of Christou *et. al.*'s {Mn₂₀} complex. Atom colours: Mn^{III}, pink; Mn^{II}, purple; O, red; N, blue; C, grey. H-atoms and counter ions omitted. Jahn-Teller elongated axes of Mn^{III} ions highlighted in yellow. CSD ref. code: WIXHUH.

The {Mn₂₀} complex [Mn^{II}₈Mn^{III}₁₂O₈(OH)₄(O₂CMe)₆(edte)₆](ClO₄)₂·5H₂O was isolated in a 20% yield from a reaction of H₄edte with Mn(O₂CMe)₂·4H₂O, NEt₃ and NaClO₄ in 1 : 2 : 2 : 1 ratio in MeOH. The reaction was stirred at room temperature for 1 h and crystals were grown by layering the mother liquor with Et₂O. The complex however showed no out-of-phase (χ'') ac susceptibility peaks down to 1.8 K. Fitting of the dc susceptibility data gave a ground state spin of $S = 8$. Another interesting example of a high nuclearity manganese

complex using H₄edte was reported by Tong *et. al.*² (Figure 6.2). Their {Mn^{III}₁₈} complex was synthesised by reacting copper powder, Mn(ClO₄)₂·6H₂O, H₄edte, NaOH, sodium dicyanamide (NaN(CN)₂, Nadca), in a 4 : 1 : 1 : 4 : 2 ratio in mixed DMF and MeOH solvent at 80°C. After several months slow evaporation, crystals of [Mn^{III}₁₈(μ₃-O)₈(μ₅-O)(edte)₆][HCO₂]₂ deposited in 30% yield.

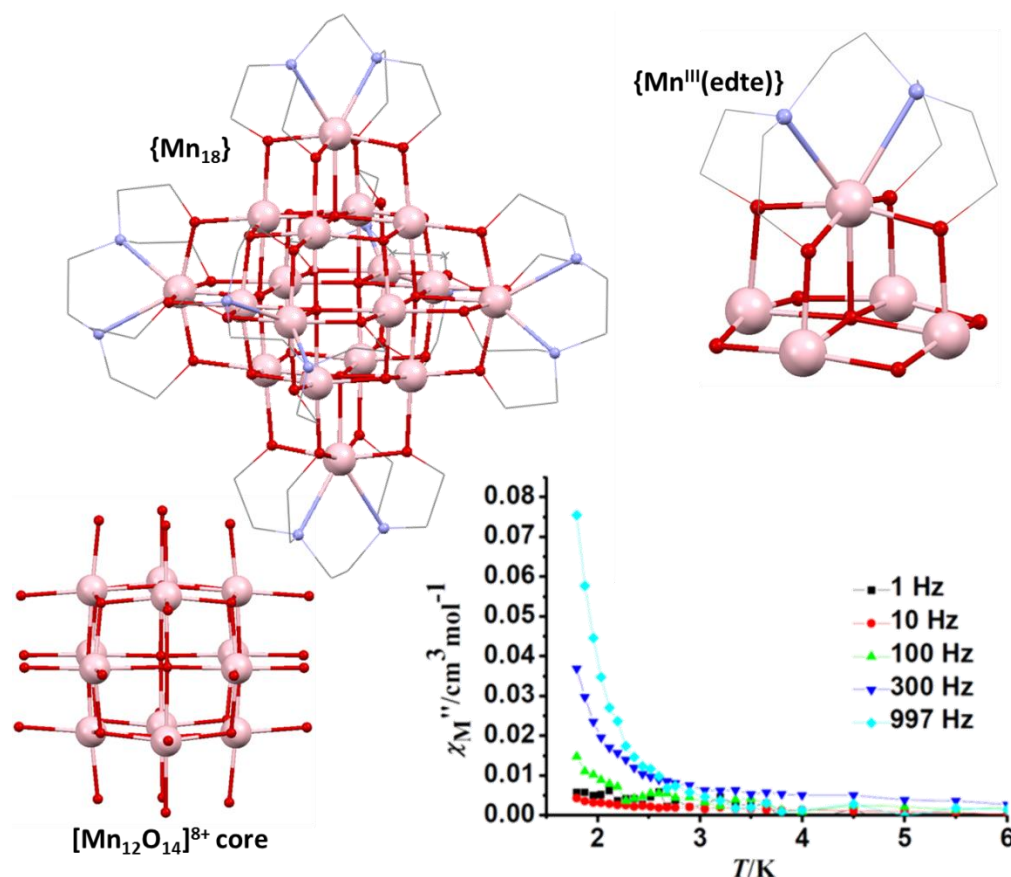


Figure 6.2: Molecular structure of [Mn^{III}₁₈(μ₃-O)₈(μ₅-O)(edte)₆][HCO₂]₂ (top left), lattice formates and H-atoms omitted. {Mn₁₂} cuboctahedron core (bottom left). {Mn^{III}(edte)} subunit shown bridging to a face of the {Mn₁₂} core (top right). Out-of-phase ac susceptibility data (bottom right).² Atom colours: Mn^{III}, pink; O, red; N, blue; C, grey.

CSD ref. code: VEZNUL.

The complex is centrosymmetric, crystallising in the cubic space group $Ia\bar{3}$. The overall structure consists of a [Mn^{III}₁₈(μ₃-O)₈(μ₅-O)₆(edte)₆]²⁺ cation and two formate anions, the latter produced by hydrolysis of DMF in the reaction.¹⁴ The {Mn₁₈}²⁺ cation can be broken down into a central [Mn₁₂O₁₄]⁸⁺ cuboctahedron core with peripheral [Mn^{III}(edte)]¹⁻ metalloligand subunits capping each of the six square faces. The ligand acts as a {N₂O₄} donor set to its Mn^{III} ion, with its four alkoxo arms acting as μ₂-bridges to Mn^{III} ions in the

cuboctahedron core. The complex exhibited the onset of χ'' signals which were frequency dependent, however no maxima were observed down to 1.8 K.

Synthesis of iron complexes with H₄edte toward new SMMs has also been explored; though not to the same extent as manganese. There have been {Fe₄}, {Fe₅}, {Fe₆} and {Fe₁₂} complexes reported,⁵⁻⁷ however, none were confirmed SMMs. The only confirmed SMMs containing H₄edte are the 3d-4f complexes reported by Murrie *et. al.*,¹¹ Christou *et. al.*¹² and Powell *et. al.*¹³ described in Chapter 2, and the {Dy₃} triangle reported by Cheng *et. al.*¹⁵ described in Section 5.1.

Research into the synthesis and applications of coordination complexes containing H₄edte has not been limited to molecular magnetism. Structural studies have been reported on monomeric Ag^I,¹⁶ Cu^{II},⁸ Ba^{II} and Ca^{II} complexes¹⁷ as well as a Cu^{II} dimeric complex.⁹ A structural, electrochemical and magnetic study has also been reported on a dimeric {V^V₂(edte)} complex.¹⁰ A new antimicrobial agent containing silver ions: {Ag^I₂(H₄edte)₂} has been reported with improved antimicrobial activity over the approved drug fluconazole.¹⁸ A {Pd^{II}(H₄edte)} complex was found to be a new and effective catalyst for the Suzuki-Miyaura reaction in water; cross coupling arylbromides with phenylboronic acids.¹⁹ Finally, a number of group 4 complexes: {Zr₂(edte)₂}, {Hf₂(edte)₂}, {Ti₄(edte)₃(OⁱPr)₄}, {Ti₄(edte)(OⁱPr)₁₂}, {Zr₃(edte)(OⁱPr)₈} and {Hf₃(edte)(OⁱPr)₈} were synthesised and studied as initiators for ring opening polymerisations of *rac*-lactide.^{20,21}

The aim of the work carried out for this chapter was to synthesise new mixed 3d-3d' complexes using the ligand H₄edte. Initially, the aim was to synthesise {M(H₄edte)} monomeric complexes for use as building blocks toward a rational synthetic approach, via deprotonation of the ligand's hydroxyethyl arms. In total, nine new complexes with the ligand H₄edte are presented, in addition, a complex containing the related ligand H₄pdte is also presented. Five monomeric {M^{II}(H_nedte)} complexes were synthesised where M^{II} = Mn^{II}, Co^{II}, Ni^{II} and Zn^{II}. Higher nuclearity structures are also reported: including an interesting mixed valence {Mn^{II}Mn^{III}} complex, a homometallic {Cu₈} complex, a heterometallic {Cu₆Ni₂} complex and finally a relatively large heterometallic {Mn^{III}₁₀Cu^{II}₅} complex. All complexes were characterised by single crystal X-ray diffraction and their structures are presented. Magnetic studies of the {Mn^{III}₁₀Cu^{II}₅} complex were also conducted, investigating temperature dependent dc susceptibility, and temperature dependent ac-susceptibility to search for SMM properties.

6.2 Experimental

6.2.1 Synthesis of [Mn(H₄edte)(NO₃)] [NO₃] (37)

To a stirred solution of Mn(NO₃)₂·4H₂O (7.14 g, 28.44 mmol) in MeCN (200 ml) was added slowly with vigorous stirring, a solution of H₄edte (6.56 g, 27.76 mmol) in MeCN (100 ml). The reaction was stirred at room temperature for 17 hours, forming a light pink precipitate which was filtered and air dried. Yield = 80% (9.52 g) Crystals of **37** were grown by dissolving 0.1 g of precipitate in 5 ml EtOH and vapour diffusing with Et₂O. Precipitate analyses as **37**·H₂O, (Mn₁C₁₀H₂₆N₄O₁₁), analysis (%) calc. (found) C 27.72 (27.70), H 6.05 (6.08), N 12.93 (12.64). Selected IR peaks (cm⁻¹): 3209 (br), 2976.26 (w), 2955.04 (w), 2916.47 (w), 2868.24 (w), 1656.91 (w), 1448.59 (m), 1417.73 (s), 1377.22 (m), 1361.79 (m), 1288.49 (s), 1261.49 (s), 1151.54 (w), 1112.96 (w), 1070.53 (s), 1058.96 (s), 1043.52 (s), 1030.02 (s), 1004.95 (m), 914.29 (m), 891.14 (w), 817.85 (m), 754.19 (m), 732.97 (m), 717.54 (w). IR data of the crystals and precipitate were a match.

6.2.2 Synthesis of [Co(H₄edte)(H₂O)] [NO₃]₂ (38)

To a stirred solution of H₄edte (0.24 g, 1 mmol) in 15 ml MeCN was added a solution of Co(NO₃)₂·6H₂O (0.349 g, 1.2 mmol) in 20 ml MeCN. The reaction was stirred at room temperature for 4 hours then filtered and the mother liquor put in a loosely capped vial. Reddish-pink block-like crystals of **38** suitable for X-ray diffraction were grown over a few days via vapour diffusion of the mother liquor with Et₂O. Yield = 32% (0.14 g). Crystals analyse as **38**, (Co₁C₁₀H₂₆N₄O₁₁), analysis (%) calc. (found) C 27.46 (27.76) H 5.99 (6.05) N 12.81 (12.63). Selected IR data (cm⁻¹) 3220 (br), 2980.12 (w), 2953.12 (w), 2922.25 (w), 2872.10 (w), 1761.07 (w), 1670.41 (w), 1448.59 (m), 1417.73 (s), 1361.79 (m), 1284.63 (s), 1257.63 (s), 1147.68 (m), 1112.96 (m), 1072.46 (s), 1060.88 (s), 1043.52 (s), 1031.95 (s), 1008.80 (m), 922.00 (m), 900.79 (m), 817.85 (m), 758.05 (m), 736.83 (m), 719.47 (m), 659.68 (br), 603.74 (m).

6.2.3 Synthesis of [Co(H₄edte)Cl][Cl] (39)

To a stirred solution of H₄edte (0.96 g, 4 mmol) in 50 ml MeCN was added a solution of CoCl₂·6H₂O (1 g, 4.2 mmol) in 50 ml MeCN. The reaction was stirred at room temperature for 6 hours then filtered. A blueish purple precipitate, yield = 48% (0.713 g), was collected and dried in an oven overnight at 60 °C. Dark purple block-like single crystals of **39** were grown overnight by dissolving 0.1 g precipitate in 5 ml MeOH and vapour diffusing with Et₂O. Both crystals and precipitate analyse as **39**, (Co₁C₁₀H₂₄N₂O₄Cl₂), analysis of precipitate (%) calc. (found): C 32.80 (32.60) H 6.61 (6.63) N 7.65 (7.52). Selected IR peaks (cm⁻¹): 3336.96 (w), 3132 (w) 2989.76 (m), 2972.40 (m), 2953.12 (m), 2904.89 (m), 2874.03 (m), 2804.59 (w), 2735.15 (w), 1473.66 (w), 1458.23 (w), 1410.01 (w), 1367.58 (w), 1356 (w), 1336.71 (w), 1313.57 (w), 1288.49 (w), 1276.92 (w), 1255.70 (w), 1246.06 (w), 1217.12 (w), 1172.76 (w), 1143.83 (w), 1107.18 (m), 1053.17 (s), 1037.74 (s), 989.52 (m), 925.86 (m), 918.15 (m), 910.43 (m), 891.14 (m), 854.49 (m), 752.26 (w), 740.69 (m), 719.47 (s), 630.74 (m), 603.74 (m). IR data of crystals and precipitate were a match.

6.2.4 Synthesis of [Ni(H₄edte)(EtOH)][NO₃]₂ (40)

To a stirred solution of H₄edte (3.85 g, 16.30 mmol) in MeCN (50 ml), was added a solution of Ni(NO₃)₂·6H₂O (5.19 g, 17.84 mmol) in MeCN (120 ml). The reaction was stirred at room temperature for 21 hours, forming a blue precipitate. The precipitate was filtered and dried in a desiccator for 1 week, followed by oven drying at 60 °C for 3 days. Yield = 80.30% (5.73 g). Precipitate analyses as [Ni(H₄edte)][NO₃]₂·H₂O, (Ni₁C₁₀H₂₆N₄O₁₁), analysis (%) calc. (found): C 27.48 (27.28) H 6.00 (5.98) N 12.82 (12.55), selected IR data (cm⁻¹): 3443.05 (w), 3138 (br), 2964.69 (w), 2916.47 (w), 2872.10 (w), 1672.34 (w), 1500.67 (w), 1440.87 (m), 1410.01 (m), 1390.72 (m), 1300.07 (s), 1165.04 (w), 1136.11 (w), 1109.01 (w), 1074.39 (m), 1051.24 (s), 1033.88 (s), 997.23 (m), 906.57 (m), 895.00 (m), 873.78 (w), 823.63 (m), 763.84 (m), 738.76 (m), 702.11 (m). Crystals of **40** suitable for X-ray diffraction were grown by dissolving 0.1 g precipitate in 5 ml EtOH and vapour diffusing with Et₂O. Crystals appear to be hygroscopic, analysing as [Ni(H₄edte)(EtOH)][NO₃]₂·H₂O, (Ni₁C₁₂H₃₀N₄O₁₁), analysis (%) calc. (found): C 29.83 (29.90) H 6.68 (6.35) N 11.60 (12.00). Selected IR data (cm⁻¹): 3120 (br), 2982.05 (w), 2918.40 (w), 2879.82 (w), 1054.53 (w), 1477.52 (w), 1433.16 (m), 1400.37 (m), 1381.08 (m), 1311.64 (s), 1253.77 (m), 1242.20 (m), 1174.69 (w), 1159.26 (w), 1134.18 (w), 1103.32 (w), 1072.46 (m), 1045.45 (s), 1003.02 (w), 933.58 (m), 910.43 (m), 885.36 (w),

871.85 (w), 823.61 (w), 779.27 (w), 758.05 (w), 736.83 (m), 711.76 (w), 702.11 (w), 621.1 (w).

6.2.5 Synthesis of [Ni(H₄pdte)][NO₃]₂ (41)

The ligand H₄pdte was synthesised as described in Section 3.2.1. To a stirred solution of H₄pdte (0.1 g 0.4 mmol) in 15 ml EtOH was added Ni(NO₃)₂·6H₂O (0.41 g, 0.12 mmol) and the reaction stirred at room temperature for 6 hours then filtered. Blue plate-like single crystals of **41** were grown over a few days via vapour diffusion of the mother liquor with Et₂O. Yield 23% (0.1 g). Crystals analyse as **41**, Ni₁C₁₁H₂₆N₄O₁₀, analysis (%) calc. (found): C 30.51 (30.66) H 6.05 (6.20) N 12.94 (12.87). Selected IR data (cm⁻¹): 3100 (br), 2989.76 (w), 2972.40 (w), 2956.97 (w), 2931.90 (w), 1469.81 (m), 1435.09 (m), 1411.94 (s), 1375.29 (m), 1346.36 (m), 1292.35 (s), 1276.92 (s), 1228.70 (m), 1168.901 (w), 1136.11 (w), 1111.03 (w), 1060.88 (m), 1043.52 (m), 1020.38 (s), 1003.02 (m), 972.16 (w), 925.86 (w), 910.43 (w), 895.0 (m), 868 (w), 819.77 (m), 746.48 (w), 717.54 (w), 698.25 (w), 669.32 (w), 642.32 (w), 619.17 (m).

6.2.6 Synthesis of [Zn(H₃edte)][NO₃] (42)

To a stirred solution of H₄edte (0.24 g, 1 mmol) and NEt₃ (0.14 ml, 1 mmol) in MeCN (20 ml) was added Zn(NO₃)₂·6H₂O (0.3 g, 1 mmol). The reaction was heated at 90°C for 6 hours, then cooled to room temperature and filtered. The mother liquor was placed in a loosely capped vial, from which single crystals of **42** suitable for X-ray diffraction grew via slow evaporation over 10 days. Yield 31% (0.11 g) Crystals analyse as **42**, (Zn₁C₁₀H₂₃N₃O₇), analysis (%) calc. (found): C 33.12 (32.95) H 6.39 (6.40) N 11.59 (11.33). Selected IR data (cm⁻¹): 2960.83 (w), 2920.32 (w), 2881.75 (w), 2850.88 (w), 2739.01 (w), 2681.14 (w), 1797 (br), 1473.66 (m), 1448.59 (w), 1402.30 (m), 1388.79 (m), 1377.22 (m), 1361.79 (m), 1342.50 (m), 1311.64 (m), 1300.07 (s), 1300.07 (s), 1282.71 (s), 1242.20 (m), 1161.19 (w), 1120.68 (w), 1084.03 (m), 1062.81 (m), 1051.24 (s), 1039.67 (m), 1020.38 (m), 1004.95 (m), 922 (m), 910.43 (m), 881.50 (m), 866.07 (m), 825.56 (m), 763.84 (w), 746.48 (m), 713.69 (w), 698.25 (w), 611.45 (m).

6.2.7 Synthesis of $[Mn^{II}Mn^{III}(Hedte)(H_3edte)][ClO_4]$ (43)

To a stirred solution of H₄edte (0.25 g, 1.05 mmol) and NEt₃ (0.15 ml, 1 mmol) in 20 ml MeOH was added Mn(ClO₄)₂ (0.13 g, 0.51 mmol). The reaction was stirred at room temperature for 4 hours then filtered to isolate a red precipitate of **44**, yield = 60% (0.1 g). Small portions of the mother liquor were taken for vapour diffusion with Et₂O, red block-like single crystals of **43** suitable for X-ray diffraction formed over the next few weeks. Precipitate analyses as **43**, (Mn₂C₂₀H₄₄N₄O₁₂Cl₁), analysis (%) calc. (found): C 35.43 (35.27) H 6.54 (6.54) N 8.26 (8.64). Selected IR data (cm⁻¹): 3516.35 (w), 2960.83 (w), 2845.10 (m), 1454.38 (w), 1435.09 (w), 1367.58 (w), 1352.14 (w), 1330.93 (w), 1292.35 (w), 1265.35 (w), 1247.99 (w), 1074.39 (s), 1066.67 (s), 1028.09 (m), 1004.95 (m), 914.29 (m), 887.28 (m), 846.78 (w), 752.26 (w), 736.83 (w), 667.39 (m), 621.10 (s), 605.67 (w). IR data of crystals and precipitate confirms they are the same compound.

6.2.8 Synthesis of

$[Cu_8(OAc)_2(MeOH)_2(OH)_2(H_3edte)_2(H_2edte)_2(OBz)_2][NO_3]_2[PF_6]_2 \cdot MeOH \cdot H_2O$ (44)

To a stirred solution of H₄edte (0.06 g, 0.25 mmol) in MeOH (20 ml) was added Cu(OAc)₂·2H₂O (0.06 g, 0.3 mmol). This was stirred at room temperature for 30 minutes, then Mn(NO₃)₂·4H₂O (0.16 g, 0.635 mmol) was added, followed 10 minutes later by NaOBz (0.07 g, 0.5 mmol). The reaction was stirred for 5 hours then NH₄PF₆ (0.26 g, 1.6 mmol) was added and the reaction stirred overnight then filtered. Small portions of the mother liquor were taken and vapour diffused with Et₂O, forming small dark green needles suitable for X-ray diffraction over 4 months, yield 1.1% (0.001 g). Unfortunately a good CHN match for the crystals was not obtained. IR data on a sample of crystals was collected; selected IR data (cm⁻¹): 3649.44 (w), 3335 (br), 2970.48 (w), 2920.32 (w), 2885.60 (w), 1593.25 (w), 1541.18 (m), 1489.10 (w), 1473.66 (w), 1444.66 (w), 1415.80 (m), 1383.01 (m), 1317.43 (w), 1271.13 (w), 1246.06 (w), 1178.55 (w), 1055.10 (m), 931.65 (w), 912.36 (w), 898.86 (w), 835.21 (s), 763.84 (w) 721.4 (m), 667.39 (m).

6.2.9 Synthesis of



To a stirred solution of [Ni(H₄edte)][NO₃]₂·H₂O (0.103 g, 0.24 mmol) and NEt₃ (0.13 ml, 0.93 mmol) in MeOH (30 ml), was added Cu(NO₃)₂·3H₂O (0.0562 g, 0.23 mmol) and the reaction heated at 80 °C for 6 hours then cooled to room temperature and filtered. Crystals suitable for X-ray diffraction of **45** were grown over 5 weeks by vapour diffusion of the filtrate with diethyl ether, yield 2.6 % (0.002 g). Crystals of **45** were hygroscopic, analysing as **45**·2H₂O, (Cu₆Ni₂C₄₄H₁₁₄N₁₄O₄₄), analysis (%) calc. (found): C 25.88 (25.44) H 5.63 (5.20) N 9.60 (9.50). Selected IR data (cm⁻¹): 3649.44 (w), 3335 (br), 2970.48 (w), 2920.32 (w), 2885.60 (w), 1593.25 (w), 1541.18 (m), 1489.10 (w), 1473.66 (w), 1444.66 (w), 1415.80 (m), 1383.01 (m), 1317.43 (w), 1271.13 (w), 1246.06 (w), 1178.55 (w), 1055.10 (m), 931.65 (w), 912.36 (w), 898.86 (w), 835.21 (s), 763.84 (w) 721.4 (m), 667.39 (m).

6.2.10 Synthesis of



Cu(OAc)₂·2H₂O (0.02 g, 0.10 mmol), [Mn(H₄edte)][NO₃]₂·H₂O (0.09 g, 0.21 mmol) and NaOBz (0.032 g, 0.22 mmol) were added to 9 ml MeOH and dissolved using sonication. The solution was then placed in a Teflon sleeve and sealed inside a metal solvothermal vessel. The oven was heated at a rate of 5 °C min⁻¹ to 60 °C and kept at this temperature for 12 hours, followed by cooling to room temperature at 0.1 °C min⁻¹. The solution was placed in a loosely capped vial and left to slowly evaporate. Small dark brown crystals suitable for X-ray diffraction grew over 6 – 8 weeks, yield 5.5% (0.004 g). Unfortunately a satisfactory CHN analysis was not obtained for a crystalline sample of **46**. IR data was collected on a sample of crystals; selected IR data (cm⁻¹): 3350 (br), 2978.19 (w), 2916.47 (w), 2879.82 (w), 1593.25 (m), 1537.32 (m), 1492.95 (w), 1473.66 (w), 1444.73 (w), 1411.94 (m), 1386.86 (s), 1342.50 (m), 1263.42 (w), 1176.62 (w), 1153.47 (w), 1105.25 (w), 1080.17 (w), 1058.96 (m), 1022.31 (m), 929.72 (w), 916.22 (m), 896.93 (m), 827.49 (w), 721.40 (s), 669.32 (s).

6.3 Results and Discussion

6.3.1 Synthesis

6.3.1.1 Synthesis of 3d Monomers

All of the monomers were synthesised by reacting a molar equivalent of H₄edte with a slight excess of the respective metal salt. Crystals of [Mn(H₄edte)(NO₃)] [NO₃] (**37**) can be grown by reacting H₄edte with Mn(NO₃)₂·4H₂O in EtOH, then vapour diffusing the reaction solution with Et₂O. A microcrystalline sample of the monohydrate of **37** can be synthesised when the reaction is carried out in MeCN, this can then be recrystallised by dissolving 0.1 g in 5 ml EtOH and vapour diffusing with Et₂O; giving crystals of **37**. It was found that adding a solution of H₄edte to a solution of Mn(NO₃)₂ gave a better yield when scaling up the synthesis. Crystals of [Ni(H₄edte)(EtOH)] [NO₃]₂ (**40**) were grown in a similar manner to **37**, either by vapour diffusion of Et₂O into the EtOH mother liquor, or by recrystallising the precipitate retrieved from the synthesis in MeCN. The precipitate was very hygroscopic; left in the open it would quickly begin to oil. The dried precipitate analyses as the monohydrate, whilst the crystals appear to be hygroscopic, analysing as **40**·H₂O. [Co(H₄edte)Cl] [Cl] (**39**) was the only monomer to be isolated with a chloride counter ion. [Zn(H₃edte)] [NO₃] (**42**) was the only monomer whose preparation required the addition of base; no complexes, monomeric or otherwise, were ever isolated in the presence of base in a ligand to metal ratio of 1:1. [Ni(H₄pdte)] [NO₃]₂ (**41**) was the only monomeric complex that was isolated with the H₄pdte ligand. Syntheses were attempted using H₄pdte and M(NO₃)_x in a 1:1 ratio where M = Cr^{III}, Mn^{II}, Co^{II}, Ni^{II} and Cu^{II}. Interestingly, Cr(NO₃)₃ appears to react with H₄pdte in EtOH under ambient conditions and without base - judging by a colour change from deep blue to green - which was not observed with H₄edte under the same conditions (no colour change). Unfortunately, slow evaporation of the mother liquor and vapour diffusion of the mother liquor with Et₂O only led to a dark green oil from which no complexes were isolated. Similar colour changes as observed for the H₄edte reactions were observed for Co(NO₃)₂ and Cu(NO₃)₂, however, again only oil was obtained from treatment of the mother liquors. Mn(NO₃)₂ did not show the same colour change; a dark brown – instead of a light pink – solution forms, suggesting

oxidation to Mn^{III} in solution. No complexes were ever obtained from reaction of Mn^{II} with H₄pdte.

6.3.1.2 Synthesis of Polynuclear Complexes

The initial aim was to use 3d monomeric complexes as building blocks toward larger complexes via deprotonation of the ligand's hydroxyethyl arms. However, the monomers appeared to be unstable to base and were not successfully used in such a rational manner. Two new complexes were serendipitously synthesised using monomeric reagents; [Cu₆Ni₂(H₂edte)₄(NO₃)₂(H₂O)₂(MeOH)₂(OH)₂][NO₃]₄·2MeOH (45) and [Mn₁₀Cu₅O₈(OBz)₈(Hedte)₄(H₂O)₄][NO₃]₄·8MeOH (46). The synthesis of 45 utilised precipitate of the {Ni(H₄edte)} monomer as a starting material but the final structure contains Cu^{II} chelated by H₂edte²⁻ instead of Ni^{II}. Interestingly though 45 does not form when the preformed Ni^{II} complex is omitted for Ni(NO₃)₂ and H₄edte. Complex 46 uses {Mn(H₄edte)} as a starting material, again however the ligand is found chelating Cu^{II} in the final structure. Crystals of 46 were initially isolated from a vapour diffusion (with Et₂O) of the mother liquor of a reaction of {Mn(H₄edte)}, Cu(OAc)₂·H₂O and NaOBz in the ratio 2:1:2. The reaction was heated at 90°C for 6 hours in ≈ 20 ml MeOH in a watch glass covered beaker. The crystallisation time was over 3 months, the yield miniscule and the reaction could not be reproduced. To try and reproduce the results a number of different approaches were followed: the same physical conditions were used but with optimised reagent ratios to match those in the complex, using different combinations of Mn^{II} and Cu^{II} salts with H₄edte, using different types of base and using different counter ions such as NH₄PF₆, NaBF₄, and NaSbF₆. All were unsuccessful. Reaction of oxo-centered triangles such as [Mn₃O(OBz)₆(py)₂(H₂O)] with [Cu(H₃edte)]₂ (complex 1) were also unsuccessful. When the reaction was carried out under solvothermal conditions, heating to 60°C for 12 h, and the reaction solution left to slowly evaporate, crystals of 46 were isolated after 6-8 weeks. The reaction is reproducible using the solvothermal method, however the yield is still relatively poor. During the slow evaporation, 46 crystallises out at the same time as colourless and green non-single crystals which were not identified. Manual separation of these crystals was performed, followed by checking unit cells of multiple {Mn₁₀Cu₅} crystals to ensure sample uniformity. The unit cell of every crystal

checked (> 10) matched that of the final structure of **46**, however, a good match of CHN data was still not obtained. During synthetic work to reproduce **46**, two other complexes were isolated: $[\text{Mn}^{\text{II}}\text{Mn}^{\text{III}}(\text{Hedte})(\text{H}_3\text{edte})][\text{ClO}_4]$ (**43**) and $[\text{Cu}_8(\text{OAc})_2(\text{OMe})_2(\text{OH})_2(\text{H}_3\text{edte})_2(\text{H}_2\text{edte})_2(\text{OBz})_2][\text{NO}_3]_2[\text{PF}_6]_2 \cdot \text{MeOH} \cdot \text{H}_2\text{O}$ (**44**). Complex **44** was initially synthesised when H₄edte, NEt₃, Mn(ClO₄)₂ and CuCl₂·2H₂O were reacted in the molar ratio 1 : 1 : 0.5 : 0.6 in MeOH. Vapour diffusion of the mother liquor with Et₂O produced crystals of **43** but in amongst a green oil. When the CuCl₂ reagent was removed, a red precipitate forms which analyses as the crystals of **43** by CHN and IR. Crystals were grown by both vapour diffusion of the mother liquor and recrystallizing the precipitate; by dissolving ≈ 0.05 g in 5 ml MeOH and vapour diffusing with Et₂O. Complex **44** was synthesised by reacting H₄edte, Cu(OAc)₂·2H₂O, Mn(NO₃)₂·4H₂O, NaOBz and NH₄PF₆ in a 1 : 1.2 : 2.4 : 2 : 6.4 molar ratio, followed by vapour diffusion of the mother liquor with Et₂O. Synthesis of **44** is reproducible, however the crystallisation time is long (4 months) and crystals did not consistently form. Due to the long crystallisation time, inconsistency of crystallisation and poor yield, a good match of CHN data was unfortunately not obtained.

6.3.2 Discussion of the crystal structure of [Mn(H₄edte)(NO₃)] [NO₃] (37)

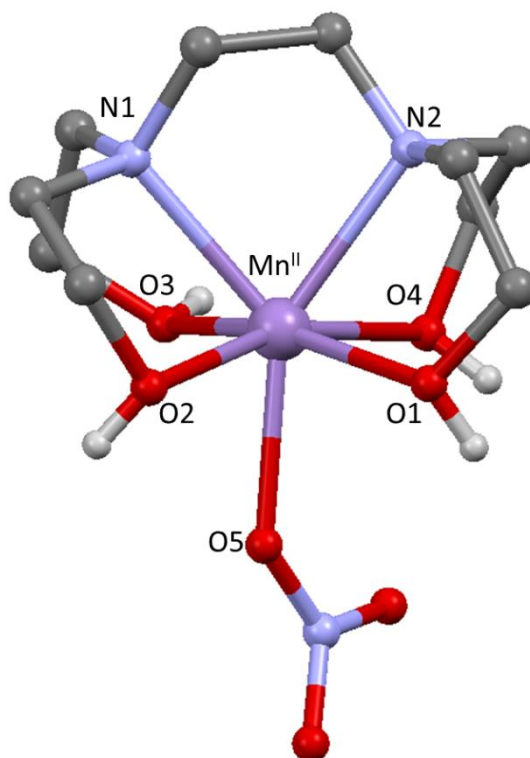


Figure 6.3: Molecular structure of **37** with lattice nitrates and C-H protons omitted. Atom colours: Mn^{II}, purple; O, red; N, blue; C, grey and H, white.

37 crystallises in the orthorhombic space group *Pbca* with its asymmetric unit containing one {Mn} molecule and one lattice nitrate anion. The {Mn} molecule contains one 7-coordinate Mn^{II} ion chelated by a H₄edte ligand and bound to a nitrate ion. The local crystal field of Mn1, as analysed by the programme SHAPE,²² is capped octahedral (ChSM = 0.932, *C_{3v}*). The ligand has retained all of its hydroxyl protons and acts as a neutral {N₂O₄} donor set. The bond lengths from Mn1 to its respective donor atoms (Table 6.2) indicate that the ion is in its +2 oxidation state, as observed in other reported structures.^{1-5,12} The +2 charge is balanced by the two nitrate ions.

<i>Empirical formula</i>	<i>MnC₁₀H₂₄N₄O₁₀</i>
Molar mass (gmol ⁻¹)	415.25
Crystal System	Orthorhombic
Space Group	<i>Pbca</i>
a (Å)	13.4000(2)
b (Å)	13.8810(2)
c (Å)	17.5344(3)
α (deg)	90
β (deg)	90
γ (deg)	90
V (Å ³)	3261.49(6)
Z	8
T (K)	100
λ (Å)	0.71073
ρ _{calc} (g/cm ³)	1.691
μ (mm ⁻¹)	0.872
^a R ₁	0.0351
^b wR ₂	0.0352
Goodness of fit	0.937
F(000)	1736
Reflections	3731
Parameters	226
Restraints	0

Table 6.1: Crystallographic data for 37.

$${}^aR_1 = \frac{\sum ||F_o| - |F_c||}{\sum |F_o|}$$

$${}^b wR_2 = \frac{[\sum [w(F_o^2 - F_c^2)^2] - \sum [(F_o^2)^2]]^{\frac{1}{2}}}{\sum w} \quad \text{where } w = 1/[\sigma^2(F_o^2) + (0.2P)^2] \text{ and } P = [F_o^2 + 2F_c^2]/3$$

Bond	Length (Å)
Mn1-O1	2.2632(11)
Mn1-O2	2.2888(12)
Mn1-O3	2.2456(12)
Mn1-O4	2.2216(11)
Mn1-N1	2.39337(13)
Mn1-N2	2.3707(14)
Mn1-O5	2.2881(12)

Table 6.2: Selected bond lengths in 38.

6.3.3 Discussion of the crystal structure of [Co(H₄edte)(H₂O)][NO₃]₂ (38)

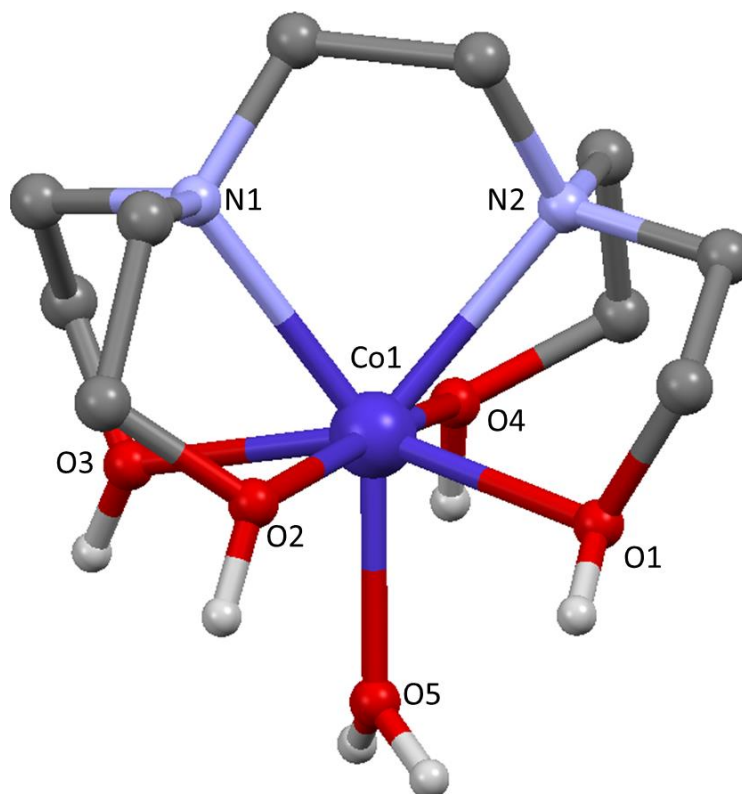


Figure 6.4: Molecular structure of **38** with lattice nitrates and C-H protons omitted. Atom colours: Co^{II}, dark blue; O, red; N, blue; C, grey and H, white.

38 crystallises in the monoclinic space group $P2_1/n$ with the asymmetric unit containing one {Co} complex molecule and two lattice nitrate anions. The complex molecule is a single 7-coordinate Co^{II} ion chelated by a H₄edte ligand and bound to a single water molecule. The local crystal field symmetry around atom Co1, as analysed by the programme SHAPE,²² is capped octahedral (ChSM = 1.259, C_{3v}), with capped trigonal prismatic a close second (ChSM = 1.439, C_{2v}). The ligand has retained all of its hydroxyl protons and acts as a neutral {N₂O₄} donor set. The bond lengths to Co1 from its donor atoms indicate that the ion is in its +2 oxidation state²³ which is balanced by the two lattice nitrates.

<i>Empirical formula</i>	<i>CoC₁₀H₂₆N₄O₁₁</i>
Molar mass (g mol ⁻¹)	437.27
Crystal System	Monoclinic
Space Group	<i>P</i> 2 ₁ / <i>n</i>
a (Å)	7.9700(7)
b (Å)	11.0174(8)
c (Å)	20.202(2)
α (deg)	90
β (deg)	94.125(2)
γ (deg)	90
V (Å ³)	1769.36(15)
Z	4
T (K)	100
λ (Å)	0.71073
ρ _{calc} (g/cm ³)	1.641
μ (mm ⁻¹)	1.035
^a R ₁	0.0455
^b wR ₂	0.1071
Goodness of fit	0.998
F(000)	916
Reflections	3588
Parameters	234
Restraints	0

Table 6.3: Crystallographic data for **38**.

$${}^aR_1 = \frac{\sum ||F_o| - |F_c||}{\sum |F_o|}$$

$${}^b wR_2 = \left[\frac{\sum [w(F_o^2 - F_c^2)^2]}{\sum [(F_o^2)]} \right]^{\frac{1}{2}} \quad \text{where } w = 1/[\sigma^2(F_o^2) + (0.2P)^2] \text{ and } P = [F_o^2 + 2F_c^2]/3$$

Bond	Length (Å)
Co1-O1	2.136(3)
Co1-O2	2.204(2)
Co1-O3	2.189(2)
Co1-O4	2.182(3)
Co1-N1	2.326(2)
Co1-N2	2.297(2)
Co1-O5	2.102(2)

Table 6.4: Selected bond lengths in **38**.

6.3.4 Discussion of the crystal structure of [Co(H₄edte)Cl][Cl] (**39**)

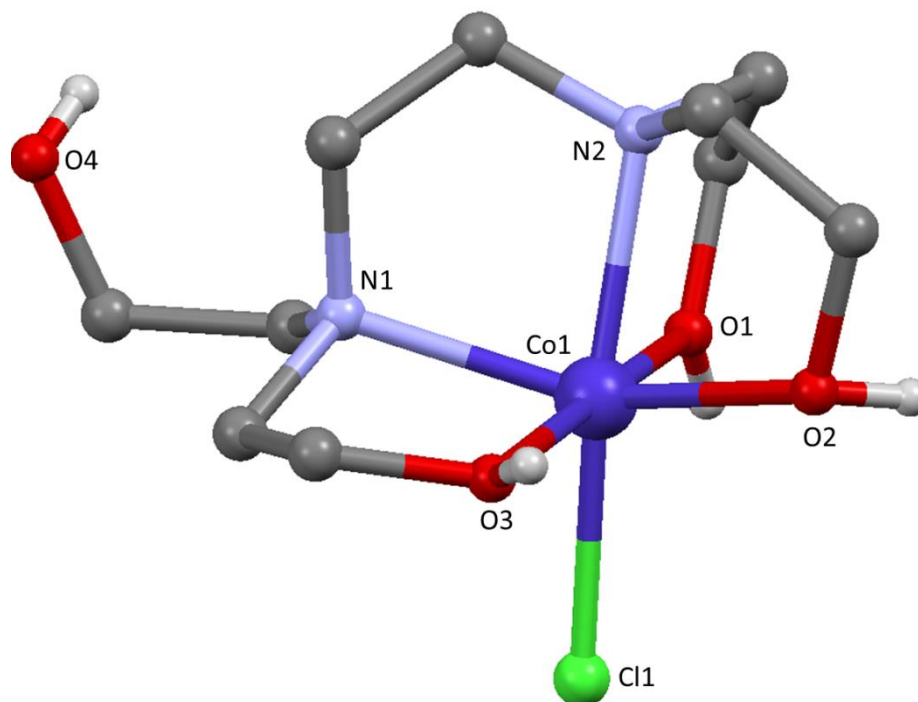


Figure 6.5: Molecular structure of **39** with lattice chloride and C-H protons omitted. Atom colours: Co^{II}, dark blue; O, red; N, blue; C, grey; Cl, green and H, white.

39 crystallises in the orthorhombic space group *Pna2₁*, with the asymmetric unit containing one molecule of the complex and one lattice chloride anion. The {Co} complex molecule contains one Co^{II} ion chelated by a H₄edte ligand and bound to a single Cl⁻ ligand resulting in a distorted octahedral crystal field (ChSM = 3.869 for *O_h*) around Co1. The ligand has retained all of its hydroxyl protons and acts as a neutral {N₂O₃} donor set. Three of the hydroxyethyl arms are bound to Co1 with the final arm extending out into the lattice where it forms hydrogen bonds between the lattice chloride (Cl2, not shown in Figure 6.5) and atom O1. The bond lengths between the ligand and the coordinating atoms (see Table 6.6) indicate that Co1 is in a +2 oxidation state²³ which is balanced by one Cl⁻ ligand and one lattice Cl⁻ ion associated with each complex molecule.

<i>Empirical formula</i>	<i>CoC₁₀H₂₄N₂Cl₂O₄</i>
Molar mass (gmol ⁻¹)	366.15
Crystal System	Orthorhombic
Space Group	<i>Pna2₁</i>
a (Å)	16.4664(5)
b (Å)	7.1172(2)
c (Å)	12.7679(3)
α (deg)	90
β (deg)	90
γ (deg)	90
V (Å ³)	1496.33(4)
Z	4
T (K)	100
λ (Å)	0.71073
ρ _{calc} (g/cm ³)	1.625
μ (mm ⁻¹)	1.514
^a R ₁	0.0375
^b wR ₂	0.0941
Goodness of fit	0.983
F(000)	764
Reflections	5306
Parameters	172
Restraints	1

Table 6.5: *Crystallographic data for 40.*

$${}^aR_1 = \frac{\sum ||F_o| - |F_c||}{\sum |F_o|}$$

$${}^b wR_2 = \frac{[\sum [w(F_o^2 - F_c^2)^2] - \sum [(F_o^2)^2]]^{\frac{1}{2}}}{\sum w F_o^2} \quad \text{where } w = 1/[\sigma^2(F_o^2) + (0.2P)^2] \text{ and } P = [F_o^2 + 2F_c^2]/3$$

Bond	Length (Å)
Co1-O1	2.1104(17)
Co1-O2	2.1172(16)
Co1-O3	2.2163(17)
Co1-N1	2.1533(17)
Co1-N2	2.1819(15)
Co1-Cl1	2.3577(5)

Table 6: *Selected bond lengths in 40.*

6.3.5 Discussion of crystal structure of [Ni(H₄edte)(EtOH)][NO₃]₂ (**40**)

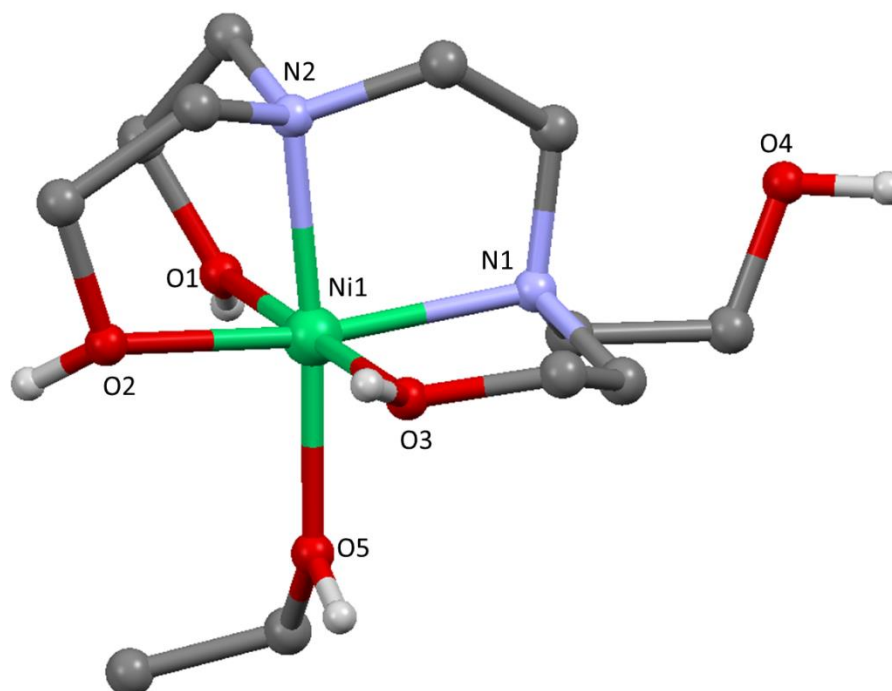


Figure 6: Molecular structure of **40** with lattice nitrates and C-H protons omitted. Atom colours: Ni^{II}, green; O, red; N, blue; C, grey and H, white.

40 crystallises in the triclinic space group *P*-1 with the asymmetric unit containing one molecule of the complex and two lattice nitrate counter ions. The complex contains a seven coordinate Ni^{II} ion chelated by a H₄edte ligand and bound to a single EtOH molecule. The local crystal field symmetry around atom Ni1, as analysed by the programme SHAPE,²² is distorted octahedral (ChSM = 0.815, *O_h*). The ligand has retained all of its hydroxyl protons and acts as a neutral {N₂O₃} donor set. The bond lengths to Ni1 from its donor atoms are presented in Table 6.8.

<i>Empirical formula</i>	<i>NiC₁₂H₃₀N₄O₁₁</i>
Molar mass (g mol ⁻¹)	465.10
Crystal System	Triclinic
Space Group	<i>P</i> -1
a (Å)	7.2678(4)
b (Å)	8.6534(5)
c (Å)	16.1210(8)
α (deg)	98.814(2)
β (deg)	97.446(2)
γ (deg)	100.791(2)
V (Å ³)	971.01(5)
Z	2
T (K)	100
λ (Å)	0.71073
ρ _{calc} (g/cm ³)	1.591
μ (mm ⁻¹)	1.063
^a R ₁	0.0318
^b wR ₂	0.0758
Goodness of fit	0.914
F(000)	492
Reflections	3389
Parameters	253
Restraints	0

Table 7: Crystallographic data for **41**.

$${}^aR_1 = \frac{\sum ||F_o| - |F_c||}{\sum |F_o|}$$

$${}^b wR_2 = \frac{[\sum [w(F_o^2 - F_c^2)^2] - \sum [(F_o^2)^2]]^{\frac{1}{2}}}{\sum w F_o^2} \quad \text{where } w = 1/[\sigma^2(F_o^2) + (0.2P)^2] \text{ and } P = [F_o^2 + 2F_c^2]/3$$

Bond	Length (Å)
Ni1-O1	2.0416(13)
Ni1-O2	2.1076(13)
Ni1-O3	2.0736(12)
Ni1-N1	2.1207(15)
Ni1-N2	2.0574(15)
Ni1-O5	2.0333(13)

Table 6.8: Selected bond lengths in **40**.

6.3.6 Discussion of the crystal structure of [Ni(H₄pdte)][NO₃]₂ (**41**)

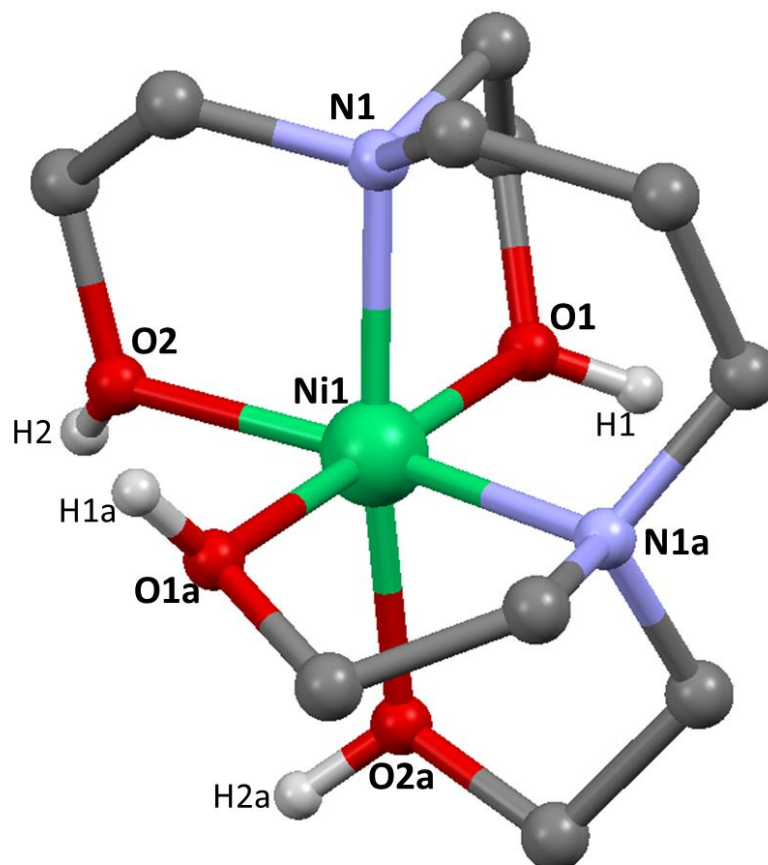


Figure 6.7: Molecular structure of **42**. C-H protons and lattice nitrates have been omitted.
Atom colours: Ni^{II}, green; O, red; N, blue; C, grey; and H, white.

41 crystallises in the tetragonal space group $P4_12_12$ with the asymmetric unit containing one molecule of the complex and two fully occupied nitrate counter ions. The complex molecule consists of a 6-coordinate Ni^{II} ion chelated by a neutral H₄pdte ligand which acts as an {N₂O₄} donor set. The crystal field of Ni1 in **41** is distorted octahedral with ChSM = 0.964 (O_h). This value is slightly larger than that for complex **40** (ChSM = 0.815, O_h), indicating a more distorted crystal field. The added carbon atom provides enough flexibility to form an octahedral coordination sphere with all ligand donor atoms bound.

Bond	Length (Å)
Ni1-O1	2.1013(16)
Ni1-O1a	2.1013(16)
Ni1-O2	2.0371(16)
Ni1-O2a	2.0371(16)
Ni1-N1	2.0762(18)
Ni1-N1a	2.0762(18)

Table 6.9: Selected bond lengths in **41**. Atoms labelled with a represent symmetry equivalents: $a = (1+y,+x,1-z)$.

<i>Empirical formula</i>	<i>NiC₁₁H₂₆N₄O₁₀</i>
Molar mass (g mol ⁻¹)	433.06
Crystal System	Tetragonal
Space Group	<i>P4₁2₁2</i>
a (Å)	7.32060(10)
b (Å)	7.32060(10)
c (Å)	33.1400(5)
α (deg)	90
β (deg)	90
γ (deg)	90
V (Å ³)	1776.01(3)
Z	4
T (K)	100
λ (Å)	0.71073
ρ _{calc} (g/cm ³)	1.627
μ (mm ⁻¹)	1.153
^a R ₁	0.0300
^b wR ₂	0.0704
Goodness of fit	0.971
F(000)	904
Reflections	1953
Parameters	121
Restraints	0

Table 6.10: Crystallographic data for **42**

$${}^aR_1 = \frac{\sum ||F_o| - |F_c||}{\sum |F_o|}$$

$${}^b wR_2 = \left[\frac{\sum [w(F_o^2 - F_c^2)^2]}{\sum [(F_o^2)^2]} \right]^{\frac{1}{2}} \quad \text{where } w = 1/[\sigma^2(F_o^2) + (0.2P)^2] \text{ and } P = [F_o^2 + 2F_c^2]/3$$

6.3.7 Discussion of the Crystal Structure of [Zn(H₃edte)][NO₃] (42)

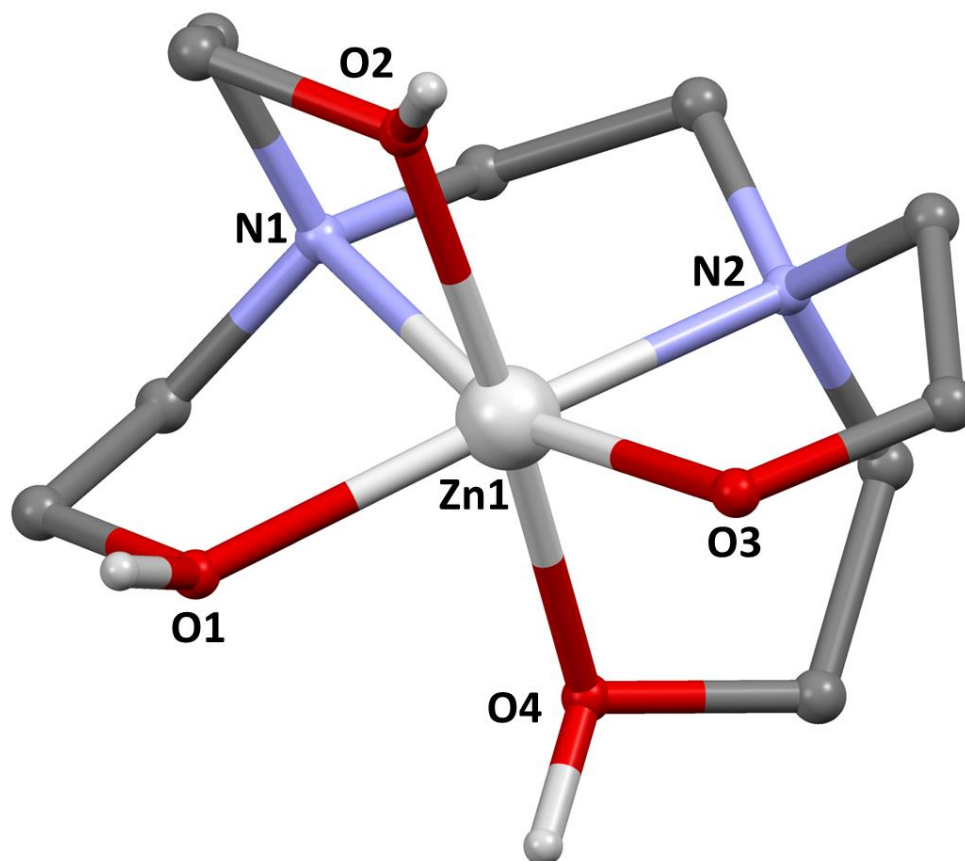


Figure 6.8: Molecular structure of **42**. Atom colours: Zn^{II}, silver; O, red; N, blue and C, grey. Lattice nitrate and C-H protons are omitted.

42 crystallises in the orthorhombic space group $Pna2_1$, with the unit cell containing one {Zn} complex molecule and one fully occupied lattice nitrate. The ligand acts as a {N₂O₄} donor set, and unlike the other monomeric structures, is singly deprotonated. The central Zn^{II} ion is 6-coordinate and adopts a distorted trigonal prismatic coordination geometry (ChSM = 11.447, D_{3h}). The 2+ charge of the metal ion is balanced by the H₃edte⁻ ligand and the lattice nitrate.

<i>Empirical formula</i>	<i>ZnC₁₀H₂₃N₃O₇</i>
Molar mass (g mol ⁻¹)	362.689
Crystal System	Orthorhombic
Space Group	<i>Pna2₁</i>
a (Å)	12.3111(2)
b (Å)	15.5868(3)
c (Å)	7.6717(1)
α (deg)	90
β (deg)	90
γ (deg)	90
V (Å ³)	1472.13(2)
Z	4
T (K)	100
λ (Å)	0.71073
ρ _{calc} (g/cm ³)	1.636
μ (mm ⁻¹)	1.705
^a R ₁	0.0266
^b wR ₂	0.0491
Goodness of fit	0.952
F(000)	788
Reflections	3336
Parameters	190
Restraints	1

Table 6.11: Crystallographic data for **42**.

$${}^aR_1 = \frac{\sum ||F_o| - |F_c||}{\sum |F_o|}$$

$${}^b_wR_2 = \frac{[\sum [w(F_o^2 - F_c^2)^2] - \sum [(F_o^2)^2]]^{\frac{1}{2}}}{\sum [w(F_o^2 + (0.2P)^2)]^{\frac{1}{2}}} \quad \text{where } w = 1/[\sigma^2(F_o^2) + (0.2P)^2] \text{ and } P = [F_o^2 + 2F_c^2]/3$$

Bond	Length (Å)
Zn1-O1	2.1232(19)
Zn1-O2	2.149 (2)
Zn1-O3	2.0161(16)
Zn1-O4	2.152(2)
Zn1-N1	2.1483(18)
Zn1-N2	2.175(2)

Table 6.12: Selected bond lengths in **42**. Symmetry operation *a* = (3/2-x,+y,+z)

6.3.8 Discussion of the Crystal Structure of [Mn^{II}Mn^{III}(Hedte)(H₃edte)][ClO₄] (44)

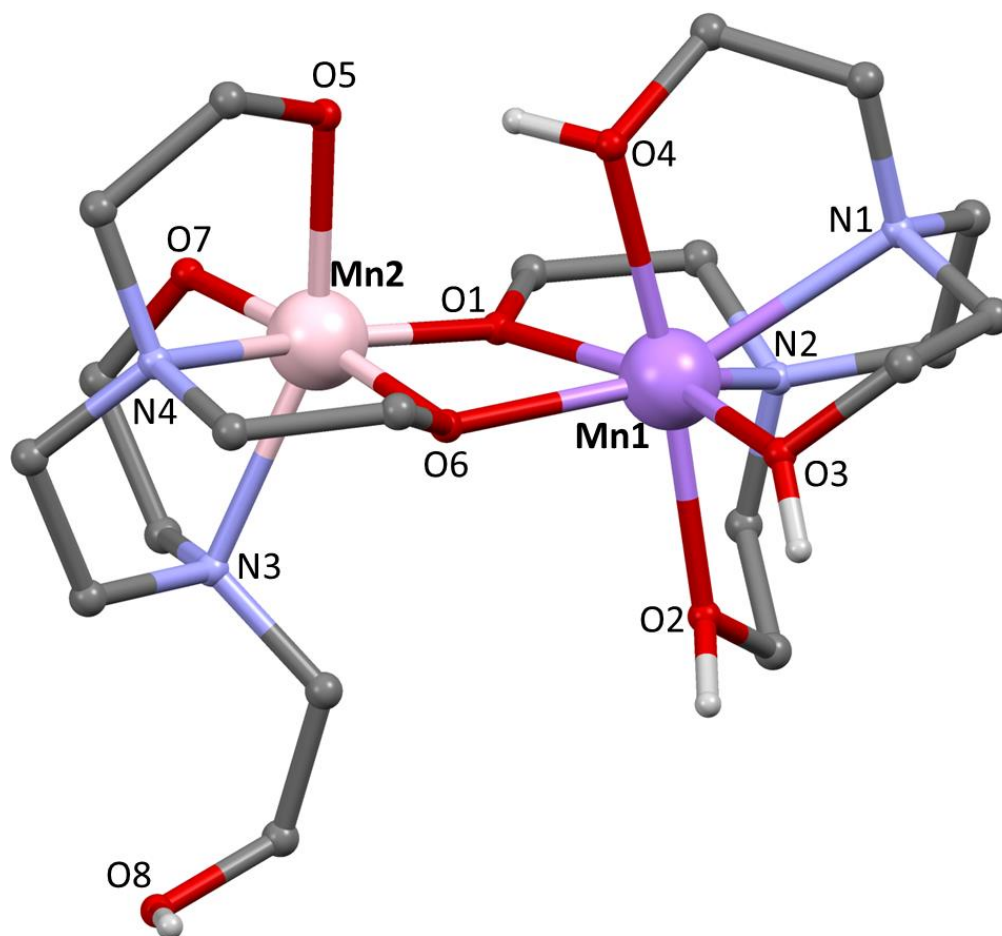


Figure 6.9: Molecular structure of **43**. C-H protons and lattice perchlorate have been omitted. Atom colours: Mn^{II}, purple; Mn^{III}, pink; O, red; N, blue; C, grey; and H, white.

43 crystallises in the monoclinic space group $P2_1/c$ with the asymmetric unit consisting of one molecule of the complex and one ClO₄⁻ anion. The molecule is a rare example of a mixed valence Mn^{II}/Mn^{III} dimer;²⁴ assignments of the oxidation states were made based on the metal-ligand bond lengths and BVS calculations²⁵ (see Tables 6.13 & 6.14). Atom Mn1 is 7-coordinate, with its H₃edte⁻ ligand acting as a {N₂O₄} donor set, the final donor atom (O6) comes from the Hedte³⁻ ligand bound to Mn2 and acts as an alkoxo-bridge between Mn1 and Mn2. The coordination geometry of Mn1, as calculated by SHAPE,²² is a closest match to capped trigonal prismatic (ChSM = 1.131, C_{2v}). Atom Mn2 is 6-coordinate and is in a distorted octahedral crystal field (ChSM = 2.234, O_h). Mn2 is chelated by a Hedte³⁻ ligand which acts as a {N₂O₃} donor set with the final donor atom (O1) belonging to the adjacent H₃edte⁻ which also acts as an alkoxo bridge between Mn1 and Mn2. There is Jahn-Teller axial elongation along bonds Mn2-O5 and Mn2-N3, as expected for an Mn^{III}

ion in an octahedral crystal field (see Table 6.14). The 5+ charge of the metal ions is balanced by the overall 4- charge of the two ligands and a single lattice perchlorate. The Mn^{II}-O-Mn^{III} bond angles are 103.9 and 103.8° (Table 6.16), these angles are known to facilitate ferromagnetic exchange between Mn^{II}-Mn^{III} pairs.^{26,27}

Atom	Mn ^{II}	Mn ^{III}
Mn1	<u>1.988</u>	1.854
Mn2	3.191	<u>2.959</u>

Table 6.13: BVS calculations²⁵ for Mn1 and Mn2 in **43**. The underlined values are those closest to the charge which was calculated.

Bond	Length (Å)
Mn1-O1	2.1938(15)
Mn1-O2	2.2215(15)
Mn1-O3	2.2202(15)
Mn1-O4	2.3185(15)
Mn1-O6	2.1865(15)
Mn1-N1	2.4422(18)
Mn1-N2	2.3716(18)
Mn2-O1	1.8911(15)
Mn2-O5	2.1686(15)
Mn2-O6	1.9030(15)
Mn2-O7	1.9005(15)
Mn2-N3	2.3401(18)
Mn2-N4	2.1106(19)

Table 6.14: Selected bond lengths in **43**. The Jahn-Teller elongated bonds associated with Mn2 are highlighted in bold.

Atoms	Angle(°)
Mn1-O1-Mn2	103.93(7)
Mn1-O6-Mn2	103.80(6)

Table 6.15: Selected bond angles in **43**

<i>Empirical formula</i>	<i>Mn₂C₂₀H₄₄N₄Cl₁O₁₂</i>
Molar mass (gmol ⁻¹)	677.92
Crystal System	Monoclinic
Space Group	<i>P</i> 2 ₁ / <i>c</i>
a (Å)	7.50340(10)
b (Å)	24.0914(4)
c (Å)	15.7903(2)
α (deg)	90
β (deg)	101.3540(10)
γ (deg)	90
V (Å ³)	2798.51(4)
Z	4
T (K)	100
λ (Å)	0.71073
ρ _{calc} (g/cm ³)	1.610
μ (mm ⁻¹)	1.064
^a R ₁	0.0378
^b wR ₂	0.0518
Goodness of fit	0.928
F(000)	1420
Reflections	5177
Parameters	380
Restraints	2

Table 6.16: Crystallographic data for **43**

$${}^aR_1 = \frac{\sum ||F_o| - |F_c||}{\sum |F_o|}$$

$${}^b wR_2 = \frac{[\sum [w(F_o^2 - F_c^2)^2] - \sum [(F_o^2)^2]]^{\frac{1}{2}}}{\sum w} \quad \text{where } w = 1/[\sigma^2(F_o^2) + (0.2P)^2] \text{ and } P = [F_o^2 + 2F_c^2]/3$$

6.3.9 Discussion of the Crystal Structure of

[Cu₈(OAc)₂(MeOH)₂(OH)₂(H₃edte)₂(H₂edte)₂(OBz)₂][NO₃]₂[PF₆]₂·MeOH·H₂O (44)

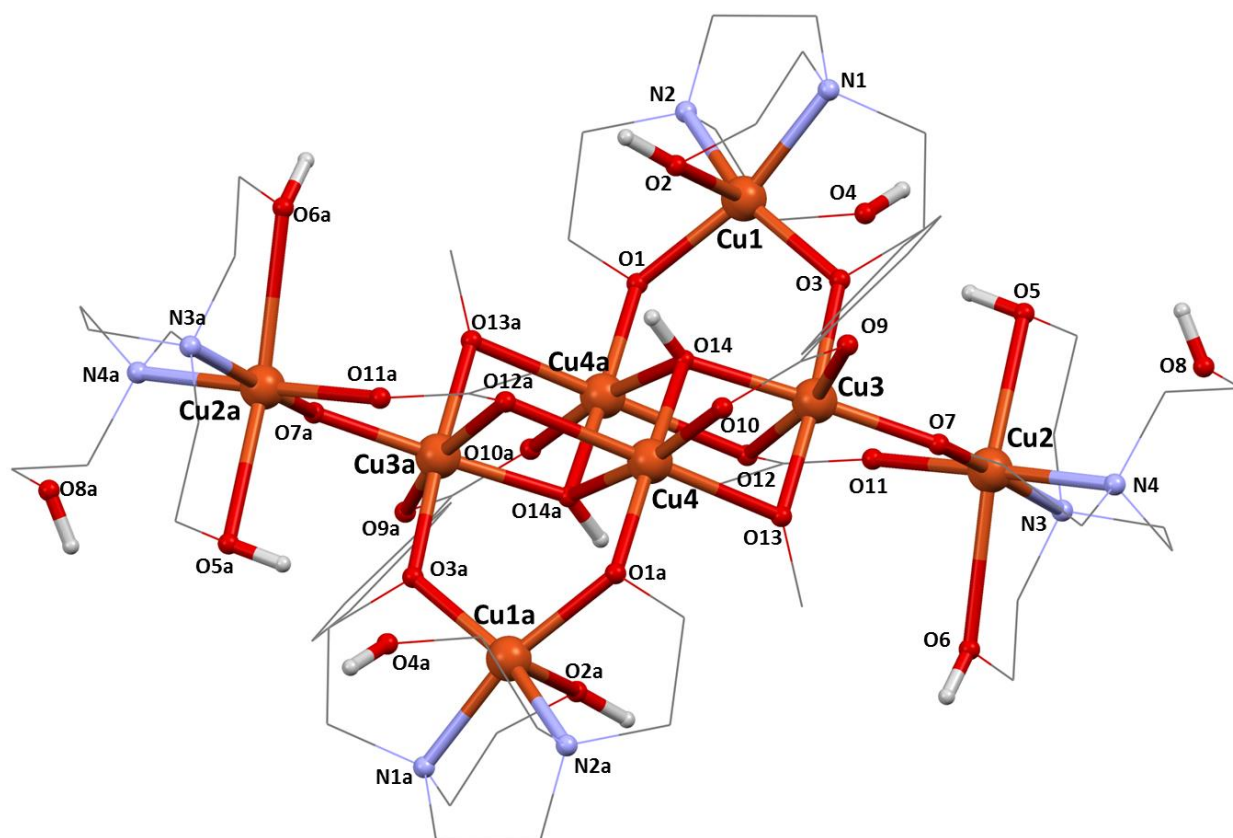


Figure 6.10: Molecular structure of **44**. C-H protons, lattice counterions and crystallisation solvent have been omitted. The proton on O13 (and O13a) could not be found during refinement of the crystal data (*vide infra*). Atom colours: Cu^{II}, orange; O, red; N, blue; C, grey; and H, white. Symmetry operation; *a* = (-*x*, 1-*y*, 1-*z*).

Complex **44** crystallises in the triclinic space group *P*-1 with an inversion point in the centre of the molecule; between Cu4 and Cu4a (Figure 6.10). The molecule as a whole can be described as an incomplete face-fused di-cubane, with capping {Cu(H_{*x*}edte)} (*x* = 2 (Cu1) or 3 (Cu2)) subunits. The 16+ charge of the 8 Cu^{II} ions is balanced by the two acetate and two benzoate ligands (-4), the two hydroxyl groups (-2), the lattice counter ions (-4) and the ligands; two H₃edte⁻ and two H₂edte²⁻ (-6). The asymmetric unit contains half of the {Cu₈} complex molecule, with four distinct Cu^{II} ions (Cu1-4); Cu1 and Cu2 are chelated by H₂edte²⁻ and H₃edte¹⁻ ligands respectively and act as the capping subunits while Cu3 and Cu4 occupy vertices of the dicubane. Cu1 exhibits square based pyramidal geometry, with its H₂edte²⁻ ligand acting as a {N₂O₂} donor set; bridging through

deprotonated alkoxo-arms, O1 and O3, to Cu4a and Cu3 respectively. Cu2 exhibits distorted octahedral coordination geometry, with bond elongation along O5-Cu2-O6 (see Table 6.18), its H₃edte⁻ ligand acts as a {N₂O₃} donor set with one deprotonated alkoxo arm bridging between Cu2 and Cu3. The remaining arms are protonated, with O5 and O6 occupying Cu2's axial sites and O8 extending into the crystal lattice as an unbound arm. Cu2 is also bridged to Cu3 by an acetate ligand, containing atoms O11 and O12. Cu3 occupies one of the vertices of the double cubane and adopts a distorted octahedral coordination geometry with elongated bonds O9-Cu3-O12. Cu4 is situated at the face-fused region of the double cubane and bridges to Cu3 through a benzoate ligand, (O9 and O10), a μ_2 MeOH ligand (O13), part of the acetate ligand (O12) and a μ_3 OH⁻ species (O14). Cu4 is also bridged to its symmetry equivalent, Cu4a, through O14 and O14a. Bond valence calculations for O14 suggest an oxidation state of one, there is also a viable H-bond pathway between O14(H) \cdots O2, as seen in similar reported structures.²⁸ During refinement of the crystal data, the proton on O13 (the μ_2 MeOH ligand) could not be found. If modelled as a methoxy ligand, two negative charges from elsewhere need to be removed. To try and account for this the PF₆⁻ and NO₃⁻ counter ions were set to half occupancy, this however gave clearly unreasonable thermal displacement parameters for these ions – they need to be fully occupied. BVS calculations²⁵ for O13 \approx 0.7, suggesting that methoxy is a more appropriate assignment. Indeed a search of the CSD finds only 17 examples of μ_2 MeOH ligands bridging Cu^{II} ions compared to 165 examples of μ_2 MeO⁻.^{29,30} The Cu-O bond lengths to μ_2 MeOH ligands in these 17 examples are \approx 2.5 Å, whereas in **44** they are 2.1 and 1.9 Å, which are closer in magnitude to the \approx 1.9 Å observed for μ_2 MeO⁻ bridges. However, based on the absence of protonatable sites, or scope to remove negative charge from the unit cell, it seems reasonable that μ_2 MeOH is the correct assignment.

<i>Empirical formula</i>	<i>Cu₈C₆₂H₁₂₈N₁₀O₃₈P₂F₁₂</i>
Molar mass (gmol ⁻¹)	2420.00
Crystal System	Triclinic
Space Group	<i>P-1</i>
a (Å)	14.1417(17)
b (Å)	14.8731(18)
c (Å)	15.0876(18)
α (deg)	101.699(2)
β (deg)	115.658(2)
γ (deg)	108.375(2)
V (Å ³)	2491.7(5)
Z	1
T (K)	100.15
λ (Å)	0.77490
ρ _{calc} (g/cm ³)	1.613
μ (mm ⁻¹)	2.289
^a R ₁	0.0748
^b wR ₂	0.2462
Goodness of fit	1.059
F(000)	1244
Reflections	15074
Parameters	588
Restraints	7

Table 6.17: Crystallographic data for **44**

$${}^aR_1 = \frac{\sum ||F_o| - |F_c||}{\sum |F_o|}$$

$${}^b wR_2 = \frac{[\sum [w(F_o^2 - F_c^2)^2] - \sum [(F_o^2)^2]]^{\frac{1}{2}}}{\sum w F_o^2} \quad \text{where } w = 1/[\sigma^2(F_o^2) + (0.2P)^2] \text{ and } P = [F_o^2 + 2F_c^2]/3$$

Bond	Length (Å)
Cu1-O1	1.957(3)
Cu1-O2	2.377(3)
Cu1-O3	1.954(3)
Cu1-N1	2.013(3)
Cu1-N2	2.011(3)
Cu2-O5	2.478(5)
Cu2-O6	2.539(5)
Cu2-O7	1.929(3)
Cu2-O11	1.962(3)
Cu2-N3	2.042(4)
Cu2-N4	2.041(4)
Cu3-O3	1.919(3)
Cu3-O7	1.898(3)
Cu3-O9	2.203(3)
Cu3-O12	2.228(3)
Cu3-O13	1.892(3)
Cu3-O14	1.963(2)
Cu4-O1a	1.922(3)
Cu4-O10	1.961(3)
Cu4-O12a	2.344(3)
Cu4-O13	2.138(3)
Cu4-O14	1.913(2)
Cu4-O14a	1.916(3)

Table 6.18: Selected bond lengths in **44**.

Atoms	Angle(°)
Cu1-O1-Cu4a	126.49(14)
Cu1-O3-Cu3	124.92(12)
Cu2-O7-Cu3	127.63(15)
Cu3-O13-Cu4	93.46(11)
Cu3-O12-Cu4a	87.34(9)
Cu3-O14-Cu4	98.60(10)
Cu3-O14-Cu4a	108.99(12)

Table 6.19: Selected bond angles in **44**. Symmetry equivalent a = (-x,1-y,1-z)

6.3.10 Discussion of the Crystal Structure of [Cu₆Ni₂(H₂edte)₄(NO₃)₂(H₂O)₂(MeOH)₂(OH)₂][NO₃]₄·2MeOH (45)

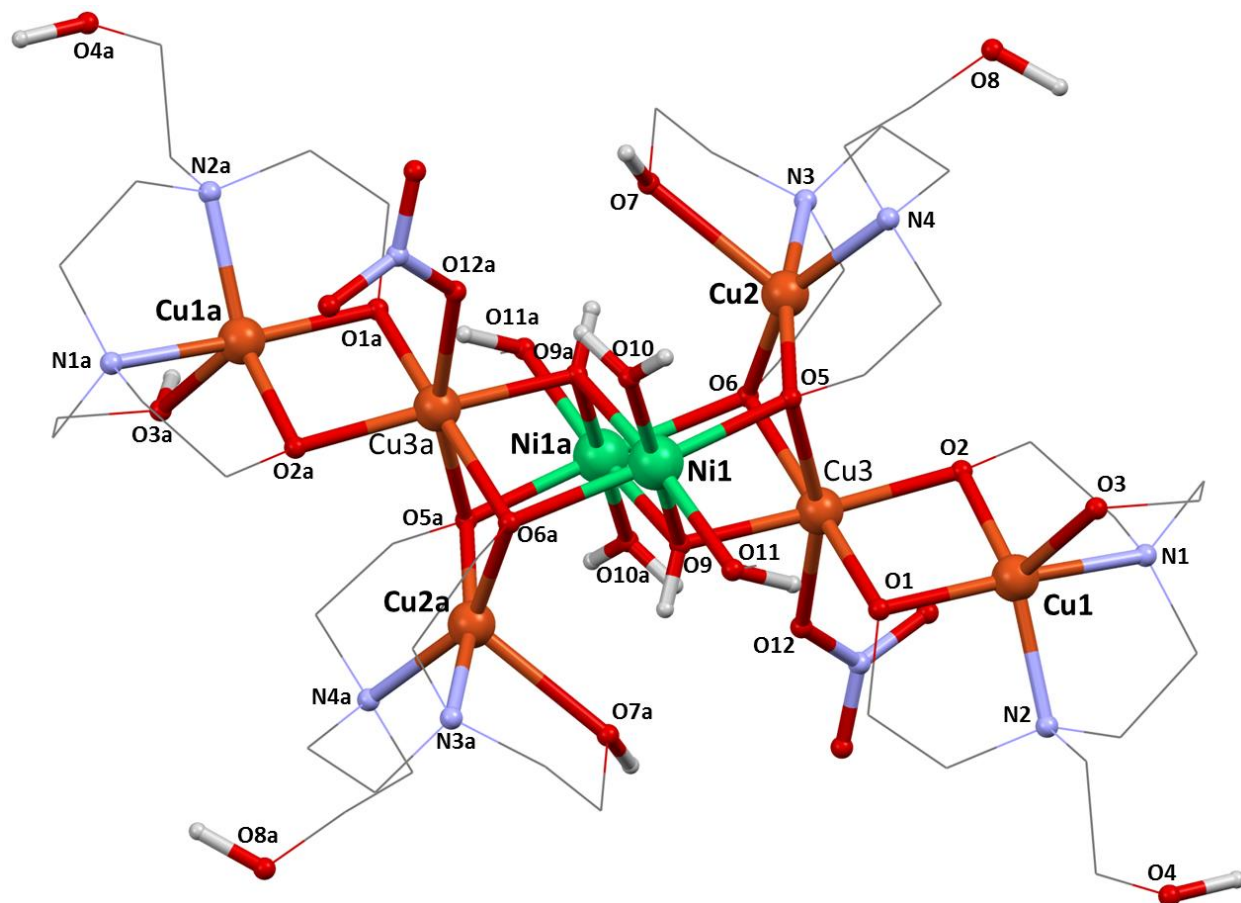


Figure 6.11: Molecular structure of **45** with C-H protons, lattice nitrates and lattice MeOH molecules omitted. Symmetry equivalent operation $a = (2-x, 1-y, 2-z)$. Atom colours: Ni^{II}, green; Cu^{II}, orange; O, red; N, blue; C, grey; and H, white.

Complex **45** crystallises in the monoclinic space group $P2_1/c$, with an inversion centre between Ni1 and its symmetry equivalent Ni1a (see Figure 6.11). It is a relatively rare example of a heterometallic {CuNi} complex, with only one other {Cu₆Ni₂} complex reported in the CSD.³¹ The molecule as a whole can be described as a defective face fused dicubane with added Cu^{II} ‘wings’; similar in structure to a previously reported {Cu₄Ni₂} complex.³² The 16+ charge of the metal ions is balanced by four H₂edte²⁻ ligands (-8), two OH⁻ groups (-2) and six NO₃⁻ ions; two as ligands and four as lattice anions (-6). The asymmetric unit contains half a {Ni₂Cu₆} molecule, two fully occupied lattice nitrates and one MeOH solvent of crystallisation. There are three crystallographically distinct Cu^{II}

environments in the asymmetric unit (Cu1-3). Cu1 and Cu2 are both 5-coordinate, each chelated by a H₂edte²⁻ ligand which acts as a {N₂O₃} donor set. Cu1 is linked to Cu3 through atoms O1 and O2 provided by the deprotonated alkoxo arms of its H₂edte²⁻ ligand. Cu2 bridges to Cu3 again through alkoxo-bridges (atoms O5 and O6) provided by its H₂edte²⁻ ligand, however, atoms O5 and O6 act as μ_3 bridges as they also form a bridge between Cu3 and Ni1. Cu3 is 6-coordinate and exhibits a distorted octahedral coordination geometry (see Figure 6.15 and Table 6.22). The bond lengths around Cu3 show a Jahn-Teller axial elongation along Cu3-O5 and Cu3-O12, as expected for a d^9 ion in an octahedral crystal field. Ni1 is also in an octahedral crystal field; Figure 6.12 compares the Ni1-O bond lengths with the Cu3-O bond lengths.

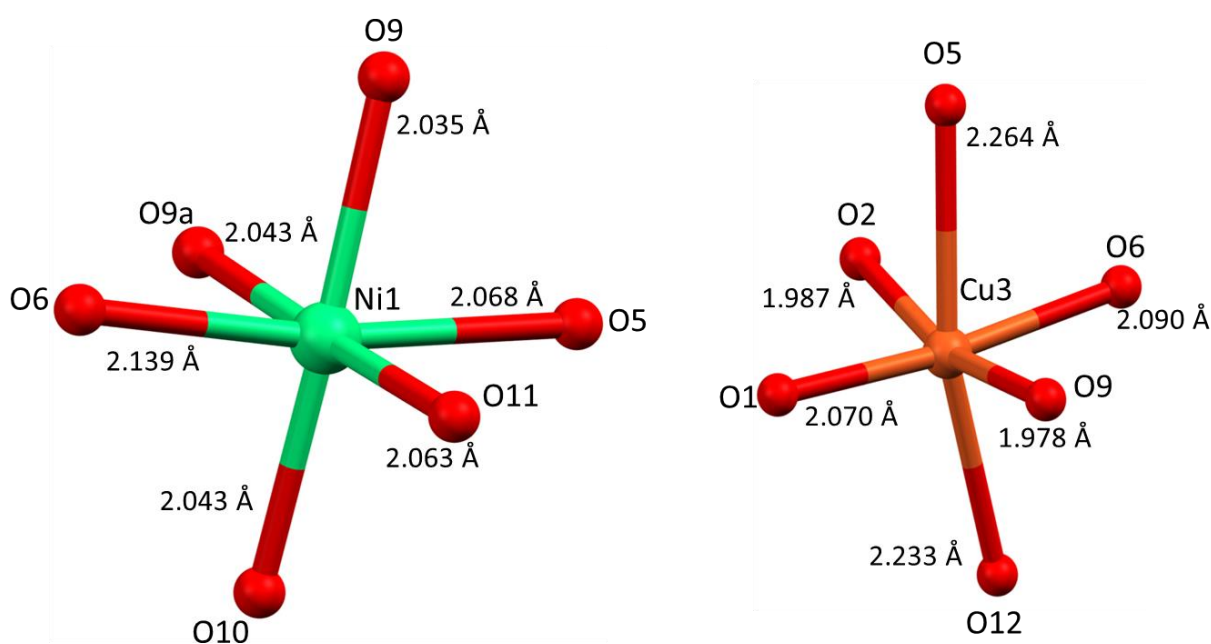


Figure 6.12: Bond lengths from octahedral Ni1 (left) and Cu3 (right). The bond lengths for Cu3 show clear Jahn-Teller axial elongation between O12-Cu3-O5. Atom colours: Ni^{II}, green; Cu^{II}, orange; O, red.

From the bond lengths, there is not an obvious Jahn-Teller elongation for Ni1 as compared to Cu3. However, Ni1-O5 (2.068 Å) and Ni1-O6 (2.139 Å) are both slightly larger than the other Ni1-O bond lengths and could correspond to an elongated bond – indicative that there could be some mixing of Jahn-Teller distorted Cu^{II} in this position. When Ni^{II} is replaced with Cu^{II} during the refinement of the crystal structure, there is a $\approx 3\%$ increase in r-factor and the atom displacement ellipsoid increases significantly in size by $\approx 16\%$, suggesting that Ni^{II} is the predominant ion in this position. Ni1 is bonded to a bridging OH group (O9), a neutral water ligand (O10) and a neutral MeOH ligand (O11) (see Figure 6.16). These ligands all take part in intramolecular hydrogen bonding interactions. O9(H)

acts as a hydrogen bond donor to O7a with a distance; O9(H) ···O7a (2.765(6) Å). BVS²⁵ for O9 gives an estimation of the oxidation state as 1.022 supporting its assignment as OH⁻. O10 acts as a hydrogen bond donor to O12 with a distance O10(H) ···O12 (2.752(6) Å). Finally, O11 acts as a hydrogen bond donor to O1 with a distance O11(H) ···O1 (2.747(6) Å).

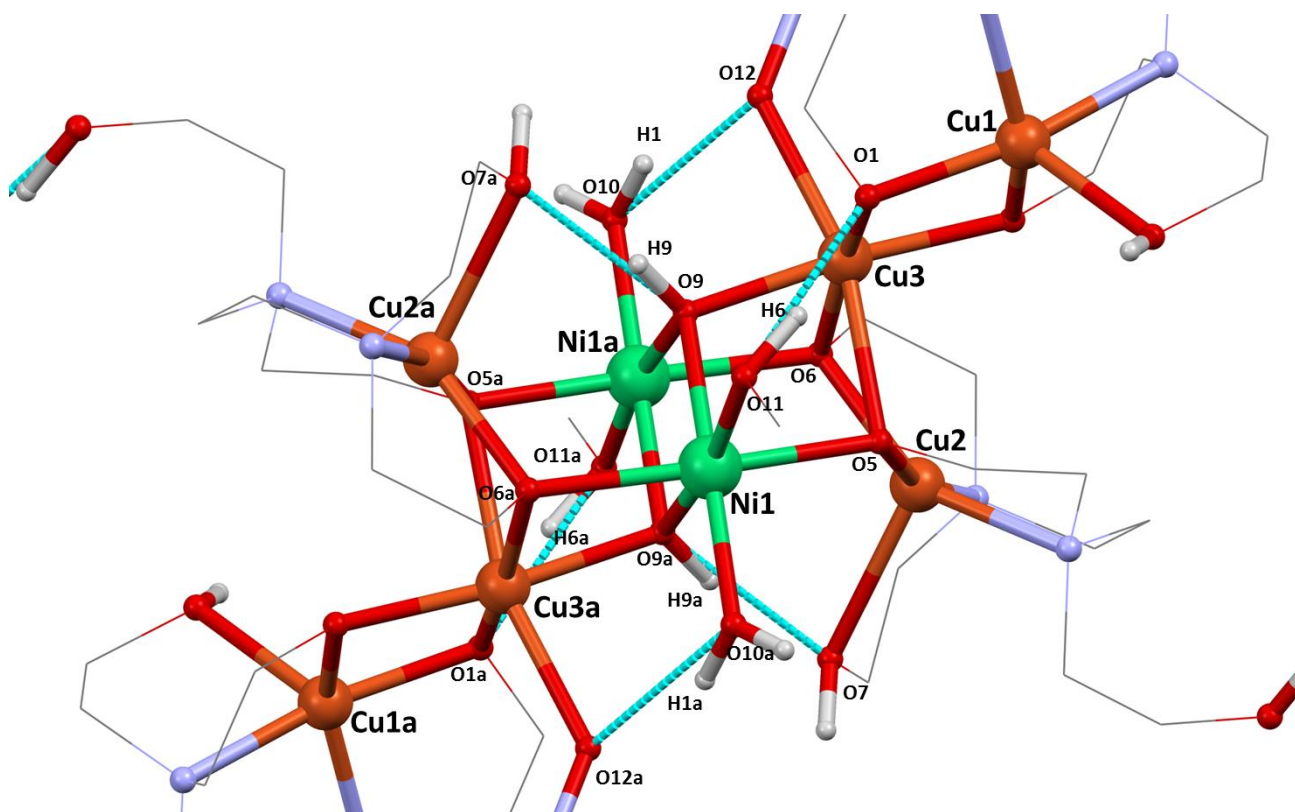


Figure 6.13: Intramolecular hydrogen bonding in 45. H-bonding interactions highlighted as blue dotted lines. C-H protons have been omitted for clarity. Atom colours: Ni^{II}, green; Cu^{II}, orange; O, red; N, blue; C, grey; and H, white. $a = (2-x, 1-y, 2-z)$

<i>Empirical formula</i>	<i>Cu₆Ni₂C₄₄H₁₁₀N₁₄O₄₂</i>
Molar mass (g mol ⁻¹)	2006.12
Crystal System	Monoclinic
Space Group	<i>P2₁/c</i>
a (Å)	10.5158(2)
b (Å)	25.7677(5)
c (Å)	13.5774(2)
α (deg)	90
β (deg)	102.00220(10)
γ (deg)	90
V (Å ³)	3598.35(5)
Z	2
T (K)	100
λ (Å)	0.71073
ρ _{calc} (g/cm ³)	1.851
μ (mm ⁻¹)	2.358
^a R ₁	0.0484
^b wR ₂	0.0623
Goodness of fit	0.940
F(000)	2076
Reflections	6384
Parameters	487
Restraints	0

Table 6.20: Crystallographic data for **46**

$${}^aR_1 = \frac{\sum ||F_o| - |F_c||}{\sum |F_o|}$$

$${}^b wR_2 = \left[\frac{\sum [w(F_o^2 - F_c^2)^2]}{\sum [(F_o^2)]} \right]^{\frac{1}{2}} \quad \text{where } w = 1/[\sigma^2(F_o^2) + (0.2P)^2] \text{ and } P = [F_o^2 + 2F_c^2]/3$$

Atoms	Angle (°)
Cu1-O1-Cu3	93.34(11)
Cu1-O2-Cu3	95.81(11)
Cu2-O5-Cu3	89.73(11)
Cu2-O6-Cu3	93.11(10)
Cu3-O5-Ni1	93.24(10)
Cu3-O6-Ni1	95.48(10)
Cu3-O9-Ni1	103.21(11)
Cu3-O9-Ni1a	102.49(11)
Ni1-O9-Ni1a	97.18(11)

Table 6.21: Selected bond angles in **45**. *a* = (2-*x*, 1-*y*, 2-*z*)

Bond	Length (Å)
Cu1-O1	1.936(3)
Cu1-O2	1.942(3)
Cu1-O3	2.221(3)
Cu1-N1	1.992(3)
Cu1-N2	2.033(3)
Cu2-O5	1.923(3)
Cu2-O6	1.991(3)
Cu2-O7	2.369(3)
Cu2-N3	1.989(3)
Cu2-N4	2.016(3)
Cu3-O1	2.070(3)
Cu3-O2	1.987(3)
Cu3-O5	2.264(3)
Cu3-O6	2.090(3)
Cu3-O9	1.978(2)
Cu3-O12	2.233(3)
Ni1-O5	2.068(3)
Ni1-O6	2.139(2)
Ni1-O9	2.035(3)
Ni1a-O9	2.043(2)
Ni1-O10	2.043(10)
Ni1-O11	2.063(3)

Table 6.22: Selected bond lengths in **45**. $a = (2-x, 1-y, 2-z)$

6.3.11 Discussion of the Crystal Structure of $[Mn_{10}Cu_5O_8(OBz)_8(Hedte)_4(H_2O)_4][NO_3]_4 \cdot 8MeOH$ (47)

From the single crystal X-ray data, the full formula of **47** is $[Mn^{III}_{10}Mn^{II}Cu^{II}_4(O_8)(OBz)_8(Hedte)_4(H_2O)_4][NO_3]_4 \cdot 8MeOH$. The +40 charge of the metal ions is balanced by eight O^{2-} ions, 8 OBz^- ligands, 4 $Hedte^{3-}$ ligands and 4 NO_3^- counterions ($16+8+12+4 = 40$).

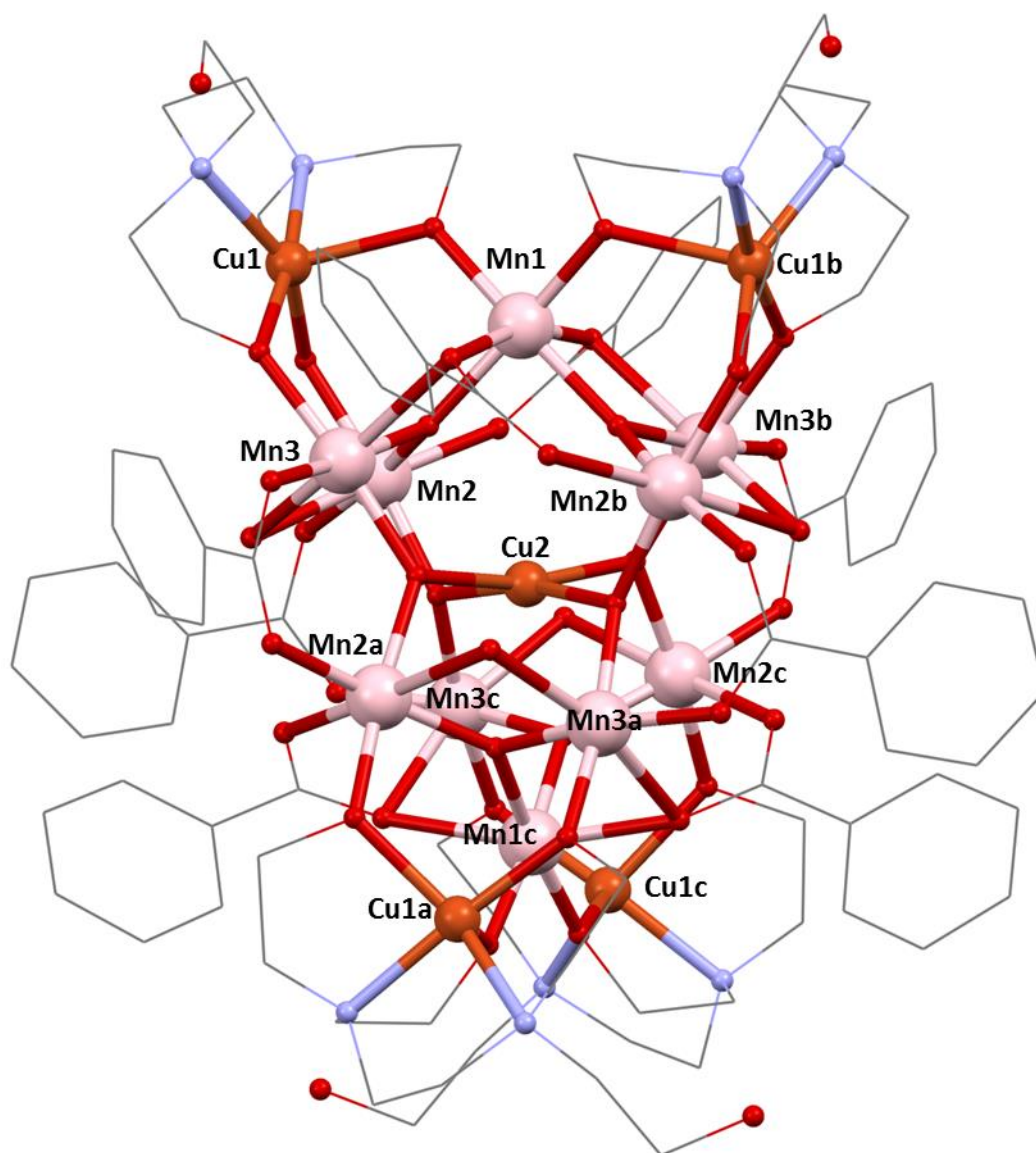


Figure 6.14: Molecular structure of **46**. All hydrogen atoms, lattice nitrates and crystallisation solvent molecules have been omitted. Atom colours: Cu^{II} , orange; Mn^{III} , pink; O, red; N, blue and C, grey. Symmetry operations: *a* ($\frac{3}{4}+y, \frac{1}{4}-x, \frac{3}{4}-z$); *b* ($1-x, \frac{1}{2}-y, +z$); *c* ($\frac{1}{4}+y, \frac{3}{4}-x, \frac{3}{4}-z$).

The asymmetric unit of **46** only contains one quarter of the entire structure (Figure 6.15). Within the asymmetric unit there are three distinct Mn^{III} ions (Mn1, Mn2 and Mn3) and two distinct Cu^{II} ions (Cu1 and Cu2). Mn1, 2 and 3 all have axially elongated bonds (Table 6.24), as expected for Mn^{III} ions in an octahedral crystal field (see Figure 6.17 for orientation of Jahn-Teller axes).

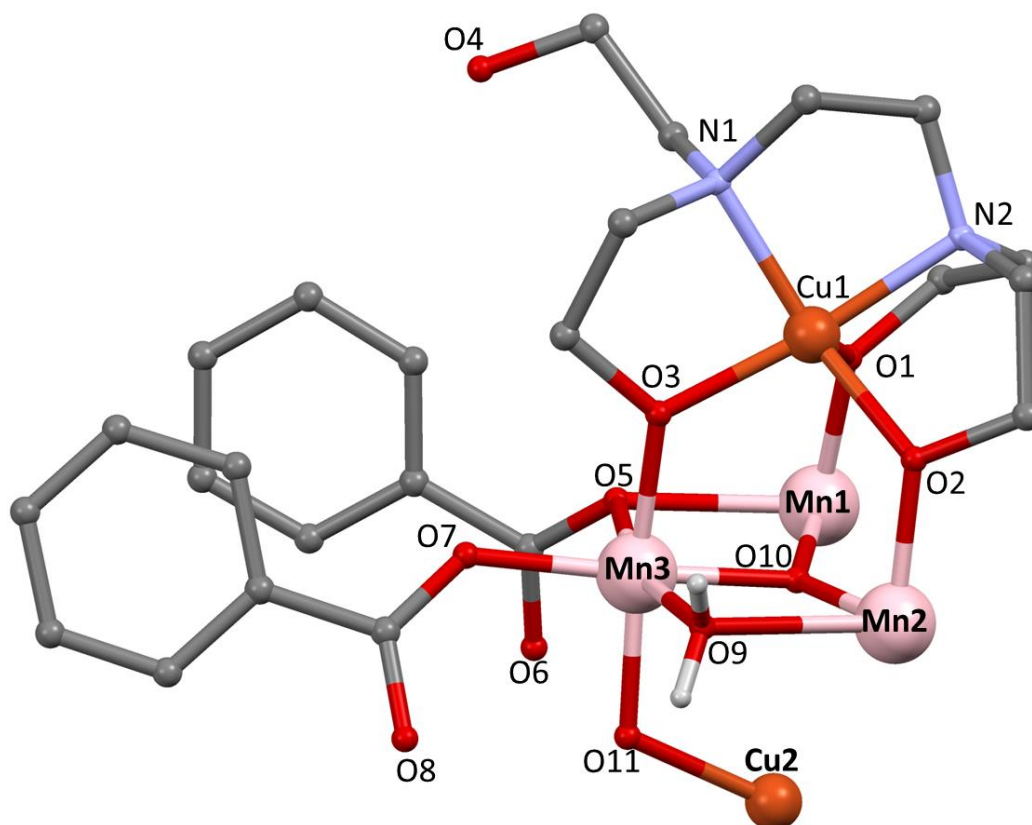


Figure 6.15: Asymmetric unit of **46**. C-H protons are not shown. Atom O4 is considered to be protonated, however, the proton could not be found during the structure refinement hence is not shown here. O4 is considered to be protonated due to charge balance and hydrogen bonding pathway considerations (*vide infra*). Atom colours: Cu^{II}, orange; Mn^{III} pink; O, red; N, blue; C, grey and H, white.

Cu1 is chelated by a Hedte³⁻ ligand which acts as a {N₂O₃} donor set, forming a {Cu(Hedte)}¹⁻ subunit. Atoms O1, 2 and 3 are the deprotonated alkoxo arms of the ligand with O4 remaining protonated and extending into the lattice as an unbound arm (Figure 6.15). The proton on O4 could not be found unfortunately during the structure refinement, however, is expected to exist through charge balance and hydrogen bonding pathway considerations (see Figure 6.20 for H-bonding pathways). The {Cu(Hedte)}¹⁻ subunit caps a pseudo {Mn^{III}₃} oxo-centred triangle subunit with the alkoxo arms of the ligand acting as

bridges with bonds between Cu1- and: O1-Mn1, O2-Mn2 and O3-Mn3 (Table 6.23 for bond lengths). Atoms Mn1, 2 and 3 are bridged to each other through the centre of the triangle by a μ_3 O²⁻ ion (O10), BVS calculations²⁵ for O10 give an estimated oxidation state closest to 2; supporting its assignment as O²⁻. Mn2 and Mn3 are bridged to each other by a μ_2 -OH₂ ligand (O9(H₂)).

Bond	Length (Å)
Cu1-O1	2.090(5)
Cu1-O2	1.988(5)
Cu1-O3	1.939(5)
Cu1-N1	2.024(8)
Cu1-N2	2.006(6)
Mn1-O1	1.886(5)
Mn1-O1b	1.886(5)
Mn1-O5	2.275(5)
Mn1-O5b	2.275(5)
Mn1-O10	1.953(5)
Mn1-O10b	1.953(5)
Mn2-O2	1.906(5)
Mn2-O6b	2.179(5)
Mn2-O8a	1.955(5)
Mn2-O9	2.449(5)
Mn2-O10	1.900(4)
Mn2-O11a	1.876(4)
Mn3-O3	1.922(5)
Mn3-O5	2.348(5)
Mn3-O7	1.940(5)
Mn3-O9	2.248(5)
Mn3-O10	1.894(4)
Mn3-O11	1.891(4)
Cu2-O11	1.944(4)
Cu2-O11a	1.944(4)
Cu2-O11b	1.944(4)
Cu2-O11c	1.944(4)

Table 6.23: Selected bond lengths in **46**. Axially distorted Jahn-Teller bonds highlighted in bold. Symmetry operations: *a* ($\frac{3}{4}+y, \frac{1}{4}-x, \frac{3}{4}-z$); *b* ($1-x, \frac{1}{2}-y, +z$); *c* ($\frac{1}{4}+y, \frac{3}{4}-x, \frac{3}{4}-z$).

Although relatively rare, there are reports of Mn ions bridged by a water ligand,³³⁻³⁵ including a {Mn₁₂} complex with H₄edte reported by Hendrickson *et. al.*⁴ BVS calculations also support the assignment as H₂O; giving an estimated oxidation state

closest to 0 for O9. Mn1 and Mn3 are bridged by a benzoate ligand through O5 in the asymmetric unit. The ligand acts as a 1,1',3-bridge with O6 coordinated to Mn2b. The second benzoate ligand acts as a 1,3-bridge, capping Mn3 through O7, with O8 bridging to Mn2c. The connectivity of symmetry related benzoate ligands and Mn^{III} ions is depicted in Figure 6.16. The benzoate ligands in the asymmetric unit π - π stack in a parallel off-set manner, with a distance of ≈ 4.1 Å between the centroids of the rings. Finally, Cu2 bonds through a bridging μ_3 O²⁻ ion (O11) in the asymmetric unit to Mn3.

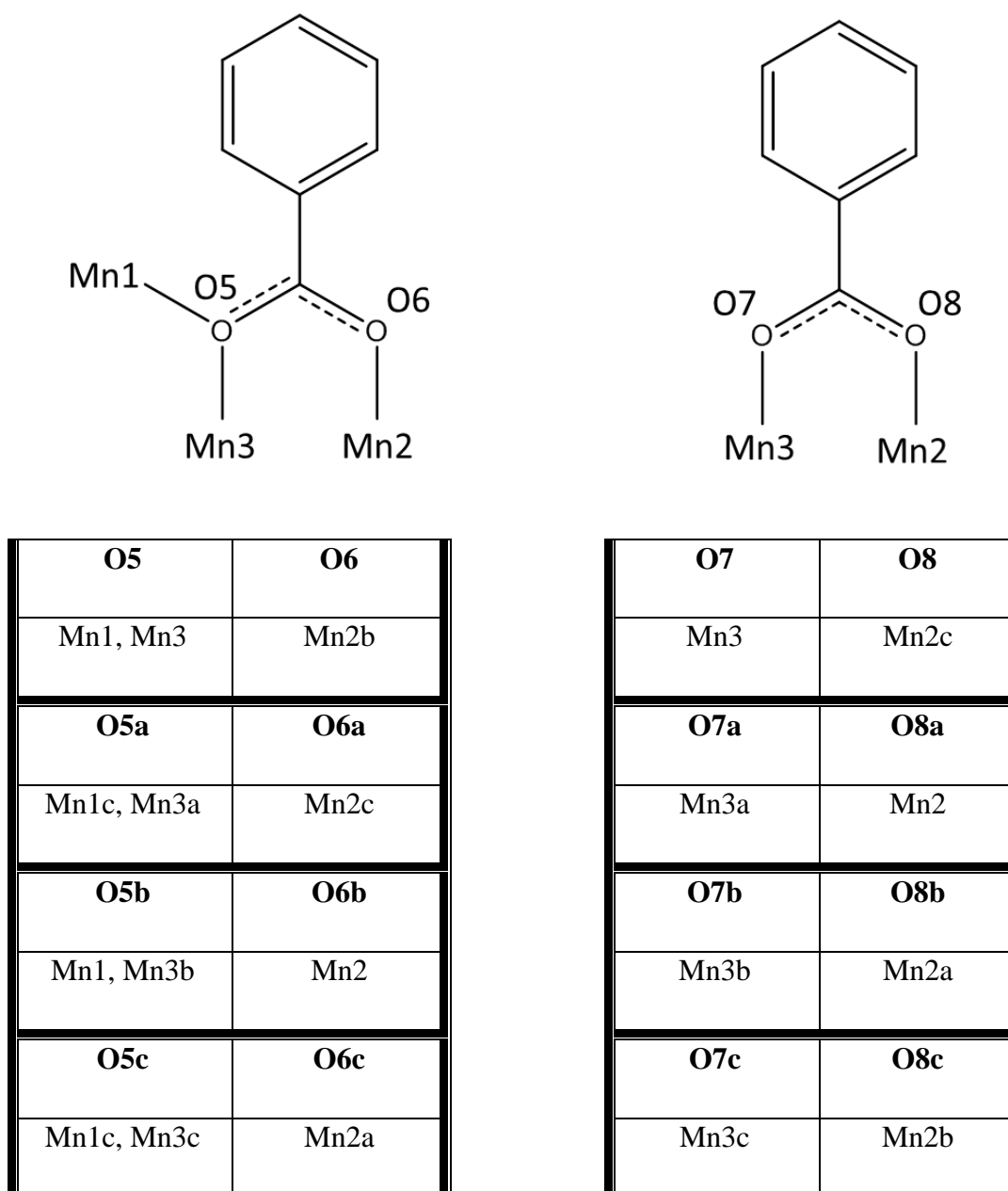


Figure 6.16: Connectivity to symmetry related atoms by benzoate ligands in 46.

During the structure refinement there was some uncertainty toward the identity of the central metal ion Cu2. The final assignment of Cu^{II} was made based on charge balance considerations, BVS calculations²⁵ (Table 6.24) and the propensity of Cu^{II} to adopt square

planar coordination geometry over Mn^{II}. A search of the CSD found 676 hits for examples of square planar Cu^{II} ions, whereas only 3 were found for Mn^{II}.³⁶⁻³⁸

Atom	Cu ^{II}	Mn ^{II}
Oxidation state	<u>1.949</u>	2.631

Table 6.24: Summary of BVS calculations for central ion in **46**.

Complex **46** crystallises in the tetragonal space group $I4_1/a$ with 4_1 and 2_1 screw axes and a C_2 rotational axis parallel to the crystallographic c -axis; passing through Mn1 and Cu2 in the asymmetric unit. The molecule as a whole contains four asymmetric units and can be described as having a ‘top’ and ‘bottom’ half; with Cu2 at the centre between the two halves. One of the halves is represented in Figure 6.17; it contains two asymmetric units related by a C_2 rotation around the crystallographic c -axis; passing through Mn1c and Cu2.

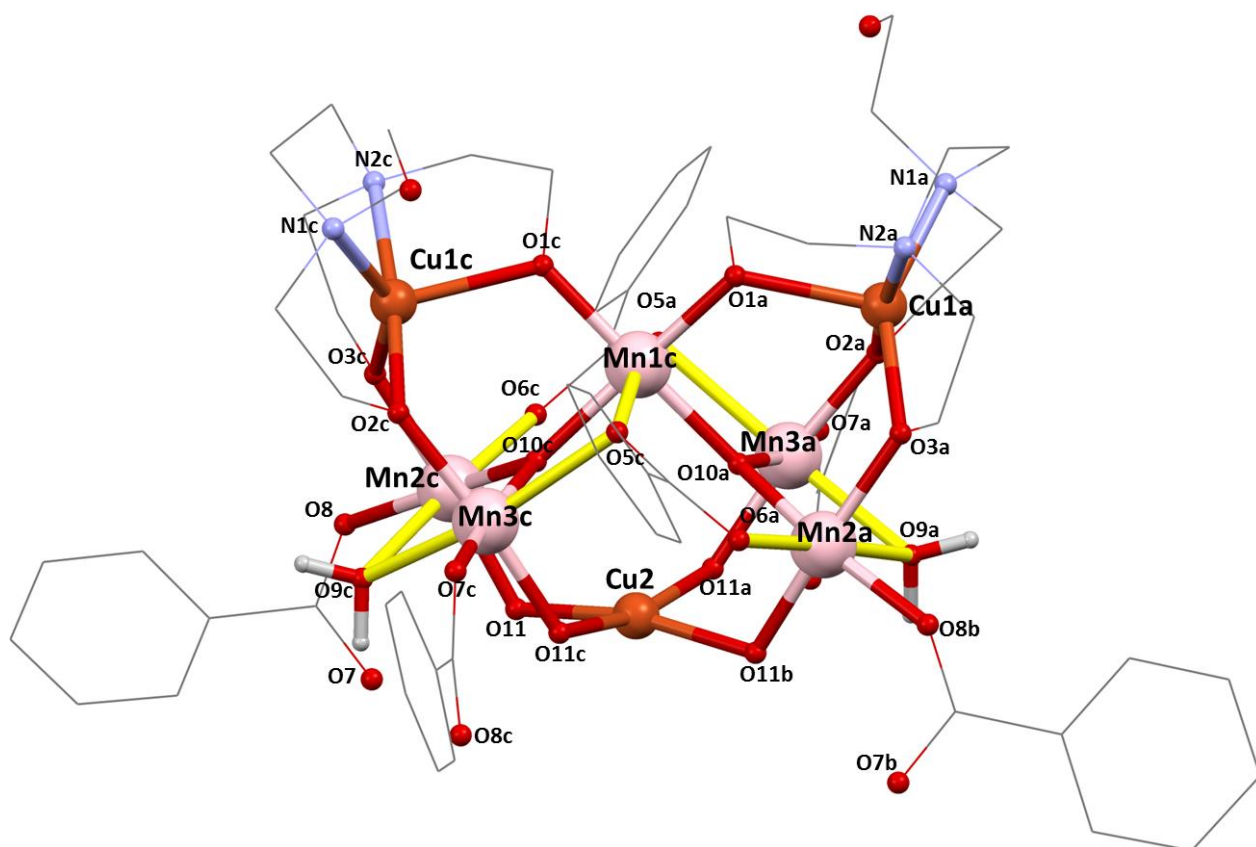


Figure 6.17: Two asymmetric units of **46**, roughly corresponding to half of the overall molecular structure. C-H protons, lattice nitrate and crystallisation solvent have been omitted. Jahn-Teller elongated axes of Mn^{III} ions highlighted in yellow. Atom colours: Cu^{II}, orange; Mn^{III} pink; O, red; N, blue; C, grey; and H, white. Symmetry operations: a ($\frac{3}{4}+y$, $\frac{1}{4}-x$, $\frac{3}{4}-z$); b ($1-x$, $\frac{1}{2}-y$, $+z$); c ($\frac{1}{4}+y$, $\frac{3}{4}-x$, $\frac{3}{4}-z$).

The ‘top’ and ‘bottom’ halves are related by an S_4 symmetry operation; a 90° rotation around the c -axis followed by inversion through Cu2 (see Figure 6.18). Atoms Cu2, Mn1 and Mn1c therefore all lie on special positions within the unit cell. The two halves are chemically linked together through four O²⁻ ions: O11, O11a, O11b and O11c, as well as four benzoate ligands containing atoms: O7, O8; O7a, O8a; O7b, O8b; O7c and O8c (Figure 6.19).

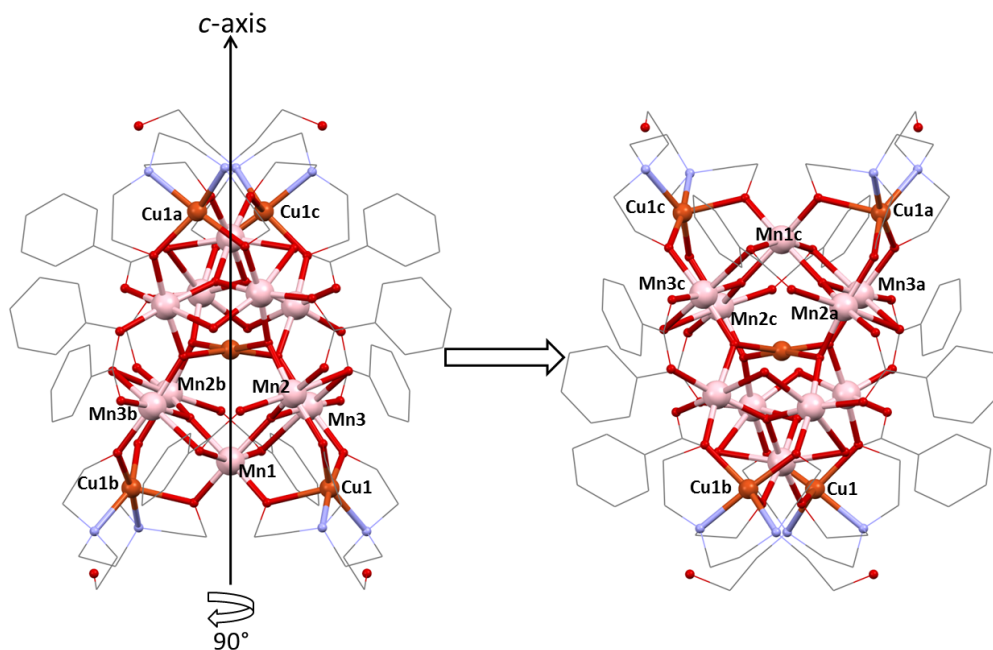


Figure 6.18: Molecular structure of **46** as viewed down the crystallographic a -axis, illustrating a 90° rotation about the c -axis.

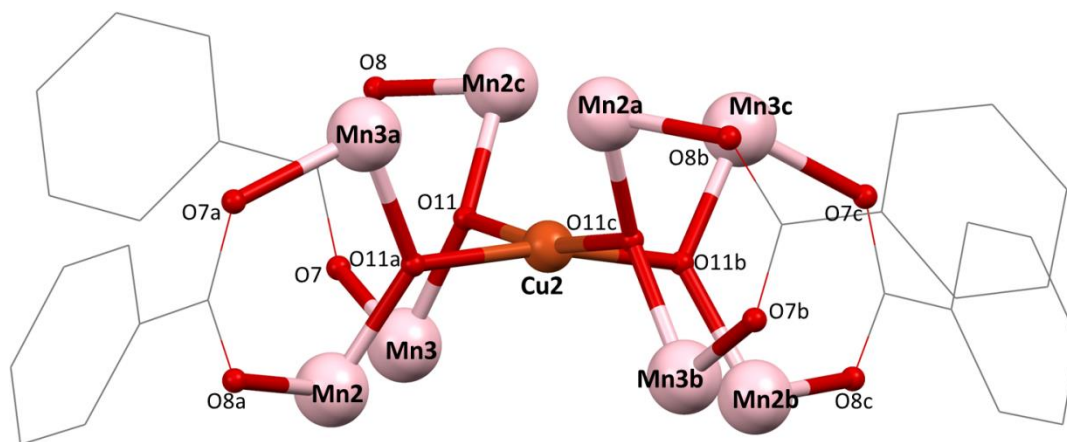


Figure 6.19: Centre region of **46** showing how the ‘top’ and ‘bottom’ halves are linked through O²⁻ ions and benzoate ligands. Cu2 sits directly on a $\bar{4}$ symmetry site within the complex.

As viewed down both the *a* and *b*-axes, **46** packs along glide planes which run parallel with these axes (Figure 6.20). Along the unique *c*-axis, the molecules pack in columns, related by a 2_1 screw axis which passes directly through Mn1-Cu2-Mn1c in each molecule (Figure 6.21).

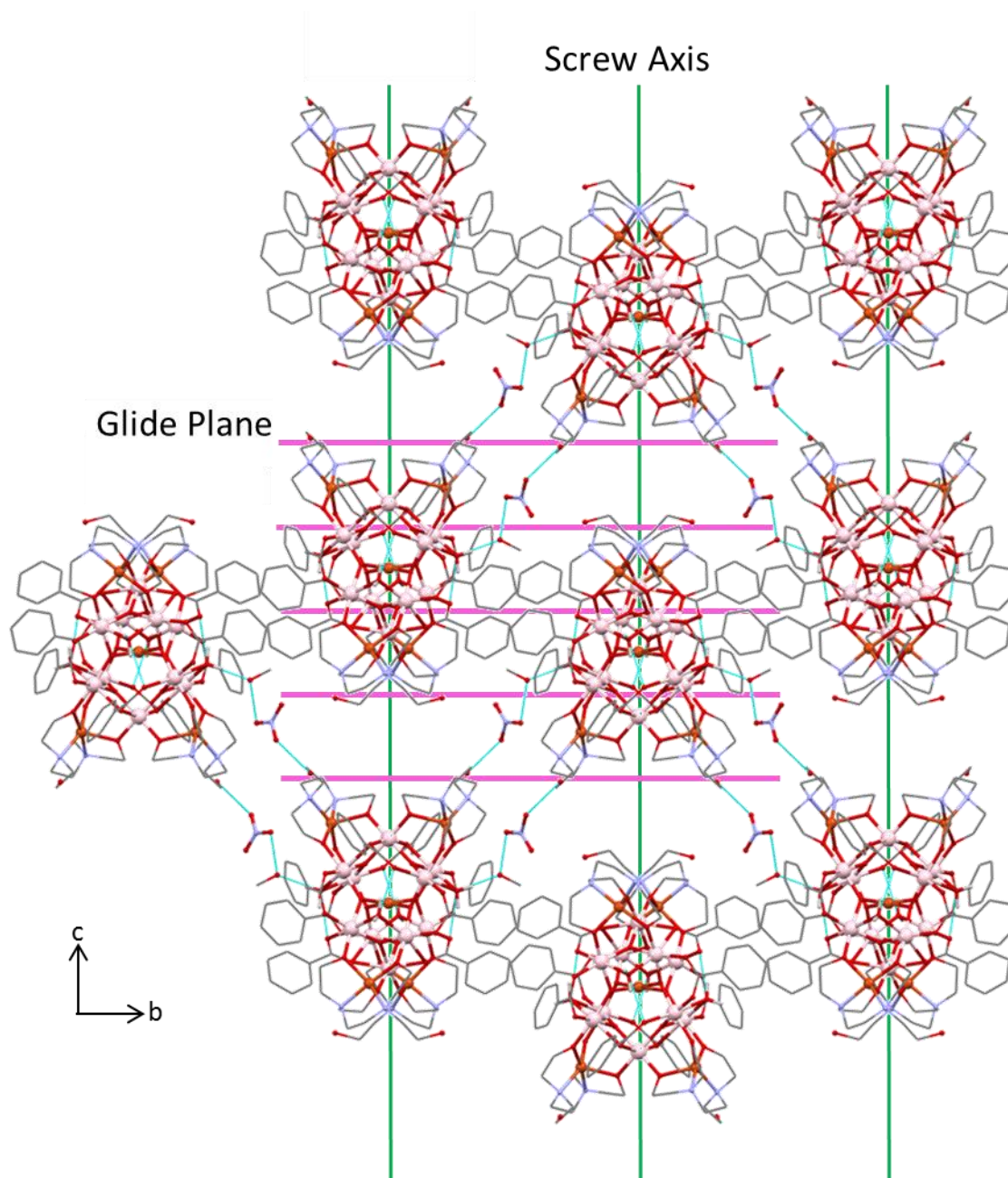


Figure 6.20: Crystal packing of **46** as viewed down the *a* axis. The $\{Mn_{10}Cu_5\}$ molecules illustrated here lie in the plane of the paper. The pink lines represent glide planes which relate molecules along the *a* or *b* axis. The green lines represent screw axes (4_1 & 2_1) that relate columns of molecules stacking along the *c*-axis. Hydrogen bonding interactions are

drawn as light blue dotted lines. Hydrogen bonding interactions into the page (along the *a*-axis) have been omitted for clarity. π -stacking interactions are also not shown.

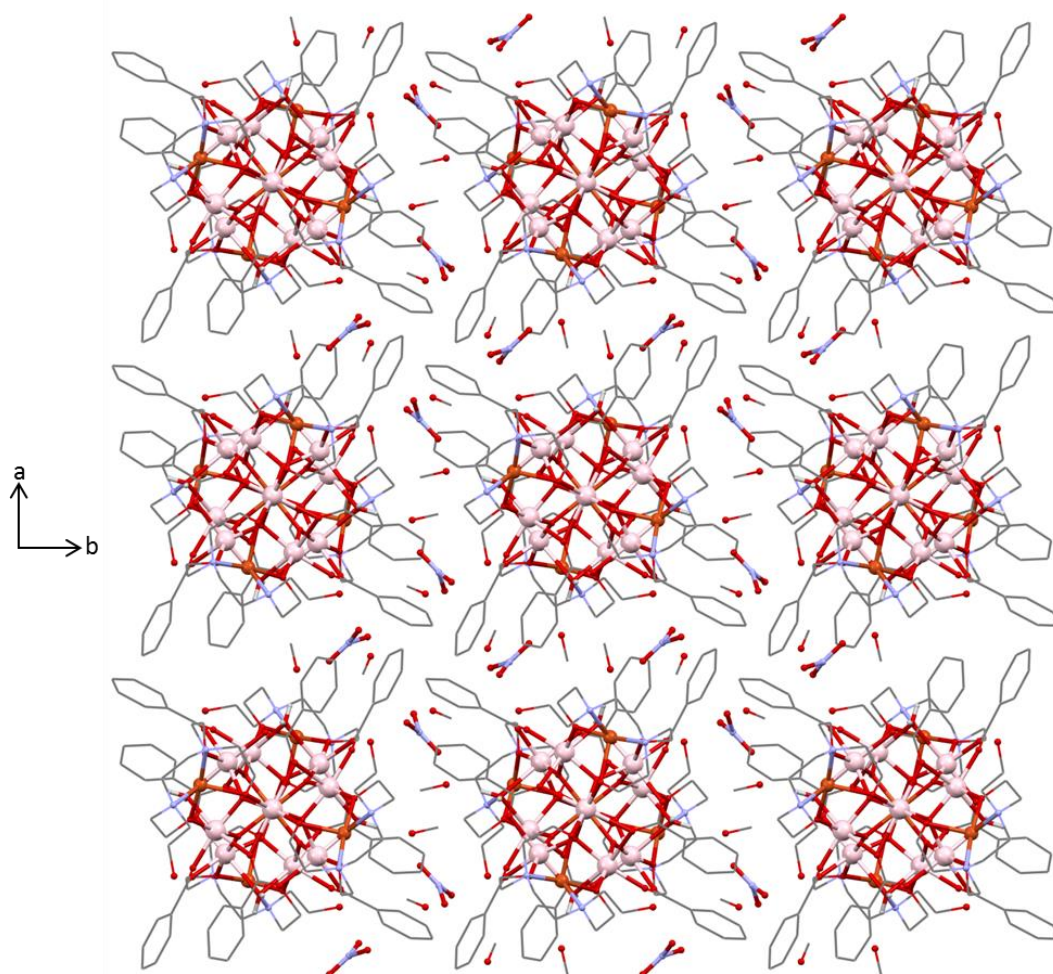


Figure 6.21: Packing of **46** as viewed down the *c*-axis.

Each molecule forms chains of intermolecular hydrogen bonds with four surrounding molecules. These chains start at the free arm of the $\{\text{CuHedte}\}^{1-}$ subunit and pass through a lattice nitrate and crystallisation MeOH and onto the water ligand (O9). Each specific molecule forms two of these pathways with four surrounding molecules (Figure 6.20). Each molecule also forms T-shaped π -stacking interactions with its nearest neighbours along the *a* and *b*-axes. The π -stacking interactions are of a distance $\approx 3.575(2)$ Å, two being formed between each of the four nearest neighbours for each molecule.

Complex **46** is a rare example of a high nuclearity $\{\text{MnCu}\}$ complex, the largest is a $\{\text{Cu}^{\text{I}}_4\text{Cu}^{\text{II}}_{13}\text{Mn}^{\text{II}}_4\text{Mn}^{\text{III}}_{12}\text{Mn}^{\text{IV}}_{12}\}$ complex reported by Hendrickson *et. al.*³⁹ Other notable examples include a $\{\text{Mn}^{\text{II}}_6\text{Mn}^{\text{III}}_{12}\text{Cu}^{\text{II}}_6\}$ reported by Murrie *et. al.*⁴⁰ $\{\text{Mn}^{\text{II}}\text{Cu}^{\text{II}}_8\}$ and $\{\text{Mn}^{\text{II}}_5\text{Cu}^{\text{II}}_4\}$ complexes by Thompson *et. al.*⁴¹ and $\{\text{Mn}^{\text{III}}_6\text{Cu}^{\text{II}}_{10}\}$ and $\{\text{Mn}^{\text{III}}_8\text{Mn}^{\text{IV}}_4\text{Cu}^{\text{II}}_8\}$ complexes by Oshio *et. al.*⁴² Perhaps the closest matching structures in the CSD to **46** are a

series of {Mn^{III}₁₀Ln^{III}₂} complexes (where Ln^{III} = Pr^{III}, Nd^{III}) reported by Turta *et. al.*⁴³ The Mn^{III} ions are arranged in pseudo oxo-centred triangles, bound together by benzoate ligands with one of the Ln^{III} ions at the centre of the molecule.

<i>Empirical formula</i>	<i>Mn₁₀Cu₅C₁₀₄H₁₆₄N₁₂O₆₄</i>
Molar mass (g mol ⁻¹)	3473.60
Crystal System	Tetragonal
Space Group	<i>I</i> 4 ₁ / <i>a</i>
a (Å)	27.5814(6)
b (Å)	27.5184(6)
c (Å)	18.4546(4)
α (deg)	90
β (deg)	90
γ (deg)	90
V (Å ³)	14039.0(3)
Z	4
T (K)	100
λ (Å)	0.71073
ρ _{calc} (g/cm ³)	1.586
μ (mm ⁻¹)	1.697
^a R ₁	0.0677
^b wR ₂	0.1620
Goodness of fit	1.102
F(000)	7116
Reflections	6405
Parameters	412
Restraints	291

Table 6.25: Crystallographic data for **46**

$${}^aR_1 = \frac{\sum ||F_o| - |F_c||}{\sum |F_o|}$$

$${}^b wR_2 = \left[\frac{\sum [w(F_o^2 - F_c^2)^2]}{\sum [(F_o^2)^2]} \right]^{\frac{1}{2}} \quad \text{where } w = 1/[\sigma^2(F_o^2) + (0.2P)^2] \text{ and } P = [F_o^2 + 2F_c^2]/3$$

Atoms	Angle (°)
Cu1-O1-Mn1	120.0(2)
Cu1-O2-Mn2	120.8(2)
Cu1-O3-Mn3	121.1(2)
Mn1-O5-Mn3	87.38(16)
Mn1-O10-Mn2	136.7(2)
Mn1-O10-Mn3	112.3.(2)
Mn2-O9-Mn3	82.00(15)
Mn3-O11-Mn2c	128.7(2)
Cu2-O11-Mn3	114.2(2)
Cu2-O11-Mn2c	113.2(2)

Table 6.26: Selected bond angles in **46**. Symmetry operation: *c* (1/4+y, 3/4-x, 3/4-z).

Atom	Mn ^{II}	Mn ^{III}
Mn1	3.38	<u>3.12</u>
Mn2	3.41	<u>3.15</u>
Mn3	3.29	<u>3.03</u>

Table 6.27: BVS calculations²⁵ for Mn1-3 in **46**. Underlined values indicate closest match to assigned oxidation state.

6.4 Magnetism

6.4.1 Static magnetic properties of {Mn₁₀Cu₅} (**46**)

The magnetic susceptibility of **46** was measured in 1 kOe field between 280-1.8 K (Figure 6.22). The calculated χT value of 31.47 cm³ K mol⁻¹ is slightly higher than the observed 30.64 cm³ K mol⁻¹.

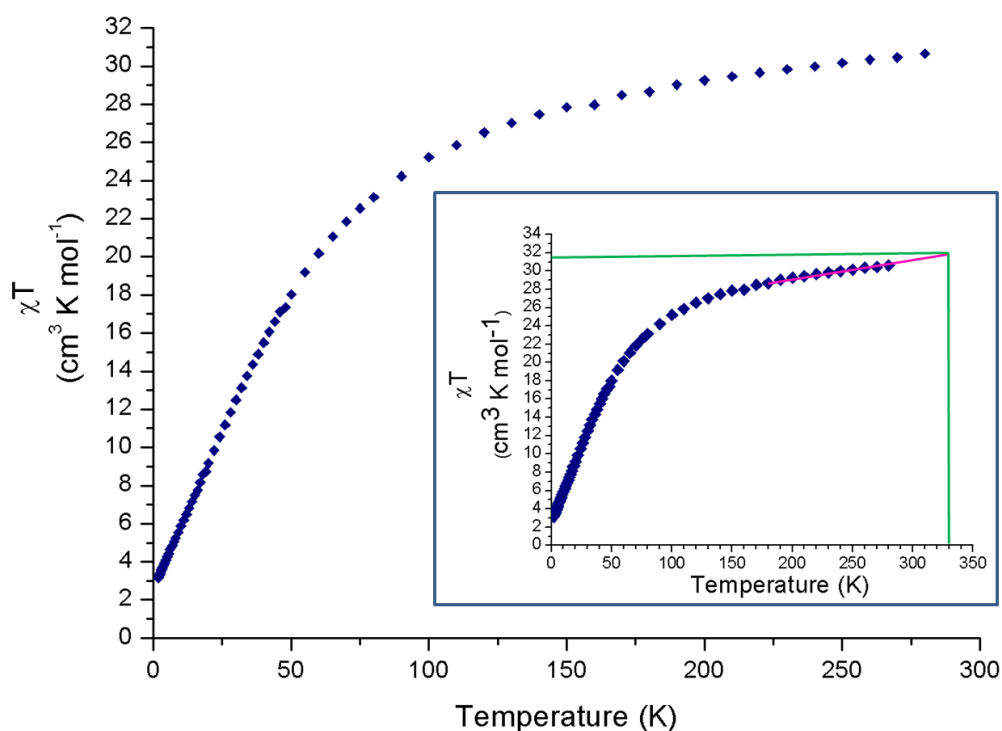


Figure 6.22: Temperature dependent magnetic susceptibility for **47** in 1000 Oe field. Inset: shows extrapolated susceptibility out to 330 K where χT would reach the calculated value of 31.5 cm³ K mol⁻¹ for {Mn₁₀Cu₅}. The green lines represent the calculated χT and T values, the pink line represents a linear fit of the high T data.

The calculated value was obtained using $\frac{ng^2}{8}s(s+1)$ where n is the number of ions, g is the Landé g -value for that ion and s is the ion's spin. Therefore, ten Mn^{III} ions ($s = 2$, $g = 1.98$) gives $\chi T = 29.40 \text{ cm}^3 \text{ K mol}^{-1}$ and five Cu^{II} ions ($s = 1/2$, $g = 2.1$) gives $\chi T = 2.06 \text{ cm}^3 \text{ K mol}^{-1}$, giving a total $\chi T = 31.47 \text{ cm}^3 \text{ K mol}^{-1}$. The discrepancy could be due to strong antiferromagnetic coupling between Mn^{III} ions which has been observed before in high nuclearity Mn^{III} complexes.^{1-5,44,45} χT decreases steadily as the temperature is lowered to $\approx 100 \text{ K}$, followed by a sharper decrease down to a minimum of $3 \text{ cm}^3 \text{ K mol}^{-1}$ at 1.8 K , strongly indicative of dominant intramolecular antiferromagnetic exchange. Assuming $g = 2$, an estimation of the ground state of **46** is calculated as $S = 2$.

6.4.2 Dynamic Magnetic Properties of

[Mn₁₀Cu₅O₈(OBz)₈(Hedte)₄(H₂O)₄][NO₃]₄·8MeOH (46)

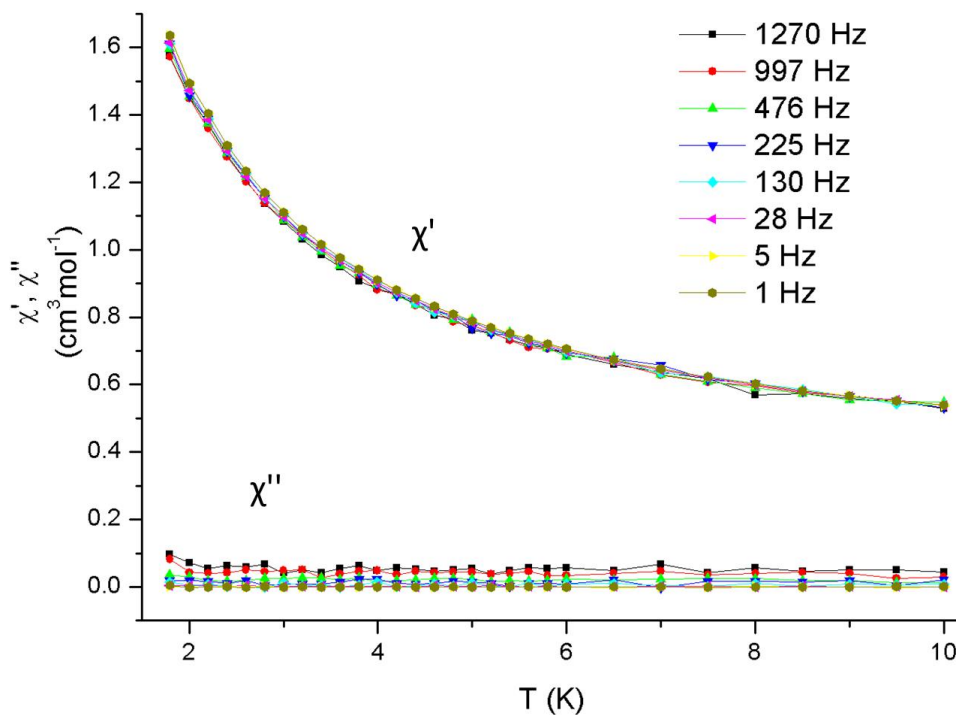


Figure 6.23: Ac susceptibility for **46** in zero applied dc field.

Ac susceptibility measurements were made for **46** to search for slow magnetic relaxation down to 1.8 K . There is no frequency dependent decrease in the in-phase susceptibility nor

a concomitant frequency dependent increase in the out-of-phase susceptibility, indicating that **46** does not display SMM behaviour. This is often observed in Mn^{III} complexes with dominant intramolecular antiferromagnetic exchange.⁴⁶ The absence of slow magnetic relaxation in the ac-measurements are likely due to the low ground state spin ($S = 2$) combined with a low overall anisotropy due to the effectively perpendicular arrangement of the Mn^{III} Jahn-Teller axes.⁴⁷

6.5 Conclusions

The aim to synthesise new monomeric {M^{II}(H_nedte)} complexes with first row transition metals was relatively successful, with the ions Mn^{II}, Co^{II}, Ni^{II} and Zn^{II} successfully incorporated. A new Ni^{II} monomeric complex with the related ligand H₄pdte was synthesised. The added carbon atom in the ligand backbone provided enough flexibility to allow all 6 donor atoms to bind to the Ni^{II} centre in contrast to {Ni(H₄edte)} where H₄edte only binds through five donor atoms. The use of the monomers as subsequent starting materials was less successful with respect to a rational building block approach. Using the monomers, two new 3d-3d' complexes were synthesised serendipitously; a {Cu^{II}₆Ni^{II}₂} complex and a large {Mn^{III}₁₀Cu^{II}₅} complex (**46**). Complex **46**'s magnetic properties were studied, with temperature dependent dc susceptibility measurements highlighting dominant intramolecular antiferromagnetic exchange leading to a small estimated ground state of $S = 2$. Ac susceptibility measurements showed no out-of-phase susceptibility signals, indicative that **46** does not show SMM properties. A new {Cu₈} complex with H₄edte exhibiting an interesting double cubane-like structure was synthesised. Magnetic measurements were not carried out, however, the complex is likely to exhibit dominant antiferromagnetic Cu^{II}-Cu^{II} exchange due to the Cu^{II}-O-Cu^{II} bond angles²⁸ (most over 97°, Table 6.21). A rare example of a mixed valent {Mn^{II}Mn^{III}} (**43**) dimeric complex was also synthesised whose Mn^{II}-O-Mn^{III} bond angles lie in a known ferromagnetic range for this ion pair.^{26,27} The magnetic anisotropy of the Mn^{III} ion combined with the large spin of the Mn^{II} ion could provide some interesting magnetic properties and could potentially be investigated.

6.6 References

- (1) R. Bagai, K. A. Abboud, G. Christou, *Inorg. Chem.* 47 (2008) 621-631.
- (2) A.-J. Zhou, J.-D. Leng, J.-S. Hu, M.-L. Tong, *Dalton Trans.* 42 (2013) 9428-9431.
- (3) A. Saha, K. A. Abboud, G. Christou, *Inorg. Chem.* 50 (2011) 12774-12784.
- (4) A.-J. Zhou, L.-J. Qin, C. C. Beedle, S. Ding, M. Nakano, J.-D. Leng, M.-L. Tong, D. N. Hendrickson, *Inorg. Chem.* 46 (2007) 8111-8113.
- (5) A.-J. Zhou, J.-L. Liu, R. Herchel, J.-D. Leng, M.-L. Tong, *Dalton Trans.* 17 (2009) 3182-3192.
- (6) K. Graham, F. J. Douglas, J. S. Mathieson, S. A. Moggach, J. Schnack, M. Murrie, *Dalton Trans.* 40 (2011) 12271-12276.
- (7) R. Bagai, M. R. Daniels, K. A. Abboud, G. Christou, *Inorg. Chem.* 47 (2008) 3318-3327.
- (8) R. Kumar, S. Obrai, A. Kaur, G. Hundal, H. Meehnian, A. K. Jana, *Polyhedron* 56 (2013) 55-61.
- (9) A. S. de Sousa, M. A. Fernandes, *Polyhedron* 21 (2002) 1883-1888.
- (10) W. Plass *Eur. J. Inorg. Chem.* (1998) 799-805.
- (11) F. J. Kettles, V. A. Milway, F. Tuna, R. Valiente, L. H. Thomas, W. Wernsdorfer, S. T. Ochsenbein, M. Murrie, *Inorg. Chem.* 53 (2014) 8970-8978.
- (12) A. Saha, M. Thompson, K. A. Abboud, W. Wernsdorfer, G. Christou, *Inorg. Chem.* 50 (2011) 10476 – 10485.
- (13) M. N. Ahktar, V. Merearcere, G. Novitchi, J-P. Tuchagues, C. E. Anson, A. K. Powell, *Chem. Eur. J.* 15 (2009) 7278-7282.
- (14) W.-G. Wang, A.-J. Zhou, W.-X. Zhang, M.-L. Tong, X.-M. Chen, M. Nakano, C. C. Beedle, D. N. Hendrickson, *J. Am. Chem. Soc.* 129 (2007) 1014-1015.
- (15) Y.X. Wang, W. Shi, H. Li, Y. Song, L. Fang, Y. Lan, A.K. Powell, W. Wernsdorfer, L. Ungur, L.F. Chibotaru, M. Shen, P. Cheng, *Chem. Sci.* 3 (2012) 3366–3370.
- (16) O. Z. Yesilel, B. Karamahmut, F. Semerci, Y. Yesiloz, *Polyhedron* 42 (2012) 307-314.
- (17) G. Hundal, M. S. Hundal, S.Obrai, N. S. Poonia, S. Kumar, *Inorg. Chem.* 41 (2002) 2077-2086.
- (18) R. Kumar, S. Obrai, A. Kaur, M. S. Hundal, H. Meehnian, A. K. Jana, *New J. Chem.* 38 (2014) 1186-1198.
- (19) S. Gulcemal, I. Kani, F. Yilmaz, B. Cetinkaya, *Tetrahedron* 66 (2010) 5602-5607.
- (20) Tulloch, A. A. D., US 2010/0292449 A.1 2010.

- (21) C. J. Chuck, M. G. Davidson, G. G. Du Sart, P. K. Ivanova-Mitseva, G. I. Kocick-Kohn, L. B. Manton, *Inorg. Chem.* 52 (2013) 10804-10811.
- (22) M. Llunell, D. Casanova, J. Cirera, P. Alemany, S. Alvarez, 'SHAPE: Program for the Stereochemical Analysis of Molecular Fragments by Means of Continuous Shape Measures and Associated Tools', Version 2.1, 2013, Barcelona.
- (23) M. Murrie, *Chem. Soc. Rev.* 39 (2010) 1986-1995.
- (24) A. Jana, N. Aliaga-Alcalde, E. Ruiz, S. Mohanta, *Inorg. Chem.* 52 (2013) 7732-7746.
- (25) N. E. Breese, M. O'Keefe, *Acta Cryst. B.* 47 (1991) 192-197.
- (26) T. C. Stamatatos, K. M. Poole, K. A. Abboud, W. Wernsdorfer, T. A. O'Brien, G. Christou, *Inorg. Chem.* 47 (2008) 5006-5021.
- (27) D. Foguet-Albiol, T. A. O'Brien, W. Wernsdorfer, B. Moulton, M. J. Zaworotko, K. A. Abboud, G. Christou, *Angew. Chem., Int. Ed.* 44 (2005) 897-901.
- (28) F. Bramsen, A. D. Bond, C. J. McKenzie, R. G. Hazell, B. Moubaraki, K. S. Murrie, *Chem. Eur. J.* 11 (2005) 825-831.
- (29) K. Deka, R. J. Sarma, J. B. Baruah, *Inorg. Chem. Commun.* 9 (2006) 931-934.
- (30) J. Gao, S. H. Zhong, R. A. Zingaro, *J. Mol. Catal. A: Chem.* 207 (2004) 15-20.
- (31) R. Angamuthu, L. Gelauff, M. A. Siegler, A. L. Spek, E. Bouwman, *Chem. Commun.* (2009) 2700-2702.
- (32) M. Hamid, A. A. Tahir, M. Mazhar, M. Zeller, K. C. Molloy, A. D. Hunter, *Inorg. Chem.* 45 (2006) 10457-10466.
- (33) J.-L. Liu, F.-S. Guo, Z.-S. Meng, Y.-Z. Zheng, J.-D. Leng, M.-L. Tong, L. Ungur, L. F. Chibotaru, K. J. Heroux, D. N. Hendrickson, *Chemical Science* 2 (2011) 1268-1272.
- (34) V. Chandrasekhar, A. Dey, S. Das, M. Rouxieres, R. Clerac, *Inorg. Chem.* 52 (2013) 2588-2598.
- (35) I. A. Kuhne, N. Magnani, V. Mereacre, W. Wernsdorfer, C. E. Anson, A. K. Powell, *Chem. Commun.* 50 (2014) 1882-1885.
- (36) L. Zhang, Y.-Q. Sun, G.-M. Yang, S.-P. Yan, Z.-H. Jiang, D.-Z. Liao, *J. Coord. Chem.* 56 (2003) 1441-1445.
- (37) W.-X. Zhang, W. Xue, X.-M. Chen, *Inorg. Chem.* 50 (2011), 309-316.
- (38) B.J. Gunderman, P.J. Squattrito, S.N. Dubey, *Acta Crystallogr. Sect. C: Cryst. Struct. Commun.* 52 (1996) 1131-1134.
- (39) W.-G. Wang, A.-J. Zhou, W.-X. Zhang, M.-L. Tong, X.-M. Chen, M. Nakano, C. C. Beedle, D. N. Hendrickson, *J. Am. Chem. Soc.* 129 (2007) 1014-1015.

- (40) V. A. Milway, F. Tuna, A. R. Farrell, L. E. Sharp, S. Parsons, M. Murrie, *Angew. Chem. Int. Ed.* 52 (2013) 1949-1952.
- (41) L. N. Dawe, K. V. Shuvaev, L. K. Thompson, *Inorg.Chem.* 48 (2009) 3323-3341.
- (42) S.Yamashita, T. Shiga, M. Kurashina, M.Nihei, H.Nojiri, H.Sawa, T.Kakiuchi, H.Oshio, *Inorg.Chem.* 46 (2007) 3810-3812.
- (43) V. Mereacre, D. Prodius, A. M. Ako, N. Kaur, J. Lipkowski, C. Simmons, N. Dalal, I. Geru, C. E. Anson, A. K. Powell, C. Turta, *Polyhedron* 27 (2008) 2459-2463.
- (44) J. S. Costa, G. A. Craig, L. A. Barrios, O. Roubeau, E. Ruiz, S. Gómez-Coca, S. J. Teat, G. Aromí, *Chem. Eur. J.* 17 (2011) 4960 – 4963.
- (45) N. C. Harden, M. A. Bolcar, W. Wernsdorfer, K. A. Abboud, W. E. Streib, G. Christou, *Inorg. Chem.* 42 (2003) 7067-7076.
- (46) H. J. Eppley, S. M. J. Aubin, W. E. Streib, J. C. Bollinger, D. N. Hendrickson, G. Christou, *Inorg. Chem.* 36 (1997) 109-115.
- (47) R. Bagai, G. Christou, *Chemical Society Reviews*, 38 (2009) 1011-1026.

7. Conclusions

The ligand H₄edte was used to synthesise thirty-four new complexes, one of which was confirmed as a new SMM. The complexes reported here with H₄edte can be broadly classified into four main families: the {LnCu₃(H₂edte)₃} series, the {Ln₄Zn₂} series, the {Ln} series and complexes containing 3*d* ions. H₄edte was capable of chelating 3*d* or 4*f* ions, and was able to provide alkoxo bridges between 3*d* and/or 4*f* ions in its deprotonated forms. Overall, the flexibility of the ligand yielded an array of interesting new structures. The second ligand, H₄pdte, was successfully synthesised and used to make an additional eleven complexes; the analogous {LnCu₃(H₂pdte)₃} series, and a {Ni} monomer. Discussed below are some of the main results found in each chapter, followed by an overall conclusion.

7.1 {LnCu₃(H₂edte)₃} Series

This series has eight isostructural members, where Ln = Pr^{III} (**2**), Nd^{III} (**3**), Eu^{III} (**4**), Gd^{III} (**5**), Tb^{III} (**6**), Dy^{III} (**7**), Er^{III} (**8**), Yb^{III} (**9**). Synthesis was achieved in a one pot reaction using the preformed Cu^{II} complex: [Cu₂(H₃edte)₂][NO₃]₂ (**1**). Of the eight complexes, **6** was found to be a new SMM; confirmed by ac susceptibility and magnetisation hysteresis measurements. **6** had an effective energy barrier to magnetic reorientation (U_{eff}) of 17.3(4) K with zero applied dc field with a 12 % increase in a 1 kOe dc field. Magnetisation hysteresis measurements found a non-zero magnetisation at zero-field, confirming **6**'s classification as a new SMM. Complex **7** behaved as a field induced SMM – requiring a dc field of 1.5 kOe to exhibit a U_{eff} of 16.2(4) K. Hysteresis measurements showed that **7** displayed fast quantum tunnelling of the magnetisation at zero-field – attributed to the non-Kramer's nature of **7**'s ground M_{tot} state. Inelastic neutron scattering spectroscopy found that magnetic relaxation in **6** and **7** proceeds through magnetic excitation to the first excited M_{tot} state which corresponds to the flipping of a Cu^{II} spin. Combinations of ions such as Tb^{III} or Dy^{III} with Cu^{II} are proven here to be an attractive route to new 3*d*-4*f* SMMs due to their propensity for ferromagnetic exchange, the future goal however lies in controlling and increasing the Ln^{III}-Cu^{II} exchange interactions to facilitate larger blocking temperatures.

7.2 $\{\text{LnCu}_3(\text{H}_2\text{pdte})_3\}$ Series

The $\{\text{LnCu}_3(\text{H}_2\text{pdte})_3\}$ series has ten isostructural members, where Ln = Y^{III} (**11**), Pr^{III} (**12**), Nd^{III} (**13**), Eu^{III} (**14**), Gd^{III} (**15**), Tb^{III} (**16**), Dy^{III} (**17**), Ho^{III} (**18**), Er^{III} (**19**) and Yb^{III} (**20**). The series shared a very similar structure to the $\{\text{LnCu}_3(\text{H}_2\text{edte})_3\}$ series except for a few key differences; the Ln^{III}-O-O-Cu^{II} torsion angles were overall slightly more distorted – facilitating weaker *3d-4f* exchange, and the crystal field around the central Ln^{III} was slightly more distorted – facilitating quantum tunnelling of the magnetisation. These key differences resulted in the absence of out-of-phase ac susceptibility signals for **16** and **17**, in stark contrast to their analogous $\{\text{LnCu}_3(\text{H}_2\text{edte})_3\}$ counterparts. Complex **15**'s static magnetic properties were simulated using a two *J* model which suggested one of the three Gd^{III}-Cu^{II} exchange interactions was antiferromagnetic. In contrast, all three Gd^{III}-Cu^{II} exchange parameters for $\{\text{GdCu}_3(\text{H}_2\text{edte})_3\}$ were effectively modelled as ferromagnetic. However, a more complex model is required to draw better comparison between the magnetic properties of the two analogous complexes.

7.3 $\{\text{Ln}_4\text{Zn}_2\}$ Series

The $\{\text{Ln}_4\text{Zn}_2\}$ series has seven isostructural members, where Ln = Eu^{III} (**21**), Gd^{III} (**22**), Tb^{III} (**23**), Dy^{III} (**24**), Ho^{III} (**25**), Er^{III} (**26**) and Yb^{III} (**27**). Ac susceptibility measurements for **24** only showed the onset of slow relaxation of the magnetisation down to 1.8 K – owed to the significant crystal field distortion around the Dy^{III} ions. Fitting of the static magnetic properties of **22** found an overall antiferromagnetic *S* = 0 ground state, therefore **22** would not be suitable as a magnetic refrigerant.

Although the magnetic properties of the $\{\text{Ln}_4\text{Zn}_2\}$ series were disappointing, future work measuring the optical properties of the Tb^{III} and Eu^{III} analogues in particular would be interesting. Eu^{III} and Tb^{III} are strong emitters in the near-IR (620 nm) and green (550 nm) regions of the electromagnetic spectrum respectively; potentially making **21** and **23** candidates for new luminescent probes for biological imaging.

7.4 {Ln} Series

H₄edte was capable of chelating the Ln^{III} ions; Y^{III} (**28**), La^{III} (**29**), Pr^{III} (**30**), Nd^{III} (**31**), Gd^{III} (**32**), Tb^{III} (**33**), Dy^{III} (**34**), Ho^{III} (**35**) and Er^{III} (**36**) to form monomeric complexes. Magnetic susceptibility measurements for **33** showed no SMM properties, and for **34**, only the onset of slow relaxation was observed even with a 1 kOe dc field. Although the ligand acted as an effective chelate, the crystal field it generated, along with the two nitrate ligands, did not induce SMM behaviour. Further work on replacing the nitrate ligands with, for example, acetylacetonate ligands may better facilitate slow magnetic relaxation. Another interesting avenue to explore would be using {Ln^{III}} molecules as rational building blocks to synthesise larger complexes. If the monomers are stable to basic conditions, there could potentially be a wealth of new complexes to be discovered using this approach.

7.5 3d Complexes

One of the aims of the project was to try and use H₄edte to form monomeric 3d complexes for use as starting materials in a building block type approach. This strategy did not prove overly successful in the intended way, however, new complexes; {Cu₆Ni₂} (**45**) and {Mn₁₀Cu₅} (**46**) were formed using {Ni} (**37**) and {Mn} (**40**) starting materials respectively. Unfortunately, **46** exhibited dominant antiferromagnetic Mn^{III}-Mn^{III} exchange, resulting in a small $S = 2$ ground state and ac susceptibility measurements found no SMM behaviour. The symmetric structure however is aesthetically pleasing and illustrates the ligand's potential toward forming large complexes. A new {Cu₈} complex was also isolated, however, the Cu^{II}-O-Cu^{II} bond angles would likely result in dominant antiferromagnetic exchange interactions leading to a $S = 0$ ground state. An interesting mixed valent Mn^{II}-Mn^{III} dimer (**43**) was also isolated whose Mn^{II}-O-Mn^{III} bond angles are within a known ferromagnetic range for this pair. Magnetic measurements on **43** would certainly be interesting future work. Use of **43** as a starting material toward larger complexes could also be explored.

7.6 Final remarks

As stated above, the flexible nature of the H₄edte and H₄pdte ligands is an excellent characteristic for finding new and interesting structures. These structures could have potential applications in other fields such as catalysis, optical devices and even pharmaceuticals. However, with respect to molecular magnetism, predicting or controlling subtle structural properties important to SMMs with these flexible ligands is extremely difficult, if not impossible. Lanthanide ions such as Tb^{III} and Dy^{III} are an increasingly popular choice for SMM research due to their potential to generate very large magnetic anisotropy. However, their sensitivity to their crystal field environment requires a much more deliberate approach in order to efficiently maximise their SMM performance.

Appendix

Single Crystal X-ray data

All crystallographic intensity data were collected using a Bruker APEX2 CCD diffractometer or a FR590 ENRAF NONIUS Kappa CCD diffractometer equipped with graphite-monochromated Mo-K α radiation ($\lambda = 0.71073 \text{ \AA}$) and an Oxford Cryosystems low-temperature device. Structures were solved by using SUPERFLIP¹ and refined using full-matrix least-squares refinement on F² using CRYSTALS.²

Magnetic Susceptibility Measurements

Magnetic measurements in the temperature range 1.8-300 K were performed on polycrystalline samples constrained in eicosane, using a Quantum design SQUID magnetometer equipped with a 5 T magnet (the Manchester SQUID is equipped with a 7 T magnet). Data were corrected for the diamagnetism using Pascal's constants and for the diamagnetic contributions of the sample holder and eicosane by measurements.

Ultralow-temperature (< 1.8 K) hysteresis studies and dc relaxation measurements were performed on a single crystal using an array of micro-SQUIDS (the field is oriented along the easy axis, which is found in situ by changing the field orientation with three coils).³

Inelastic Neutron Scattering (INS)

For the INS experiments, the samples were sealed under helium in a hollow aluminium cylinder (for complex **6**; outer diameter 12 mm, inner diameter 9 mm. For complex **7**; outer diameter 12 mm, inner diameter 10 mm). Initial neutron wavelengths (energies) of 4.3 \AA (35.6 cm^{-1}) and 5.5 \AA (21.8 cm^{-1}) were selected with the (002) reflection of the pyrolytic graphite monochromator. The spectra were corrected for the contributions of the sample environment and the sample holder by measuring an empty aluminium cell, while the detector efficiency was assessed using a vanadium sample. Data reduction was performed with DAVE.⁴

References

- (1) L. Platinus, G. Chapuis, *Journal of Applied Crystallography* 40 (2007) 786
- (2) P. W. Betteridge, J. R. Carruthers, R. I. Cooper, K. Prout, D. J. Watkin, *Journal of Applied Crystallography* 36 (2003) 1487
- (3) W. Wernsdorfer, *W. Adv. Chem. Phys.* 118 (2001) 99
- (4) R. T. Azulah, L. R. Kneller, Y. M. Qui, P. L. W. Tregenna-Piggott, C. M. Brown, J. R. D. Copley, R. M. Dimeo, *J. Res. Natl. Inst. Stand. Technol.* 114 (2009) 341